Magnetisation transfer NMR spectroscopy in a kinetic and mechanistic study of fluoride transfer from tetra-*n*-butylammonium difluorotriphenylsilicate (TBAT)

Maciej M. Kucharski

Doctor of Philosophy

The University of Edinburgh

2023

Declaration

I declare that this thesis has been written by myself, and that the findings it describes are original and my own. This work has not been submitted for any other degree or professional qualification and has not yet been communicated in any publications.

Date: 13 February 2023

Signature: Maciej M. Kucharski

Abstract

Tetra-*n*-butylammonium difluorotriphenylsilicate ($^{n}Bu_4NPh_3SiF_2$, known as TBAT) is a pentacoordinate silicon-based fluoride source, commonly used in nucleophilic fluorinations and as an anionic initiator. The mechanism *via* which TBAT transfers the fluoride is not understood, but prior studies have shown that the process is rapid with respect to standard *in situ* NMR spectroscopic measurements. We used two ^{19}F magnetisation transfer NMR techniques to interrogate the process directly: ^{19}F chemical exchange saturation transfer (CEST) to examine whether TBAT dissociates into fluorotriphenylsilane (Ph_3SiF, FTPS) and tetra-*n*-butylammonium fluoride ($^{n}Bu_4NF$, TBAF) in solution; and ^{19}F inversion transfer to interrogate the kinetics and mechanism of fluoride transfer from TBAT.

We first derived analytical solutions which describe the kinetics of ^{19}F magnetisation transfer in mixtures of TBAT and the appropriate fluoride acceptors, in the inversion transfer experiments. These kinetic models enabled the interrogation of the transfer pathways in the systems, as the dependence of the magnetisation transfer rate between the spins on concentrations of the involved species varies between the proposed mechanisms in each system.

CEST experiments showed that in THF and MeCN, TBAT dissociates reversibly into FTPS and TBAF. The degree of dissociation is low and the spins exchange rapidly at 300 K. Depending on the amount of adventitious water, TBAF may be involved in further equilibria or decompose. Tetra-*n*-butylammonium bifluoride ($^{n}Bu_4NHF_2$, TBABF) is likely formed in either case.

Preliminary inversion transfer experiments showed a very rapid exchange between TBAT and FTPS in their equilibrium mixture in THF. An inherent temporal instability was observed, whereby the rate of exchange between the spins increased over time in closed systems (under N_2 atmosphere). Upon screening of potential stabilising conditions, it was found that two additives, 2,6-di-*tert*-butylpyridine and 3 Å molecular sieves, reversed the trend when used concurrently, slowing down the reaction until temporal stability of exchange rate in the system was reached. The effect of concentration of FTPS under these conditions (at a constant concentration of TBAT)

showed that both dissociative and direct pathways proceed in parallel. The dissociative pathway was also confirmed in the non-stabilised system by observing an initial decrease of the inversion transfer rate in a rapid titration of a concentrated solution of TBAT with small aliquots of FTPS.

Inversion transfer between TBAT and 2-naphthalenyl fluorosulfate ($ArOSO_2F$, ARSF) was detected in MeCN at 300 K, and inhibited to below the detection limit upon addition of exogeneous FTPS (~4 mM). At 335 K, progressive inhibition of the exchange was observed in solutions of TBAT and ARSF in MeCN due to decomposition of TBAT and hence formation of FTPS.

Overall, we postulate that the fluoride transfer from TBAT occurs *via* both dissociative and direct transfer pathways proceeding in parallel, and that the contributions of these pathways are dependent upon the conditions (solvent, temperature, adventitious water, nature and concentration of the fluoride acceptor *etc*.).

Moreover, ^1H diffusion analysis of TBAT in THF-d_8 and MeCN-d_3 indicated strong ion pairing, confirmed by the observation of nuclear Overhauser effect (NOE) between the ^1H spins of $^nBu_4N^+$ and $Ph_3SiF_2^-$.

Lay summary

Tetra-*n*-butylammonium difluorotriphenylsilicate (known as TBAT) is a reagent used in chemical synthesis to perform certain transformations on other molecules. In most cases it is used as a fluoride donor, *i.e.* a small "part" of the reagent (fluoride) is detached from it and placed onto a different molecule – either to stay there as a part of the newly formed product, or to initiate a chain of events which lead to the desired product(s) eventually. In either case, the leftover part of TBAT is a by-product, there to stay until the reaction is over and the desired product(s) can be isolated. As the chemical name of this leftover part of TBAT is a mouthful (most of them are), we abbreviated it to FTPS. The mechanism of the fluoride transfer from TBAT, that is the exact choreography of events which describe the reaction, is unknown. Of particular importance is whether the transfer is dissociative or direct. In the dissociative pathway, TBAT detaches the fluoride by itself and any potential acceptor can then "claim" it. In the direct pathway, TBAT "meets" the acceptor to hand over the fluoride.

The overall process was previously shown to be very rapid and thus challenging to study. Mechanisms of reactions are usually elucidated by measuring how the concentrations of species change over time, and how these changes are affected by conditions, *e.g.* how much of each substrate ("ingredient") is used. Here, the fluoride transfer is over before we can make the first measurement using routine methods. However, FTPS, which is the by-product of the fluoride transfer from TBAT, can also accept the fluoride from it. Therefore, mixing TBAT and FTPS in solution results in the exchanging of the fluoride between the species. TBAT donates the fluoride, changing into FTPS, and FTPS accepts the fluoride, changing into TBAT. This exchange leads to no change in the amounts of TBAT and FTPS but always happens rapidly, nonetheless. It turns out that in a certain measurement technique, nuclear magnetic resonance (NMR) spectroscopy, we can (almost instantaneously) selectively "label" either TBAT or FTPS, by inverting the nuclei of ^{19}F atoms present in either of these species – *i.e.* changing the magnetic properties of these ^{19}F nuclei. This label does not change the chemical properties of the species, but now any exchange event (TBAT to FTPS and FTPS to TBAT) results in the transfer of the label between the species. Therefore, the rate of fluoride exchange between TBAT and FTPS can be monitored.

This rate depends on the concentrations of TBAT and FTPS in the solution, differently for each of the proposed transfer pathways. Thus, the selective labelling of one species and detecting the label in the other one enables us to interrogate the mechanism of the reaction.

Using this label transfer method, we first confirmed the presence of a very small amount of the free fluoride and FTPS in solutions of TBAT, *i.e.* that TBAT does indeed detach fluoride by itself. The fluoride and FTPS were not observed in the solution by direct measurement (as they were below the detection limit), but rather *via* selectively labelling them (continuously for some time), and then observing the label transfer to TBAT.

Then, we mixed TBAT and FTPS in a certain solvent (THF) and selectively labelled FTPS. The reaction was indeed found to be very rapid. The solution was also found to be temporally unstable with respect to the rate with which the label was transferred between the species. For a given solution this rate should be constant, *i.e.* if we label FTPS, wait for some time and then detect the label in TBAT, the same amount of the label should be transferred between the species each time we perform the experiment, provided that we wait equally long between the labelling and detecting the label each time. The observation that this was not the case in our system meant that something was happening in the solution over time, which we could not observe and which affected the rate of exchange.

Although we could not observe whatever was happening to the solution, we found that when certain two additives were used together, we could render the exchange rate temporally stable. In such stabilised mixtures, the effect of the concentration of FTPS on the exchange rate showed that both dissociative and direct fluoride transfer pathways were present. In other words, TBAT detached the fluoride, which was then picked up by FTPS. Concurrently, TBAT and FTPS met directly, also to exchange it.

In a different solvent (MeCN), we used mixtures of TBAT and another fluoride acceptor (we called it ARSF). Here, the addition of FTPS to the mixture should have no effect on the rate of exchange *via* the direct pathway (TBAT and ARSF meet and perform the “transaction”, regardless of the presence of FTPS). However, FTPS picks up a lot of the free fluoride in the mixture, leaving less of it available for ARSF, and hence slowing down the dissociative exchange of fluoride between TBAT and ARSF. We observed this effect and the extent of it depended on the conditions, confirming again that both exchange pathways are present in the system.

Acknowledgements

First things first, I thank Guy for the opportunity to work on this project and for his mentorship throughout my PhD. I am grateful for his expertise, wisdom, ever-encouraging words and unlimited patience.

I thank Dr Andrew Hall, Dr Juraj Bella, Dr Claire Dickson, and Prof. Dušan Uhrín for their invaluable help with all-things-NMR.

I thank all the wonderful members of the Lloyd-Jones (GL-Just Fabulous) group. I can't imagine ever again finding such a passionate, inspiring, supportive and loyal bunch. I am profusely grateful to them for being a second family to me during my time in the lab and cannot describe with words how much I will miss them.

I thank my high school chemistry teacher, Dr Ludmiła Szterenberg, for helping me spread my scientific wings many moons ago, and for accompanying me to a pint or coffee whenever I visit home.

I thank my parents for their unconditional love and support, and for always encouraging my freedom of choice and expression.

I thank my no-longer-so-little brother for simply being great.

I thank my grandma for always keeping me fed, among all other classic-grandma-stuff.

I thank all of my friends, whom I love dearly but will never text back. I am truly honoured to have each one of them in my life.

I thank my man, Smokey, and his crew. (They know what for).

I thank my kweens, Amy, Britney, CupcakKe, Dolly, Elton, Freddie, Kasia, Kora, Madonna, Miley, Nina, Patti, Rhianna, and Stevie, for the best drug there is.

Last but not least, I thank my enemies – for fuelling me.

To each of these mentioned above and everyone else I met along this unbelievable ride, I owe my most sincere gratitude – for helping me become who I am today and who I will be tomorrow.

M.

Contents

Abbreviations

–	anion
(s)	solid
+	cation
1,2-DFB	1,2-difluorobenzene
1D	one-dimensional
2D	two-dimensional
Ac	acetyl
acq	acquisition
aliq.	aliquot
Ar	aryl
ARSF	2-naphthalenyl fluorosulfate
AS	autosampler
BARF$^-$	tetrakis[3,5-bis(trifluoromethyl)phenyl]borate (anion **1.11**)
cat	catalyst
CEST	chemical exchange saturation transfer
COSY	correlation spectroscopy
d.f.	dilution factor
DMPU	*N*,*N′*-dimethylpropyleneurea
DMSO	dimethyl sulfoxide
D^{t}BP	di-*tert*-butylpyridine
E$^+$	electrophile
eq	equilibrium

equiv.	equivalent(s)
ESI-MS	electrospray ionisation mass spectrometry
Et	ethyl
exp	experimental
EXSY	exchange spectroscopy
FTPS	fluorotriphenylsilane
GB	glovebox
GRG	generalized reduced gradient
HIV-1	human immunodeficiency virus 1
HMBC	heteronuclear multiple bond correlation
HSQC	heteronuclear single quantum coherence
^{i}Pr	isopropyl
Me	methyl
MS	molecular sieves
Ms	methanesulfonyl (mesyl)
n	normal
NAPH	1-fluoronaphthalene
^{n}Bu	normal butyl
NFSI	*N*-fluorobenzenesulfonimide
NMR	nuclear magnetic resonance
NOE	nuclear Overhauser effect
NOESY	nuclear Overhauser effect spectroscopy
obs	observed
PET	positron emission tomography

Ph	phenyl
ppm	parts per million
p-Tol	*para*-tolyl
R	alkyl or aryl
r.t.	room temperature
R1	reaction 1
R2	reaction 2
R3	reaction 3
R4	reaction 4
rds	rate-determining step
RO	reverse osmosis
s	stabilised
sat	saturation
solv	solvent
TBABARF	tetra-*n*-butylammonium tetrakis[3,5-bis(trifluoromethyl)phenyl]borate
TBABF	tetra-*n*-butylammonium bifluoride
TBAF	tetra-*n*-butylammonium fluoride
TBAT	tetra-*n*-butylammonium difluorotriphenylsilicate
TBS	*tert*-butyldimethylsilyl
Tf	trifluoromethanesulfonyl (triflyl)
THF	tetrahydrofuran
TMB	1,3,5-trimethoxybenzene
TMS	trimethylsilyl
w	water

Chapter 1

Introduction

1.1. Fluorine in organic and organometallic chemistry

1.1.1. Organofluorine compounds

Fluorine is an important element to modern organic and organometallic chemistry. Organofluorine compounds, although rarely found in nature (Figure 1.1a),[1,2] are commonly used in academic and industrial research. Several features of fluorine render the properties of these compounds interesting and potentially desirable.[3] Fluorine is the most electronegative element and one of the smallest in size in the periodic table.[4,5] Consequently, carbon–fluorine bonds ($C^{\delta+}$–$F^{\delta-}$) are short, strong, and highly polarised.[3] Despite the polarised nature of these bonds, they tend not to involve in hydrogen, nor dative bonding. This phenomenon stems from the proximity of the fluorine lone electron pairs to the nucleus, which decreases their availability for Lewis acids.[3] Therefore, swapping certain moieties for fluorine-containing ones, can offer otherwise inaccessible changes to the properties of organic compounds. For example, a fluorine atom in place of a hydrogen may have a significant effect on the electronic properties of the molecule, whilst the steric properties are influenced to a much lesser extent.[3,6] Due to these properties of fluorine and C–F bonds, organofluorine compounds have been used widely in many industries, for example pharmaceutical and agrochemical,[7–9] where the incorporation of one or more fluorine atoms can offer enhanced chemical and metabolic stability, activity and bioavailability of the compounds compared to their non-fluorinated analogues. Some examples of organofluorine pharmaceuticals (Figure 1.1b) include an antidepressant fluoxetine (**1.2**),[10] emtricitabine (**1.3**),[11] which in combination with other antiretroviral drugs is used in prevention and treatment of HIV-1, and a breast cancer drug fulvestrant (**1.4**).[12] Flupentiofenox (**1.5**) and fluopimomide (**1.6**) are examples acaricides and fungicides, respectively (Figure 1.1c).[7] Many of everyday use polymers also contain C–F bonds (*e.g.* polytetrafluoroethylene, known as Teflon, **1.7**, Figure 1.1d), which offer increased stability to harsh conditions, decreased friction, and weakened adhesion.[13,14] Fluorophores, organic electronics and liquid crystals are among other types of materials where organofluorine compounds are found.[15–17]

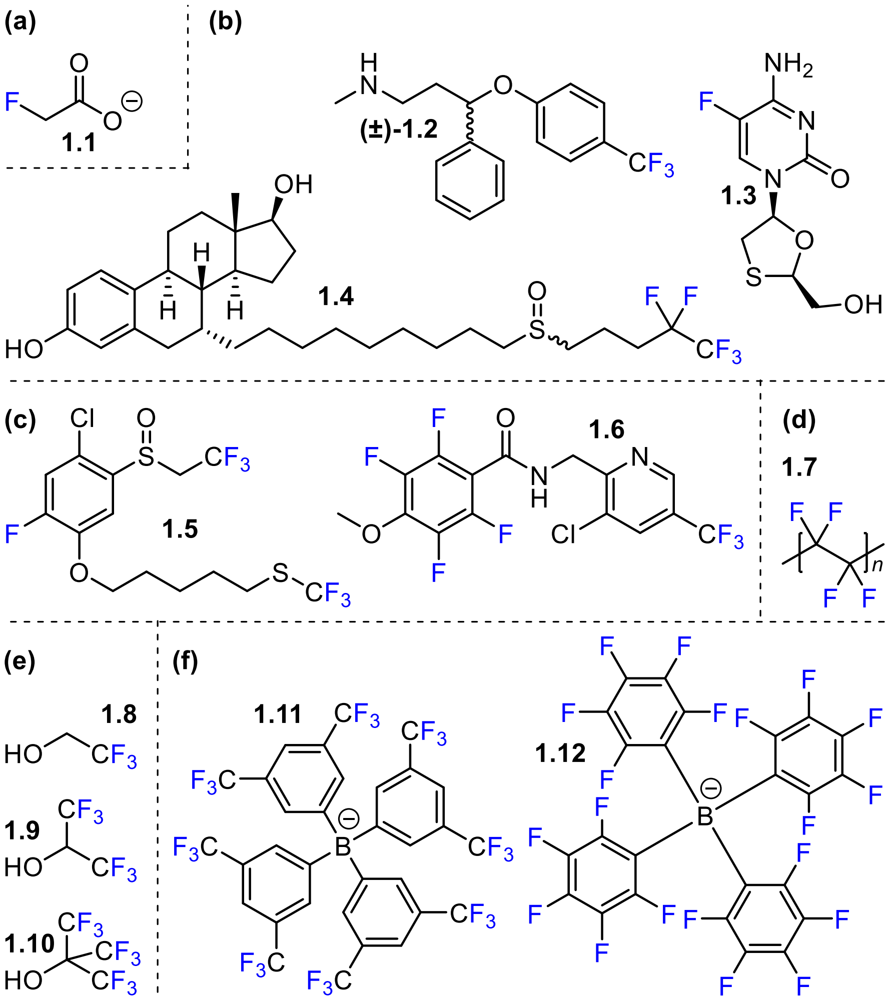

Figure 1.1: Examples of organofluorine compounds. (a) Highly toxic fluoroacetate (1.1) was isolated from *Dichapetalum cymosum* (a South African plant known as gifblaar) in 1943 and is one of few known fluorinated natural products.[2] (b) Organofluorine pharmaceuticals fluoxetine (1.2), emtricitabine (1.3) and fulvestrant (1.4).[10–12] (c) Organofluorine agrochemicals flupentiofenox (1.5) and fluopimomide (1.6).[7] (d) Polytetrafluoroethylene (1.7) is arguably the most famous polymer.[13,14] (e) 2,2,2-Trifluoroethanol (1.8), 1,1,1,3,3,3-hexafluoropropan-2-ol (1.9) and 1,1,1,3,3,3-hexafluoro-2-(trifluoromethyl)propan-2-ol (1.10) are common fluorinated solvents.[18] (f) Tetrakis[3,5-bis(trifluoromethyl)phenyl]borate (1.11) and tetrakis(pentafluorophenyl)borate (1.12) are weakly-coordinating anions.[19–21] (The B–C bonds in the structure of anion 1.12 are elongated for clarity).

In synthetic chemistry, organofluorine compounds are valuable reagents, catalysts, ligands, additives, and solvents. For example, the triflate group ($–OSO_2CF_3$, abbreviated as –OTf) is, among other perfluoroalkylsulfonates, one of the best anionic leaving groups,[22] and triflate salts of rare-earth metals are used as Lewis acid catalysts in important carbon–carbon and carbon–heteroatom bond-forming reactions.[23] Common fluorinated solvents include 2,2,2-trifluoroethanol (**1.8**), 1,1,1,3,3,3-hexafluoropropan-2-ol (**1.9**) and 1,1,1,3,3,3-hexafluoro-2-(trifluoromethyl)propan-2-ol (**1.10**), presented in Figure 1.1e, and are known to have a stabilising effect on carbocationic reactive intermediates.[18] Fluorinated tetraarylborates (Figure 1.1f), such as tetrakis[3,5-bis(trifluoromethyl)phenyl]borate and tetrakis(pentafluorophenyl)borate (**1.11** and **1.12**, respectively), found use in synthesis and electrochemistry as weakly-coordinating anions.[19–21] 1,2-Disubstituted ethene motifs, where a fluorine substituent is vicinal to an electron-withdrawing group (*e.g.* fluorine, ester or ammonium, Figure 1.2a), are used to control the stereoselectivity of some transformations as a result of the fluorine *gauche* effect (Figure 1.2b; for comparison, Figure 1.2c shows a decrease in yield and selectivity in the absence of the effect).[24–26] This effect stems from the stabilisation of the substituents in the *gauche* conformation due to hyperconjugation and/or electrostatic attraction, which is greater than the steric strain imposed by their proximity (*e.g.* intermediate **1.16** in reaction shown in Figure 1.2b).

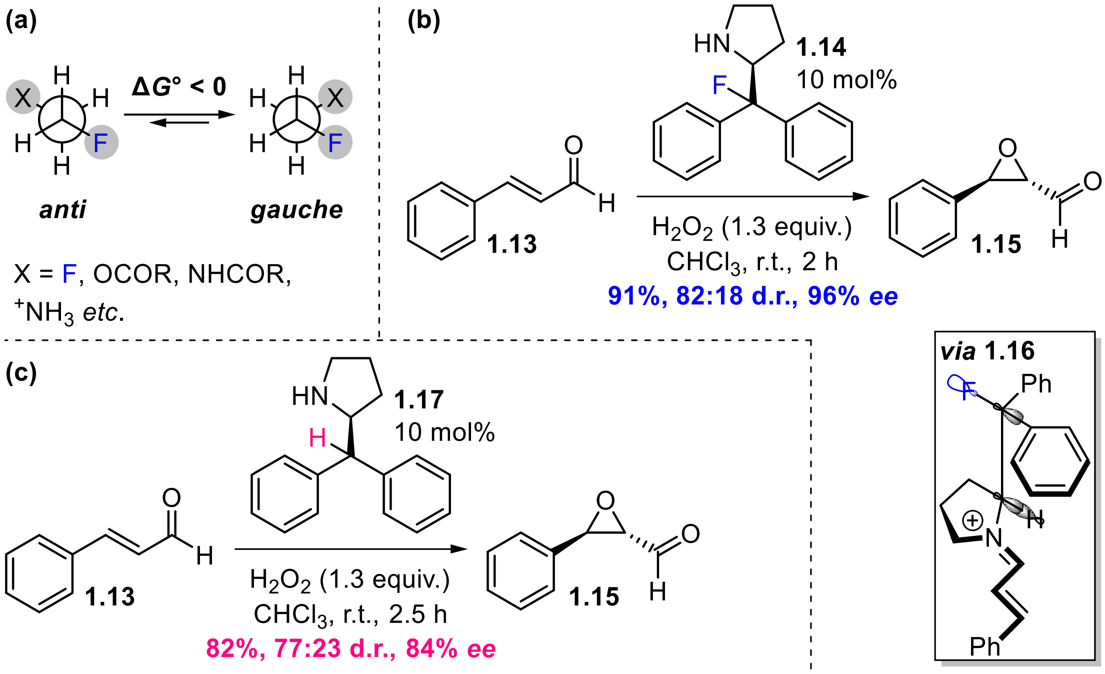

Figure 1.2: (a) The *gauche* effect in $CH_2F–CH_2X$, where X is an electron-withdrawing group.[24–26] (b) Application of the fluorine *gauche* effect in an organocatalytic epoxidation of *trans*-cinnamaldehyde (1.13).[27] (c) Using a non-fluorinated analogue of the catalyst, 1.17, results in a decrease in yield and stereoselectivity of the epoxidation.[27]

Unsurprisingly, considering the discussed properties of fluorine and its bonds to carbon, phrasings such as “one of the most” are used often to describe fluorine (including organofluorine) compounds. In many cases, these statements are not exaggerated, making fluorine a fascinating element from the point of view of pure chemistry. For example, all-*cis*-1,2,3,4,5,6-hexafluorocyclohexane was reported in 2015 as one of the most polar non-ionic molecules discovered to date (dipole moment, $\mu = 6.2$ D).[28]

Furthermore, fluorine is used in analytical chemistry, within nuclear magnetic resonance (NMR) spectroscopy and positron emission tomography (PET). ^{19}F is a 100% abundant, stable isotope of fluorine, well suitable for NMR spectroscopy.[29–32] The ^{19}F nucleus is NMR active with a spin of 1/2 and magnetogyric ratio of $2.52 \cdot 10^8$ rad s^{-1} T^{-1}, thus making it the second most receptive after ^1H (receptivity of 0.834 relative to ^1H). Longitudinal relaxation times of ^{19}F nuclei are typically relatively short, enabling for quick quantitative analyses. The wide window of resonance frequencies, their sensitivity to chemical environment and generally smaller number of ^{19}F spins in organic and organometallic molecules compared to ^1H may be of advantage in terms of lower likelihood of signal overlap. Far-reaching couplings are also typically observed in the NMR spectra of fluorine-containing species.[33] Therefore, ^{19}F NMR spectroscopy offers complimentary means of structural and conformational assignment of molecules and their mixtures, as well as the possibility of quantitating the signals, which is often used in monitoring of irreversible and reversible organic and organometallic reactions. Another fluorine isotope, radioactive ^{18}F, is commonly used in PET.[34,35] Due to its optimal half-life (110 min) and mode of decay (97% positron emission and 3% electron capture), it became one of the earliest tracers used in medicine. Although the isotope is naturally occurring, it is only found in trace amounts and hence must be synthesised prior to placing the ^{18}F tag on the parent molecule.

1.1.2. Synthesis of organofluorine compounds

Due to the high and continuously growing demand for organofluorine compounds coupled with the scarcity of them in nature, methods for chemo-, regio- and stereoselective incorporation of moieties such as $-F$, $-CF_3$, $-OCF_3$, $-SCF_3$ (among others) are in demand. Several methods of incorporating these moieties have been developed, and can be grouped into three main types: nucleophilic,[36–52] electrophilic,[36,39,41,44,48,52–55] and radical.[36,39,44,48,52,53,56]

Fluorine atoms can be incorporated into organic molecules by means of addition and substitution reactions of electrophiles with sources of nucleophilic fluoride. Various reagents can be used in the reactions, and include: complexes of hydrofluoric acid with organic bases (*e.g.* pyridine or Et_3N),[45] or more recently with weakly basic and nucleophilic hydrogen bond acceptors (*e.g.* DMPU);[50] metal fluorides, often in the presence of phase-transfer catalysts (*e.g.* alkali metal fluorides and chiral hydrogen-bonding phase-transfer catalysts for enantioselective fluorinations, Scheme 1.1a);[42,49] tetraalkylammonium fluorides (*e.g.* $^{n}Bu_4NF$, known as TBAF);[51] hypervalent 'ate' complexes containing X–F bonds (where X is most commonly Si, *e.g.* TBAT, Section 1.2);[38,46,47] or sophisticated nucleophilic organofluorine agents.[37,40,43]

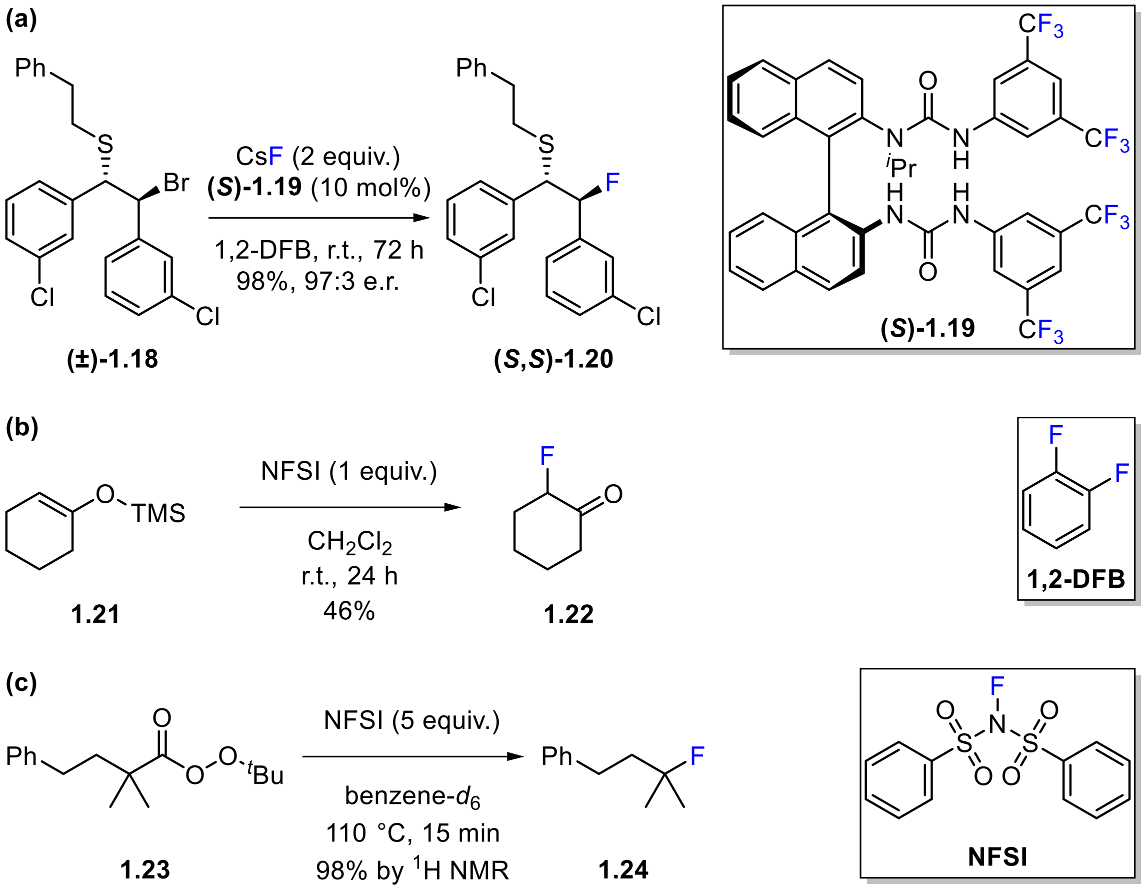

Scheme 1.1: Examples of fluorination reactions. (a) Enantioselective nucleophilic fluorination using CsF in the presence of a hydrogen-bonding phase-transfer catalyst (*S*)-1.19 (in a fluorinated solvent, 1,2-difluorobenzene, 1,2-DFB).[42] (b) Electrophilic and (c) radical fluorination reactions using NFSI.[55,56]

Electrophilic fluorinating agents were developed as attractive alternatives to elemental fluorine (F_2) and are largely based on N–F bonds.[41] These reagents can also be used in radical fluorination reactions under appropriate conditions.[36,56] For example, *N*-fluorobenzenesulfonimide (NFSI) is a common source of electrophilic fluorine (Scheme 1.1b), which was also shown to fluorinate alkyl radicals generated from *tert*-butyl peresters (Scheme 1.1c).[55,56]

Similarly to fluorinations, various reagents have been developed that act as reservoirs of organofluorine moieties in their incorporations into organic molecules.[39,41,44,48,52–55] Of particular importance are trifluoromethylating reagents; a selection of which is presented in Figure 1.3. Sources of electrophilic “CF_3^+” include the Togni reagent II (**1.25**) and Umemoto reagents I and II (**1.26** and **1.27**, respectively).[53,54] Nucleophilic trifluoromethylation is most commonly carried out using the Ruppert-Prakash reagent, $TMSCF_3$ (**1.28**).[52]

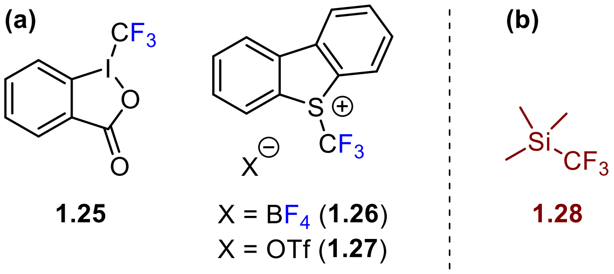

Figure 1.3: Examples of trifluoromethylating agents. (a) Sources of electrophilic “CF_3^+”: Togni reagent II (1.25) and Umemoto reagents I and II (1.26 and 1.27, respectively).[53,54] (b) Source of nucleophilic “CF_3^-”, Ruppert-Prakash reagent ($TMSCF_3$, 1.28).[52]

1.1.3. Fluoride anion

As described in Section 1.1.2, fluorine can be introduced into organic molecules by means of nucleophilic fluorinations using the fluoride anion. However, the importance of fluorine in organic chemistry extends beyond organofluorine compounds themselves. Fluoride in various forms described above is used as a nucleophile and hydrogen-bond acceptor, capable of cleaving Si–X bonds (X = C, N, O) as well as increasing the nucleophilicity of hydrogen-bond donors (*e.g.* alcohols).[57]

The use of metal and tetraalkylammonium fluorides may be problematic. Firstly, salts of the fluoride anion tend to be hygroscopic. Whilst water can be removed from alkali metal fluorides upon heating them *in vacuo*, tetraalkylammonium fluorides decompose at high temperatures, as naked fluoride is a strong Lewis base.[58] The tetraalkylammonium cations are therefore susceptible to Hofmann elimination.[59] For example tetra-*n*-butylammonium fluoride, TBAF, is a hygroscopic solid, which due to the high affinity of the fluoride to water, cannot be dried to below 10 mol% water without decomposition.[59,60] The bifluoride anion (HF_2^-) is formed during the process in significant quantities. A method was developed for *in situ* generation of anhydrous TBAF, where the formed salt is stable only at low temperatures.[61] The presence of water (and other hydrogen-bonding donors) affects the properties of fluoride significantly, and thus the varying water content may induce irreproducibility in reactions and mechanistic analyses. In fact, the true nature of the “fluoride” itself is not well studied in solution.

1.2. Tetra-*n*-butylammonium difluorotriphenylsilicate (TBAT)

1.2.1. Synthesis and properties

Tetra-*n*-butylammonium difluorotriphenylsilicate (TBAT) was first reported in 1995 by DeShong *et al*. as an alternative fluoride source to TBAF in nucleophilic fluorination reactions.[62] It is an anhydrous, non-hygroscopic and relatively high-melting (155-156 °C) crystalline solid, soluble in various organic solvents and significantly less basic (albeit concurrently less nucleophilic) than TBAF.[63] It was synthesised in a two-step process (Scheme 1.2a): (i) reaction of triphenylsilanol (**1.29**) with hydrofluoric acid to form fluorotriphenylsilane (FTPS); (ii) reaction of the obtained FTPS with TBAF.[62,63] TBAT was then recrystallised from ethyl acetate, although mixtures of dichloromethane with hexanes and acetonitrile with diethyl ether were also found to be suitable solvent systems.[63,64] In the same year, a safer route was reported by Albanese *et al*. (Scheme 1.2b), where a reaction of triphenylsilane (**1.30**) with tetra-*n*-butylammonium bifluoride (TBABF) under anhydrous conditions gave the salt in high yield and with no purification required.[65] Lastly, Mąkosza and Bujok reported that TBAT is formed in a reaction of FTPS (prepared from phenylmagnesium bromide and SiF_4) with tetra-*n*-butylammonium hydrogen sulfate ($^{n}Bu_4NHSO_4$) and excess KF (Scheme 1.2c).[64] TBAT is now available commercially from a range of suppliers.

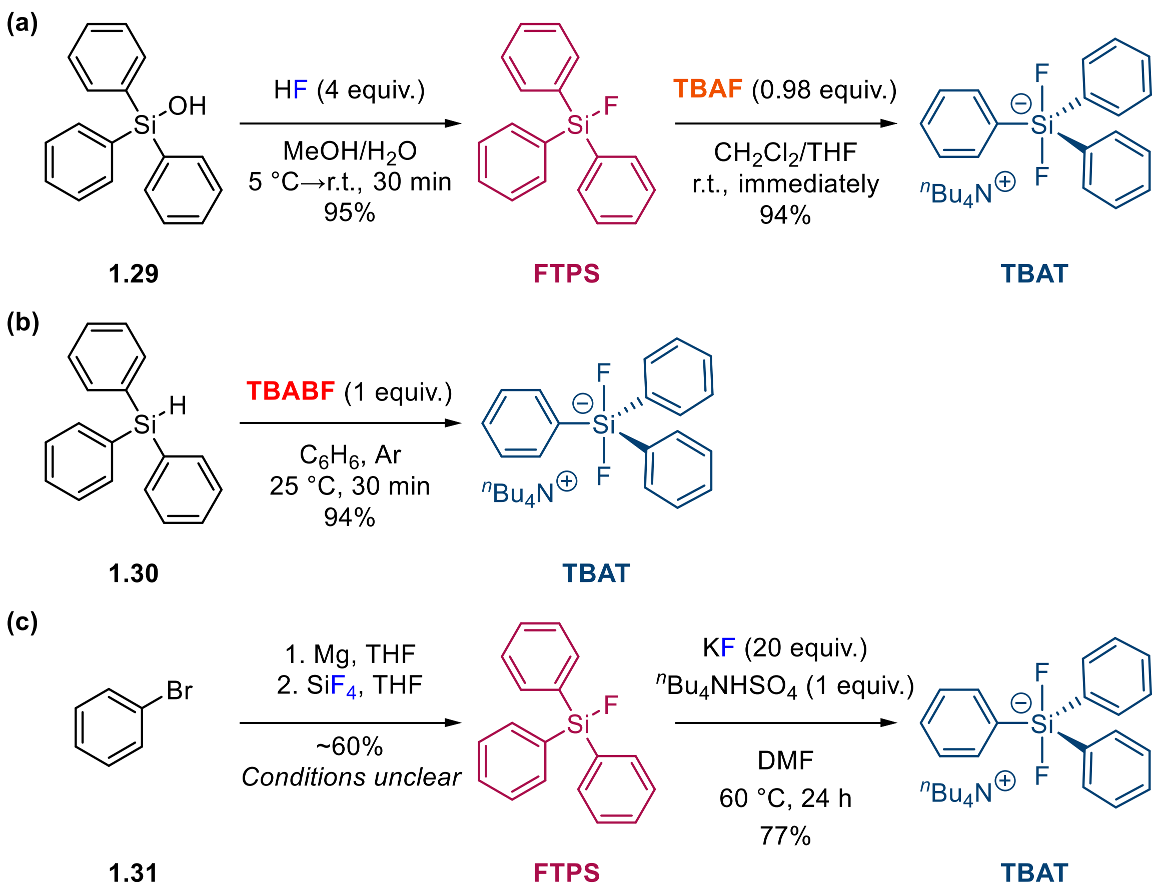

Scheme 1.2: Synthesis of TBAT. (a) DeShong *et al*. reported the synthesis of TBAT in a reaction of FTPS (prepared from triphenylsilanol and HF) with TBAF.[62,63] (b) Albanese *et al.* synthesised TBAT in a reaction of triphenylsilane with TBABF.[65] (c) Mąkosza and Bujok reported the synthesis of TBAT in a reaction of FTPS (prepared from phenylmagnesium bromide and SiF_4) with tetra-*n*-butylammonium hydrogen sulfate ($^nBu_4NHSO_4$) and excess KF.[64]

1.2.2. Synthetic applications of TBAT

Three main modes of reactivity of TBAT were identified to date. In two of them, it is used as a source of nucleophilic fluoride, “$F^–$”, either in fluorination reactions (*i.e.* incorporation of the fluorine atom from TBAT in the product or by-product) or *in situ* generation of reactive intermediates (*i.e.* where the fluorine atom from TBAT is not incorporated into the products but rather an initiator of the catalytic cycles or a catalyst itself). In the third mode, TBAT is a source of phenyl synthon in cross-coupling reactions. An overview of the reactivity of the salt can be found in the *Encyclopedia of Reagents for Organic Synthesis* (last updated in 2020).[47]

As a phenyl source, TBAT has been used modestly. In the presence of a palladium(0) catalyst, it phenylates aryl (pseudo-)halides (iodides, triflates and electron-deficient bromides) and allyl benzoates.[66–68]

As a nucleophilic fluorinating agent, TBAT has been used in substitution reactions of alkyl halides and sulfonates,[62,69] which can also be generated *in situ*;[70] as well as activated epoxides.[71] Ring-openings by fluoride addition to iminium ethers and α-fluorinations of activated amides were also reported.[72,73] Ar–F (*via* nucleophilic aromatic substitution or oxidative fluorination) and Ar–CF_3 (in the presence of *in situ* generated difluorocarbene) bonds can be constructed using the reagent.[74–77] Moreover, TBAT is commonly used in desilylation reactions (with formation of a Si–F by-product), where the formed anion(oid) can protonate or further react with electrophiles.[78–84] Desilylation of *ortho*-(trimethylsilyl)aryl triflates using the reagent is a convenient way of accessing arynes as reactive intermediates in valuable transformations.[85–108] Recently, TBAT was used in nucleophilic substitution of iodide and mesylate (–OMs) with fluoride in a study of the reactivity of steroid hormones and their fluorinated derivatives towards cytochromes (Scheme 1.3).[109] Notably, here TBS (*tert*-butyldimethylsilyl) and Ac (acetyl) protecting groups in the I → F substitutions were stable to refluxing the substrate in the presence of TBAT in MeCN. The deprotection steps were achieved using HF·pyridine and K_2CO_3, respectively.

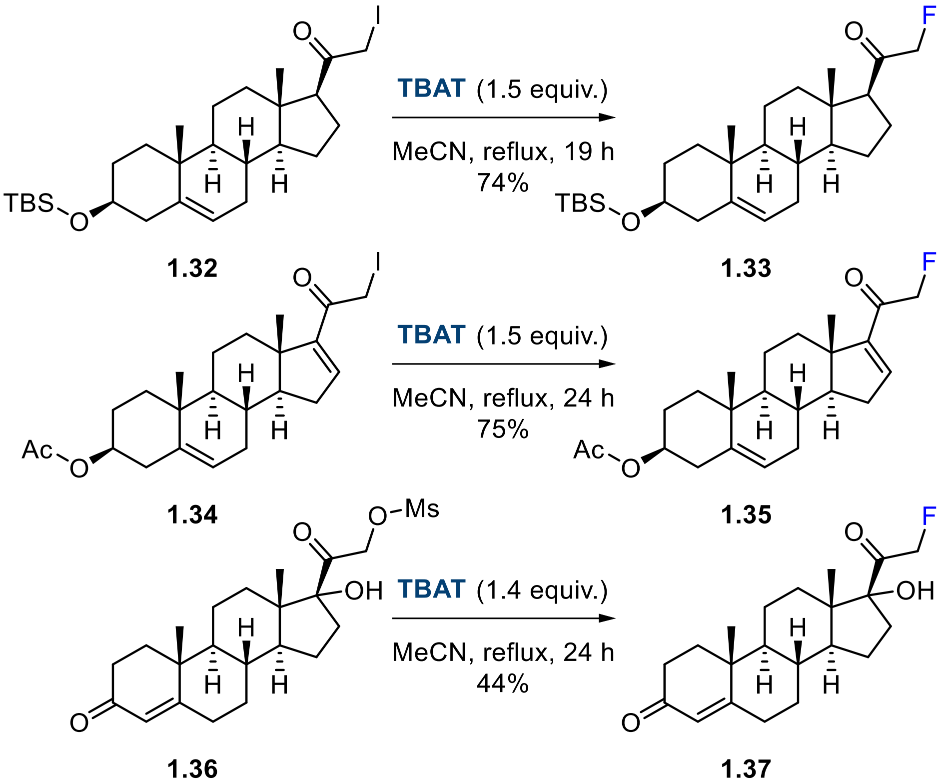

1.32 1.33 1.34 1.35 1.36 1.37

Scheme 1.3: Nucleophilic fluorination reactions using TBAT, in the synthesis of fluorinated steroid hormone derivatives.[109] The fluorination reactions of iodides 1.32 and 1.34 were performed by refluxing their solutions in MeCN in the presence of excess of TBAT (1.5 equiv.) for 19 h and 24 h, respectively. The fluorination reaction of mesylate 1.36 was performed by refluxing its solution in MeCN in the presence of excess of TBAT (1.4 equiv.) for 24 h.

Finally, TBAT is used as an initiator to generate nucleophiles by cleavage of Si–X bonds (X = C,[110–142] N,[143–146] O,[147–161] S).[149] In most cases, the newly formed nucleophiles then attack suitable electrophiles.

An important reagent used in the presence of catalytic amounts of TBAT as initiator is $TMSCF_3$ (the Ruppert-Prakash reagent, **1.28**, Figure 1.3b in Section 1.1.2).[130,132,162,163] Depending on the substrate, it is capable of trifluoromethylation,[124–131] difluorocarbene insertion,[122,132,133] and trimethylsilylation reactions.[122,137] A representative example of the multifunctional role of $TMSCF_3$ (**1.28**) is presented in Scheme 1.4,[122] where the CF_3^- anion(oid), formed in TBAT-initiated cleavage of the Si–CF_3 bond, first deprotonates ethyl salicylate (**1.38**). The conjugate base **1.39** then traps difluorocarbene formed in an equilibrium elimination reaction of fluoride from CF_3^-. Intermediate **1.40** is trimethylsilylated, followed by deprotection of the silyl ether **1.41** by fluoride (formed in the equilibrium elimination reaction from CF_3^-), which results in the formation of the cyclisation product **1.42**.

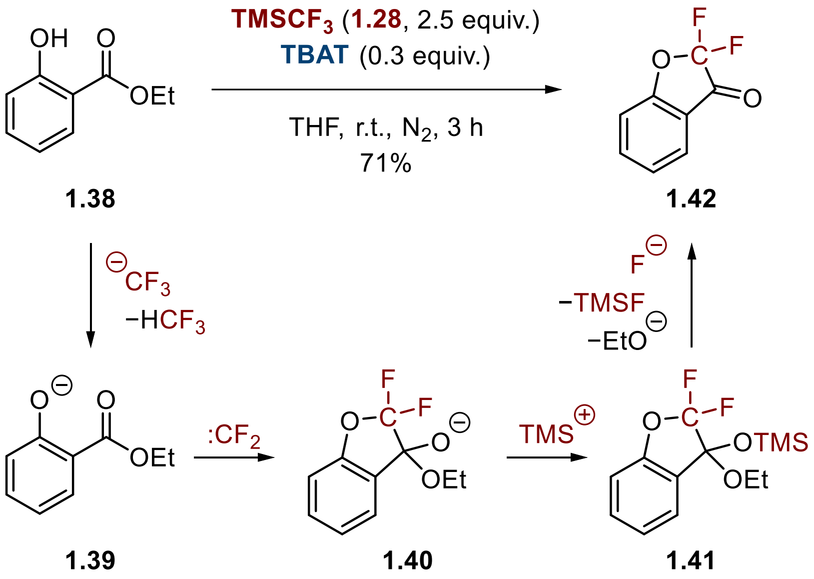

Scheme 1.4: A cyclisation reaction of ethyl salicylate (1.38) using $TMSCF_3$ and TBAT as an initiator, and the simplified mechanism of the reaction highlighting key roles of $TMSCF_3$ as donor of CF_3^-, $:CF_2$, TMS^+ and F^-.[122]

Allylations are performed from the appropriate allylsilanes (*via* nucleophilic allyl moieties) or electrophilic allyl moieties in the presence of palladium catalysts,[110,111,134–136,138,147,148,154] Aldol reactions (with TBAT as a co-initiator in the Mukayiama aldol reaction or as a mildly basic catalyst),[155–161,164] and polymerisations *via* nucleophilic aromatic substitutions of polyfluoroarenes are common as well.[139–141,149] TBAT has been utilised as an effective catalyst in fluorinations,[165] and as a co-catalyst/additive, which enhances the performance of organometallic catalysts (in terms of yields and/or regioselectivities).[166–169] Hydrodefluorinations in the presence of hydrosilanes,[170,171] and desilylative defluorinations were reported.[172–174] Moreover, activation and subsequent formation of reactive intermediates was also reported for organoaluminium and organotin reagents.[175,176]

1.2.3. Mechanistic considerations

The solution-phase dynamic behaviour of pentafluorosilicate and pentacoordinate fluoroorganosilicates ($R_xSiF_{5-x}^-$, where R is an alkyl or aryl group and x = 0, 1, 2 or 3) has been studied *via* NMR spectroscopy.[177–188] These anions adopt (pseudo-)trigonal bipyramidal geometries with the two axial positions occupied by fluorine atoms (Scheme 1.5a). Klanberg and Muetterties first reported that SiF_5^-, $RSiF_4^-$ (R = Me, ^{n}Bu, Ph) and $Ph_2SiF_3^-$ silicates (as tetraalkylammonium salts) exhibit fast exchange between the axial and equatorial fluorine atoms relative to NMR acquisition timescale (simply referred to as "fast exchange" onwards).[177] Although they postulated a structure- and temperature-dependent competition between intra- (no Si–F bond cleavage) and intermolecular (Si–F bond cleavage) exchange mechanisms, the interference of impurities with the exchange dynamics could not be excluded. These observations were followed by Marat and Janzen's detailed study of the effect of certain additives on the rate of fast intermolecular exchange in $MeSiF_4^-$.[178] Hydrofluoric acid, methanol and water were found to catalyse the process, whereas fluoride anion, $MeSiF_4^-$ and pyridine inhibited it. They then studied fast intermolecular fluorine exchange in SiF_4/SiF_5^-, $RSiF_3/RSiF_4^-$ (R = Me, Ph), SiF_5^-/SiF_6^{2-}, SiF_4/SiF_6^{2-} and $MeSiF_3/SiF_6^{2-}$ systems, and proposed the intermediacy of fluorine-bridged binuclear silicates in all pairs of exchanging partners (Scheme 1.5b).[181] Finally, studies on air- and moisture-insensitive 18-crown-6–K^+ salts of these silicates confirmed that the exchange between axial and equatorial fluorine atoms in $RSiF_4^-$ and $R_2SiF_3^-$ anions is fast at ambient temperature (Scheme 1.5c).[180,182–186] Coalescence and subsequent splitting of the time-averaged ^{19}F signal was observed for $R_2SiF_3^-$ silicates upon cooling the solutions.[182,184–186] For most $RSiF_4^-$ anions, however, the exchange is fast at all achievable temperatures.[180,182,183]. Contrarily to Klanberg and Muetterties' postulate,[177] intramolecular exchange was proposed as a sole axial-equatorial fluorine exchange pathway in (18-Crown-6–K^+) $RSiF_4^-$ and $R_2SiF_3^-$ silicates at all studied temperatures.[180,182–186] 18-Crown-6–K^+ salt of $Ph_3SiF_2^-$, reported by Damrauer and Danahey in 1986 (nine years prior to the first report of synthesis and use of TBAT, Section 1.2.1), showed no dependence of the NMR spectra on temperature. Based on this observation, they concluded that the two fluorine atoms occupy axial positions of the trigonal bipyramid and do not undergo exchange (Scheme 1.5d).[182]

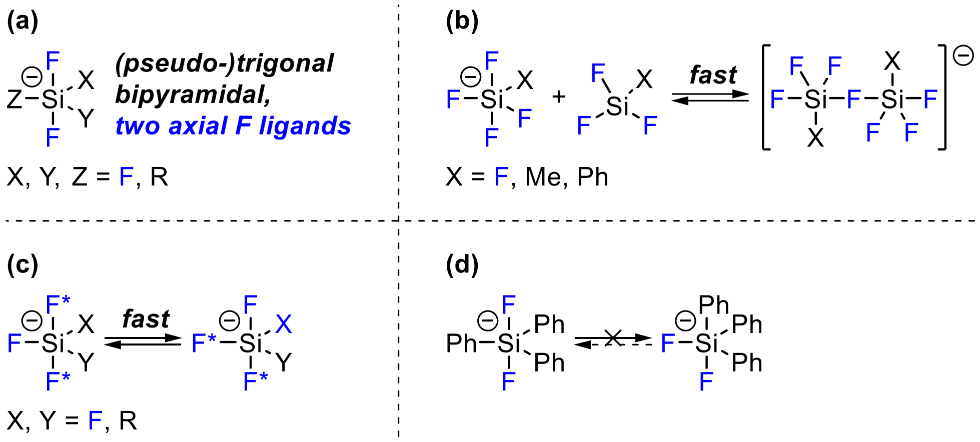

Scheme 1.5: (a) Pentafluorosilicate and pentacoordinate fluoroorganosilicates adopt (pseudo-)trigonal bipyramidal geometries with the two axial positions occupied by fluorine atoms.[177–188] (b) Intermolecular exchange between $XSiF_3$ and $XSiF_4^-$ (X = F, Me, Ph) was proposed to occur *via* fluorine-bridged binuclear silicates.[181] (c) At ambient temperature, the axial and equatorial fluorine atoms in SiF_5^-, $RSiF_4^-$ and $R_2SiF_3^-$ silicates undergo fast exchange.[177–188] The axial fluorine atoms in the left-hand-side structure are marked with asterisks for clarity. (d) In the difluorotriphenylsilicate anion, $Ph_3SiF_2^-$, axial fluorine atoms and equatorial phenyl groups do not exchange.[182]

Little is therefore known about the mechanism of the transfer of fluoride from TBAT in the reactions described in Section 1.2.2. There are few mechanistic studies to date which interrogate the process. Literature on the properties of TBAT in solution phase is also scarce and limited to standard characterisation, ^1H longitudinal relaxation in DMSO-d_6, a comment on extreme acid sensitivity of the reagent,[62,63] as well as stability under Hiyama coupling conditions.[189]

Mąkosza and Bujok found that an equimolar mixture of co-catalytic FTPS (Ph_3SiF) and $^nBu_4NHSO_4$ give a lower yield than Ph_3SnF and $^nBu_4NHSO_4$ in a phase-transfer fluorination of benzyl bromide with KF in MeCN (Scheme 1.6a). The reaction proceeds *via* TBAT ($^nBu_4NPh_3SiF_2$) or the corresponding stannate, $^nBu_4NPh_3SnF_2$, as an intermediate. The use of stoichiometric TBAT and $^nBu_4NPh_3SnF_2$ reverses the outcome in terms of the relative rate constants of the fluorinations (1.37 for TBAT relative to $^nBu_4NPh_3SnF_2$; although reaction profiles were not provided).[190] *para*-Substitution of H with Me in the phenyl groups increases the rate constant for TBAT by nearly eight-fold, and five-fold for $^nBu_4NPh_3SnF_2$ (Scheme 1.6b). They also concluded that for the co-catalytic Ph_3SnF/$^nBu_4NHSO_4$ system, the fluoride transfer from the $^nBu_4NPh_3SnF_2$ intermediate is direct, as (i) $^nBu_4NPh_3SnF_2$ shows no TBAF nor Ph_3SnF signals in ^{19}F and ^{119}Sn NMR spectra, and (ii) there is significantly less β-elimination alkene side-product in the fluorination of secondary (pseudo)halides using this method compared to unmasked fluoride. Although the substitution *vs* β-elimination product ratios were not provided for the Ph_3SiF/$^n Bu_4NHSO_4$ system, they can be compared for the reaction of 1-iodoalkanes with several fluoride sources, including $^n Bu_4NPh_3SnF_2$, TBAT and TBAF·$3H_2O$ (Scheme 1.6c).[62,191] The reaction conditions are different in all cases, but the ratios of products of substitution and β-elimination are vastly different for these fluoride sources. Notably, the main product for $^n Bu_4NPh_3SnF_2$ and TBAT is that of substitution, whereas the use of TBAF·$3H_2O$ yields mainly the elimination product.

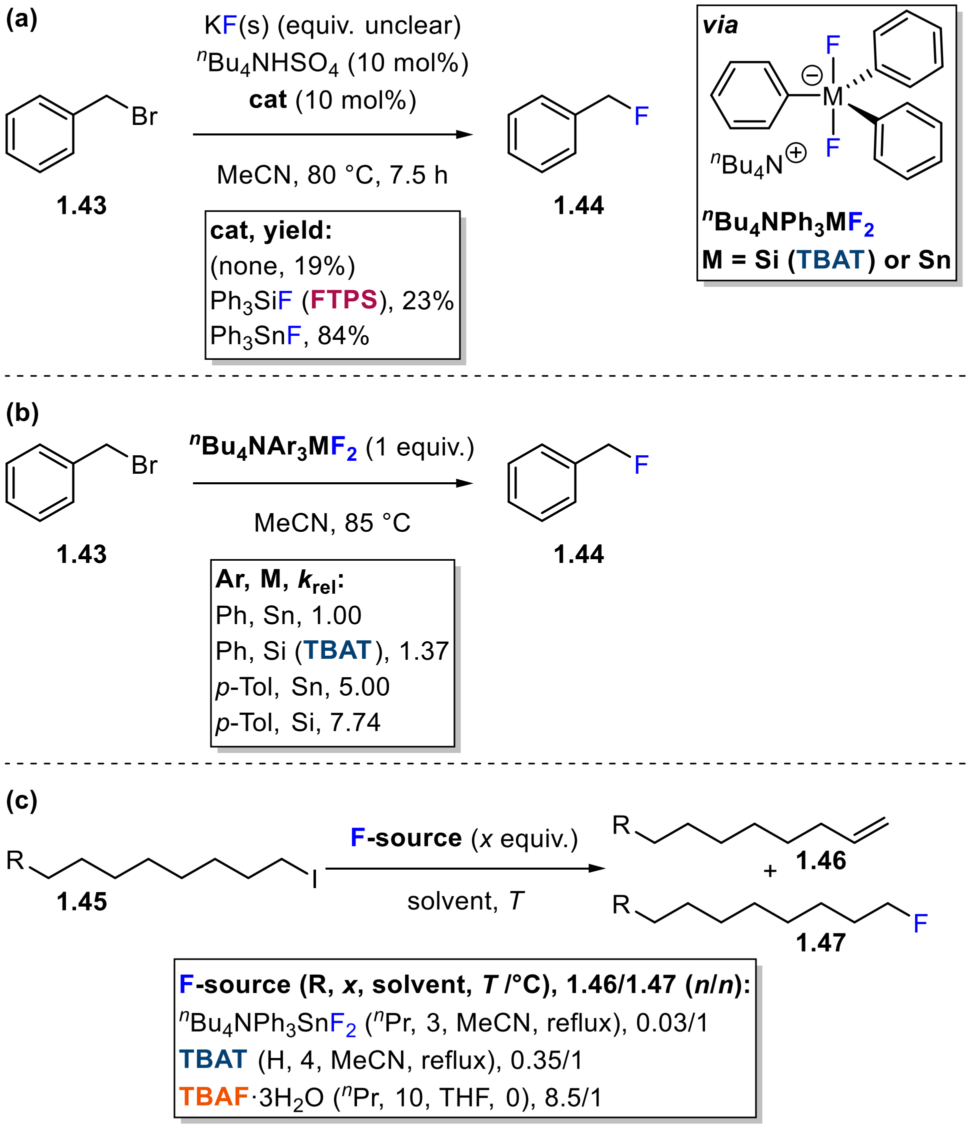

Scheme 1.6: (a) Comparison of Ph_3SiF and Ph_3SnF as co-catalysts in a phase-transfer fluorination of benzyl bromide (1.43) with KF(s). The reaction proceeds *via* $^n Bu_4NPh_3MF_2$ as intermediate, where M = Si (TBAT) or Sn.[190] (b) Relative rate constants of fluorination of benzyl bromide (1.43) using $^n Bu_4NAr_3MF_2$, where M = Si (TBAT) or Sn and Ar = Ph or *p*-Tol.[190] (c) Ratios of β-elimination to substitution products in reactions of 1-iodoalkanes (1.45) with $^n Bu_4NPh_3SnF_2$, TBAT and TBAF·$3H_2O$.[62,191]

Similarly, Woodward *et al.*[120] in their study of TBAT-initiated 1,4-addition of $TMSCCl_3$ to nitroalkenes concluded that "direct F-atom transfer from TBAT seems most likely", based on the observation of only trace signals which could be attributed to TBAF in ^{19}F NMR spectra obtained upon the mixing of $TMSCCl_3$ or $TMSCCl_3$/nitroalkene with TBAT in THF/benzene-d_6 at –20 °C. In the case of solution of $TMSCCl_3$ and TBAT (under anaerobic conditions, where trapping experiments provided no evidence for a radical pathway), they observed immediate formation of TMSF and FTPS (by ^{29}Si and ^{19}F NMR spectroscopy); and $^nBu_4NCCl_3$ (^{13}C NMR). Heating the solution to 20 °C showed little line broadening, which they attributed to no (or very slow) exchange between the spins, *i.e.* the apparent irreversibility of formation of $^nBu_4NCCl_3$. Subsequent addition of the nitroalkene substrate gave no expected addition product due to insufficient nucleophilicity of $^nBu_4NCCl_3$. Changing the order of addition (TBAT added to a mixture of $TMSCCl_3$ and nitroalkene) showed that mechanistically, the nitroalkene and $TMSCCl_3$ must first form an intermediate adduct, followed by TBAT-initiated CCl_3-anionoid transfer (Scheme 1.7). As the fluoride is converted to TMSF, other nucleophiles replace it as promoters in the catalytic reaction.

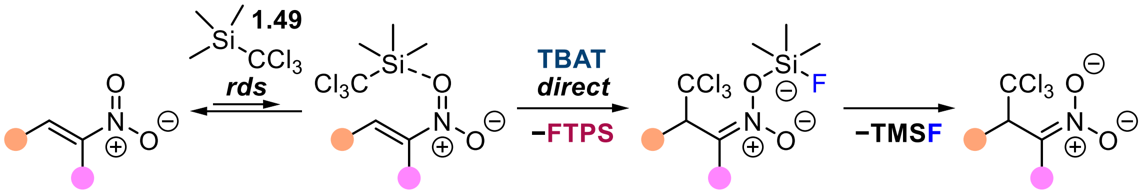

1.48 **1.48---1.49** **1.50** **1.51**

Scheme 1.7: Mechanistic proposal in Woodward's study on the addition of $TMSCCl_3$ to nitroalkenes.[120] According to the authors, "direct F-atom transfer from TBAT seems most likely".

Although no more literature was found where direct *versus* dissociative pathways of fluoride transfer from TBAT are commented on, some more kinetic information is known about the reagent. A recent study by Sharpless *et al.*[192] reported the pseudo-first-order rate constant of fluoride transfer from TBAT (180 mM) to phenyl fluorosulfate ($PhOSO_2F$, **1.52**, 18 mM) at 298 K in deuteriated acetonitrile (MeCN-d_3), $k_{obs} = 0.067$ s^{-1}. Computational analysis of the degenerate fluoride substitution on the sulfur centre of $PhOSO_2F$ with either naked fluoride (F^-) or tetramethylammonium fluoride (Me_4NF) in MeCN showed the exchange occurring *via* an anionic $PhOSO_2F_2^-$ intermediate (**1.53**) for both fluoride sources as feasible (Scheme 1.8a). A large positive standard Gibbs free energy of the fluoride association, $\Delta G° >> 0$, indicated that intermediate

1.53 is in low concentration in solution and hence the exchange may be approximated to concerted substitution (Scheme 1.8b). They then used ^{19}F magnetisation transfer NMR spectroscopy (Section 1.3) to study the rates of exchange between aryl fluorosulfates and various fluoride sources with the approximation of concerted F-substitution with respect to the sulfur centre in fluorosulfate. The fluoride sources were used in excess and selectively saturated for a series of saturation times, followed by measuring the resulting longitudinal magnetisation of $PhOSO_2F$ after each selective saturation. A detailed kinetic study of the exchange was reported for tetra-*n*-butylammonium bifluoride (TBABF) and $PhOSO_2F$, whereby the concentration of the bifluoride was varied, and the observed pseudo-first-order rate constants of exchange at each concentration gave the second-order rate constant $k = 0.43\ \text{M}^{-1}\ \text{s}^{-1}$. Variable-temperature experiments gave an activation enthalpy of +47.3 kJ mol^{-1}. Hammett analysis confirmed the associative mechanism of the exchange with respect to the sulfur centre, with $\log_{10}(k_X/k_H) = 1.56\sigma_{X,para}$ (which indicates a significant build-up of negative charge during the rate-determining step). It was also shown that polar aprotic solvents gave the highest exchange rates and that the material of the reaction vessel (NMR tube) had no effect on the exchange rate. Screening of the anions showed a 2.4-fold decrease in the exchange rate for TBAT compared to bifluoride; a comparable rate to that of TBAT was determined for $^{n}Bu_4NH_2F_3$. Difluorotriphenylstannane ($Ph_3SnF_2^{-}$) showed no detectable exchange under these conditions, and $TBAF{\cdot}3H_2O$ gave the highest rate, 120 times that of TBAT. It must be noted, however, that all of these fluoride sources were used as 200 mM solutions, except for TBAT (180 mM). Bifluorides with various cations were also screened.

(a) associative fluoride transfer

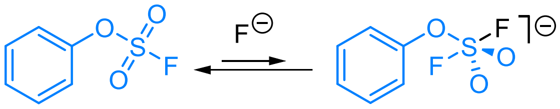

1.52 **1.53**

(b) concerted transfer approximation

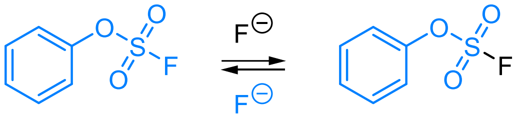

1.52 **1.52**

F⊖ = **TBAT**:
k_{obs} = 0.067 s^{-1}

Scheme 1.8: (a) $PhOSO_2F$ (1.52) exchanges fluoride in an associative process *via* a pentacoordinate intermediate 1.53 ($\Delta G°$ >> 0). (b) Due to the intermediate 1.53 being short-lived, the reaction kinetics can be approximated to concerted with respect to $PhOSO_2F$. When TBAT was used as the fluoride source, the observed pseudo-first-order rate constant of exchange, k_{obs} = 0.067 s^{-1}.[192]

Dean and McIndoe used ESI-MS spectrometry to study the reaction of FTPS with $TBAF{\cdot}3H_2O$.[189] Mixing FTPS with two equivalents of $TBAF{\cdot}3H_2O$ at ambient temperature showed rapid (complete before the measurement was made) formation of difluorotriphenylsilicate anion ($Ph_3SiF_2^-$), which exhibited stability “over an extended period”. At 110 °C, the initially formed $Ph_3SiF_2^-$ decomposed over the course of minutes into a mixture of $Ph_xSiF_{5-x}^-$, $x = 0, 1, 2$, and $^nBu_4N(HF_2)_2^-$. Notably, variability in the relative amounts of the decomposition products was observed between the experiments.

To the best of the author’s knowledge, the only computational evaluation of a difluorotriorganosilicate as a fluoride donor was provided for direct-transfer activation of tetraorganosilane **1.55** with difluorotrimethylsilicate anion (**1.54**) in THF, where the transition state was located at $\Delta G^‡$ = +92 kJ mol^{-1} for both phenyl and 2-pyridyl substituents (Scheme 1.9).[82]

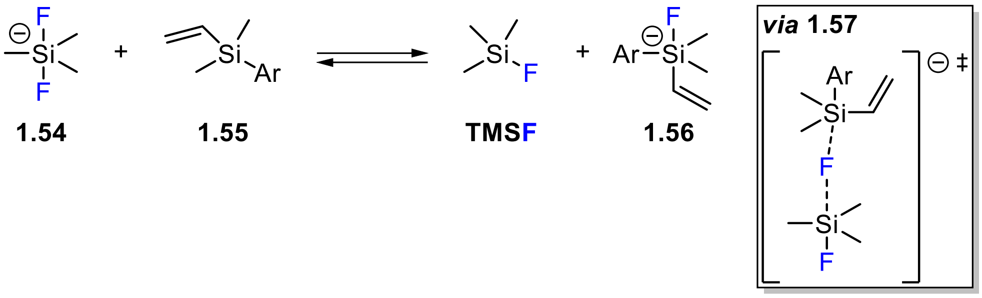

Scheme 1.9: Transition state of direct transfer of fluoride from difluorotrimethylsilicate 1.54 to tetraorganosilane 1.55 was found at +92 kJ mol^{-1}.[82]

Other studies show that fluoride transfer from TBAT is a rapid process with respect to NMR spectroscopy.[130,132,160,162,163,193] For example, in mechanistic studies of a range of TBAT-initiated reactions of TMSCF$_3$,[130,132,162,163] the initial formation of TMSF and a transient CF$_3^-$ anion(oid) was found to be very rapid with respect to standard *in situ* NMR spectroscopic measurements (Scheme 1.10).

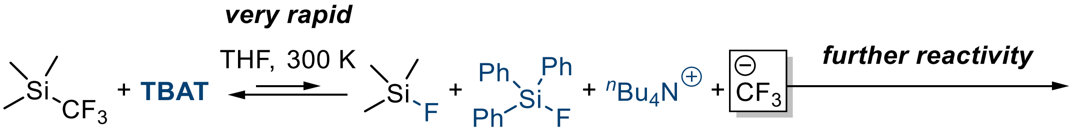

Scheme 1.10: Previous mechanistic work by Lloyd-Jones *et al.* on TBAT-initiated reactivity of TMSCF$_3$, [130,132,162,163] where the fluoride transfer from TBAT is very rapid with respect to NMR spectroscopy. In the presence of excess TMSCF$_3$, the CF$_3^-$ anion(oid) is transient, undergoing rapidly-reversible exergonic equilibrium with [TMS(CF$_3$)$_2$]$^-$.

1.3. Magnetisation transfer NMR spectroscopy

1.3.1. Rapid equilibria in NMR spectroscopy

NMR spectroscopy is a powerful tool in monitoring dynamic aspects of chemical reactions, aiding the elucidation of their mechanisms.[32] The choice of an appropriate NMR method for reaction monitoring depends predominantly on the reaction rate and reversibility. Rapid reversible reactions, *i.e.* reactions whose half-lives typically span milliseconds to seconds (or qualitatively – which, once assembled, reach equilibrium before a measurement can be made), can be monitored conveniently using several methods in NMR spectroscopy. These methods can be grouped into: (i) chemical relaxation methods (based on the return to a new equilibrium following an instantaneous change of conditions, *i.e.* “jump”),[194] (ii) line-shape analysis and spin-echo methods (based on transverse relaxation of the exchanging spins),[195–199] (iii) magnetisation transfer methods (based on longitudinal relaxation of the exchanging spins),[200,201] and 2D EXSY (based on coherence exchange).[202]

1.3.2. Principles of and methods in magnetisation transfer NMR spectroscopy

Magnetisation transfer methods detect the transfer of longitudinal magnetisation between exchanging spins of different resonance frequencies. The first such method was introduced in 1963 by Forsén and Hoffman,[200] who used double-resonance continuous-wave ^{1}H NMR spectroscopy to study acetic acid-catalysed proton exchange between salicylaldehyde and 2'-hydroxyacetophenone. One year later, they generalised the method to multi-site exchange networks.[201]

All magnetisation transfer methods follow the same principle: selective disturbance of the longitudinal magnetisation of one (or more) spins is detected in all spins which exchange with the initially perturbed one(s), provided sufficiently rapid exchange rate relative to longitudinal relaxation under the applied conditions. Some commonly used magnetisation transfer methods (in pulsed NMR spectroscopy) are exemplified herein on a two-site $A \rightleftharpoons B$ exchange system, where A and B each contain an NMR-observable, spin-half nucleus. For simplicity, we assume no cross-relaxation and no scalar couplings in the system.[203,204]

An inversion transfer experiment (Figure 1.4a), developed by Dahlquist *et al*.[205] for an equally-populated two-spin system, and subsequently generalised by Alger and Prestegard,[206] and Brown and Ogawa,[207] uses a soft (frequency-selective) π pulse to invert one of the two spins to the –*z*-axis, whereas the second spin remains at magnetic equilibrium. The soft pulse is followed by a variable delay, during which the magnetisation vectors of the spins evolve *via* longitudinal relaxation and if present – exchange, prior to the signal detection. This pulse sequence is repeated for incremented variable delays. Consider a scenario where A and B are of equal populations and exchange *via* an elementary unimolecular reaction with the rate constant k (in both directions). The longitudinal relaxation time constants of the spins are equal and such that $kT_1 = 1$ (Figure 1.4b). Initially, both spins are at magnetic equilibrium along the +*z*-axis (Figure 1.4c). This equilibrium corresponds to the "standard" NMR spectrum of the mixture of A and B. The soft (frequency-selective) π pulse inverts one signal, here A, to the –*z*-axis, whilst leaving the magnetisation of the other spin (B) intact. If the resulting longitudinal magnetisations are detected immediately (variable delay, $\tau = 0$), and assuming perfect inversion by the soft pulse and no relaxation nor exchange during the irradiation by the pulses, the acquired NMR spectrum shows negative equilibrium longitudinal magnetisation, $-M_{z,\mathrm{eq}}$, for A, and equilibrium longitudinal magnetisation, $M_{z,\mathrm{eq}}$, for B. As the variable delay, τ, increases, two processes occur for both spins: (i) the redistribution of inversion between A and B heading towards equal (fractional) magnetisations resulting from chemical exchange, and (ii) longitudinal relaxation of both spins. Both these processes increase the magnetisation of the inverted spin, whereas for the non-inverted spin they act in the opposite fashion (exchange decreases and relaxation increases its magnetisation). The result is, for the inverted spin, a more rapid recovery, and for the non-inverted spin – an initial decrease in magnetisation, and then recovery. Finally, as the variable delay approaches infinity, both spins recover fully to their magnetic equilibrium. In practice for the A ⇌ B system herein, $M_z^{\mathrm{A}} = M_z^{\mathrm{B}} = 0.993M_{z,\mathrm{eq}}$ is achieved for both spins at $\tau = 5T_1$.

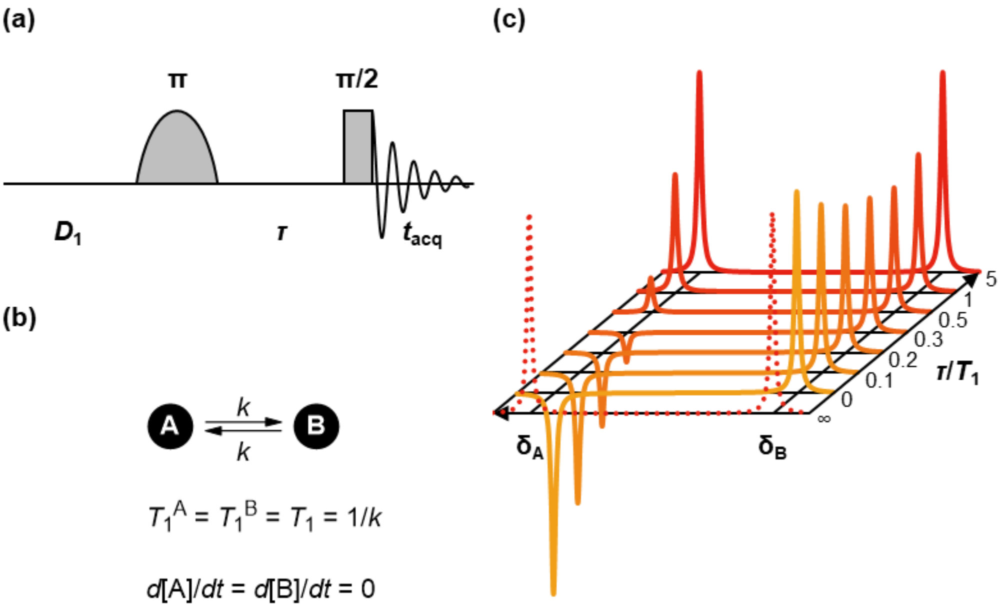

Figure 1.4: (a) The pulse sequence of an inversion transfer experiment. Initially (provided a sufficiently long relaxation delay, D_1, is used), all spins are at magnetic equilibrium along the +*z*-axis. Selective inversion of one or more spins using a soft π pulse is followed by a variable delay, τ, during which the spins exchange and relax. The resulting longitudinal magnetisations are then detected using a hard π/2 pulse to rotate the magnetisation onto the XY-plane (with acquisition time t_{acq}). The sequence is repeated for incremented variable delays. (b) An A ⇌ B general system is used here to describe the principles of an inversion transfer experiment. A and B undergo unimolecular exchange with rate constant k in each direction and $kT_1 = 1$, where T_1 is the longitudinal relaxation time constant, equal for both spins for simplicity. (c) A simulation of the spectra at different stages of an inversion transfer experiment for the system described in (b), where δ_{A} and δ_{B} are the chemical shifts of A and B, respectively. Initially (dotted spectrum), the spins are at magnetic equilibrium. Selective inversion of A and immediate acquisition results in the second spectrum in the series (from the bottom). Increasing variable delay results in more magnetisation transfer between the spins, as well as their recovery *via* longitudinal relaxation. Finally, at sufficiently long variable delays, τ, the spins return to magnetic equilibrium.

Figure 1.5a–b shows a plot of the normalised longitudinal magnetisations of the two spins ($M_z/M_{z,\mathrm{eq}}$) against the ratio of variable delay to longitudinal relaxation time, τ/T_1, for the system described above ($kT_1 = 1$), as well as for $kT_1 = 0, 2, 5, 50$. The dotted lines represent A (the inverted spin) and the continuous lines of the same colour – B (the initially non-inverted spin). If there is no exchange between the spins ($kT_1 = 0$), the recovery of the inverted signal (A) follows first-order longitudinal relaxation kinetics with the rate constant $1/T_1$, and the non-inverted signal (B) is unaffected by the soft pulse and remains at magnetic equilibrium regardless of variable delay. If exchange is present ($kT_1 = 1, 2, 5, 50$ in the plot), the recovery of A becomes faster and no longer first-order (a special case of Equations 1.2–1.5 in Section 1.3.3), whereas the magnetisation of B *vs* τ gives a characteristic “V-shaped” plot. The plot is asymmetrically-stretched, and the minimum of the function (*i.e.* the point where $dM_z^{\mathrm{B}}/d\tau = 0$) heads towards lower τ and M_z^{B} as kT_1 increases (Figure 1.5c–d).

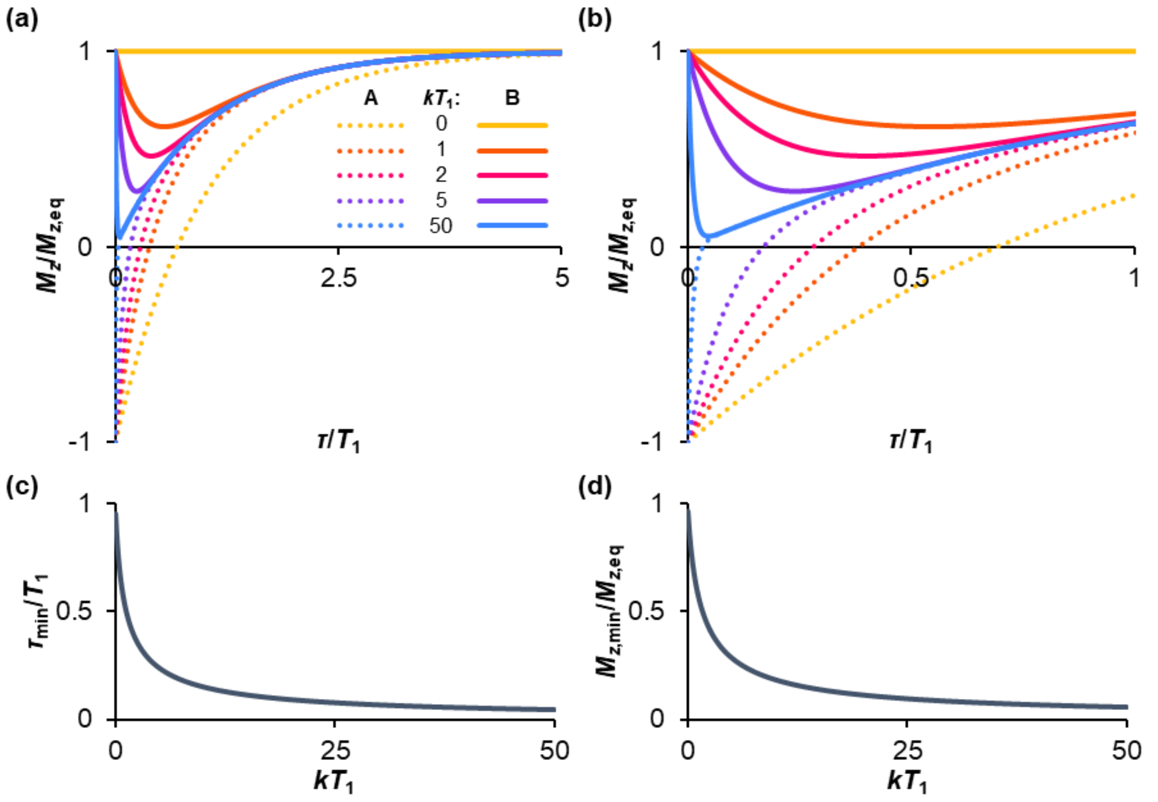

Figure 1.5: (a) The evolution of longitudinal magnetisation of exchanging spins depending on the exchange rate constant relative to relaxation. Lines with the same colour represent the inverted spin (A, dotted lines) and the initially non-inverted one (B, continuous lines). (b) An expansion of the plot from (a) for $\tau \leq T_1$. Magnetisation of the initially non-inverted signal reaches the minimum (c) more rapidly and (d) with larger relative decrease in magnetisation – with increased kT_1.

Alternatively, one can perform saturation transfer experiments, where a selective π/2 pulse saturates one (or more) of the spins.[208] Whereas selective saturation offers decreased experiment duration (faster recovery to magnetic equilibrium for saturation than for inversion), it in turn decreases the signal-to-noise ratio (the "dip" in the magnetisation transfer plot), as the minimum value of $M_z/M_{z,\mathrm{eq}}$ for the non-inverted spin (B) approaches 0.5 instead of 0 for sufficiently large kT_1 in the $A \rightleftharpoons B$ system described above.

Chemical exchange saturation transfer (CEST) is a magnetisation transfer method, which enables one to observe low-concentration species present in solution, provided that they exchange with an observable spin to a sufficient extent compared to longitudinal relaxation.[209,210] In a typical CEST experiment (Figure 1.6a), a series of narrow frequency ranges are in turn saturated for a certain time, called the saturation time, t_{sat}. The saturation of each frequency range is followed by a pulse-acquire sequence, which after Fourier transformation yields a series of NMR spectra. The magnetisation of the observable spin is then plotted against saturation frequency and if a low-concentration spin is present in the scanned range and the rate of exchange considerable, a decrease in the magnetisation of the observable spin is observed for that frequency. Consider a system where A and B are at chemical equilibrium, and the degree of conversion of A to B is small, $K = [B]/[A] << 1$ (Figure 1.6b). In an NMR spectrum of the equilibrium mixture, only A is observed at its resonance frequency, δ_A, and B (resonating at δ_B) is below the detection limit. When a frequency range is selectively saturated where neither A nor B resonate, the spectrum shows equilibrium longitudinal magnetisation for A (and no signal for B). When a frequency range containing δ_A is saturated, the resulting spectrum shows the magnetisation of A suppressed to (in theory) 0. Saturation of the frequency range containing B, δ_B, results in the decrease of magnetisation of A, to the extent which depends on the saturation time, exchange rate and longitudinal relaxation times of A and B (Figure 1.6c–d).

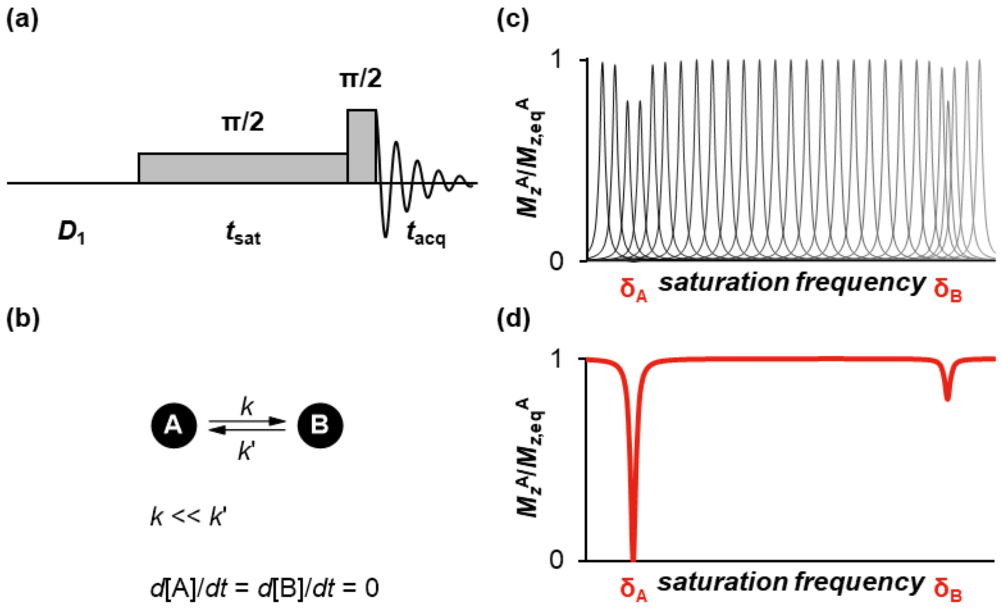

Figure 1.6: (a) The pulse sequence of a CEST experiment. Initially (provided a sufficiently long relaxation delay, D_1, is used), all spins are at magnetic equilibrium along the +*z*-axis. Selective saturation of a narrow frequency range using a soft π/2 pulse is followed by immediate detection of the longitudinal magnetisation of an observable spin (with acquisition time t_{acq}). The sequence is repeated for several frequency ranges. (b) An A ⇌ B general system is used herein to describe the principles of a CEST experiment. A and B exchange *via* a unimolecular elementary step in each direction, with unequal rate constants. The system is at dynamic equilibrium and B in low concentration (below the detection limit in pulse-acquire NMR spectra). (c) Simulated peaks of A detected for a series of saturation frequencies immediately after saturation, and (d) the corresponding simulated plot of normalised magnetisation of A against the saturation frequency (*i.e.* the centre frequency of the range). δ_A and δ_B are the chemical shifts of A and B, respectively.

A variety of soft pulses can be used in magnetisation transfer experiments,[211] and the selection of a suitable pulse depends primarily on the method (inversion transfer, saturation transfer, CEST *etc*.), separation of the signals and exchange rate. The simplest soft pulse is a long rectangular pulse with low power. It is typically avoided in inversion and saturation transfer, as information about exchange and relaxation processes occurring during the long pulse duration is lost. Poor selectivity, due to far-extending side-lobes, is also characteristic to the pulse. More commonly, it is used in CEST (as presented in Figure 1.6a), although in this method, series of back-to-back shaped pulses (“pulse trains”) are also used.[212]

1.3.3. Mathematical considerations

Quantitative description of the evolution of longitudinal magnetisation in magnetisation transfer experiments is derived from Bloch equations modified for exchange.[195,213,214] For an (equally- or unequally-populated) *n*-site exchanging system ($n \geq 2$), a system of *n* coupled differential equations which describe the rate of change of longitudinal magnetisation at each site is presented in Equation 1.1,[201] where M_z^i is the longitudinal magnetisation of site i at variable delay τ, $M_{z,\mathrm{eq}}^i$ is the corresponding equilibrium magnetisation (*i.e.* for the fully magnetised spin), k_{ij} is the first-order rate constant of exchange from i to j, and T_1^i is the longitudinal relaxation time constant of i.

1.1

$$\frac{dM_z^i}{d\tau} = -\sum_{\substack{j=1 \\ (i\neq j)}}^{n} k_{ij}M_z^i + \sum_{\substack{j=1 \\ (i\neq j)}}^{n} k_{ji}M_z^j + \frac{M_{z,\mathrm{eq}}^i - M_z^i}{T_1^i}$$

For inversion transfer experiments and when $n = 2$, this model leads to longitudinal magnetisations of both sites (A and B, M_z^A and M_z^B) as biexponential functions of the variable delay, τ, Equations 1.2–1.5 where A is inverted.[198,215] Fractional inversion of A, $f = -M_{z,0}^\mathrm{A}/M_{z,\mathrm{eq}}^\mathrm{A}$, where $M_{z,0}^\mathrm{A}$ is the magnetisation of A immediately after inversion, was introduced to account for imperfect inversion by the soft π pulse. For a perfect inversion scenario, $f = 1$.

1.2

$$\frac{M_z^\mathrm{A}}{M_{z,\mathrm{eq}}^\mathrm{A}} = \frac{f+1}{2\gamma}\left[\left(\beta - \gamma + k_\mathrm{AB} + \frac{1}{T_1^\mathrm{A}}\right)e^{(\beta+\gamma)\tau} - \left(\beta + \gamma + k_\mathrm{AB} + \frac{1}{T_1^\mathrm{A}}\right)e^{(\beta-\gamma)\tau}\right] + 1$$

1.3

$$\frac{M_z^\mathrm{B}}{M_{z,\mathrm{eq}}^\mathrm{B}} = \frac{k_\mathrm{BA}(f+1)}{2\gamma}\left[e^{(\beta-\gamma)\tau} - e^{(\beta+\gamma)\tau}\right] + 1$$

Where:

1.4

$$\beta = -\frac{k_\mathrm{AB} + k_\mathrm{BA} + \frac{1}{T_1^\mathrm{A}} + \frac{1}{T_1^\mathrm{B}}}{2}$$

1.5

$$\gamma = \frac{\sqrt{\left(k_\mathrm{AB} + \frac{1}{T_1^\mathrm{A}} - k_\mathrm{BA} - \frac{1}{T_1^\mathrm{B}}\right)^2 + 4k_\mathrm{AB}k_\mathrm{BA}}}{2}$$

As n increases, data analysis becomes more complex. For $n = 3$, the general solution is a triexponential function,[216] which can be simplified to a biexponential one in specific exchange scenarios.[201] For $n \geq 4$, numerical solutions can be obtained with an aid of appropriate software.[217,218] Alternatively, n-site exchanging systems can be simplified to two-site ones by continuous saturation of all spins but the two of interest, concurrently to the magnetisation transfer.[219]

Another approach to deriving these models is the formalism whereby discrete inverted and non-inverted spins are treated as separate, although chemically degenerate, species.[205] This formalism was used in the first inversion transfer experiment, and leads to identical results to these described above, based on bulk magnetisations.

1.4. Aims of this study

As discussed in Section 1.2.3, no literature to date has reported a direct investigation of the mechanism by which fluoride is transferred from TBAT to fluorophiles. The aim of this study is therefore to interrogate the rapid fluoride transfer process from TBAT, in particular whether the reaction proceeds *via* direct or dissociative transfer pathway, or both. The observed rate constant of exchange between TBAT and phenyl fluorosulfate (**1.52**, Scheme 1.8 in Section 1.2.3) provided by Sharpless *et al*.[192] indicates the possibility of monitoring the reaction *via* magnetisation transfer NMR spectroscopy. Inversion transfer was chosen as a suitable magnetisation transfer method. In Chapter 2, two spin systems are described, which were used to interrogate the reaction, and the kinetic models in the inversion transfer experiments using these two systems derived, based on the two proposed transfer pathways. In Chapter 3, an investigation into the kinetics and mechanism of the fluoride transfer is presented, based on the models derived in Chapter 2. Two solvents were chosen for this study, THF (or THF-d_8) and MeCN (or MeCN-d_3), as the two most commonly used solvents in reactions involving TBAT.

Chapter 2

System design and kinetic model

2.1. General scheme of dissociative and direct transfer exchange pathways

The two proposed pathways of fluoride transfer from tetra-*n*-butylammonium difluorotriphenylsilicate (TBAT) are presented in Scheme 2.1. In the dissociative fluoride transfer pathway (reaction 1, Scheme 2.1a), TBAT first dissociates reversibly into fluorotriphenylsilane (FTPS) and tetra-*n*-butylammonium fluoride (TBAF). TBAF is then the active fluorinating agent in the (irreversible or reversible) reaction with the fluorophile (electrophile, E^+). In the direct fluoride transfer pathway (reaction 2, Scheme 2.1b), TBAT reacts directly with E^+ in a bimolecular elementary reaction (irreversibly or reversibly).

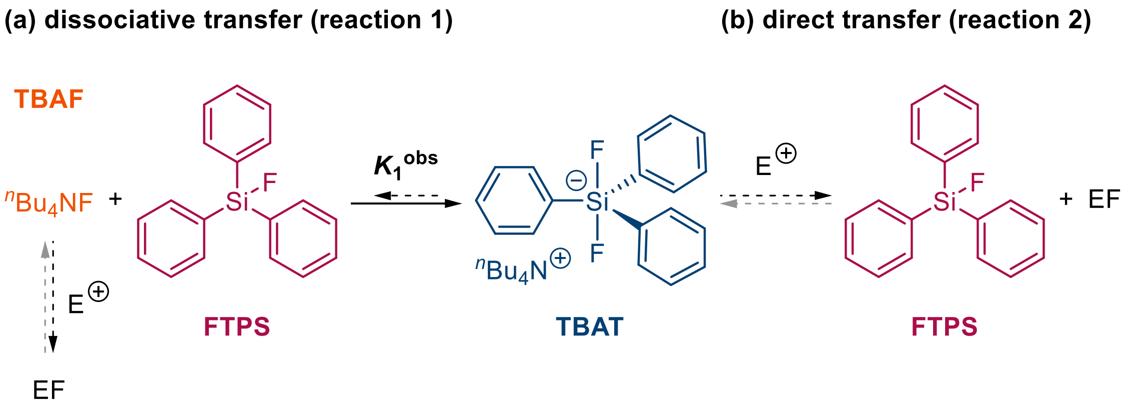

Scheme 2.1: Two proposed pathways of fluoride transfer from TBAT. (a) Dissociative transfer *via* TBAF (reaction 1) and (b) direct bimolecular transfer (reaction 2).

2.2. Thermodynamics of TBAT dissociation into FTPS and TBAF

As discussed in Section 2.1, TBAT in solution may dissociate into FTPS and TBAF with the equilibrium constant K_1^{obs} ("obs" denotes the possibility of the equilibrium constant being dependent on TBAT speciation and/or ionic strength of the solution). Assuming that $0 \leq K_1^{obs} << 1$ (*i.e.* TBAT either does not dissociate into FTPS and TBAF or dissociates into FTPS and TBAF to a small degree), and that no further equilibria involve the three species, a simple TBAT ⇌ FTPS + TBAF model is derived to describe the process.

Consider TBAT and FTPS dissolved in the solvent in such amounts that their initial concentrations (before the system "starts" equilibrating) are c^{TBAT} and c^{FTPS}, respectively ($c^{TBAF} = 0$). When the system reaches equilibrium, the equilibrium concentrations of the three species are: $[TBAT] = c^{TBAT} - x$, $[FTPS] = c^{FTPS} + x$, [TBAF]

= x, where x is the concentration of TBAT which dissociates into FTPS and TBAF. The expression for K_1^{obs} is:

2.1

$$K_1^{\text{obs}} = \frac{[\text{FTPS}][\text{TBAF}]}{[\text{TBAT}]} = \frac{(c^{\text{FTPS}} + x)x}{c^{\text{TBAT}} - x}$$

Solving Equation 2.1 for x gives the following equilibrium concentrations:

2.2

$$[\text{TBAT}] = \frac{2c^{\text{TBAT}} + c^{\text{FTPS}} + K_1^{\text{obs}} - \sqrt{\left(c^{\text{FTPS}} + K_1^{\text{obs}}\right)^2 + 4K_1^{\text{obs}}c^{\text{TBAT}}}}{2}$$

2.3

$$[\text{FTPS}] = \frac{c^{\text{FTPS}} - K_1^{\text{obs}} + \sqrt{\left(c^{\text{FTPS}} + K_1^{\text{obs}}\right)^2 + 4K_1^{\text{obs}}c^{\text{TBAT}}}}{2}$$

2.4

$$[\text{TBAF}] = \frac{-c^{\text{FTPS}} - K_1^{\text{obs}} + \sqrt{\left(c^{\text{FTPS}} + K_1^{\text{obs}}\right)^2 + 4K_1^{\text{obs}}c^{\text{TBAT}}}}{2}$$

Since $K_1^{\text{obs}} << 1$, $x << c^{\text{TBAT}}$, and hence Equations 2.1–2.4 can be approximated to:

2.5

$$K_1^{\text{obs}} \approx \frac{(c^{\text{FTPS}} + x)x}{c^{\text{TBAT}}}$$

2.6

$$[\text{TBAT}] \approx c^{\text{TBAT}}$$

2.7

$$[\text{FTPS}] \approx \frac{c^{\text{FTPS}} + \sqrt{(c^{\text{FTPS}})^2 + 4K_1^{\text{obs}}c^{\text{TBAT}}}}{2}$$

2.8

$$[\text{TBAF}] \approx \frac{-c^{\text{FTPS}} + \sqrt{(c^{\text{FTPS}})^2 + 4K_1^{\text{obs}}c^{\text{TBAT}}}}{2}$$

Two extremes are considered below: for systems with high initial concentration of FTPS (Equations 2.9–2.12) and for systems where $c^{\text{FTPS}} = 0$ (Equations 2.13–2.16).

If c^{FTPS} is considerable (*e.g.* above detection limit in ^{19}F NMR spectroscopy), then $x << c^{\text{FTPS}}$, and Equations 2.5–2.8 can be further approximated to:

2.9

$$K_1^{\text{obs}} \approx \frac{c^{\text{FTPS}}x}{c^{\text{TBAT}}}$$

2.10

$$[\text{TBAT}] \approx c^{\text{TBAT}}$$

2.11

$$[\text{FTPS}] \approx c^{\text{FTPS}}$$

2.12

$$[\text{TBAF}] \approx K_1^{\text{obs}} \frac{c^{\text{TBAT}}}{c^{\text{FTPS}}}$$

On the other hand, if there is no FTPS in the system initially:

2.13

$$K_1^{\text{obs}} \approx \frac{x^2}{c^{\text{TBAT}}}$$

2.14

$$[\text{TBAT}] \approx c^{\text{TBAT}}$$

2.15

$$[\text{FTPS}] \approx \sqrt{K_1^{\text{obs}} c^{\text{TBAT}}}$$

2.16

$$[\text{TBAF}] \approx \sqrt{K_1^{\text{obs}} c^{\text{TBAT}}}$$

Hence, assuming the simple equilibrium dissociation model with $K_1^{\text{obs}} << 1$, the equilibrium concentrations of TBAT and FTPS can be approximated to their initial concentrations, c^{TBAT} and c^{FTPS}, respectively, in solutions of TBAT and FTPS described in Section 2.3 (as is the case if TBAT does not dissociate).

2.3. Dissociative and direct transfer pathways in the TBAT/FTPS system

2.3.1. FTPS as a fluorophile in TBAT/FTPS exchange

If TBAT is mixed with FTPS, the latter being the fluorophile (electrophile, E^+, in Scheme 2.1), both the direct and dissociative pathways can in principle be interrogated *via* ^{19}F magnetisation transfer between the two spins (Scheme 2.2). The overall rate constants of the two processes are, as shown in Scheme 2.2, $2k_2^{\text{obs}}$ for the direct fluoride transfer (in either direction, as the net equilibrium reaction is “0”, *i.e.* degenerate, with $\Delta G° = 0$), $2k_1^{\text{obs}}$ for dissociation of TBAT into FTPS and TBAF and k_{-1}^{obs} for the recombination of FTPS and TBAF into TBAT ($K_1^{\text{obs}} = 2k_1^{\text{obs}}/k_{-1}^{\text{obs}} << 1$).

The “2” in $2k_2^{obs}$ and $2k_1^{obs}$ means that in both processes, k_2^{obs} and k_1^{obs} are the corresponding rate constants “per (chemically equivalent) fluorine atom” in TBAT.

(a) dissociative transfer (reaction 1)

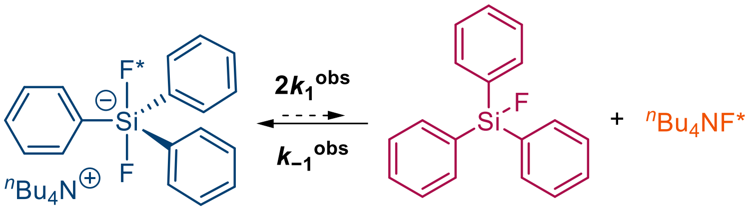

TBAT **FTPS** **TBAF**

(b) direct transfer (reaction 2)

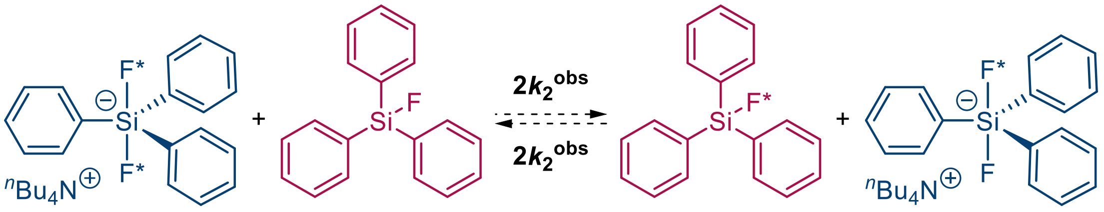

TBAT **FTPS** **FTPS** **TBAT**

Scheme 2.2: Two proposed pathways of fluoride transfer from TBAT to FTPS. (a) Dissociative transfer *via* TBAF, where $K_1^{obs} = 2k_1^{obs}/k_{-1}^{obs} << 1$). (b) Direct bimolecular transfer (the rate constants in each direction are identical, as $\Delta G° = 0$). In each transfer pathway, exchanging fluorine atoms are marked with an asterisk for clarity.

2.3.2. Magnetisation states of TBAT, FTPS and TBAF

The kinetic models for the inversion transfer between the spins in this study are derived based on the discrete inverted and non-inverted spin formalism (Section 1.3.3).[205] A spin-half nucleus (here ^{19}F) can exist in two chemically equivalent magnetisation states, herein referred to as magnetised (*i.e.* at magnetic equilibrium along the $+z$ axis, $^{19}F^{\blacktriangle}$) and inverted (to the $-z$ axis, $^{19}F^{\blacktriangledown}$). Hence, a species S with n equivalent ^{19}F nuclei can exist in $(n + 1)$ chemically equivalent magnetic states. Each of the magnetised spins in S contributes $+m_z$, and each of the inverted ones $-m_z$ to the overall longitudinal magnetisation of S, M_z^S (Equations 2.17 and 2.18, where m_z is the longitudinal magnetisation of a single ^{19}F spin at magnetic equilibrium, *i.e.* $^{19}F^{\blacktriangle}$; $M_{z,eq}^S$ is the longitudinal magnetisation of S at magnetic equilibrium; and $N_{\blacktriangle}^S$ and $N_{\blacktriangledown}^S$ are the number of inverted and magnetised spins in S, respectively). For example, an equimolar mixture of $FTPS^{\blacktriangledown}$ and $FTPS^{\blacktriangle}$ shows a null in a ^{19}F NMR spectrum.

Here is introduced the fractional magnetisation of S, m^S, which is the molar fraction of magnetised ^{19}F spins in S; and its relationship to M_z^S and $M_{z,eq}^S$ (Equation 2.19). The equilibrium fractional magnetisation, $m_{\mathrm{eq}}^{\mathrm{S}}$ is 1 (and the fractional magnetisation when all spins are inverted is 0).

2.17

$$M_z^{\mathrm{S}} = \left(N_{\blacktriangle}^{\mathrm{S}} - N_{\blacktriangledown}^{\mathrm{S}}\right) m_z$$

2.18

$$M_{z,\mathrm{eq}}^{\mathrm{S}} = \left(N_{\blacktriangle}^{\mathrm{S}} + N_{\blacktriangledown}^{\mathrm{S}}\right) m_z$$

2.19

$$m^{\mathrm{S}} = \frac{N_{\blacktriangle}^{\mathrm{S}}}{N_{\blacktriangle}^{\mathrm{S}} + N_{\blacktriangledown}^{\mathrm{S}}} = \frac{M_z^{\mathrm{S}} + M_{z,\mathrm{eq}}^{\mathrm{S}}}{2M_{z,\mathrm{eq}}^{\mathrm{S}}}$$

FTPS and TBAF therefore can exist in two magnetisation states each and their fractional magnetisations are given by Equations 2.20 and 2.21. TBAT, which possesses two equivalent ^{19}F nuclei, can exist in three magnetisation states, and its fractional magnetisation is given by Equation 2.22.

2.20

$$m^{\mathrm{FTPS}} = \frac{[\mathrm{FTPS}^{\blacktriangle}]}{[\mathrm{FTPS}]} = \frac{[\mathrm{FTPS}^{\blacktriangle}]}{[\mathrm{FTPS}^{\blacktriangledown}] + [\mathrm{FTPS}^{\blacktriangle}]} = \frac{M_z^{\mathrm{FTPS}} + M_{z,\mathrm{eq}}^{\mathrm{FTPS}}}{2M_{z,\mathrm{eq}}^{\mathrm{FTPS}}}$$

2.21

$$m^{\mathrm{TBAF}} = \frac{[\mathrm{TBAF}^{\blacktriangle}]}{[\mathrm{TBAF}]} = \frac{[\mathrm{TBAF}^{\blacktriangle}]}{[\mathrm{TBAF}^{\blacktriangledown}] + [\mathrm{TBAF}^{\blacktriangle}]} = \frac{M_z^{\mathrm{TBAF}} + M_{z,\mathrm{eq}}^{\mathrm{TBAF}}}{2M_{z,\mathrm{eq}}^{\mathrm{TBAF}}}$$

2.22

$$m^{\mathrm{TBAT}} = \frac{[\mathrm{TBAT}^{\blacktriangledown\blacktriangle}] + 2[\mathrm{TBAT}^{\blacktriangle\blacktriangle}]}{2[\mathrm{TBAT}]} = \frac{[\mathrm{TBAT}^{\blacktriangledown\blacktriangle}] + 2[\mathrm{TBAT}^{\blacktriangle\blacktriangle}]}{2([\mathrm{TBAT}^{\blacktriangledown\blacktriangledown}] + [\mathrm{TBAT}^{\blacktriangledown\blacktriangle}] + [\mathrm{TBAT}^{\blacktriangle\blacktriangle}])} = \frac{M_z^{\mathrm{TBAT}} + M_{z,\mathrm{eq}}^{\mathrm{TBAT}}}{2M_{z,\mathrm{eq}}^{\mathrm{TBAT}}}$$

2.3.3. Longitudinal relaxation of TBAT, FTPS and TBAF

Longitudinal relaxation schemes of TBAT, FTPS and TBAF are presented in Scheme 2.3. Since FTPS and TBAF possess one ^{19}F nucleus each and therefore exist in two magnetisation states, their longitudinal relaxation follows simple first order kinetics with the rate constant $k_{\mathrm{S}} = 1/T_1^{\mathrm{S}}$ (T_1^{S} is the longitudinal relaxation time constant of S). However, the existence of two chemically and magnetically equivalent ^{19}F nuclei in TBAT introduces a complication in determining the relative rate constants of the $\mathrm{TBAT}^{\blacktriangledown\blacktriangledown} \rightarrow \mathrm{TBAT}^{\blacktriangledown\blacktriangle}$ and $\mathrm{TBAT}^{\blacktriangledown\blacktriangle} \rightarrow \mathrm{TBAT}^{\blacktriangle\blacktriangle}$ events, and their relationship to the net relaxation time constant, T_1^{TBAT}. These two processes were found to be described by the rate constants $2k_{\mathrm{TBAT}} = 2/T_1^{\mathrm{TBAT}}$ and $k_{\mathrm{TBAT}} = 1/T_1^{\mathrm{TBAT}}$, respectively, as derived in Section 7.1.1.

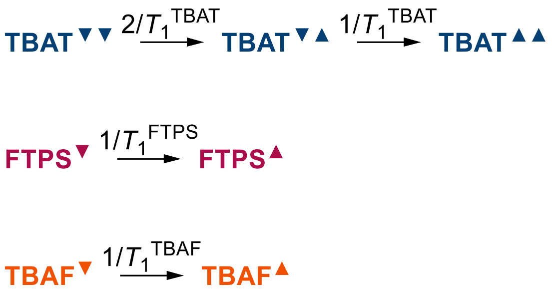

Scheme 2.3: Longitudinal relaxation schemes of TBAT, FTPS and TBAF.

2.3.4. Magnetisation transfer rate laws

The dissociative and direct transfer pathways (reaction 1 and reaction 2, respectively), accounting for all (chemically degenerate) magnetisation states of TBAT, FTPS and TBAF are presented in Scheme 2.4. Based on the scheme, rate laws can be derived that describe the temporal changes (*d*/*d*τ, where *τ* is the variable delay) in fractional magnetisations of TBAT, FTPS and TBAF in systems of these three spins.

(a) dissociative transfer (reaction 1):

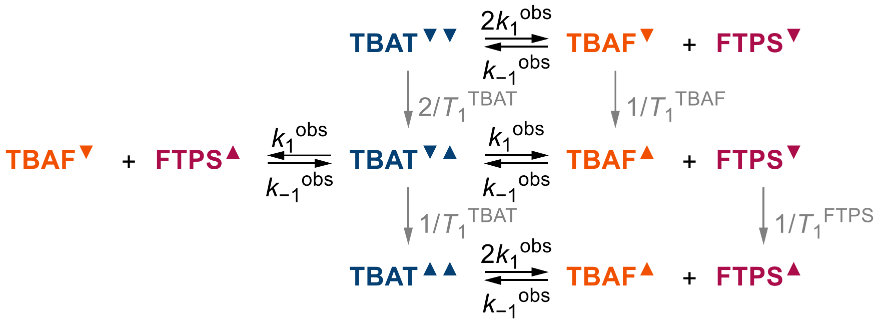

(b) direct transfer (reaction 2):

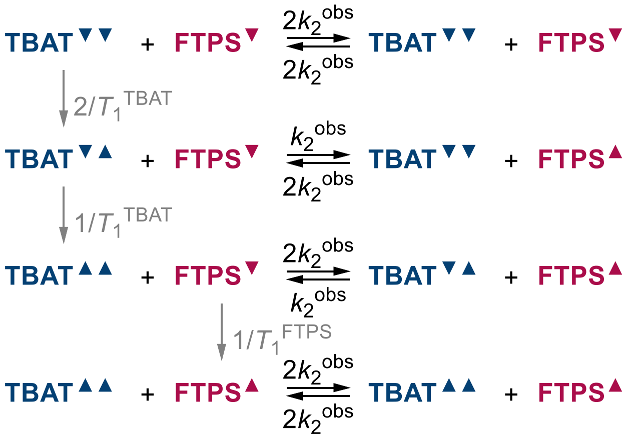

Scheme 2.4: The breakdown of the (a) dissociative and (b) direct transfer exchange pathways between TBAT, FTPS and TBAF, accounting for their longitudinal magnetisation states. Note the rate constants of the chemically degenerate equilibrium transfer reactions relative to the overall rate constants $2k_1^{obs}$ and $2k_2^{obs}$ depending on the magnetisation states of the spins.

Longitudinal (T_1) relaxation:

2.23

$$\left(\frac{d[\mathrm{TBAT}^{\blacktriangledown\blacktriangle}]}{d\tau}\right)_{T_1} = \frac{2}{T_1^{\mathrm{TBAT}}}[\mathrm{TBAT}^{\blacktriangledown\blacktriangledown}] - \frac{1}{T_1^{\mathrm{TBAT}}}[\mathrm{TBAT}^{\blacktriangledown\blacktriangle}]$$

2.24

$$\left(\frac{d[\mathrm{TBAT}^{\blacktriangle\blacktriangle}]}{d\tau}\right)_{T_1} = \frac{1}{T_1^{\mathrm{TBAT}}}[\mathrm{TBAT}^{\blacktriangledown\blacktriangle}]$$

2.25

$$\left(\frac{d[\mathrm{FTPS}^{\blacktriangle}]}{d\tau}\right)_{T_1} = \frac{1}{T_1^{\mathrm{FTPS}}}[\mathrm{FTPS}^{\blacktriangledown}]$$

2.26

$$\left(\frac{d[\mathrm{TBAF}^{\blacktriangle}]}{d\tau}\right)_{T_1} = \frac{1}{T_1^{\mathrm{TBAF}}}[\mathrm{TBAF}^{\blacktriangledown}]$$

Dissociative transfer (reaction 1, “R1”):

2.27

$$\left(\frac{d[\mathrm{TBAT}^{\blacktriangledown\blacktriangle}]}{d\tau}\right)_{\mathrm{R1}} = k_{-1}^{\mathrm{obs}}[\mathrm{FTPS}^{\blacktriangledown}][\mathrm{TBAF}^{\blacktriangle}] + k_{-1}^{\mathrm{obs}}[\mathrm{FTPS}^{\blacktriangle}][\mathrm{TBAF}^{\blacktriangledown}] - 2k_{1}^{\mathrm{obs}}[\mathrm{TBAT}^{\blacktriangledown\blacktriangle}]$$

2.28

$$\left(\frac{d[\mathrm{TBAT}^{\blacktriangle\blacktriangle}]}{d\tau}\right)_{\mathrm{R1}} = k_{-1}^{\mathrm{obs}}[\mathrm{FTPS}^{\blacktriangle}][\mathrm{TBAF}^{\blacktriangle}] - 2k_{1}^{\mathrm{obs}}[\mathrm{TBAT}^{\blacktriangle\blacktriangle}]$$

2.29

$$\left(\frac{d[\mathrm{FTPS}^{\blacktriangle}]}{d\tau}\right)_{\mathrm{R1}} = k_{1}^{\mathrm{obs}}[\mathrm{TBAT}^{\blacktriangledown\blacktriangle}] + 2k_{1}^{\mathrm{obs}}[\mathrm{TBAT}^{\blacktriangle\blacktriangle}] - k_{-1}^{\mathrm{obs}}[\mathrm{FTPS}^{\blacktriangle}][\mathrm{TBAF}^{\blacktriangledown}] - k_{-1}^{\mathrm{obs}}[\mathrm{FTPS}^{\blacktriangle}][\mathrm{TBAF}^{\blacktriangle}]$$

2.30

$$\left(\frac{d[\mathrm{TBAF}^{\blacktriangle}]}{d\tau}\right)_{\mathrm{R1}} = k_{1}^{\mathrm{obs}}[\mathrm{TBAT}^{\blacktriangledown\blacktriangle}] + 2k_{1}^{\mathrm{obs}}[\mathrm{TBAT}^{\blacktriangle\blacktriangle}] - k_{-1}^{\mathrm{obs}}[\mathrm{TBAF}^{\blacktriangle}][\mathrm{FTPS}^{\blacktriangledown}] - k_{-1}^{\mathrm{obs}}[\mathrm{TBAF}^{\blacktriangle}][\mathrm{FTPS}^{\blacktriangle}]$$

Direct transfer (reaction 2, “R2”):

2.31

$$\begin{aligned}\left(\frac{d[\mathrm{TBAT}^{\blacktriangledown\blacktriangle}]}{d\tau}\right)_{\mathrm{R2}} &= 2k_{2}^{\mathrm{obs}}[\mathrm{TBAT}^{\blacktriangledown\blacktriangledown}][\mathrm{FTPS}^{\blacktriangle}] + 2k_{2}^{\mathrm{obs}}[\mathrm{TBAT}^{\blacktriangle\blacktriangle}][\mathrm{FTPS}^{\blacktriangledown}] - k_{2}^{\mathrm{obs}}[\mathrm{TBAT}^{\blacktriangledown\blacktriangle}][\mathrm{FTPS}^{\blacktriangledown}] \\ &\quad - k_{2}^{\mathrm{obs}}[\mathrm{TBAT}^{\blacktriangledown\blacktriangle}][\mathrm{FTPS}^{\blacktriangle}]\end{aligned}$$

2.32

$$\left(\frac{d[\mathrm{TBAT}^{\blacktriangle\blacktriangle}]}{d\tau}\right)_{\mathrm{R2}} = k_{2}^{\mathrm{obs}}[\mathrm{TBAT}^{\blacktriangledown\blacktriangle}][\mathrm{FTPS}^{\blacktriangle}] - 2k_{2}^{\mathrm{obs}}[\mathrm{TBAT}^{\blacktriangle\blacktriangle}][\mathrm{FTPS}^{\blacktriangledown}]$$

2.33

$$\left(\frac{d[\mathrm{FTPS}^{\blacktriangle}]}{d\tau}\right)_{\mathrm{R2}} = k_2^{\mathrm{obs}}[\mathrm{TBAT}^{\blacktriangledown\blacktriangle}][\mathrm{FTPS}^{\blacktriangledown}] + 2k_2^{\mathrm{obs}}[\mathrm{TBAT}^{\blacktriangle\blacktriangle}][\mathrm{FTPS}^{\blacktriangledown}] - 2k_2^{\mathrm{obs}}[\mathrm{TBAT}^{\blacktriangledown\blacktriangledown}][\mathrm{FTPS}^{\blacktriangle}] - k_2^{\mathrm{obs}}[\mathrm{TBAT}^{\blacktriangledown\blacktriangle}][\mathrm{FTPS}^{\blacktriangle}]$$

The following is noted (Equations 2.20–2.22, recalled):

2.20, recalled

$$m^{\mathrm{FTPS}} = \frac{[\mathrm{FTPS}^{\blacktriangle}]}{[\mathrm{FTPS}]} = \frac{[\mathrm{FTPS}^{\blacktriangle}]}{[\mathrm{FTPS}^{\blacktriangledown}] + [\mathrm{FTPS}^{\blacktriangle}]}$$

2.21, recalled

$$m^{\mathrm{TBAF}} = \frac{[\mathrm{TBAF}^{\blacktriangle}]}{[\mathrm{TBAF}]} = \frac{[\mathrm{TBAF}^{\blacktriangle}]}{[\mathrm{TBAF}^{\blacktriangledown}] + [\mathrm{TBAF}^{\blacktriangle}]}$$

2.22, recalled

$$m^{\mathrm{TBAT}} = \frac{[\mathrm{TBAT}^{\blacktriangledown\blacktriangle}] + 2[\mathrm{TBAT}^{\blacktriangle\blacktriangle}]}{2[\mathrm{TBAT}]} = \frac{[\mathrm{TBAT}^{\blacktriangledown\blacktriangle}] + 2[\mathrm{TBAT}^{\blacktriangle\blacktriangle}]}{2([\mathrm{TBAT}^{\blacktriangledown\blacktriangledown}] + [\mathrm{TBAT}^{\blacktriangledown\blacktriangle}] + [\mathrm{TBAT}^{\blacktriangle\blacktriangle}])}$$

Hence:

2.34

$$\left(\frac{dm^{\mathrm{TBAT}}}{d\tau}\right)_{T_1} = \frac{1}{T_1^{\mathrm{TBAT}}}(1 - m^{\mathrm{TBAT}})$$

2.35

$$\left(\frac{dm^{\mathrm{FTPS}}}{d\tau}\right)_{T_1} = \frac{1}{T_1^{\mathrm{FTPS}}}(1 - m^{\mathrm{FTPS}})$$

2.36

$$\left(\frac{dm^{\mathrm{TBAF}}}{d\tau}\right)_{T_1} = \frac{1}{T_1^{\mathrm{TBAF}}}(1 - m^{\mathrm{TBAF}})$$

2.37

$$\left(\frac{dm^{\mathrm{TBAT}}}{d\tau}\right)_{\mathrm{R1}} = \frac{k_{-1}^{\mathrm{obs}}[\mathrm{FTPS}][\mathrm{TBAF}]}{2[\mathrm{TBAT}]}(m^{\mathrm{FTPS}} + m^{\mathrm{TBAF}}) - 2k_1^{\mathrm{obs}}m^{\mathrm{TBAT}}$$

2.38

$$\left(\frac{dm^{\mathrm{FTPS}}}{d\tau}\right)_{\mathrm{R1}} = \frac{2k_1^{\mathrm{obs}}[\mathrm{TBAT}]}{[\mathrm{FTPS}]}m^{\mathrm{TBAT}} - k_{-1}^{\mathrm{obs}}[\mathrm{TBAF}]m^{\mathrm{FTPS}}$$

2.39

$$\left(\frac{dm^{\mathrm{TBAF}}}{d\tau}\right)_{\mathrm{R1}} = \frac{2k_1^{\mathrm{obs}}[\mathrm{TBAT}]}{[\mathrm{TBAF}]}m^{\mathrm{TBAT}} - k_{-1}^{\mathrm{obs}}[\mathrm{FTPS}]m^{\mathrm{TBAF}}$$

2.40

$$\left(\frac{dm^{\mathrm{TBAT}}}{d\tau}\right)_{\mathrm{R2}} = k_2^{\mathrm{obs}}[\mathrm{FTPS}](m^{\mathrm{FTPS}} - m^{\mathrm{TBAT}})$$

2.41

$$\left(\frac{dm^{\mathrm{FTPS}}}{d\tau}\right)_{\mathrm{R2}} = 2k_2^{\mathrm{obs}}[\mathrm{TBAT}](m^{\mathrm{TBAT}} - m^{\mathrm{FTPS}})$$

The total temporal change in the fractional magnetisation of a species, $dm^{\mathrm{S}}/d\tau$ is the sum of contributions from relaxation, dissociative (reaction 1) and direct (reaction 2) transfer pathways. Hence, summing Equations 2.34, 2.37 and 2.40; 2.35, 2.38 and 2.41; and 2.36 and 2.39, gives the fractional magnetisation rate laws of TBAT, FTPS and TBAF (Equations 2.42, 2.43 and 2.44), respectively.

2.42

$$\begin{aligned}\frac{dm^{\mathrm{TBAT}}}{d\tau} &= \left(\frac{dm^{\mathrm{TBAT}}}{d\tau}\right)_{T_1} + \left(\frac{dm^{\mathrm{TBAT}}}{d\tau}\right)_{\mathrm{R1}} + \left(\frac{dm^{\mathrm{TBAT}}}{d\tau}\right)_{\mathrm{R2}} \\ &= \frac{1}{T_1^{\mathrm{TBAT}}}(1 - m^{\mathrm{TBAT}}) + \frac{k_{-1}^{\mathrm{obs}}[\mathrm{FTPS}][\mathrm{TBAF}]}{2[\mathrm{TBAT}]}(m^{\mathrm{FTPS}} + m^{\mathrm{TBAF}}) - 2k_1^{\mathrm{obs}} m^{\mathrm{TBAT}} \\ &+ k_2^{\mathrm{obs}}[\mathrm{FTPS}](m^{\mathrm{FTPS}} - m^{\mathrm{TBAT}})\end{aligned}$$

2.43

$$\begin{aligned}\frac{dm^{\mathrm{FTPS}}}{d\tau} &= \left(\frac{dm^{\mathrm{FTPS}}}{d\tau}\right)_{T_1} + \left(\frac{dm^{\mathrm{FTPS}}}{d\tau}\right)_{\mathrm{R1}} + \left(\frac{dm^{\mathrm{FTPS}}}{d\tau}\right)_{\mathrm{R2}} \\ &= \frac{1}{T_1^{\mathrm{FTPS}}}(1 - m^{\mathrm{FTPS}}) + \frac{2k_1^{\mathrm{obs}}[\mathrm{TBAT}]}{[\mathrm{FTPS}]} m^{\mathrm{TBAT}} - k_{-1}^{\mathrm{obs}}[\mathrm{TBAF}] m^{\mathrm{FTPS}} \\ &+ 2k_2^{\mathrm{obs}}[\mathrm{TBAT}](m^{\mathrm{TBAT}} - m^{\mathrm{FTPS}})\end{aligned}$$

2.44

$$\frac{dm^{\mathrm{TBAF}}}{d\tau} = \left(\frac{dm^{\mathrm{TBAF}}}{d\tau}\right)_{T_1} + \left(\frac{dm^{\mathrm{TBAF}}}{d\tau}\right)_{\mathrm{R1}} = \frac{1}{T_1^{\mathrm{TBAF}}}(1 - m^{\mathrm{TBAF}}) + \frac{2k_1^{\mathrm{obs}}[\mathrm{TBAT}]}{[\mathrm{TBAF}]} m^{\mathrm{TBAT}} - k_{-1}^{\mathrm{obs}}[\mathrm{FTPS}] m^{\mathrm{TBAF}}$$

When TBAT is mixed with FTPS, two or three spins exist in equilibrium. If TBAT does not dissociate into FTPS and TBAF, only TBAT and FTPS are present in the solution ([TBAF] = 0, $2k_1^{\mathrm{obs}} = 0$, [TBAT] = c^{TBAT}, [FTPS] = c^{FTPS}). Equations 2.42 and 2.43 are then simplified to Equations 2.45 and 2.46, which now describe the system where TBAT and FTPS exchange solely *via* direct transfer (reaction 2).

2.45

$$\frac{dm^{\mathrm{TBAT}}}{d\tau} = \frac{1}{T_1^{\mathrm{TBAT}}}(1 - m^{\mathrm{TBAT}}) + k_2^{\mathrm{obs}} c^{\mathrm{FTPS}}(m^{\mathrm{FTPS}} - m^{\mathrm{TBAT}})$$

2.46

$$\frac{dm^{\mathrm{FTPS}}}{d\tau} = \frac{1}{T_1^{\mathrm{FTPS}}}(1 - m^{\mathrm{FTPS}}) + 2k_2^{\mathrm{obs}} c^{\mathrm{TBAT}}(m^{\mathrm{TBAT}} - m^{\mathrm{FTPS}})$$

In the other case, TBAT dissociates into FTPS and TBAF, and their concentrations are below the limit of detection in ^{19}F NMR spectroscopy. The overall fluorine exchange in the system is due to the dissociative or direct pathway (reaction 1 and reaction 2, respectively), or both.

In order to simplify the mathematical analysis, we apply the steady state approximation of the fractional magnetisation of TBAF as a low-concentration intermediate in the magnetisation transfer between TBAT and FTPS (Equation 2.47).

2.47

$$\frac{dm^{\mathrm{TBAF}}}{d\tau} = \frac{1}{T_1^{\mathrm{TBAF}}}(1 - m^{\mathrm{TBAF}}) + \frac{2k_1^{\mathrm{obs}}[\mathrm{TBAT}]}{[\mathrm{TBAF}]} m^{\mathrm{TBAT}} - k_{-1}^{\mathrm{obs}}[\mathrm{FTPS}] m^{\mathrm{TBAF}} \approx 0$$

Solving Equation 2.47 for m^{TBAF} (ignoring the longitudinal relaxation of TBAF):

2.48

$$m^{\mathrm{TBAF}} \approx \frac{\dfrac{1}{T_1^{\mathrm{TBAF}}} + \dfrac{2k_1^{\mathrm{obs}}[\mathrm{TBAT}]}{[\mathrm{TBAF}]} m^{\mathrm{TBAT}}}{\dfrac{1}{T_1^{\mathrm{TBAF}}} + k_{-1}^{\mathrm{obs}}[\mathrm{FTPS}]} \approx \frac{2k_1^{\mathrm{obs}}[\mathrm{TBAT}]}{k_{-1}^{\mathrm{obs}}[\mathrm{FTPS}][\mathrm{TBAF}]} m^{\mathrm{TBAT}}$$

Reintroducing the equilibrium constant of the dissociation of TBAT into FTPS and TBAF (K_1^{obs}, Equation 2.49), Equation 2.48 is simplified to Equation 2.50, where the fractional magnetisation of TBAF can be approximated to that of TBAT.

2.49

$$K_1^{\mathrm{obs}} = \frac{2k_1^{\mathrm{obs}}}{k_{-1}^{\mathrm{obs}}} = \frac{[\mathrm{FTPS}][\mathrm{TBAF}]}{[\mathrm{TBAT}]}$$

2.50

$$m^{\mathrm{TBAF}} \approx m^{\mathrm{TBAT}}$$

Inserting Equations 2.49 and 2.50 into Equations 2.42 and 2.43 (and approximating equilibrium concentrations of TBAT and FTPS to their initial concentrations) gives Equations 2.51 and 2.52, which describe the TBAT/FTPS system, where TBAT and FTPS exchange fluoride *via* a low-concentration TBAF intermediate (reaction 1), directly in a bimolecular reaction (reaction 2), or *via* both these mechanisms proceeding in parallel.

2.51

$$\frac{dm^{\mathrm{TBAT}}}{d\tau} = \frac{1}{T_1^{\mathrm{TBAT}}}(1 - m^{\mathrm{TBAT}}) + \left(k_1^{\mathrm{obs}} + k_2^{\mathrm{obs}} c^{\mathrm{FTPS}}\right)(m^{\mathrm{FTPS}} - m^{\mathrm{TBAT}})$$

2.52

$$\frac{dm^{\mathrm{FTPS}}}{d\tau}=\frac{1}{T_1^{\mathrm{FTPS}}}(1-m^{\mathrm{FTPS}})+\left(\frac{2k_1^{\mathrm{obs}}c^{\mathrm{TBAT}}}{c^{\mathrm{FTPS}}}+2k_2^{\mathrm{obs}}c^{\mathrm{TBAT}}\right)(m^{\mathrm{TBAT}}-m^{\mathrm{FTPS}})$$

Introducing herein an auxiliary term, *α*, and the ratio of equilibrium longitudinal magnetisations of TBAT-to-FTPS, *r* (Equations 2.53 and 2.54), rate laws take the form as in Equations 2.55 and 2.56.

2.53

$$\alpha=k_1^{\mathrm{obs}}+k_2^{\mathrm{obs}}c^{\mathrm{FTPS}}$$

2.54

$$r=\frac{M_{z,\mathrm{eq}}^{\mathrm{TBAT}}}{M_{z,\mathrm{eq}}^{\mathrm{FTPS}}}=\frac{2[\mathrm{TBAT}]}{[\mathrm{FTPS}]}\approx\frac{2c^{\mathrm{TBAT}}}{c^{\mathrm{FTPS}}}$$

2.55

$$\frac{dm^{\mathrm{TBAT}}}{d\tau}=\frac{1}{T_1^{\mathrm{TBAT}}}(1-m^{\mathrm{TBAT}})+\alpha(m^{\mathrm{FTPS}}-m^{\mathrm{TBAT}})$$

2.56

$$\frac{dm^{\mathrm{FTPS}}}{d\tau}=\frac{1}{T_1^{\mathrm{FTPS}}}(1-m^{\mathrm{FTPS}})+r\alpha(m^{\mathrm{TBAT}}-m^{\mathrm{FTPS}})$$

2.3.5. Integration of the rate laws

Equations 2.55 and 2.56 can be solved analytically in the following way. Rearranging Equations 2.55 and 2.56 for m^{FTPS} and m^{TBAT}, respectively, yields Equations 2.57 and 2.58.

2.57

$$m^{\mathrm{TBAT}}=\frac{\frac{dm^{\mathrm{FTPS}}}{d\tau}+\left(r\alpha+\frac{1}{T_1^{\mathrm{FTPS}}}\right)m^{\mathrm{FTPS}}-\frac{1}{T_1^{\mathrm{FTPS}}}}{r\alpha}$$

2.58

$$m^{\mathrm{FTPS}}=\frac{\frac{dm^{\mathrm{TBAT}}}{d\tau}+\left(\alpha+\frac{1}{T_1^{\mathrm{TBAT}}}\right)m^{\mathrm{TBAT}}-\frac{1}{T_1^{\mathrm{TBAT}}}}{\alpha}$$

Inserting Equations 2.57 and 2.58 into Equations 2.55 and 2.56, respectively, and rearranging gives Equations 2.59 and 2.60.

2.59

$$\frac{d^2m^{\mathrm{TBAT}}}{d\tau^2}+\left(\alpha+\frac{1}{T_1^{\mathrm{TBAT}}}+r\alpha+\frac{1}{T_1^{\mathrm{FTPS}}}\right)\frac{dm^{\mathrm{TBAT}}}{d\tau}+\frac{\alpha T_1^{\mathrm{TBAT}}+r\alpha T_1^{\mathrm{FTPS}}+1}{T_1^{\mathrm{TBAT}}T_1^{\mathrm{FTPS}}}(m^{\mathrm{TBAT}}-1)=0$$

2.60

$$\frac{d^2m^{\mathrm{FTPS}}}{d\tau^2}+\left(\alpha+\frac{1}{T_1^{\mathrm{TBAT}}}+r\alpha+\frac{1}{T_1^{\mathrm{FTPS}}}\right)\frac{dm^{\mathrm{FTPS}}}{d\tau}+\frac{\alpha T_1^{\mathrm{TBAT}}+r\alpha T_1^{\mathrm{FTPS}}+1}{T_1^{\mathrm{TBAT}}T_1^{\mathrm{FTPS}}}(m^{\mathrm{FTPS}}-1)=0$$

Equations 2.59 and 2.60 are second-order, non-homogeneous ordinary differential equations, which can be solved analytically to give m^{TBAT} and m^{FTPS}, as presented in Equations 2.61–2.64.

2.61

$$m^{\mathrm{TBAT}}=c_1e^{(\beta+\gamma)\tau}+c_2e^{(\beta-\gamma)\tau}+1$$

2.62

$$m^{\mathrm{FTPS}}=c_3e^{(\beta+\gamma)\tau}+c_4e^{(\beta-\gamma)\tau}+1$$

Where:

2.63

$$\beta=-\frac{\alpha(r+1)+\frac{1}{T_1^{\mathrm{TBAT}}}+\frac{1}{T_1^{\mathrm{FTPS}}}}{2}$$

2.64

$$\gamma=\frac{\sqrt{\left(\alpha+\frac{1}{T_1^{\mathrm{TBAT}}}-r\alpha-\frac{1}{T_1^{\mathrm{FTPS}}}\right)^2+4r\alpha^2}}{2}$$

2.53, recalled

$$\alpha=k_1^{\mathrm{obs}}+k_2^{\mathrm{obs}}c^{\mathrm{FTPS}}$$

2.54, recalled

$$r=\frac{M_{z,\mathrm{eq}}^{\mathrm{TBAT}}}{M_{z,\mathrm{eq}}^{\mathrm{FTPS}}}=\frac{2[\mathrm{TBAT}]}{[\mathrm{FTPS}]}\approx\frac{2c^{\mathrm{TBAT}}}{c^{\mathrm{FTPS}}}$$

The constants c_1–c_4 depend on the inversion scenario and are given in Equations 2.65–2.68, where m_0^{TBAT} and m_0^{FTPS} are the fractional magnetisations of TBAT and FTPS at $\tau = 0$ (see Section 7.1.2 for the derivation).

2.65

$$c_1=\frac{\alpha\left(m_0^{\mathrm{FTPS}}-m_0^{\mathrm{TBAT}}\right)+\left(\beta-\gamma+\frac{1}{T_1^{\mathrm{TBAT}}}\right)(1-m_0^{\mathrm{TBAT}})}{2\gamma}$$

2.66

$$c_2=-\frac{\alpha\left(m_0^{\mathrm{FTPS}}-m_0^{\mathrm{TBAT}}\right)+\left(\beta+\gamma+\frac{1}{T_1^{\mathrm{TBAT}}}\right)(1-m_0^{\mathrm{TBAT}})}{2\gamma}$$

2.67

$$c_3 = \frac{r\alpha\left(m_0^{\mathrm{TBAT}} - m_0^{\mathrm{FTPS}}\right) + \left(\beta - \gamma + \frac{1}{T_1^{\mathrm{FTPS}}}\right)\left(1 - m_0^{\mathrm{FTPS}}\right)}{2\gamma}$$

2.68

$$c_4 = -\frac{r\alpha\left(m_0^{\mathrm{TBAT}} - m_0^{\mathrm{FTPS}}\right) + \left(\beta + \gamma + \frac{1}{T_1^{\mathrm{FTPS}}}\right)\left(1 - m_0^{\mathrm{FTPS}}\right)}{2\gamma}$$

2.3.6. Further approximations

Based on the preliminary magnetisation transfer experiments between TBAT and FTPS in THF and MeCN (see Section 3.3), exchange is significantly faster than relaxation. Additional approximations can therefore be applied in order to simplify the model further for the fractional magnetisation (or integral) of the initially non-inverted signal (here, TBAT) as a function of variable delay.

Firstly, the longitudinal relaxation time constants of TBAT and FTPS in their mixture (T_1^{obs}) become equal and are the weighted average of the longitudinal relaxation time constants of the isolated spins under given conditions (Equation 2.69).[220]

2.69

$$T_1^{\mathrm{obs}} = \frac{T_1^{\mathrm{TBAT}} T_1^{\mathrm{FTPS}}(r+1)}{T_1^{\mathrm{TBAT}} + rT_1^{\mathrm{FTPS}}}$$

Substituting T_1^{TBAT} and T_1^{FTPS} with T_1^{obs} in β and γ, approximates them to:

2.70

$$\beta \approx -\frac{\alpha(r+1)}{2} - \frac{1}{T_1^{\mathrm{obs}}}$$

2.71

$$\gamma \approx \frac{\alpha(r+1)}{2}$$

The two exponentials in Equations 2.61 and 2.62 now represent separated exchange and relaxation processes (Equations 2.72 and 2.73).

2.72

$$\beta - \gamma \approx -\alpha(r+1) - \frac{1}{T_1^{\mathrm{obs}}} \approx -\alpha(r+1) \approx -2\gamma$$

2.73

$$\beta + \gamma \approx -\frac{1}{T_1^{\mathrm{obs}}}$$

The constants c_1 and c_2 can therefore be approximated to:

2.74

$$c_1 \approx -\frac{\Delta m_0}{r+1} + m_0^{\mathrm{TBAT}} - 1$$

2.75

$$c_2 \approx \frac{\Delta m_0}{r+1}$$

Where Δm_0 is the difference between the fractional magnetisations of TBAT and FTPS immediately after the soft pulse (at $\tau = 0$):

2.76

$$\Delta m_0 = m_0^{\mathrm{TBAT}} - m_0^{\mathrm{FTPS}}$$

For solutions in THF (see Sections 3.3.1–3.3.4), the exchange between the spins is slow with respect to the duration of the soft inversion pulse (~1.3 ms), and therefore $\Delta m_0 < 1$ solely due to imperfect inversion of FTPS (*i.e.* $m_0^{\mathrm{TBAT}} \approx 1$ and $m_0^{\mathrm{FTPS}} > 0$). Equation 2.61 is therefore simplified to:

2.77

$$m^{\mathrm{TBAT}} \approx \frac{\Delta m_0}{r+1}\left[e^{-\alpha(r+1)\tau} - e^{-\frac{\tau}{T_1^{\mathrm{obs}}}}\right] + 1 \approx \frac{1 - m_0^{\mathrm{FTPS}}}{r+1}\left[e^{-\alpha(r+1)\tau} - e^{-\frac{\tau}{T_1^{\mathrm{obs}}}}\right] + 1$$

Which can be expressed as $M_z^{\mathrm{TBAT}}(\tau)$ according to Equation 2.19 (x is the pre-exponential term, which contains the initial magnetisations of the two spins and the ratio of their equilibrium magnetisations).

2.78

$$M_z^{\mathrm{TBAT}} \approx \frac{M_{z,\mathrm{eq}}^{\mathrm{TBAT}} - rM_{z,0}^{\mathrm{FTPS}}}{r+1}\left[e^{-\alpha(r+1)\tau} - e^{-\frac{\tau}{T_1^{\mathrm{obs}}}}\right] + M_{z,\mathrm{eq}}^{\mathrm{TBAT}} = x\left[e^{-\alpha(r+1)\tau} - e^{-\frac{\tau}{T_1^{\mathrm{obs}}}}\right] + M_{z,\mathrm{eq}}^{\mathrm{TBAT}}$$

As discussed in Section 3.3.5, the exchange between the spins in MeCN is more rapid than in THF, and no longer negligible with respect to the duration of the soft inversion pulse (~1.3 ms). Therefore, $m_0^{\mathrm{TBAT}} < 1$ and $m_0^{\mathrm{FTPS}} > 0$, and Equation 2.61 is simplified to:

2.79

$$m^{\mathrm{TBAT}} \approx \frac{\Delta m_0}{r+1} e^{-\alpha(r+1)\tau} + \frac{r(m_0^{\mathrm{TBAT}} - 1) + m_0^{\mathrm{FTPS}} - 1}{r+1} e^{-\frac{\tau}{T_1^{\mathrm{obs}}}} + 1$$

Which can be expressed as $M_z^{\mathrm{TBAT}}(\tau)$ according to Equation 2.19 (x and x' are the two unequal pre-exponential terms).

2.80

$$M_z^{\mathrm{TBAT}} \approx \frac{M_{z,0}^{\mathrm{TBAT}} - rM_{z,0}^{\mathrm{FTPS}}}{r+1} e^{-\alpha(r+1)\tau} + \frac{r\left(M_0^{\mathrm{TBAT}} + M_0^{\mathrm{FTPS}} - M_{\mathrm{eq}}^{\mathrm{TBAT}}\right) - M_{\mathrm{eq}}^{\mathrm{TBAT}}}{r+1} e^{-\frac{\tau}{T_1^{\mathrm{obs}}}} + M_{z,\mathrm{eq}}^{\mathrm{TBAT}}$$
$$= xe^{-\alpha(r+1)\tau} - x'e^{-\frac{\tau}{T_1^{\mathrm{obs}}}} + M_{z,\mathrm{eq}}^{\mathrm{TBAT}}$$

2.4. Exchange in the TBAT/ARSF system and inhibition by FTPS

The kinetic model for the TBAT/2-naphthalenyl fluorosulfate (ARSF) spin system, where ARSF is the electrophilic acceptor of the fluoride (Scheme 2.5a), is derived in an analogous way to the TBAT/FTPS one. We note that equilibrium dissociation of TBAT (if present), produces low-concentration FTPS and TBAF. Hence, Equations 2.42–2.44 are the starting point in the derivation of the model herein.

2.42, recalled

$$\frac{dm^{\mathrm{TBAT}}}{d\tau} = \frac{1}{T_1^{\mathrm{TBAT}}}(1 - m^{\mathrm{TBAT}}) + \frac{k_{-1}^{\mathrm{obs}}[\mathrm{FTPS}][\mathrm{TBAF}]}{2[\mathrm{TBAT}]}(m^{\mathrm{FTPS}} + m^{\mathrm{TBAF}}) - 2k_1^{\mathrm{obs}}m^{\mathrm{TBAT}}$$
$$+ k_2^{\mathrm{obs}}[\mathrm{FTPS}](m^{\mathrm{FTPS}} - m^{\mathrm{TBAT}})$$

2.43, recalled

$$\frac{dm^{\mathrm{FTPS}}}{d\tau} = \frac{1}{T_1^{\mathrm{FTPS}}}(1 - m^{\mathrm{FTPS}}) + \frac{2k_1^{\mathrm{obs}}[\mathrm{TBAT}]}{[\mathrm{FTPS}]}m^{\mathrm{TBAT}} - k_{-1}^{\mathrm{obs}}[\mathrm{TBAF}]m^{\mathrm{FTPS}} + 2k_2^{\mathrm{obs}}[\mathrm{TBAT}](m^{\mathrm{TBAT}} - m^{\mathrm{FTPS}})$$

2.44, recalled

$$\frac{dm^{\mathrm{TBAF}}}{d\tau} = \frac{1}{T_1^{\mathrm{TBAF}}}(1 - m^{\mathrm{TBAF}}) + \frac{2k_1^{\mathrm{obs}}[\mathrm{TBAT}]}{[\mathrm{TBAF}]}m^{\mathrm{TBAT}} - k_{-1}^{\mathrm{obs}}[\mathrm{FTPS}]m^{\mathrm{TBAF}}$$

ARSF is assumed to exchange the fluoride in an associative process, where an anionic intermediate **2.1** containing two equivalent fluorine atoms on the sulfur centre is formed with Δ*G*° >> 0 (Scheme 2.5a). The addition of ARSF to the solution of TBAT, therefore, results in two more exchanging species present in the system, ARSF and anion **2.1**, the latter being a low-concentration intermediate. Since intermediate **2.1** is short-lived (and thus in low concentration), the exchange of the S–F fluoride may be approximated to a concerted process with respect to ARSF (Scheme 2.5b).

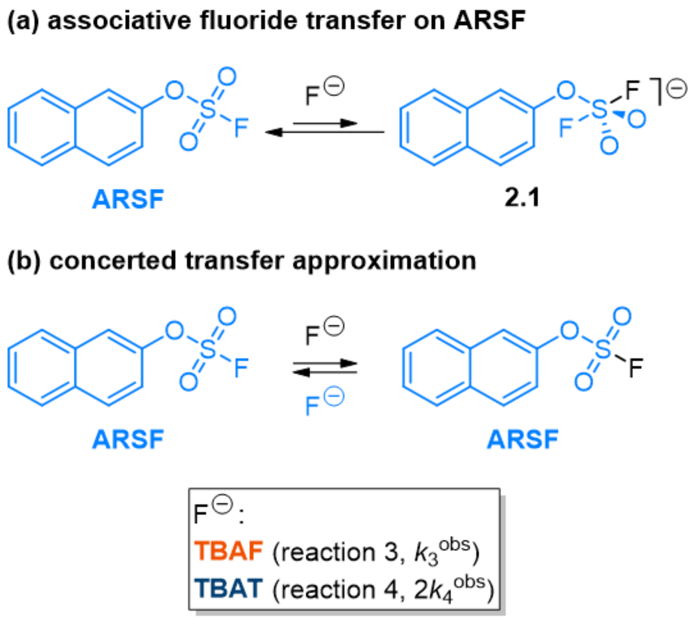

Scheme 2.5: (a) ARSF exchanges fluoride in an associative process *via* a pentacoordinate difluoro intermediate 2.1 (Δ*G*° >> 0). (b) Due to the intermediate 2.1 being short-lived, it can be assumed in the derivation of the model that the fluoride exchange is concerted with respect to ARSF. In both cases, “F^-” denotes a nucleophilic fluoride source, which may be TBAF and/or TBAT in the TBAT/ARSF system.

The fluoride that exchanges with ARSF in the system may be the low-concentration TBAF formed from dissociation of TBAT (Scheme 2.1a) and/or TBAT directly (Scheme 2.1b). These reactions, described by the rate constants k_3 and $2k_4$ (or k_3 and k_4 “per fluoride”), respectively, correspond to the dissociative and direct transfer pathways with respect to TBAT. These two pathways, accounting for the magnetisation states of TBAT, TBAF and ARSF, are presented in Scheme 2.6.

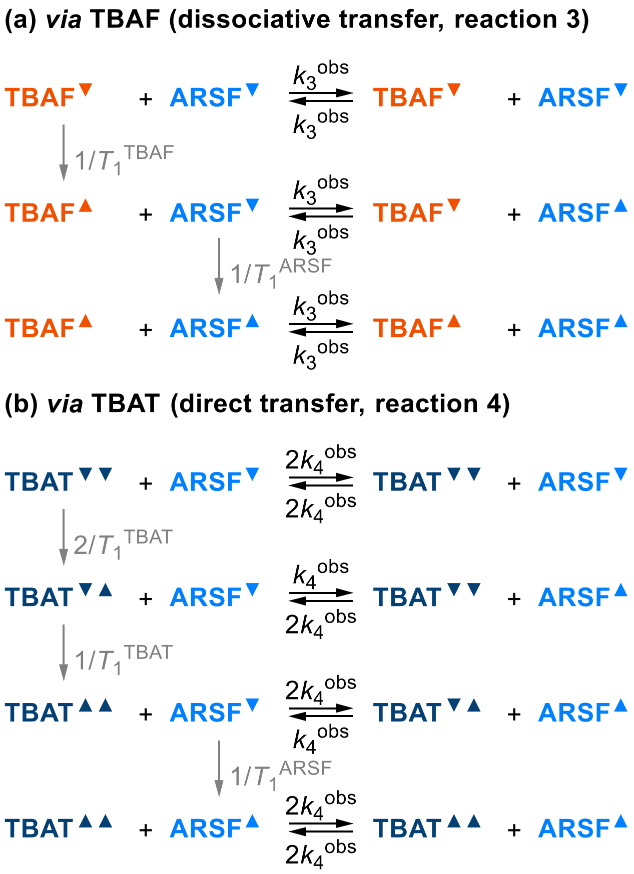

Scheme 2.6: The breakdown of the (a) dissociative and (b) direct transfer exchange pathways between TBAT and ARSF, accounting for their longitudinal magnetisation states. Note the rate constants of the chemically degenerate equilibrium transfer reactions relative to the overall rate constant $2k_4^{obs}$ depending on the magnetisation states of the spins.

The rate laws arising from the exchange pathways in Scheme 2.6, and the relaxation of ARSF, are presented in Equations 2.82–2.92 (the expression for fractional magnetisation of ARSF is analogous to those of FTPS and TBAF, and is given by Equation 2.81).

2.81

$$m^{\mathrm{ARSF}} = \frac{[\mathrm{ARSF}^{\blacktriangle}]}{[\mathrm{ARSF}]} = \frac{[\mathrm{ARSF}^{\blacktriangle}]}{[\mathrm{ARSF}^{\blacktriangledown}] + [\mathrm{ARSF}^{\blacktriangle}]} = \frac{M_z^{\mathrm{ARSF}} + M_{z,\mathrm{eq}}^{\mathrm{ARSF}}}{2M_{z,\mathrm{eq}}^{\mathrm{ARSF}}}$$

Relaxation of ARSF:

2.82

$$\left(\frac{d[\mathrm{ARSF}^{\blacktriangle}]}{d\tau}\right)_{T_1} = \frac{1}{T_1^{\mathrm{ARSF}}}[\mathrm{ARSF}^{\blacktriangledown}]$$

2.83

$$\left(\frac{dm^{\mathrm{ARSF}}}{d\tau}\right)_{T_1} = \frac{1}{T_1^{\mathrm{ARSF}}}(1 - m^{\mathrm{ARSF}})$$

Dissociative transfer (reaction 3, “R3”):

2.84

$$\left(\frac{d[\mathrm{TBAF}^{\blacktriangle}]}{d\tau}\right)_{\mathrm{R3}} = k_3^{\mathrm{obs}}[\mathrm{TBAF}^{\blacktriangledown}][\mathrm{ARSF}^{\blacktriangle}] - k_3^{\mathrm{obs}}[\mathrm{TBAF}^{\blacktriangle}][\mathrm{ARSF}^{\blacktriangledown}]$$

2.85

$$\left(\frac{dm^{\mathrm{TBAF}}}{d\tau}\right)_{\mathrm{R3}} = k_3^{\mathrm{obs}}[\mathrm{ARSF}](m^{\mathrm{ARSF}} - m^{\mathrm{TBAF}})$$

2.86

$$\left(\frac{d[\mathrm{ARSF}^{\blacktriangle}]}{d\tau}\right)_{\mathrm{R3}} = k_3^{\mathrm{obs}}[\mathrm{TBAF}^{\blacktriangle}][\mathrm{ARSF}^{\blacktriangledown}] - k_3^{\mathrm{obs}}[\mathrm{TBAF}^{\blacktriangledown}][\mathrm{ARSF}^{\blacktriangle}]$$

2.87

$$\left(\frac{dm^{\mathrm{ARSF}}}{d\tau}\right)_{\mathrm{R3}} = k_3^{\mathrm{obs}}[\mathrm{TBAF}](m^{\mathrm{TBAF}} - m^{\mathrm{ARSF}})$$

Direct transfer (reaction 4, “R4”):

2.88

$$\begin{aligned}\left(\frac{d[\mathrm{TBAT}^{\blacktriangledown\blacktriangle}]}{d\tau}\right)_{\mathrm{R4}} &= 2k_4^{\mathrm{obs}}[\mathrm{TBAT}^{\blacktriangledown\blacktriangledown}][\mathrm{ARSF}^{\blacktriangle}] + 2k_4^{\mathrm{obs}}[\mathrm{TBAT}^{\blacktriangle\blacktriangle}][\mathrm{ARSF}^{\blacktriangledown}] - k_4^{\mathrm{obs}}[\mathrm{TBAT}^{\blacktriangledown\blacktriangle}][\mathrm{ARSF}^{\blacktriangledown}] \\ &\quad - k_4^{\mathrm{obs}}[\mathrm{TBAT}^{\blacktriangledown\blacktriangle}][\mathrm{ARSF}^{\blacktriangle}]\end{aligned}$$

2.89

$$\left(\frac{d[\mathrm{TBAT}^{\blacktriangle\blacktriangle}]}{d\tau}\right)_{\mathrm{R4}} = k_4^{\mathrm{obs}}[\mathrm{TBAT}^{\blacktriangledown\blacktriangle}][\mathrm{ARSF}^{\blacktriangle}] - 2k_4^{\mathrm{obs}}[\mathrm{TBAT}^{\blacktriangle\blacktriangle}][\mathrm{ARSF}^{\blacktriangledown}]$$

2.90

$$\left(\frac{dm^{\mathrm{TBAT}}}{d\tau}\right)_{\mathrm{R4}} = k_4^{\mathrm{obs}}[\mathrm{ARSF}](m^{\mathrm{ARSF}} - m^{\mathrm{TBAT}})$$

2.91

$$\left(\frac{d[\mathrm{ARSF}^{\blacktriangle}]}{d\tau}\right)_{\mathrm{R4}} = k_4^{\mathrm{obs}}[\mathrm{ARSF}^{\blacktriangledown}]([\mathrm{TBAT}^{\blacktriangledown\blacktriangle}] + 2[\mathrm{TBAT}^{\blacktriangle\blacktriangle}]) - k_4^{\mathrm{obs}}[\mathrm{ARSF}^{\blacktriangle}](2[\mathrm{TBAT}^{\blacktriangledown\blacktriangledown}] + [\mathrm{TBAT}^{\blacktriangledown\blacktriangle}])$$

2.92

$$\left(\frac{dm^{\mathrm{ARSF}}}{d\tau}\right)_{\mathrm{R4}} = 2k_4^{\mathrm{obs}}[\mathrm{TBAT}](m^{\mathrm{TBAT}} - m^{\mathrm{ARSF}})$$

Summing Equations 2.42 and 2.90 gives the rate law of the fractional magnetisation of TBAT; Equations 2.44 and 2.85 – of TBAF; and Equations 2.83, 2.87 and 2.92 – of ARSF. These three rate laws are presented in Equations 2.93–2.95. The rate law of the fractional magnetisation of FTPS remains as in Equation 2.43.

2.93

$$\frac{dm^{\mathrm{TBAT}}}{d\tau}=\frac{1}{T_1^{\mathrm{TBAT}}}(1-m^{\mathrm{TBAT}})+k_2^{\mathrm{obs}}[\mathrm{FTPS}](m^{\mathrm{FTPS}}-m^{\mathrm{TBAT}})+k_1^{\mathrm{obs}}(m^{\mathrm{FTPS}}+m^{\mathrm{TBAF}}-2m^{\mathrm{TBAT}}) \\ +k_4^{\mathrm{obs}}[\mathrm{ARSF}](m^{\mathrm{ARSF}}-m^{\mathrm{TBAT}})$$

2.43, recalled

$$\frac{dm^{\mathrm{FTPS}}}{d\tau}=\frac{1}{T_1^{\mathrm{FTPS}}}(1-m^{\mathrm{FTPS}})+\frac{2k_1^{\mathrm{obs}}[\mathrm{TBAT}]}{[\mathrm{FTPS}]}m^{\mathrm{TBAT}}-k_{-1}^{\mathrm{obs}}[\mathrm{TBAF}]m^{\mathrm{FTPS}}+2k_2^{\mathrm{obs}}[\mathrm{TBAT}](m^{\mathrm{TBAT}}-m^{\mathrm{FTPS}})$$

2.94

$$\frac{dm^{\mathrm{TBAF}}}{d\tau}=\frac{1}{T_1^{\mathrm{TBAF}}}(1-m^{\mathrm{TBAF}})+\frac{2k_1^{\mathrm{obs}}[\mathrm{TBAT}]}{[\mathrm{TBAF}]}m^{\mathrm{TBAT}}-k_{-1}^{\mathrm{obs}}[\mathrm{FTPS}]m^{\mathrm{TBAF}}+k_3^{\mathrm{obs}}[\mathrm{ARSF}](m^{\mathrm{ARSF}}-m^{\mathrm{TBAF}})$$

2.95

$$\frac{dm^{\mathrm{ARSF}}}{d\tau}=\frac{1}{T_1^{\mathrm{ARSF}}}(1-m^{\mathrm{ARSF}})+k_3^{\mathrm{obs}}[\mathrm{TBAF}](m^{\mathrm{TBAF}}-m^{\mathrm{ARSF}})+2k_4^{\mathrm{obs}}[\mathrm{TBAT}](m^{\mathrm{TBAT}}-m^{\mathrm{ARSF}})$$

Here, both FTPS and TBAF are low-concentration intermediates and hence the steady state approximation of both can be applied, similarly to the steady state approximation of TBAF in Section 2.3.4 (ignoring the relaxation of FTPS and TBAF, and noting the expression for the equilibrium constant of reaction 1, Equation 2.49).

FTPS:

2.96

$$\frac{dm^{\mathrm{FTPS}}}{d\tau}=\frac{1}{T_1^{\mathrm{FTPS}}}(1-m^{\mathrm{FTPS}})+\frac{2k_1^{\mathrm{obs}}[\mathrm{TBAT}]}{[\mathrm{FTPS}]}m^{\mathrm{TBAT}}-k_{-1}^{\mathrm{obs}}[\mathrm{TBAF}]m^{\mathrm{FTPS}}+2k_2^{\mathrm{obs}}[\mathrm{TBAT}](m^{\mathrm{TBAT}}-m^{\mathrm{FTPS}}) \\ \approx 0$$

2.97

$$m^{\mathrm{FTPS}}\approx m^{\mathrm{TBAT}}$$

TBAF:

2.98

$$\frac{dm^{\mathrm{TBAF}}}{d\tau}=\frac{1}{T_1^{\mathrm{TBAF}}}(1-m^{\mathrm{TBAF}})+\frac{2k_1^{\mathrm{obs}}[\mathrm{TBAT}]}{[\mathrm{TBAF}]}m^{\mathrm{TBAT}}-k_{-1}^{\mathrm{obs}}[\mathrm{FTPS}]m^{\mathrm{TBAF}}+k_3^{\mathrm{obs}}[\mathrm{ARSF}](m^{\mathrm{ARSF}}-m^{\mathrm{TBAF}}) \\ \approx 0$$

2.99

$$m^{\mathrm{TBAF}}\approx\frac{k_{-1}^{\mathrm{obs}}[\mathrm{FTPS}]m^{\mathrm{TBAT}}+k_3^{\mathrm{obs}}[\mathrm{ARSF}]m^{\mathrm{ARSF}}}{k_{-1}^{\mathrm{obs}}[\mathrm{FTPS}]+k_3^{\mathrm{obs}}[\mathrm{ARSF}]}$$

Inserting Equation 2.97 into Equation 2.93 “cancels” the effect of reaction 2 (direct transfer between TBAT and FTPS) on the magnetisation transfer in the TBAT/ARSF system:

2.100

$$\frac{dm^{\mathrm{TBAT}}}{d\tau}=\frac{1}{T_1^{\mathrm{TBAT}}}(1-m^{\mathrm{TBAT}})+k_1^{\mathrm{obs}}(m^{\mathrm{TBAF}}-m^{\mathrm{TBAT}})+k_4^{\mathrm{obs}}[\mathrm{ARSF}](m^{\mathrm{ARSF}}-m^{\mathrm{TBAT}})$$

Inserting Equation 2.99 into Equations 2.100 and 2.95, and rearranging:

2.101

$$\frac{dm^{\mathrm{TBAT}}}{d\tau}=\frac{1}{T_1^{\mathrm{TBAT}}}(1-m^{\mathrm{TBAT}})+\left(\frac{k_1^{\mathrm{obs}}k_3^{\mathrm{obs}}[\mathrm{ARSF}]}{k_{-1}^{\mathrm{obs}}[\mathrm{FTPS}]+k_3^{\mathrm{obs}}[\mathrm{ARSF}]}+k_4^{\mathrm{obs}}[\mathrm{ARSF}]\right)(m^{\mathrm{ARSF}}-m^{\mathrm{TBAT}})$$

2.102

$$\frac{dm^{\mathrm{ARSF}}}{d\tau}=\frac{1}{T_1^{\mathrm{ARSF}}}(1-m^{\mathrm{ARSF}})+\left(\frac{k_{-1}^{\mathrm{obs}}k_3^{\mathrm{obs}}[\mathrm{FTPS}][\mathrm{TBAF}]}{k_{-1}^{\mathrm{obs}}[\mathrm{FTPS}]+k_3^{\mathrm{obs}}[\mathrm{ARSF}]}+2k_4^{\mathrm{obs}}[\mathrm{TBAT}]\right)(m^{\mathrm{TBAT}}-m^{\mathrm{ARSF}})$$

Assuming that k_{-1}^{obs}[FTPS] >> k_3^{obs}[ARSF] and noting the expression for the equilibrium constant of reaction 1 (Equation 2.49):

2.103

$$\begin{aligned}\frac{dm^{\mathrm{TBAT}}}{d\tau}&=\frac{1}{T_1^{\mathrm{TBAT}}}(1-m^{\mathrm{TBAT}})+[\mathrm{ARSF}]\left(\frac{K_1^{\mathrm{obs}}k_3^{\mathrm{obs}}}{2[\mathrm{FTPS}]}+k_4^{\mathrm{obs}}\right)(m^{\mathrm{ARSF}}-m^{\mathrm{TBAT}})\\&=\frac{1}{T_1^{\mathrm{TBAT}}}(1-m^{\mathrm{TBAT}})+\alpha(m^{\mathrm{ARSF}}-m^{\mathrm{TBAT}})\end{aligned}$$

2.104

$$\begin{aligned}\frac{dm^{\mathrm{ARSF}}}{d\tau}&=\frac{1}{T_1^{\mathrm{ARSF}}}(1-m^{\mathrm{ARSF}})+[\mathrm{TBAT}]\left(\frac{K_1^{\mathrm{obs}}k_3^{\mathrm{obs}}}{[\mathrm{FTPS}]}+2k_4^{\mathrm{obs}}\right)(m^{\mathrm{TBAT}}-m^{\mathrm{ARSF}})\\&=\frac{1}{T_1^{\mathrm{ARSF}}}(1-m^{\mathrm{ARSF}})+r\alpha(m^{\mathrm{TBAT}}-m^{\mathrm{ARSF}})\end{aligned}$$

Where (approximating the equilibrium concentrations of TBAT and ARSF to their initial concentrations):

2.105

$$\alpha=[\mathrm{ARSF}]\left(\frac{K_1^{\mathrm{obs}}k_3^{\mathrm{obs}}}{2[\mathrm{FTPS}]}+k_4^{\mathrm{obs}}\right)\approx c^{\mathrm{ARSF}}\left(\frac{K_1^{\mathrm{obs}}k_3^{\mathrm{obs}}}{2[\mathrm{FTPS}]}+k_4^{\mathrm{obs}}\right)$$

2.106

$$r=\frac{M_{z,\mathrm{eq}}^{\mathrm{TBAT}}}{M_{z,\mathrm{eq}}^{\mathrm{ARSF}}}=\frac{2[\mathrm{TBAT}]}{[\mathrm{ARSF}]}\approx\frac{2c^{\mathrm{TBAT}}}{c^{\mathrm{ARSF}}}$$

Lastly, assuming the simple dissociation model derived in Section 2.2 and hence inserting Equation 2.7 into Equation 2.105, the expression for *α* becomes:

2.107

$$\alpha\approx c^{\mathrm{ARSF}}\left(\frac{K_1^{\mathrm{obs}}k_3^{\mathrm{obs}}}{c^{\mathrm{FTPS}}+\sqrt{(c^{\mathrm{FTPS}})^2+4K_1^{\mathrm{obs}}c^{\mathrm{TBAT}}}}+k_4^{\mathrm{obs}}\right)$$

This expression describes the rate of magnetisation transfer between TBAT and ARSF as a function of the appropriate equilibrium and rate constants, as well as initial concentrations of TBAT, ARSF and FTPS (in the regime of steady-state magnetisation of FTPS). In the absence of added FTPS (*i.e.* where the sole source of FTPS is dissociation of TBAT), this is simplified to:

2.108

$$\alpha \approx c^{\mathrm{ARSF}}\left(\frac{k_3^{\mathrm{obs}}}{2}\sqrt{\frac{K_1^{\mathrm{obs}}}{c^{\mathrm{TBAT}}}}+k_4^{\mathrm{obs}}\right)$$

Equations 2.103 and 2.104 are Equivalent to Equations 2.55 and 2.56, and hence can be integrated as in Section 2.3.5. The overall integrated rate laws of the fractional magnetisation of TBAT and ARSF are therefore given by Equations 2.61, 2.106, 2.107 and 2.109–2.115.

2.61, recalled

$$m^{\mathrm{TBAT}} = c_1 e^{(\beta+\gamma)\tau} + c_2 e^{(\beta-\gamma)\tau} + 1$$

2.109

$$m^{\mathrm{ARSF}} = c_3 e^{(\beta+\gamma)\tau} + c_4 e^{(\beta-\gamma)\tau} + 1$$

Where:

2.110

$$\beta = -\frac{\alpha(r+1)+\frac{1}{T_1^{\mathrm{TBAT}}}+\frac{1}{T_1^{\mathrm{ARSF}}}}{2}$$

2.111

$$\gamma = \frac{\sqrt{\left(\alpha+\frac{1}{T_1^{\mathrm{TBAT}}}-r\alpha-\frac{1}{T_1^{\mathrm{ARSF}}}\right)^2+4r\alpha^2}}{2}$$

2.107, recalled

$$\alpha \approx c^{\mathrm{ARSF}}\left(\frac{K_1^{\mathrm{obs}}k_3^{\mathrm{obs}}}{c^{\mathrm{FTPS}}+\sqrt{(c^{\mathrm{FTPS}})^2+4K_1^{\mathrm{obs}}c^{\mathrm{TBAT}}}}+k_4^{\mathrm{obs}}\right)$$

2.106, recalled

$$r = \frac{M_{z,\mathrm{eq}}^{\mathrm{TBAT}}}{M_{z,\mathrm{eq}}^{\mathrm{ARSF}}} = \frac{2[\mathrm{TBAT}]}{[\mathrm{ARSF}]} \approx \frac{2c^{\mathrm{TBAT}}}{c^{\mathrm{ARSF}}}$$

2.112

$$c_1 = \frac{\alpha\left(m_0^{\mathrm{ARSF}}-m_0^{\mathrm{TBAT}}\right)+\left(\beta-\gamma+\frac{1}{T_1^{\mathrm{TBAT}}}\right)(1-m_0^{\mathrm{TBAT}})}{2\gamma}$$

2.113

$$c_2 = -\frac{\alpha\left(m_0^{\mathrm{ARSF}} - m_0^{\mathrm{TBAT}}\right) + \left(\beta + \gamma + \frac{1}{T_1^{\mathrm{TBAT}}}\right)\left(1 - m_0^{\mathrm{TBAT}}\right)}{2\gamma}$$

2.114

$$c_3 = \frac{r\alpha\left(m_0^{\mathrm{TBAT}} - m_0^{\mathrm{ARSF}}\right) + \left(\beta - \gamma + \frac{1}{T_1^{\mathrm{ARSF}}}\right)\left(1 - m_0^{\mathrm{ARSF}}\right)}{2\gamma}$$

2.115

$$c_4 = -\frac{r\alpha\left(m_0^{\mathrm{TBAT}} - m_0^{\mathrm{ARSF}}\right) + \left(\beta + \gamma + \frac{1}{T_1^{\mathrm{ARSF}}}\right)\left(1 - m_0^{\mathrm{ARSF}}\right)}{2\gamma}$$

Magnetisation transfer between TBAT and ARSF is slow with respect to the longitudinal relaxation times of these spins (*cf*. the TBAT/FTPS exchange); as shown in Section 3.4. The magnitude of exchange and relaxation rates in TBAT/ARSF systems enables the approximation, whereby the extent of both these processes over the duration of the soft pulse are negligible, and hence the fractional magnetisation of the (initially) non-inverted spin at $\tau = 0$ is 1. Accounting for any imperfections in the selective π pulse, the fractional magnetisation of the inverted spin at $\tau = 0$ may be >0. For selective inversion of TBAT and detection of ARSF, the constants c_3 and c_4 then take the forms:

2.116

$$c_3 \approx -\frac{r\alpha\left(1 - m_0^{\mathrm{TBAT}}\right)}{2\gamma}$$

2.117

$$c_4 \approx \frac{r\alpha\left(1 - m_0^{\mathrm{TBAT}}\right)}{2\gamma}$$

With this approximation, Equation 2.118 describes the system where TBAT is selectively inverted and (the initially non-inverted) ARSF is observed. The auxiliary terms *α*, *β* and *γ* are given by Equations 2.107, 2.110 and 2.111.

2.118

$$m^{\mathrm{ARSF}} \approx \frac{r\alpha\left(1 - m_0^{\mathrm{TBAT}}\right)}{2\gamma}\left[e^{(\beta-\gamma)\tau} - e^{(\beta+\gamma)\tau}\right] + 1$$

2.107, recalled

$$\alpha \approx c^{\mathrm{ARSF}}\left(\frac{K_1^{\mathrm{obs}} k_3^{\mathrm{obs}}}{c^{\mathrm{FTPS}} + \sqrt{\left(c^{\mathrm{FTPS}}\right)^2 + 4K_1^{\mathrm{obs}} c^{\mathrm{TBAT}}}} + k_4^{\mathrm{obs}}\right)$$

2.110, recalled

$$\beta = -\frac{\alpha(r+1) + \frac{1}{T_1^{\mathrm{TBAT}}} + \frac{1}{T_1^{\mathrm{ARSF}}}}{2}$$

2.111, recalled

$$\gamma = \frac{\sqrt{\left(\alpha + \frac{1}{T_1^{\mathrm{TBAT}}} - r\alpha - \frac{1}{T_1^{\mathrm{ARSF}}}\right)^2 + 4r\alpha^2}}{2}$$

Equation 2.118 can be expressed as $M_z^{\mathrm{ARSF}}(\tau)$ according to Equation 2.19.

2.119

$$M_z^{\mathrm{ARSF}} \approx \frac{r\alpha M_{\mathrm{eq}}^{\mathrm{ARSF}}(1 - m_0^{\mathrm{TBAT}})}{\gamma}\left[e^{(\beta-\gamma)\tau} - e^{(\beta+\gamma)\tau}\right] + M_{z,\mathrm{eq}}^{\mathrm{ARSF}}$$

Chapter 3

Kinetic and mechanistic analysis

3.1. Solution-phase NMR spectroscopy of TBAT

Several NMR-active nuclei of natural abundance are present in a molecular unit of tetra-*n*-butylammonium difluorotriphenylsilicate (TBAT, Figure 3.1a), namely: ^{1}H, ^{2}H, ^{13}C, ^{14}N, ^{15}N, ^{19}F and ^{29}Si. Of these nuclei, ^{1}H and ^{19}F were used throughout this study due to their 1/2-spins, high receptivities, relatively short longitudinal relaxation times, and the nature of the processes studied. For example, $Ph_3SiF_2^-$ and $^{n}Bu_4N^+$ contain ^{1}H nuclei and therefore ^{1}H NMR spectroscopy was practical in the studies of ion pairing in solutions of the salt, discussed in Section 3.2.1. ^{19}F magnetisation transfer NMR spectroscopy, on the other hand, was suitable for the interrogation of the plausible equilibrium dissociation of TBAT into fluorotriphenylsilane (FTPS) and tetra-*n*-butylammonium fluoride (TBAF), Section 3.2.2; as well as the mechanism of fluoride transfer from TBAT to FTPS, Section 3.3, and to 2-naphthalenyl fluorosulfate (ARSF), Section 3.4.

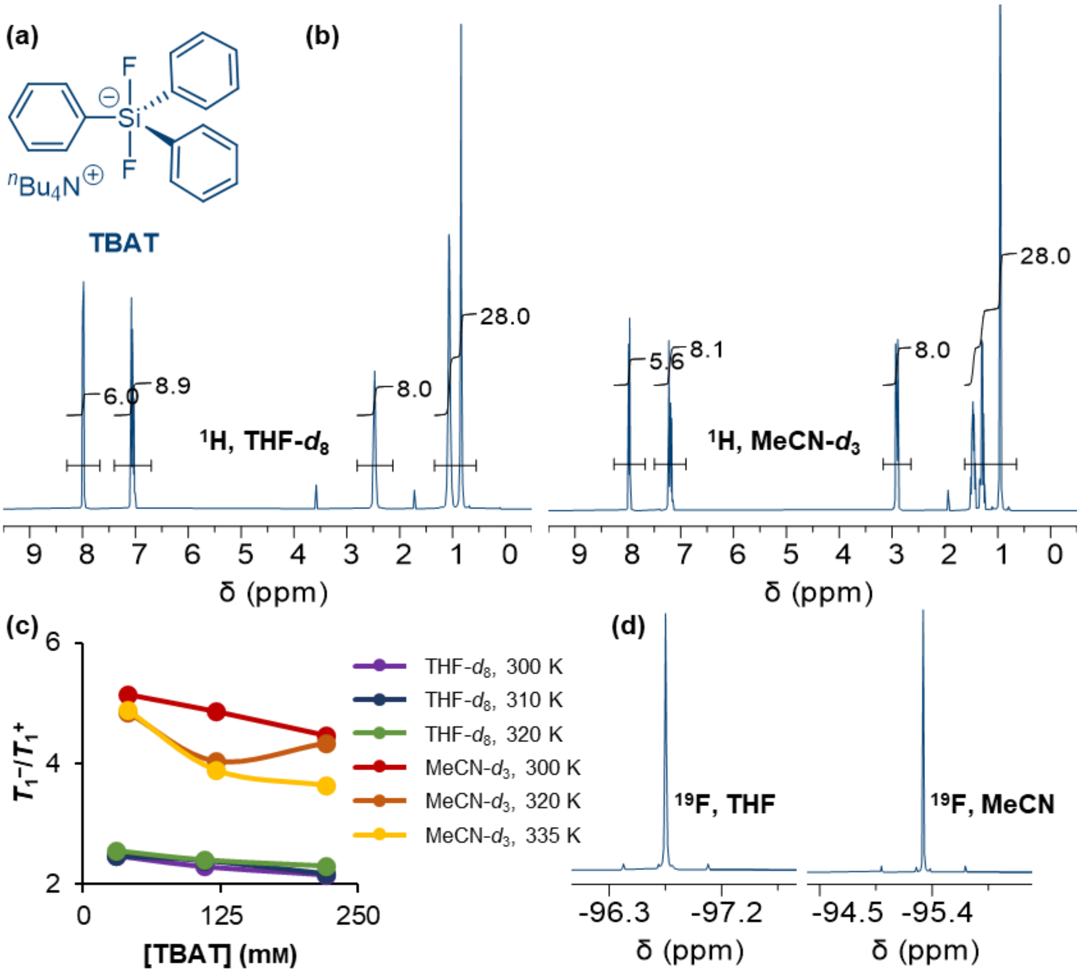

Figure 3.1: (a) The structure of a molecular unit of tetra-*n*-butylammonium difluorotriphenylsilicate, TBAT. (b) ^{1}H NMR spectra of TBAT in THF-d_8 (left) and MeCN-d_3 (right). (c) Plots of the ratio of longitudinal relaxation time constants of $Ph_3SiF_2^-$ to $^nBu_4N^+$ against the concentration of TBAT in THF-d_8 (300, 310 and 320 K) and MeCN-d_3 (300, 320 and 335 K). (d) ^{19}F NMR spectra of TBAT in THF (left) and MeCN (right).

^{1}H NMR (400 MHz) spectra of TBAT in THF-d_8 and MeCN-d_3 (Figure 3.1b; see Section 7.3 for full assignment) showed two signals in the aromatic region. The alkyl groups in $^nBu_4N^+$ showed three signals in THF-d_8 and four in MeCN-d_3. DeShong *et al*. reported slower longitudinal relaxation of the aromatic protons than of the aliphatic ones in solutions of TBAT in DMSO-d_6.[63] ^{1}H longitudinal relaxation time constant measurements in this study confirmed this trend, although it was found that the ratio of ^{1}H longitudinal relaxation time constants of $Ph_3SiF_2^-$ and $^nBu_4N^+$, T_1^-/T_1^+, depends on the conditions (see Section 7.4). A plot of this ratio against the concentration of TBAT illustrates these findings (Figure 3.1c, see Table 7.2 in Section 7.4 for the T_1 values). The difference between the T_1 constants of the anion and cation were significantly more pronounced in MeCN-d_3 than in THF-d_8 under all studied conditions.

For example, the determined T_1^-/T_1^+ for a 220 mᴍ solution of TBAT at 300 K was 4.46 in MeCN-d_3 and 2.16 in THF-d_8.

^{19}F NMR (377 MHz) spectra of TBAT in THF and MeCN (both non-deuteriated) showed one singlet for the two chemically and magnetically equivalent fluorine atoms in the $Ph_3SiF_2^-$ anion (Figure 3.1d). ^{29}Si and ^{13}C satellites, $^{1}J_{SiF}$ = (254 ± 0) Hz and $^{2}J_{FC}$ = (41.4 ± 0.3) Hz, were also present; see Section 5.4.1. These *J*-coupling values agree with ones reported by DeShong *et al*.[63] It was found in this study that in THF, both the chemical shift and longitudinal relaxation time constant of the fluorine atoms in TBAT, δ_F^{TBAT} and T_1^{TBAT}, respectively, are dependent upon its concentration. In the 10–210 mᴍ concentration range at 300 K, empirical models were developed to fit the observed experimental changes to concentration, as in Equations 3.1 and 3.2 (Figure 5.5; Section 5.4.1). In contrast, the chemical shift of TBAT, δ_F^{TBAT} = (–95.34 ± 0.01) ppm, was found to be independent of its concentration in MeCN in the 15–230 mᴍ concentration range at 300 K (Figure 5.7a; Section 5.4.1). However, while the measured ^{19}F T_1^{TBAT} was larger in MeCN than in THF for any given concentration in the studied range, and an empirical model was necessary again to fit ^{19}F T_1^{TBAT} to concentration (Equation 3.3, Figure 5.7b; Section 5.4.1).

In THF:

3.1

$$\frac{\delta_{\mathrm{F}}^{\mathrm{TBAT}}}{\mathrm{ppm}} \approx 0.494 \ln \frac{[\mathrm{TBAT}]}{\mathrm{m\textsc{m}}} - 97.9$$

3.2

$$\frac{T_1^{\mathrm{TBAT}}}{\mathrm{s}} \approx -0.258 \ln \frac{[\mathrm{TBAT}]}{\mathrm{m\textsc{m}}} + 2.58$$

In MeCN:

3.3

$$\frac{T_1^{\mathrm{TBAT}}}{\mathrm{s}} \approx 32.0 \left(\frac{[\mathrm{TBAT}]}{\textsc{m}}\right)^2 - 20.1 \frac{[\mathrm{TBAT}]}{\textsc{m}} + 7.41$$

3.2. Speciation of TBAT in solution

Prior to the investigation into the equilibrium transfer of fluoride from TBAT, the speciation of the salt was examined in tetrahydrofuran (non-deuteriated or deuteriated, THF and THF-d_8, respectively) and acetonitrile (non-deuteriated or deuteriated, MeCN and MeCN-d_3, respectively). Two aspects of speciation were considered: the interactions between difluorotriphenylsilicate anion, $Ph_3SiF_2^-$, and tetra-*n*-butylammonium cation, $^nBu_4N^+$ (ion pairing); and the equilibrium dissociation of fluoride from $Ph_3SiF_2^-$.

3.2.1. Ion pairing

As a salt of an organic anion and an organic cation, TBAT may exist as a tight or loose ion pair (Figure 3.2a–b), or an equilibrium mixture of these forms, in organic solvents. Depending on this model, the plausible structures formed by the anion and cation in solution can be represented by those shown in Figure 3.2c–e.[221,222]

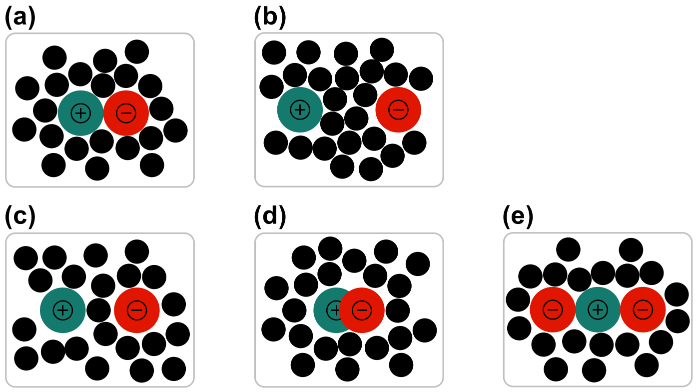

Figure 3.2: A schematic representation of types of ion arrangements which can exist in solutions of salts in organic solvents. In the simple model, these are namely (a) tight (contact) ion pairs and (b) loose ion pairs. The model can be expanded to account for (c) solvent-shared and (d) penetrated ion pairs, as well as (e) aggregates of more than two ions (here, an anionic triple-ion).[221,222] The coloured spheres represent salt ions ("+" for cation and "–" for anion), whereas the black spheres are solvent molecules.

The nature and extent of ion pairing in solutions of TBAT in THF-d_8 and MeCN-d_3 were analysed by means of diffusion analysis using a pulsed field gradient NMR experiment described in Section 5.2.3. Since $Ph_3SiF_2^-$ and $^nBu_4N^+$ show signals in the ^{1}H NMR spectra of their salt, the translational self-diffusion coefficients of both ions, D^- and D^+, respectively, can be determined from a single ^{1}H diffusion experiment using Equation 3.4, where I_g^S is the integral of spin S at gradient strength g, I_0^S is the integral of spin S at gradient strength $g = 0$, $\gamma = 2.68 \cdot 10^4$ rad s^{-1} G^{-1} is the magnetogyric ratio of ^{1}H and D^S is the translational diffusion coefficient of S (Δ and δ are acquisition parameters, described in Section 5.2.3).[223]

3.4

$$I_g^S = I_0^S e^{-(\gamma g \delta)^2 \left(\Delta - \frac{\delta}{3}\right) D^S}$$

For each of the two solvents, three solutions of TBAT were prepared and the diffusion analysis of each solution was studied at three temperatures. 18 sets of conditions were therefore studied in total, and for each one of them, D^- and D^+ were determined by fitting the above model numerically. A selection of diffusion profiles (110 mM TBAT in THF-d_8, 300–320 K) is presented in Figure 3.3 (see Section 5.3.1 for all 18 plots). The translational diffusion coefficients of $Ph_3SiF_2^-$ relative to $^nBu_4N^+$, D^-/D^+, are reported for each dataset in Table 3.1.

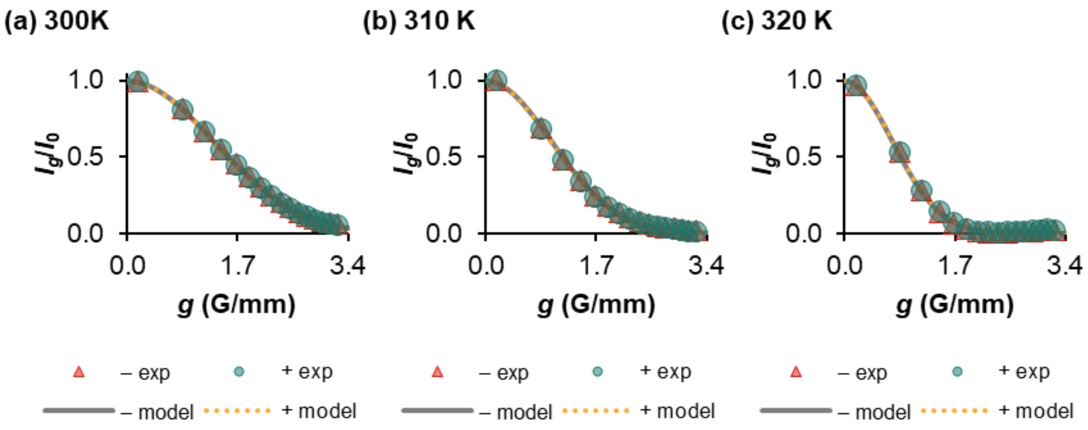

Figure 3.3: Experimental and model diffusion profiles of $Ph_3SiF_2^-$ and $^nBu_4N^+$ for 110 mM TBAT in THF-d_8; (a) at 300 K, (b) at 310 K, (c) at 320 K.

Table 3.1: The ratios of translational diffusion coefficients of $Ph_3SiF_2^-$ and $^nBu_4N^+$, D^-/D^+, in THF-d_8 and MeCN-d_3. See Table 5.2 in Section 5.3.1 for root mean square errors of the fits.

Solvent	[TBAT] (mM)	Temperature (K)	D^-/D^+
THF-d_8	220	300	0.994
THF-d_8	220	310	0.984
THF-d_8	220	320	0.981
THF-d_8	110	300	0.980
THF-d_8	110	310	0.973
THF-d_8	110	320	1.01
THF-d_8	30	300	0.981
THF-d_8	30	310	0.980
THF-d_8	30	320	1.00
MeCN-d_3	220	300	1.04
MeCN-d_3	220	320	0.986
MeCN-d_3	220	335	0.971
MeCN-d_3	120	300	1.04
MeCN-d_3	120	320	1.01
MeCN-d_3	120	335	0.994
MeCN-d_3	40	300	1.03
MeCN-d_3	40	320	1.05
MeCN-d_3	40	335	1.01

The determined ratio D^-/D^+ is nearly unity across all entries in Table 3.1 (average of 0.987 ± 0.008 in THF-d_8 and 1.02 ± 0.02 in MeCN-d_3), indicating strong ion pairing of

$Ph_3SiF_2^-$ and $^nBu_4N^+$ in solution under these conditions, provided that the ions do not coincidentally exhibit identical diffusive properties. In order to account for this possibility, we sought to create conditions under which the molecular unit of TBAT could, in principle, separate into individual ions (and show either diverging diffusive properties under these conditions as the ions separate, or inconclusively – again identical ones). To maximise the opportunity of achieving such conditions, we aimed to prepare a very dilute solution of TBAT in a high polarity (aprotic) solvent. A 1.5 mM solution of TBAT in DMSO-d_6 was therefore prepared (in the presence of 1,3,5-trimethoxybenzene, TMB, as an internal diffusion standard). A ^1H diffusion experiment of this solution at 300 K showed $D^-/D^+ = 1.21$, Figure 3.4a. This value is indicative of vastly different mobilities of $Ph_3SiF_2^-$ and $^nBu_4N^+$ in dilute solutions of TBAT in DMSO-d_6. This result confirms that the identical diffusion properties of the cation and anion in THF-d_8 and MeCN-d_3 were indeed a result of ion pairing rather than similar diffusion coefficients of the separate ions in these solutions. Moreover, the diffusion coefficients of $Ph_3SiF_2^-$ and $^nBu_4N^+$ relative to TMB were $D_-/D_{TMB} = 0.710$ and $D_+/D_{TMB} = 0.586$, respectively, in 1.5 mM TBAT in DMSO-d_6. These values are significantly higher than $D_-/D_{TMB} = 0.467$ and $D_+/D_{TMB} = 0.466$ for 207 mM TBAT in THF-d_8 at 300 K (Figure 3.4b). In fact, $D_+/D_{TMB} = 0.586$ for 1.5 mM TBAT in DMSO-d_6 is nearly identical to the D_+/D_{TMB} of 0.576 for free $^nBu_4N^+$ in 201 mM TBABARF in THF-d_8 at 300 K ($D^-/D^+ = 0.931$, Section 5.3.3; TBABARF is a salt of $^nBu_4N^+$ and the $BARF^-$ anion ≡ anion **1.11** in Figure 1.1).

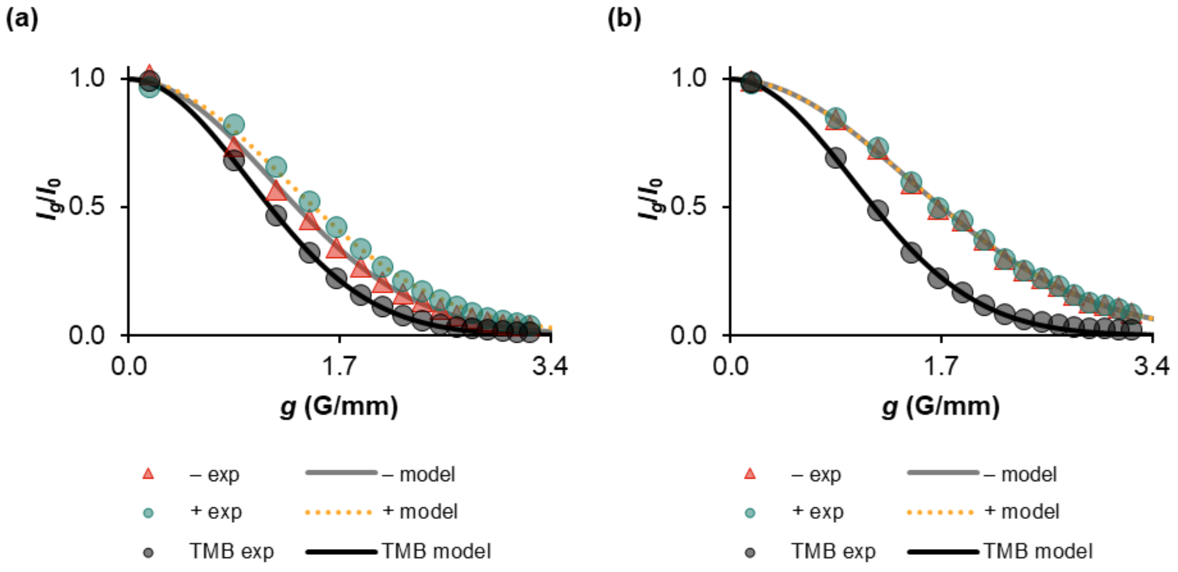

Figure 3.4: Experimental and model diffusion profiles of $Ph_3SiF_2^-$ and $^n Bu_4N^+$ (and the internal diffusion standard, TMB) for (a) 1.5 mM TBAT in DMSO-d_6 and (b) 207 mM TBAT in THF-d_8 (both at 300 K).

^{1}H 1D NOESY spectra of 210 mM TBAT in THF-d_8 and MeCN-d_3 confirmed the presence of ion pairing in both solvents. As presented in Figure 3.5, selective perturbation of either aromatic proton signal, resulted in NOE to the aliphatic protons (and the remaining aromatic protons).

(a) THF-d_8

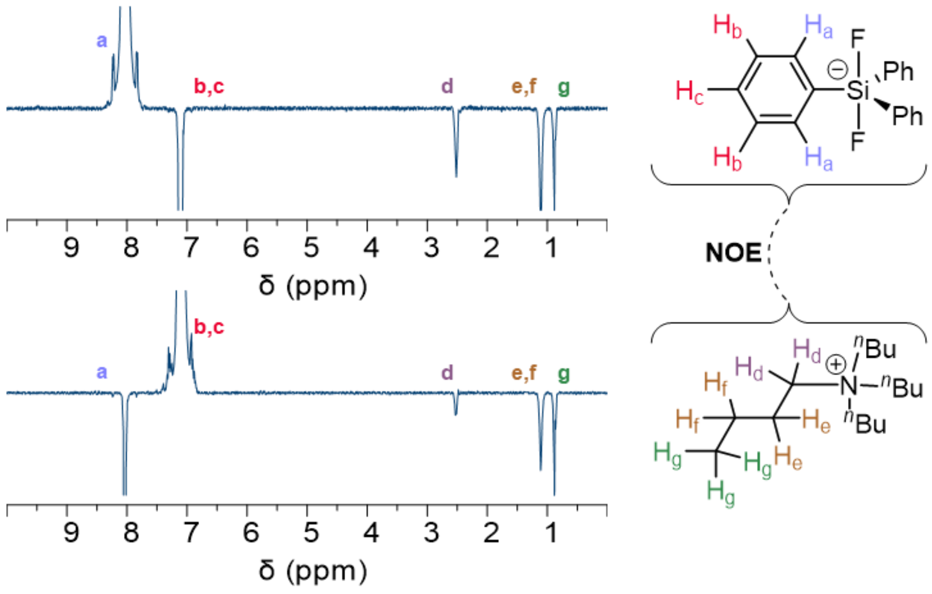

(b) MeCN-d_3

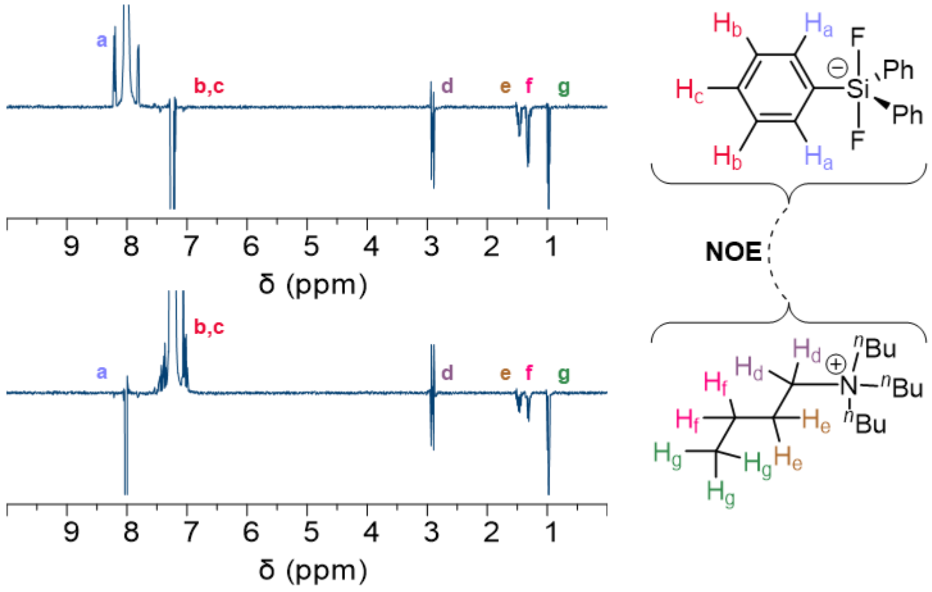

Figure 3.5: ^{1}H NOE spectra showing evidence for interactions between aromatic and aliphatic protons in solutions of 210 mM TBAT in (a) THF-d_8 and (b) MeCN-d_3 (at 300 K for both solutions). A structure of the molecular unit of TBAT is included with the NOE contacts between $Ph_3SiF_2^-$ and $^nBu_4N^+$ indicated by dashed lines. Due to the overlap of *meta*- and *para*- protons in ^{1}H NMR spectra of the salt in both solvents, the exact NOE contacts for these spins are unclear. In THF-d_8, two CH_2 environments overlap, and therefore the contacts corresponding to these spins are also unclear. (The initially perturbed signal is clipped in all spectra).

3.2.2. Dissociation into FTPS and TBAF

TBAT is prepared in a reaction of FTPS with fluoride (*e.g.* TBAF, Scheme 1.2a). It was unknown prior to this study whether the reaction is reversible or irreversible, *i.e.* whether TBAT dissociates reversibly into FTPS and TBAF upon dissolution in organic solvents. If it does, the degree of dissociation must be low enough for the dissociation products to remain undetectable by NMR spectroscopy. We turned to ^{19}F chemical exchange saturation transfer (CEST) NMR in search of these dissociation products in solutions of TBAT in THF and MeCN (at 300 K). As discussed in Section 1.3.2, in order to be observed in a CEST experiment, a low-concentration spin must exchange with an observable spin with sufficient rate relative to its longitudinal relaxation time constant, T_1. In this case, observation of both FTPS and TBAF in exchange with TBAT would be a conclusive evidence that an equilibrium exists between these species in solution. Observation, however, of only FTPS or only TBAF would be inconclusive, as either one could potentially be an impurity in direct exchange with TBAT.

As the ^{19}F chemical shift of FTPS was found to be independent of its concentration (see Section 5.4.2), if it were to be present in the solutions of TBAT, a chemical shift of –170 ppm would be expected. The chemical shift of TBAF, on the other hand, is significantly dependent on the conditions, according to literature reports. Anhydrous TBAF resonates at –86 ppm and –72 ppm in THF and MeCN, respectively, and the signal moves upfield as the water content in the solution is increased.[61] The upfield extreme of the chemical shift of TBAF in these two (or any other solvents) is not known. We also note that tetra-*n*-butylammonium bifluoride (TBABF) and tetra-*n*-butylammonium hydroxide (^{n}Bu$_4$NOH) may form in equilibrium with TBAF in the presence of any adventitious water, Scheme 3.1 (δ_F^{TBABF} = –147 ppm).[60]

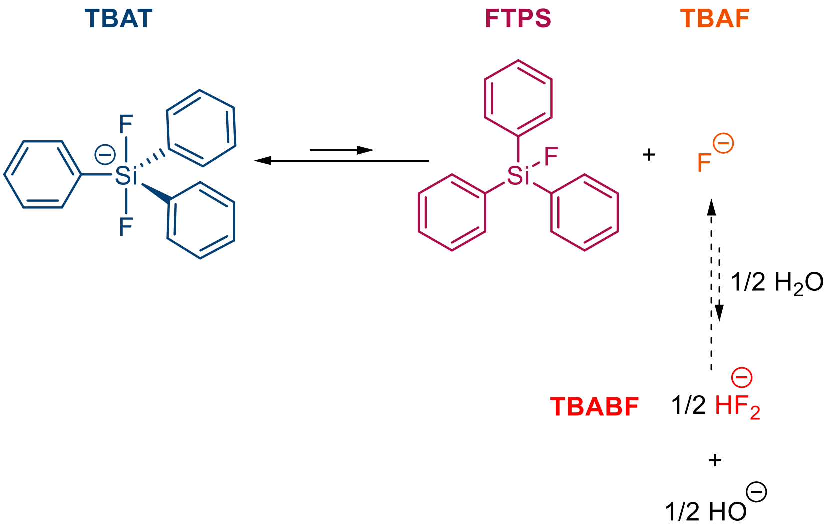

Scheme 3.1: A proposed scheme for the dissociation of TBAT in THF and MeCN. In the presence of water, TBABF may form in equilibrium from TBAF. (The tetra-*n*-butylammonium counterion was omitted for clarity).

Two saturated solutions of TBAT, one in THF and one in MeCN, were prepared freshly in the glovebox, decanted into J Young® valve capped NMR tubes, and used for the ^{19}F CEST experiments; see Section 5.2.5 for details. The reasoning behind preparing saturated solutions was two-fold. Firstly, increasing the concentration of TBAT maximises the chance of observing any low-concentration spins in exchange with it in CEST. Secondly, as shown in Section 3.1, the longitudinal relaxation time constant of TBAT decreases with concentration in both solvents (a trend which we expected to continue until saturation), hence allowing for more scans in a given time period. Indeed, T_1^{TBAT} in these saturated solutions was determined (immediately prior to the corresponding CEST experiments) as 1.10 s in THF and 3.60 s in MeCN.

As presented in Figure 3.6a–b, both experiments showed an expected large decrease of the integral of TBAT upon saturation of its resonance frequency. In each solvent, a pair of small dips of similar shape and size was also observed (more so in THF), with the relative decrease of magnetisation of TBAT significantly larger in MeCN than THF (~5–15% and ~2%, respectively). The upfield dip, at –170 ppm in both solvents, was readily assigned to FTPS. The frequency of the downfield one was –149 ppm in THF and –147 ppm in MeCN (the experiment was repeated for the solution in THF, with a smaller number of saturation frequencies – all around the downfield dip, due to insufficient data density in the first measurement). It is unclear whether the downfield dip corresponds to TBAF or TBABF in the two solutions. It appears coincidental that the chemical shift of TBAF, known to be extremely sensitive to water, was found at such similar frequencies in two different samples, and where TBABF was expected to resonate. Nevertheless, according to Scheme 3.1, any reversible formation of TBABF in the solutions would have had to occur *via* TBAF.[60]

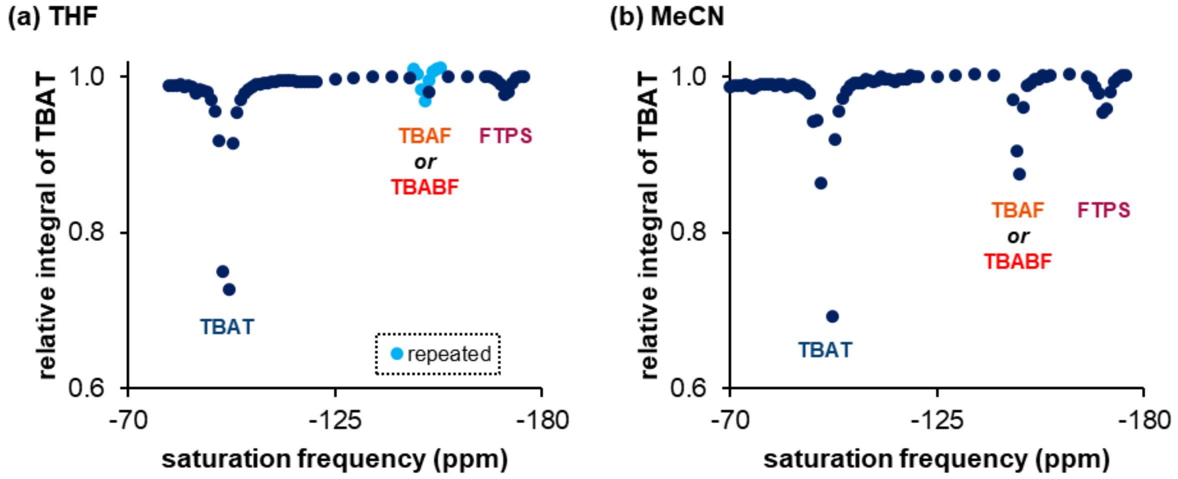

Figure 3.6: ^{19}F CEST NMR spectra of saturated solutions of TBAT in (a) THF and (b) MeCN (both at 300 K). In each solvent, a pair of signals of similar shape and size was observed at approximately –150 ppm and at –170 ppm. The upfield signal was readily identified as arising from FTPS, whereas the downfield one could correspond to TBAF or TBABF. (The relative integrals of TBAT are ratios of absolute (measured) integrals of TBAT and the "baseline integral", arbitrarily chosen from datapoints where visually no saturation occurred).

Analogous solutions were then freshly prepared, this time in the presence of a small amount of exogeneous FTPS (~3 mg FTPS added to the NMR tubes under N_2, each containing ~0.5 mL of the solution; hence corresponding to ~20 mM FTPS). FTPS was detected in a ^{19}F pulse-acquire spectrum of the solution in THF (~5 mol% FTPS by integration against TBAT). The CEST profile of this solution in THF is presented in Figure 3.7 (left), along with data from the previously studied solution, with no added FTPS, for comparison (data from Figure 3.6a, grey points in Figure 3.7). Unsurprisingly, the dip at –170 ppm became larger. Both dips corresponding to TBAT and FTPS also exhibited broadening (or more precisely – saturation over a broader frequency range), which is indicative of rapid exchange between TBAT and FTPS. However, as is clear from the expansion of the profile (Figure 3.7, right), saturation transfer from the signal at –147 ppm was supressed to below the detection limit by the addition of FTPS. In MeCN, the FTPS signal was just above qualitative detection limit in the ^{19}F pulse-acquire spectrum, due to very significant line broadening (baseline correction "deletes" the signal completely), which is indicative of very rapid exchange between TBAT and FTPS. Consequently, in the ^{19}F CEST NMR spectrum, the line broadening of both TBAT and FTPS dips covered the entire saturation frequency range, as detailed in Figure 3.8 (with the integral corresponding to the most downfield datapoint as the arbitrary "baseline integral"). Again, data from the experiment without added FTPS is included in the plot (grey points). Although the two major dips (TBAT and FTPS) overlap with any TBAF/TBABF previously observed at –149 ppm, no specific saturation transfer maxima were observed at that frequency, which was significant in the absence of FTPS. The suppression of saturation transfer from TBAF/TBABF by addition of FTPS to saturated TBAT in MeCN can therefore be concluded. As, according to the Le Chatelier's principle, exogenous FTPS shifts the equilibrium between the species towards TBAT, these results were expected and confirm the low degree of reversible dissociation of TBAT into FTPS and TBAF (which may undergo further equilibria) in THF and MeCN.

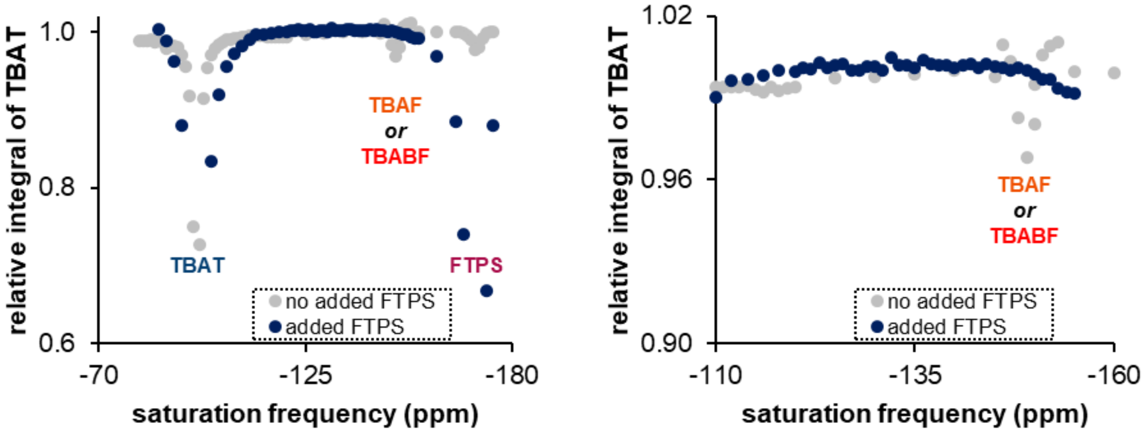

Figure 3.7: ^{19}**F CEST NMR spectra of a saturated solution of TBAT with exogeneous FTPS (~20 mM of added FTPS) in THF; and the expansion of the profile. In both plots, data from Figure 3.6a was included (grey points).**

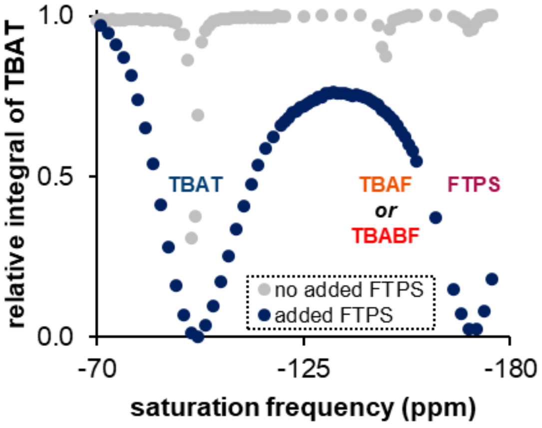

Figure 3.8: ^{19}**F CEST NMR spectrum of a saturated solution of TBAT with exogeneous FTPS (~20 mM of added FTPS) in MeCN. Data from Figure 3.6b was included (grey points).**

Lastly, two saturated solutions of TBAT, in THF and in MeCN, were prepared analogously to the ones described at the beginning of this section. This time, 3 Å molecular sieves (~40 mg) were added to the samples in the NMR tubes in such a way that the sieves remained in the top compartments of the tubes (achieved with the aid of filter papers). The NMR tubes were then inverted, for the solutions inside them to come to contact with the molecular sieves, and left in such position for ~2 months. After this time, the tubes were inverted back to the “standard” position, the sieves removed from their top compartments (inside the glovebox), and CEST experiments performed analogously to the ones described above. The ^{19}F CEST profile of the dried solution of TBAT in THF is presented in Figure 3.9 (and the plot from the original solution is again included). The CEST profile shows the suppression of both FTPS and TBAF/TBABF signals to below the detection limit. This observation may be indicative of either (i) the equilibrium of TBAT dissociation shifting towards recombination of the dissociation products (*i.e.* the degree of TBAT dissociation decreasing), and/or (ii) the rate of saturation transfer (exchange) between the spins decreasing after storage in the presence of molecular sieves.

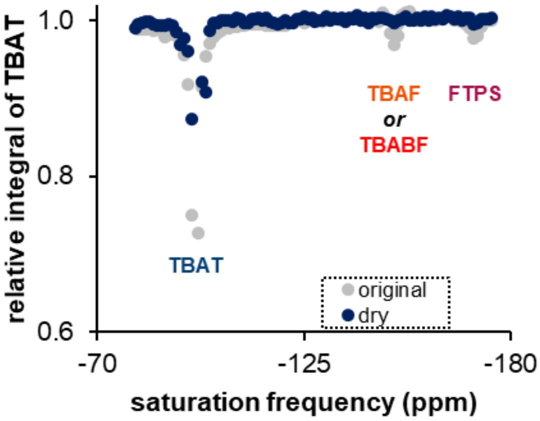

Figure 3.9: ^{19}F CEST NMR spectrum of a saturated solution of TBAT in THF dried over molecular sieves for ~2 months. Data from Figure 3.6a is included (grey points).

The corresponding MeCN solution saw a new signal appear in the ^{19}F pulse-acquire NMR spectrum, at approximately –125 ppm, with an integral of ~0.004 relative to TBAT. The ^{19}F CEST profile, presented in Figure 3.10a (with the data from the original solution included in grey) shows that the group giving rise to this signal did not exchange with TBAT, as no saturation transfer was observed for –125 ppm. However, five dips were observed in the experiment apart from the saturation of TBAT itself. Interestingly, the “baseline integral” increased significantly over the duration of the experiment (~20 hours, saturation frequencies from downfield to upfield), and the reason for this phenomenon is unclear (the integral corresponding to the most upfield signal was used as “baseline integral” in Figure 3.10a). A linear correction was applied to the baseline, and the corrected profile is presented in Figure 3.10b. From downfield to upfield, the dips were found at: –77 ppm, –115 ppm, –128 ppm, –147 ppm and –169 ppm.

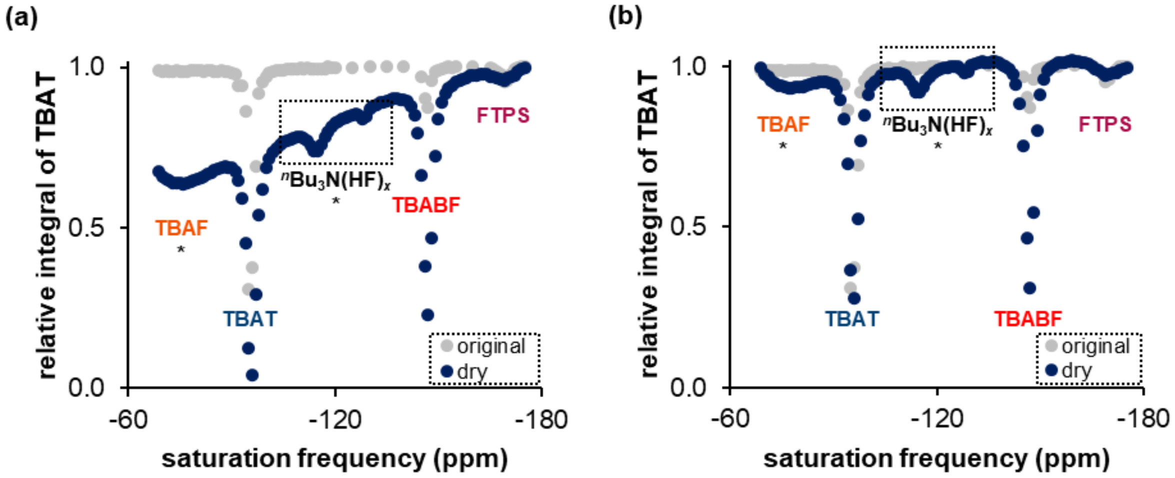

Figure 3.10: (a) ^{19}F CEST NMR spectrum of a saturated solution of TBAT in MeCN dried over molecular sieves for ~2 months. Data from Figure 3.6b is included (grey points). (b) A linear baseline correction was applied of the plot from (a). In both cases, the asterisks indicate tentative assignments.

Based on the discussion above, the dip at –169 ppm was readily assigned as FTPS. The dip at –147 ppm gave significantly more saturation transfer than for the solution in Figure 3.6b. Considering that the system was dried with molecular sieves, we confidently assigned the signal to TBABF for this solution, as any TBAF would likely move downfield due to a lesser degree of hydration. Indeed, a broad dip of similar intensity to one at –169 ppm (FTPS) was observed at –77 ppm, which is only slightly upfield from anhydrous TBAF in MeCN (–72 ppm).[61] Therefore, we tentatively assigned this spin as TBAF. In anhydrous MeCN, the equilibrium of TBABF formation from TBAF should be supressed and hence we propose that TBABF was formed in the solution from the decomposition of TBAF *via* Hofmann elimination,[59] rather than from the equilibrium in Scheme 3.1. The proposed irreversible decomposition, and the resulting equilibrium network, are presented in Scheme 3.2. Analogously to the system in Scheme 3.1, TBAT dissociated reversibly into FTPS and TBAF. However, due to the enhanced basicity of the less hydrated fluoride in TBAF, the salt decomposed (to a low degree) to form tributylamine, but-1-ene and TBABF; perhaps *via* formation of HF in the first step, followed by an equilibrium reaction between HF and TBAF. The intermediacy of HF could explain the additional signals (–115 ppm and –128 ppm in the CEST spectrum, and –125 ppm in the pulse-acquire spectrum), as a series of ^{n}Bu$_3$N(HF)$_x$ complexes could form in solutions of ^{n}Bu$_3$N and HF. Thus, we tentatively assigned these three unknown spins as such adducts of different stoichiometries.

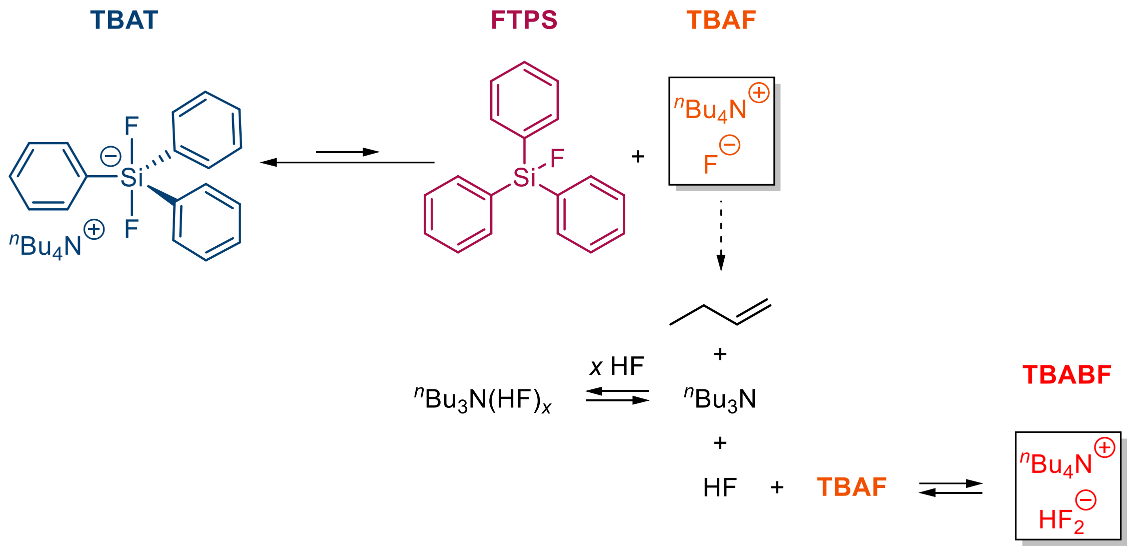

Scheme 3.2: A proposed scheme for the dissociation of TBAT in anhydrous MeCN, and the subsequent Hofmann elimination from the anhydrous TBAF (dashed arrow).

3.3. TBAT/FTPS exchange

3.3.1. Magnitude of exchange rate in THF

As shown in Section 3.2.2, TBAT dissociates reversibly into FTPS and TBAF to a small degree in solutions in THF and MeCN, and the spins undergo chemical exchange on a timescale convenient for magnetisation transfer experiments. In order to gain quantitative insight into the exchange, inversion transfer between TBAT and FTPS was studied in solutions prepared by mixing the two species in THF (Sections 3.3.1–3.3.4) and MeCN (Section 3.3.5). The rationale behind using FTPS as the exchange partner to TBAT was three-fold: (i) as discussed in Section 2.3, both the dissociative and direct exchange pathways could, in principle, be interrogated using this single two-spin system; (ii) tetravalent silanes are common fluoride acceptors;[110–161] (iii) FTPS is commercially available in anhydrous form (Section 7.2).

At 300 K, the ^{19}F (377 MHz) longitudinal relaxation time constant of FTPS in THF, T_1^{FTPS} = 12.0 s, was found to be independent of its concentration and significantly larger than the one of TBAT, 2.00 ≥ T_1^{TBAT} ≥ 1.22 in the 10.3–208 mM range (Section

3.1). When the two species were dissolved in the same solution ([TBAT] = 52.5 mM, [FTPS] = 83.9 mM), both ^{19}F spins relaxed with equal rates in a non-selective inversion-recovery experiment. The observed longitudinal relaxation time constant, T_1^{obs} = 2.45 s (an average of 2.43 s and 2.47 s obtained for TBAT and FTPS, respectively), was nearly identical to the weighted average of the values expected for the separated spins under these conditions (2.54 s weighted average from T_1^{TBAT} = 1.56 s and T_1^{FTPS} = 12.0 s, Equation 2.69). This observation was indicative of a very rapid exchange between the ^{19}F spins on the longitudinal relaxation timescale. Indeed, selective ^{19}F inversion of FTPS was detected in TBAT (Figure 3.11a). Fitting of the model derived in Section 2.3.6 (Equation 2.78) to the experimental magnetisations (integrals) of TBAT gave α = 12.1 s^{-1} (αT_1^{obs} = 29.7); where α is a function, whose form is dependent upon the fluoride transfer pathway(s), see Equation 2.53. The experimental and model magnetisations were then converted into fractional magnetisations of TBAT, m^{TBAT}, and are presented in Figure 3.11b–c.

2.69, recalled

$$T_1^{\text{obs}} = \frac{T_1^{\text{TBAT}} T_1^{\text{FTPS}} (r+1)}{T_1^{\text{TBAT}} + r T_1^{\text{FTPS}}}$$

2.78, recalled

$$M_z^{\text{TBAT}} = x\left[e^{-\alpha(r+1)\tau} - e^{-\frac{\tau}{T_1^{\text{obs}}}}\right] + M_{z,\text{eq}}^{\text{TBAT}}$$

2.53, recalled

$$\alpha = k_1^{\text{obs}} + k_2^{\text{obs}}[\text{FTPS}]$$

2.54, recalled

$$r = \frac{M_{z,\text{eq}}^{\text{TBAT}}}{M_{z,\text{eq}}^{\text{FTPS}}} = \frac{2[\text{TBAT}]}{[\text{FTPS}]}$$

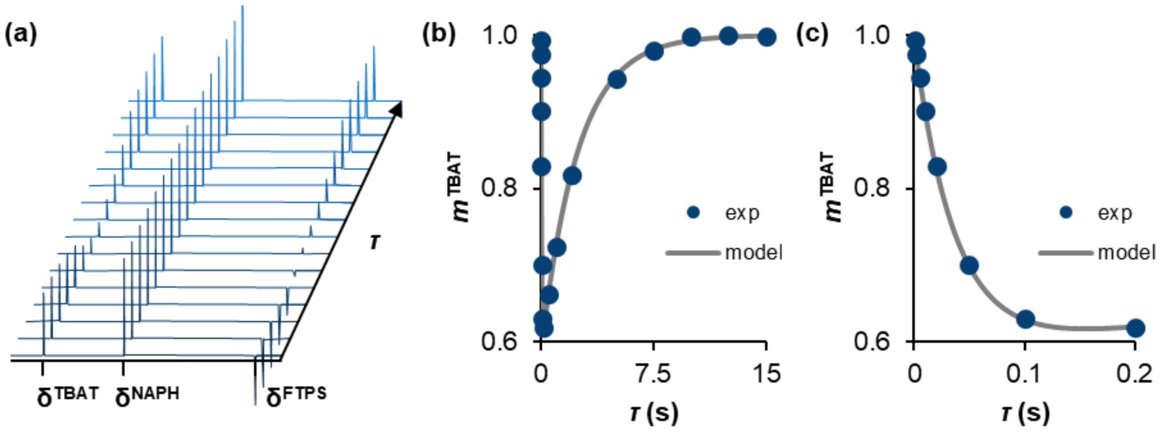

Figure 3.11: ^{19}F inversion transfer in a solution of TBAT (52.5 mM) and FTPS (83.9 mM) in THF at 300 K. (a) Selective inversion of FTPS is transferred to TBAT *via* chemical exchange. The extent of the inversion transfer and longitudinal relaxation of the spins depends on the variable delay, τ. The magnetisation of NAPH (internal standard) is unaffected in the experiment. (b) A plot of experimental and model fractional magnetisation of TBAT, m^{TBAT}, against variable delay, τ, resulting from the selective inversion of FTPS. The chemical exchange between the spins is very rapid compared to their longitudinal relaxation, αT_1^{obs} = 29.7. (c) An expansion of the plot from (b) showing the first eight experimental datapoints ($\tau \leq$ 0.2 s).

3.3.2. Temporal instability and sensitivity to conditions

An early attempt at interrogating the exchange pathways between TBAT and FTPS was promising. Four solutions of TBAT and FTPS (and the internal standard, NAPH) were prepared in THF, [TBAT] (mM) {52.9, 99.0, 150, 202}, and transferred to J Young® valve capped NMR tubes. ^{19}F inversion transfer between the spins was measured for each solution. To each solution in the NMR tube were then directly added five solid aliquots of FTPS, and the inversion transfer was measured for each newly obtained solution.

As derived in Section 2.3.4 (Equation 2.53), α, determined in the inversion transfer experiments is independent of [FTPS] for the dissociative pathway, and a linear function of [FTPS] for the direct transfer pathway. For both pathways, α is independent of [TBAT], provided that the rate constants k_1^{obs} and k_2^{obs} remain constant in the studied [TBAT] range.

2.53, recalled

$$\alpha = k_1^{\text{obs}} + k_2^{\text{obs}}[\text{FTPS}]$$

Titrations of the 52.9 mM and 99.0 mM solutions of TBAT showed linear plots of α against [FTPS] with nearly identical slopes of 210 M^{-1} s^{-1} and 217 M^{-1} s^{-1}, respectively (Figure 3.12). In both cases, the intercepts were slightly negative, and their absolute values were negligible with respect to the slopes (intercept/slope = –1.28 mM and

–7.89 mM, respectively). In fact, forcing the trendline to go through (0,0) increased the linearity of both plots, and gave very similar slopes of 207 M^{-1} s^{-1} and 202 M^{-1} s^{-1}, respectively. Based on these two datasets, one could therefore postulate the direct transfer of fluoride from TBAT to FTPS, with the rate constant of $k_2 \approx 200$ M^{-1} s^{-1} "per fluoride", independent of [TBAT].

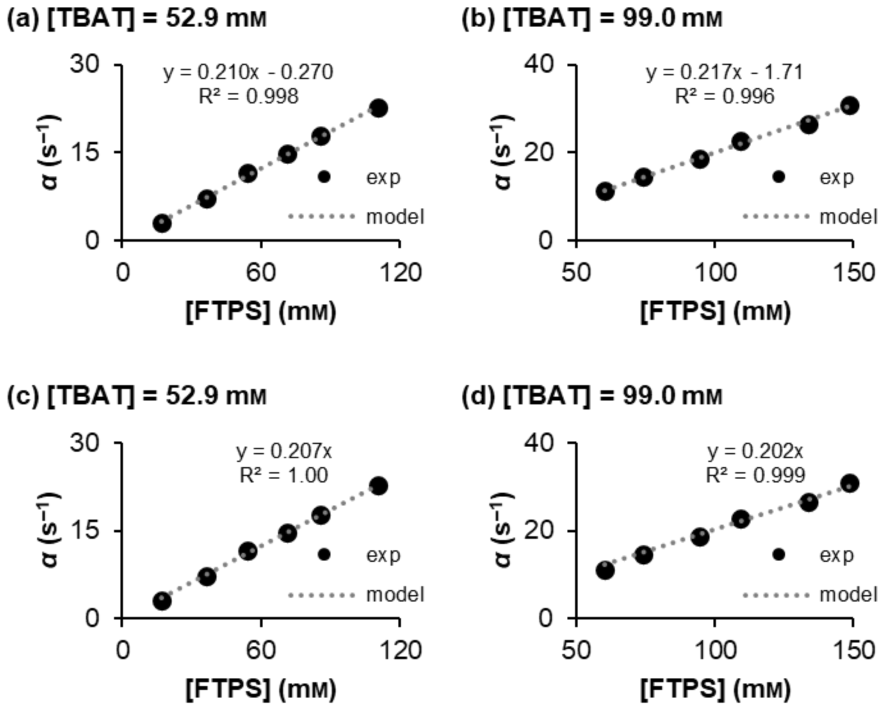

Figure 3.12: Plots of α against [FTPS] in titrations of a solution of (a) and (c) 52.9 mM TBAT, and (b) and (d) 99.0 mM TBAT in THF with solid aliquots of FTPS. The dotted lines ("model") represent linear trendlines. In (a) and (b), no constraints were placed on the fitting of the trendlines. In (c) and (d), the trendlines were forced through (0,0).

However, in titrations of the 150 mM and 202 mM solutions of TBAT, only the first five datapoints gave linear plots of α against [FTPS] (Figure 3.13). In each case, the solution obtained from the last addition of FTPS exhibited more rapid exchange than expected based on the linearity of the previous measurements. Whilst the slope of the linear part of the plot for 202 mM TBAT (240 M^{-1} s^{-1}) was comparable to the slopes for 52.9 mM and 99.0 mM solutions of TBAT, the slope for the 150 mM solution was much larger (502 M^{-1} s^{-1}). Moreover, the negative intercepts were no longer negligible (intercept/slope = –89.2 mM for 150 mM TBAT and –37.3 mM for 202 mM TBAT).

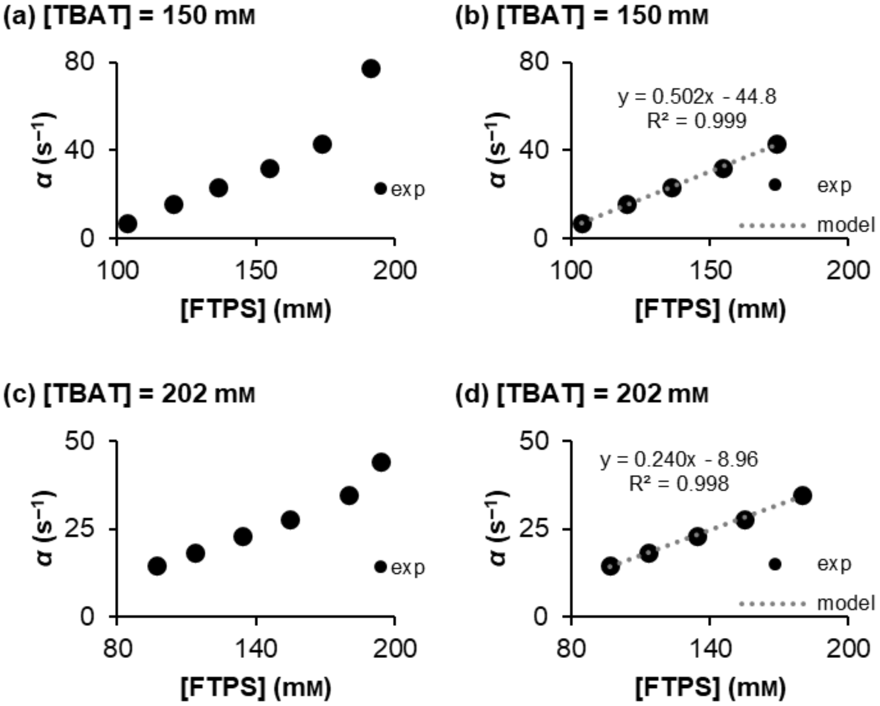

Figure 3.13: Plots of *α* against [FTPS] in titrations of a solution of (a) and (b) 150 mM TBAT, and (c) and (d) 202 mM TBAT in THF with solid aliquots of FTPS. Plots (a) and (c) show all datapoints in both titrations. The first five datapoints in each titration are shown in (c) and (d) with linear trendlines (dotted lines, "model") fitted to them.

The results obtained from the titrations of the 150 mM and 202 mM solutions of TBAT indicated clearly that the behaviour of the system was more complex than initially assumed. This conclusion was not instantly obvious for the 52.9 mM and 99.0 mM solutions of the reagent. However, $\alpha = 17.8\ s^{-1}$ determined for 52.9 mM TBAT and 85.5 mM FTPS in the titration (the fourth aliquot of FTPS, *i.e.* fifth measurement for the sample) was found to be ~50% larger than $\alpha = 12.1\ s^{-1}$ determined for the solution in Section 3.3.1, *i.e.* one of nearly identical concentrations of both species (52.5 mM TBAT and 83.9 mM FTPS), but prepared by dissolving the appropriate amounts of both solutes all at once and measured immediately. The upward curvatures in the initially linear plots, considerable negative intercepts of the trendlines in these linear parts, and discrepancy between *α* determined for two solutions under apparently the same conditions all suggested that the TBAT/FTPS system in THF may be (with respect to the inversion transfer rate between the spins): (i) highly sensitive to conditions, which may induce irreproducibility between samples, and/or (ii) temporally-unstable, with the rate of exchange changing over time. These two possibilities were therefore examined next.

Firstly, a solution of TBAT and FTPS (and the internal standard, NAPH) in THF was prepared in the glovebox and split into two parts, which were transferred to J Young® valve capped NMR tubes. The concentrations of the spins, T_1^{obs} and inversion transfer rates were measured over time initially (first 10 h) for one sample, and then for both samples. The plots of [TBAT], [FTPS] and T_1^{obs} *vs* time are presented in Figure 3.14. In order to test the effect of surroundings, *i.e.* whether ambient atmosphere leaked into the system, the sample measured immediately was kept in the spectrometer autosampler between the measurements (sample "AS"), whereas the other sample ("GB") was kept in the glovebox at all times except for each measurement.

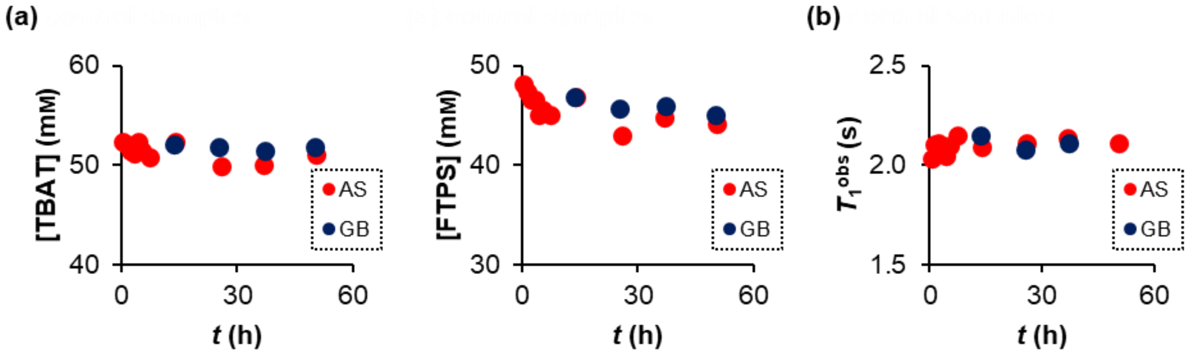

Figure 3.14: (a) Temporal concentration profiles for TBAT and FTPS, and (b) temporal evolution of T_1^{obs} for a mixture of TBAT and FTPS in THF. In all plots, "AS" refers to the sample in a J Young® valve capped NMR tube kept in the autosampler, and "GB" – to the sample in a J Young® valve capped NMR tube stored in the glovebox in between the measurements.

The concentration of TBAT appeared to be constant throughout the experiment, [TBAT] = (51.5 ± 0.4) mM, as did T_1^{obs} = (2.10 ± 0.02) s. However, the plot of [FTPS] against *t* shows apparent decomposition of FTPS initially (a 6.5% decrease of [FTPS] over 7.4 hours), followed by a somewhat noisy plateau for the later measurements, where the absolute difference between the two extreme concentrations is larger than in the first 7.4 hours. It is unclear whether this initial apparent decrease in [FTPS] was due to decomposition. Both signals were found to exhibit some line broadening over time (which in itself was indicative of an increasing exchange rate for the exchanging spins with time, Figure 3.15a). For FTPS, the error introduced by broadening could be larger than the one for TBAT, as the signal appears in a region of significant baseline distortion. Moreover, no new signals appeared above the detection limit in the ^{19}F NMR spectra of the solution. We tried to use the longitudinal relaxation time as another way of quantitating [FTPS], as T_1^{obs} is a (known) function of both [TBAT] and [FTPS] in

THF (at 300 K). However, as presented in Figure 3.15b, where a recalled plot of experimental T_1^{obs} *vs t* from Figure 3.14b is overlaid with theoretical T_1^{obs} calculated from the experimental concentrations of the spins, any potential changes in T_1^{obs} were too small to detect.

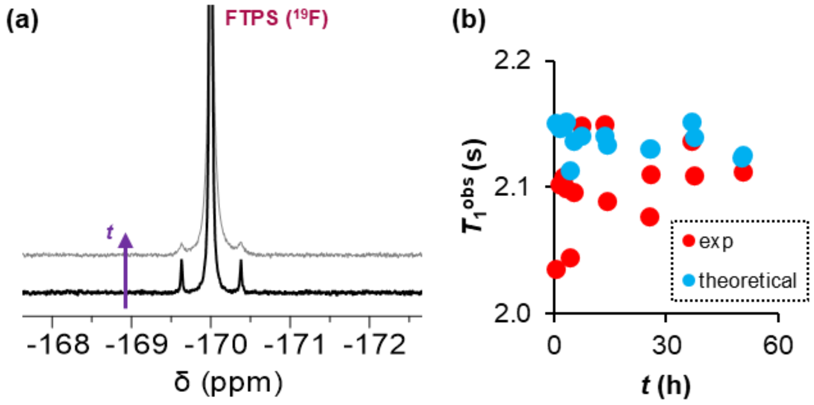

Figure 3.15: (a) Line broadening of the FTPS signal (^{19}F) between the first and last measurement for the "AS" sample (the spectra were phase- and baseline-corrected). (b) Although T_1^{obs} seemed like an attractive alternative to monitoring the broadening signal of FTPS over time, any changes in [FTPS], if present, affected T_1^{obs} negligibly.

Nonetheless, the inversion transfer model in Equation 2.78 was fitted to the experimental data and a plot of $\alpha(r + 1)$ *vs t* is presented in Figure 3.16a. Firstly, it is evident from the plot that the rate of inversion transfer between TBAT and FTPS increased over time. The plot is initially (the first 5.4 hours; Figure 3.16b) linear with a slope of 7.32 s^{-1} h^{-1} and an intercept of 23.9 s^{-1}. Importantly, the apparent decrease of [FTPS] over the first 5.4 hours is negligible in comparison to the corresponding increase in the observed rate constant of inversion transfer, $\alpha(r + 1)$; approximately 5% and 140%, respectively. In other words, this observed increase of the rate of inversion transfer over time was a result of the increase of the observed rate constant(s) of exchange, k_1^{obs} and/or k_2^{obs}. Lastly, Figure 3.16c shows the later part of the $\alpha(r + 1)$ *vs t* plot, where the rate of the increase of inversion transfer rate seemed to dramatically decrease, albeit was still linear. Inversion transfer in the control sample ("GB"), which was kept inside the glovebox prior to the first measurement at 13.6 hours (and between any two measurements), showed similar behaviour to the one which was kept in the autosampler (*i.e.* ambient surroundings) at all times. The slopes and intercepts nearly overlayed for both samples (4% and 10% smaller for "GB", respectively). Therefore, the use of J Young® valve capped NMR tubes offered systems sufficiently gas-tight for the surroundings not to interfere with the samples (*i.e.*

the rate increase in both samples was inherent to the solution, and not adventitious air or moisture).

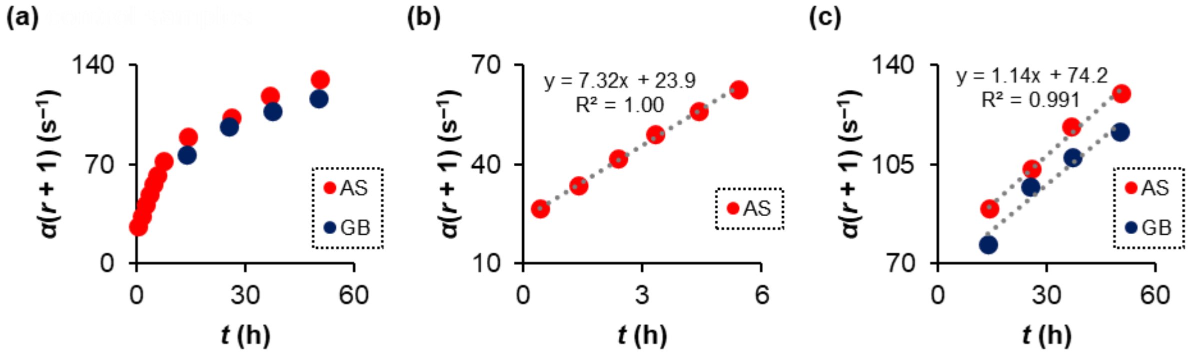

Figure 3.16: (a) Temporal evolution of the rate of inversion transfer for a mixture of TBAT and FTPS in THF. (b) An expansion of the plot in (a) showing the first six measurements on the "AS" sample. (c) An expansion of the plot in (a) showing the last four measurements on the "AS" sample, and all four measurements on the "GB" sample. In all plots, "AS" refers to the sample in a J Young® valve capped NMR tube kept in the autosampler, and "GB" – to the sample in a J Young® valve capped NMR tube stored in the glovebox in between the measurements.

Apart from this inherent increase of exchange rate between the spins over time, the upward curvatures in Figure 3.12 indicated that the exchange rate may also be highly sensitive to even slight changes in conditions. To examine this possibility, a sample was prepared analogously to one above and with similar concentrations of the spins (45.9 mM TBAT and 50.7 mM FTPS). The inversion transfer rate was again measured over time, this time however, certain operations were performed on the sample, as specified below.

The first measurement was taken as for the previous solution. Before the second measurement, the NMR tube was shaken thoroughly for one minute (without opening the system to air). Before the third and the fourth measurements, the NMR tube was introduced into the glovebox, opened to the glovebox atmosphere (N_2) for one minute each time, and then closed again. Before the fifth and the sixth measurements, the NMR tube was also introduced into the glovebox, but was not opened. Instead, the bottom seal of the cap was loosened and, whilst the NMR tube was still closed, the bulb compartment of it was rinsed with its contents (the solution). The bulb compartment was then emptied (back to the bottom of the NMR tube) and the NMR tube resealed fully. Finally before the seventh measurement, the NMR tube was open to air for ~1 s, closed and shaken thoroughly.

The plot of $\alpha(r + 1)$ *vs* t is presented in Figure 3.17, overlaid with the data from the inherent rate increase experiment ("AS").

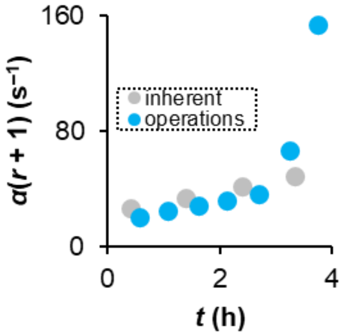

Figure 3.17: Temporal evolution of the inversion transfer rate as a response to performing operations on the NMR tube (described in the main text). The corresponding inherent rate increase in the "AS" system from Figure 3.16 is also presented (grey points).

The inversion transfer rate constants, $\alpha(r + 1)$, for the first five measurements were a linear function of time, with a nearly identical slope to one for the inherent exchange rate increase (7.21 s^{-1} h^{-1} *cf*. 7.32 s^{-1} h^{-1}; intercept = 16.7 s^{-1}, $R^2 = 0.993$). This initial increase of $\alpha(r + 1)$ indicated that no rate-increasing factors other than the inherent one(s) observed previously were present for these five measurements. However, the sixth measurement gave a larger rate constant increase than expected from the initial linearity (66.4 s^{-1} *cf*. expected 40.2 s^{-1}). A possible rationale behind this observation is that the bulb compartments of J Young® valve capped NMR tubes (used throughout this study) are not perfectly sealed from the surroundings. Normally, the seals are good enough, so that even if any air and moisture is present in the "bulb", briefly applying vacuum in the antechamber, prior to introducing the NMR tube into the glovebox, removes it. Therefore, the first rinsing of the bulb compartment with the solution did not introduce any air and moisture to the system. However, it left a trace amount of the solution in the bulb compartment, which absorbed the air and moisture when the NMR tube was removed from the glovebox for the fifth measurement. This trace amount of the compromised solution was then introduced back into the sample in the second rinsing (prior to the sixth measurement). The absorbed water had a catalysing effect on the exchange rate between the spins. Finally, even very briefly opening the sample to ambient atmosphere resulted in a dramatic increase in the inversion transfer rate constant (154 s^{-1} *cf*. expected 43.7 s^{-1}).

Each of the four titration experiments described in this section was completed within four hours of the preparation of the original solution, a period for which the exchange rate increase between TBAT and FTPS was found to increase linearly with time (in the absence of any catalysing "operations" on the NMR tubes, such as accidentally rinsing the bulb compartment with the sample, which likely was the case for the last measurements in the 150 mM and 202 mM TBAT solutions). Also considering the high sensitivity of the system to (most likely) water from air, we note that the exchange rate increase resulting from increasing [FTPS] in the titrations could be indicative of either or both fluoride transfer pathways, where the rate constant(s) increased over time. Moreover, FTPS could be wet and hence water, which catalyses the exchange between TBAT and FTPS, could be introduced to the system along with the reagent.

The effect of added water on the exchange rate was therefore studied quantitatively. A solution of 59.2 mM TBAT and 67.3 mM FTPS (~0.4 mL in a J Young® valve capped NMR tube) was titrated with five (<1 μL) aliquots of a 129 mM solution of water in THF (in the presence of PhF, used to quantify added water). Inversion transfer between TBAT and FTPS was measured prior to the titration and for each aliquot, and a plot of $\alpha(r + 1)$ against the concentration of added water, c^{w}, is presented in Figure 3.18a. The same $\alpha(r + 1)$ data plotted against time (t, from sample preparation) is presented in Figure 3.18b. The inversion transfer rate increase between each two measurements was large relative to the inherent rate increase over time (7.32 $\mathrm{s}^{-1}\ \mathrm{h}^{-1}$ determined for "AS"). A line of this slope going through the first datapoint in Figure 3.18b illustrates the extent of this difference. Therefore, it was assumed that the increase of $\alpha(r + 1)$ was solely a result of the added water in the titration.

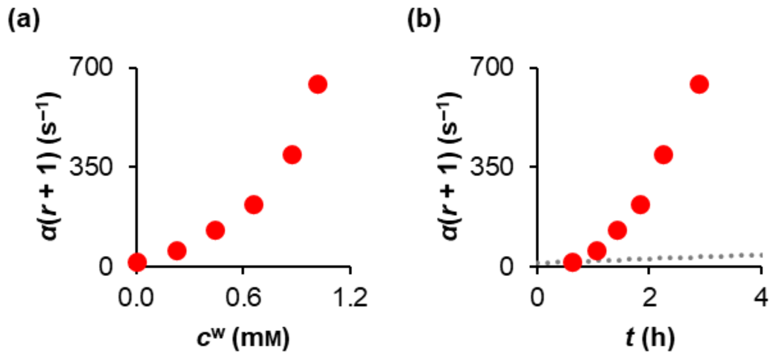

Figure 3.18: (a) Titration of the TBAT/FTPS system in THF with water (at 300 K). (b) The experimental $\alpha(r + 1)$ from (a) plotted against t, and compared to a linear $\alpha(r + 1)$ *vs* t model with a slope of 7.32 $\mathrm{s}^{-1}\ \mathrm{h}^{-1}$ going through the first experimental datapoint.

The order of the reaction with respect to water was estimated by assuming a linear dependence of α on $[H_2O]^x$, where x is the empirical order with respect to water and $[H_2O]$ is the total concentration of water in the solution, *i.e.* sum of added water, c^w, and water present in the solution initially, $[H_2O]_0$ (Equation 3.5). Hence, $\ln[\alpha(r + 1)]$ was plotted against $\ln(c^w + [H_2O]_0)$, where $[H_2O]_0$ was optimised (in increments of 0.1 mM) for the best linear fit. A selection of the plots is presented in Figure 3.19. The best linear fit was obtained for ~0.6 mM $[H_2O]_0$, and thus the order with respect to water was estimated as ~3.5. The estimated amount of water (~0.6 mM) in the system was reasonable considering that ~0.2 mM water was present in a sample of (dry) MeCN-d_3 transferred to a (dry) J Young® valve capped NMR tube inside the glovebox (see Section 7.2).

3.5

$$\alpha = \alpha_{\text{true}}(c^{\text{w}} + [\text{H}_2\text{O}]_0)^x$$

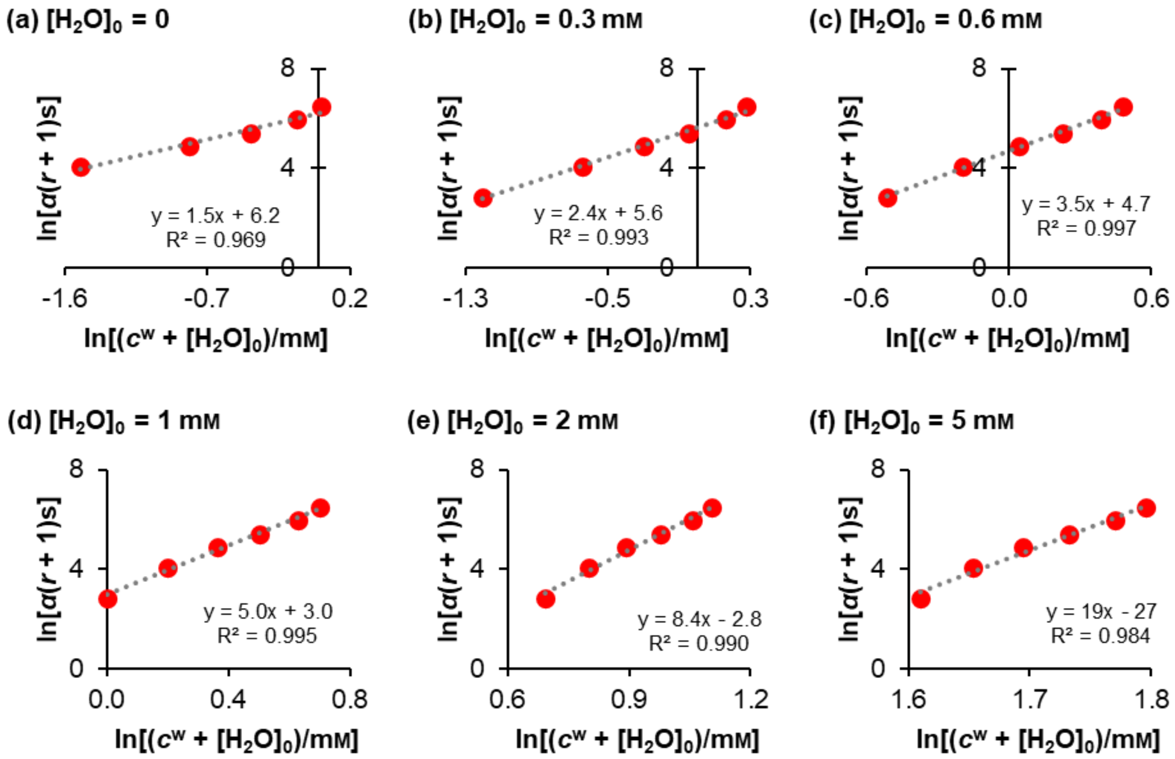

Figure 3.19: The order with respect to water estimated by finding the best linear fit for incremented $[H_2O]_0$.

It is therefore evident that the exchange rate between TBAT and FTPS in THF is extremely sensitive to water. However, with respect to this sensitivity, the amount of water introduced to the system as an impurity in the FTPS titrations was negligible, if any (Section 7.2).

In search for a system which exhibits temporal stability of the inversion transfer rate, a series of solutions of ~50 mM TBAT and ~50 mM FTPS were prepared with certain additives/modifications, and the response of each system to the applied change was monitored. Additives which had little effect on the temporal evolution of the inversion transfer rate include di-*tert*-butylpyridine (D^{t}BP, ~20 mM), powdered glass (Section 5.1.1, ~40 mg) and TMS_2O (~20 mM); Figure 3.20a (overlaid with the data for "AS", grey points). Using a dried Teflon insert had a dramatic effect on the increase of inversion transfer rate over time, as presented in Figure 3.20b ("AS" data again included in grey). Initially (t = 0.550 h), $\alpha(r + 1)$ = 30.4 s^{-1} was similar to the value obtained for "AS" (26.7 s^{-1} at t = 0.414 h). It then increased very rapidly to 488 s^{-1} at t = 12.9 h, *i.e.* by approximately 16-fold over 12 hours (*cf*. an approximately 3-fold increase for "AS" over a similar period). Repeating the inversion transfer measurements for a further 20 h showed that an apparent stability with respect to the inversion transfer rate was achieved over this period. An interesting temporal profile was obtained for the solution in the presence of 3 Å molecular sieve beads (MS, ~40 mg), whereby the inversion transfer rate initially increased and then decreased with time; Figure 3.20c. A control sample (no MS added initially) showed the expected increase of $\alpha(r + 1)$ over time. However, when molecular sieves were added (t ≈ 24 h) to the control sample (the sample was then shaken thoroughly for ~5 min and the inversion transfer was measured immediately), $\alpha(r + 1)$ decreased from 58.1 s^{-1} to 9.69 s^{-1}, much closer to $\alpha(r + 1)$ = 7.09 s^{-1} for the sample with MS present initially (although still ~40% larger). Nevertheless, this experiment showed the reversibility of the process which caused the inversion transfer between the spins to increase over time in the absence of MS.

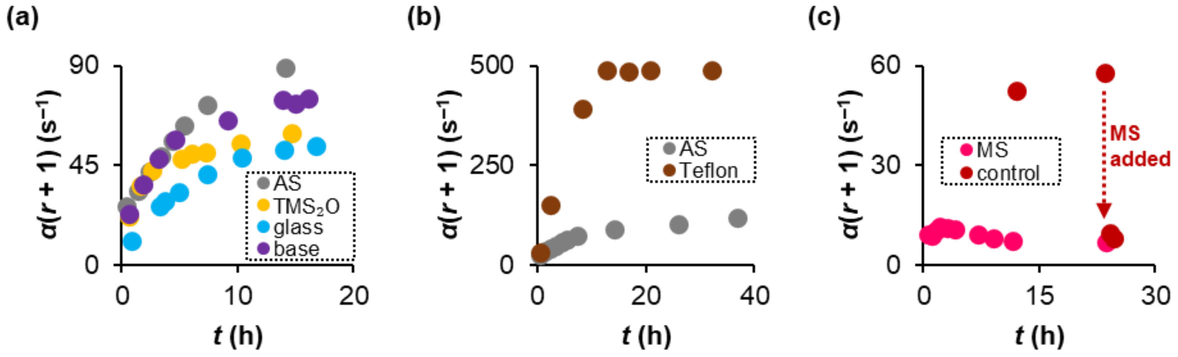

Figure 3.20: Effect of additives on the temporal evolution of the TBAT/FTPS inversion transfer. (a) D^{t}BP, powdered glass and TMS$_2$O had little effect on the increase of $\alpha(r + 1)$ over time. (b) The solution placed in a Teflon insert exhibited a dramatic increase of $\alpha(r + 1)$ to nearly 500 s^{-1} over 12 hours, followed by apparent stabilisation of the inversion transfer rate for a further 20 h. (c) In the presence of MS beads, $\alpha(r + 1)$ initially increased, followed by a maximum at $t \approx 2$ h, and a subsequent decrease. Notably, addition of MS to a control sample reversed the inversion transfer rate increase from prior to the addition.

However, a combination of D^{t}BP (~20 mM) and MS (~40 mg) caused the inversion transfer rate in the system (50 mM TBAT, 45 mM FTPS) to initially decrease, eventually heading towards temporal stability (Figure 3.21).

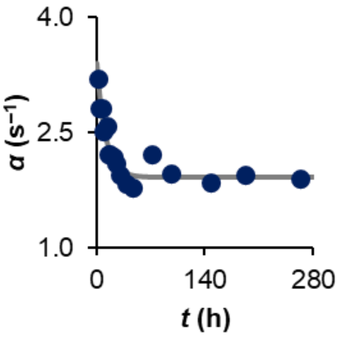

Figure 3.21: The heading towards temporal stability of the TBAT/FTPS exchange rate in the presence of D^{t}BP and MS.

An empirical exponential decay model was fitted to the experimental data with three fitting parameters: α_0 (α immediately after sample preparation), α_S (α in the stabilised system, *i.e.* the value of the plateau) and k_S (the rate constant of the “slowing down” of the exchange); Equation 3.6. The determined fitting parameters were: $\alpha_0 = 3.40$ s^{-1}, $\alpha_S = 1.92$ s^{-1}, $k_S = 0.0885$ h^{-1}. The root mean square error, $R = 0.12$ s^{-1} (8.1% of the absolute difference between α_0 and α_S), indicated an excellent fit to the experimental data, despite poor shimming resulting from the heterogeneity of the system.

3.6

$$\alpha = (\alpha_0 - \alpha_s)e^{-k_s t} + \alpha_s$$

Once the system was stable with respect to the exchange rate, the NMR tube was shaken thoroughly for ten minutes, which did not seem to affect the system. Neither the addition of more D^{t}BP (another ~20 mM), nor MS (another ~20 mg), disturbed the stability of the system, although in both cases α changed slightly (11% above and below the model plateau, α_S, respectively). These results are presented in Figure 3.22.

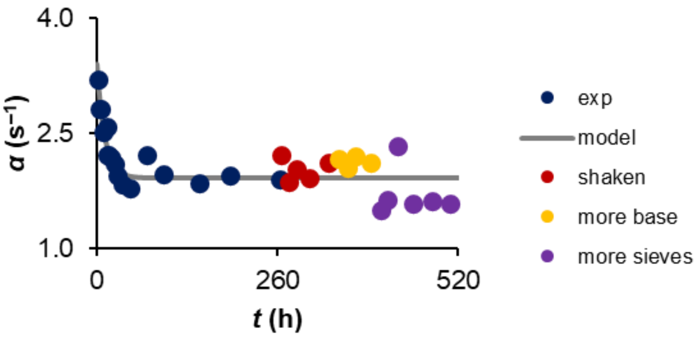

Figure 3.22: Relative insensitivity of the stabilised system to shaking the NMR tube, as well as the addition of more D^{t}BP ("base") and MS ("sieves").

3.3.3. Exchange pathways in the temporally-stabilised systems

Upon the observation that in the presence of a both 2,6-di-*tert*-butylpyridine (D^{t}BP) and molecular sieve (MS) beads, the TBAT/FTPS system in THF reaches temporal stability with respect to the exchange rate between the spins, we aimed to establish the dependence of this rate on [FTPS] under the stabilising conditions.

Five solutions of TBAT, FTPS, D^{t}BP (and the internal standard, NAPH) in THF were prepared in the glovebox and transferred to J Young® valve capped NMR tubes preloaded with MS beads (the NMR tubes were then shaken thoroughly). The concentration of TBAT was equal in all five solutions (101 mM) and the concentration of FTPS was varied, c^{FTPS} (mM) {22.6, 62.9, 101, 144, 204}. For each of the solutions, ten sets of experiments were performed over 340 h. In each set, TBAT and FTPS were quantitated against NAPH, T_1^{obs} was determined from ^{19}F non-selective inversion-recovery of TBAT, and α was determined from ^{19}F inversion transfer between the spins. The time, t, of each set of measurements is given relative to preparation of each solution and the results are discussed below.

The plot of [TBAT] against time is presented in Figure 3.23a for all five solutions and shows that [TBAT] was indeed equal between the solutions, and constant over the duration of the experiment (340 h from preparation of the samples). An expansion of this plot (Figure 3.23b) shows a 4-mM range centred around 99 mM (all 50 datapoints are within the range). A closer examination of the expanded plot showed a possibility of a low-degree of decomposition of TBAT over time for the solutions containing 22.6 mM and 101 mM FTPS, where linear trendlines give very slightly negative slopes (albeit with low R^2). It is unclear whether the apparent decrease of [TBAT] for these two solutions was a result of decomposition or experimental error (perhaps from poor shimming). However, no decrease was observed for the remaining three solutions and hence the latter seemed likely. Even if decomposition was responsible for the apparent decrease of [TBAT] in the two solutions, only 1.4% and 1.7% of TBAT decomposed in the 22.6 mM and 101 mM FTPS solutions, respectively, based on the linear trendlines. The plots for all five solutions, including the linear trendlines, are presented in the experimental section. Therefore, the concentration of TBAT was assumed to be equal and independent of time for all five systems. An average of all the 50 experimental concentrations was taken as the “true” concentration in these experiments, [TBAT] = (99.1 ± 0.2) mM, which is in excellent agreement with the theoretical 101 mM based on mass of the solute (98% of the theoretical value).

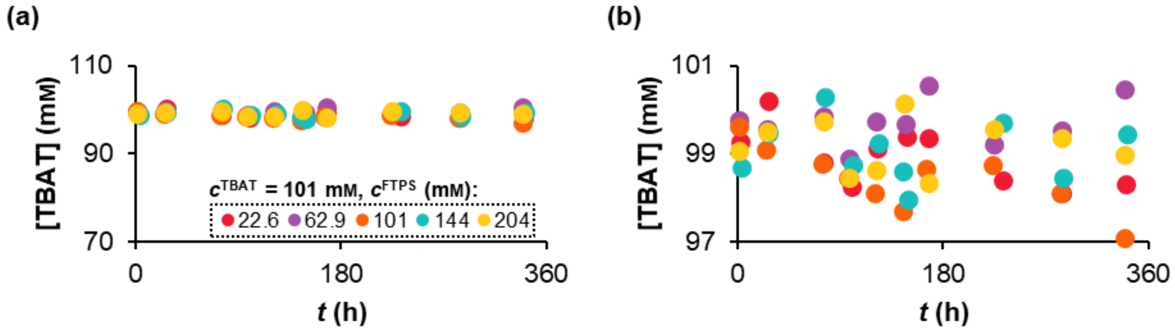

Figure 3.23: (a) An analysis of [TBAT] *vs* *t* under the stabilising conditions (2,6-di-*tert*-butylpyridine and molecular sieves). (b) An expansion of the plot in (a) to a 4-mM *y*-axis range, centred around 99 mM.

The analysis of [FTPS] against time (Figure 3.24, individual plots with linear trendlines are presented in the experimental section) was slightly more ambiguous. Whilst it appears from Figure 3.24 that [FTPS] was independent of time for all solutions, the expansions of the plots (6–8-mM ranges, Figure 5.13) revealed that likely FTPS decomposed in at least some of the solutions. In the solution which contained 22.6 mM FTPS based on the mass of the solute, a decrease from [FTPS] = 22.6 mM to [FTPS] = 17.5 mM (23%) was observed over 340 h, based on quantitation against NAPH. The decomposition profile appears to be relatively linear (R^2 = 0.86), with an intercept of 22.3 mM (98% of the theoretical value) and a slope of –0.0142 mM h^{-1}. The linear decomposition model of Equation 3.7 was therefore used to determine [FTPS] at each time *t* for this solution. The other four solutions showed more ambiguity in whether FTPS decomposes. Whilst the 101 mM and 204 mM solutions show scatter, it may be argued that a slight decrease in [FTPS] was observed for the 62.9 mM and 144 mM solutions (5.0% and 3.2%, respectively, based on the linear trendlines). Nonetheless, the difference between the highest and lowest [FTPS] determined for each of these solutions was between 3.5% and 7.4% of the corresponding concentrations by mass of the solute. Any potential decrease in [FTPS] in these four solutions was therefore negligible compared to the differences in [FTPS] between them. As a result, the concentration of FTPS was assumed to be independent of time for the four solutions which contained 62.9–204 mM FTPS by mass of the solute. An average of all 10 values from quantitation of FTPS against NAPH for each solution was taken as the "true" concentration in that solution, [FTPS] (mM) {(60.8 ± 0.9), (100 ± 1), (143 ± 1), (202 ± 1)}; all of these values are in excellent agreement with the theoretical concentrations based on mass of the solute (97–99% of the corresponding theoretical values).

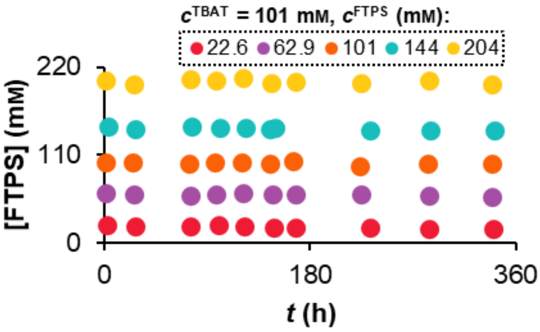

Figure 3.24: An analysis of [FTPS] *vs t* under the stabilising conditions (2,6-di-*tert*-butylpyridine and molecular sieves).

3.7

$$\frac{[\mathrm{FTPS}]}{\mathrm{mM}} = -0.0142t + 22.3$$

The average T_1^{obs} (s) {(1.46 ± 0.01), (1.59 ± 0.03), (1.70 ± 0.05), (1.87 ± 0.05), (2.10 ± 0.05)} from all ten measurements for each solution, presented in the order of increasing [FTPS], are also in excellent agreement with the expected values based on the weighted averages of T_1^{TBAT} and T_1^{FTPS} as isolated spins (4–16% lower than the corresponding expected values). The plot of T_1^{obs} against *t* is presented in Figure 3.25

for all five solutions. All datasets show a slight decrease of T_1^{obs} over the 340 hours of monitoring (individual plots along with linear trendlines are presented the experimental section). Despite the observed decrease, T_1^{obs} determined from the non-selective inversion-recovery experiments were directly used in the fitting of the inversion transfer model to the corresponding measurements (*i.e.* in the same set of experiments). Firstly, T_1^{obs} may be dependent on even slight changes in conditions and hence the noise in the T_1^{obs} *vs* *t* plots may not represent experimental errors but rather true T_1^{obs} at the time of the measurement. Secondly, a (significant) error in T_1^{obs} used in the inversion transfer model would show in the magnetisation transfer plot and can be easily corrected by refitting the model with T_1^{obs} as the fourth unknown parameter.

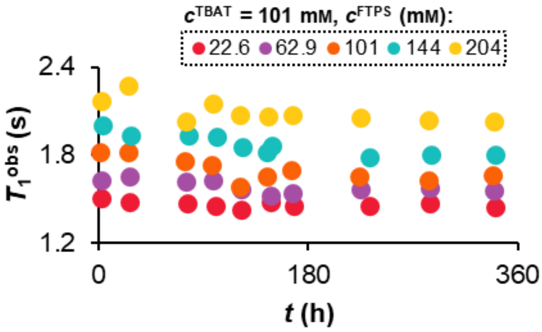

Figure 3.25: Analysis of T_1^{obs} *vs* *t* under the stabilising conditions (2,6-di-*tert*-butylpyridine and molecular sieves).

The inversion transfer model gave excellent fits to all 50 experimental datasets (the average root mean square error relative to model equilibrium integral, R/I_{eq} = 0.99%). The plots of α against *t* for the five solutions are presented in Figure 3.26a–e. All plots show a decrease of α and subsequent plateauing. For the 204 mM FTPS solution, an apparent increase is observed initially, which could either be an error or a similar trend to the one observed for the TBAT/FTPS system in the presence of only MS (and no D^{t}BP) described in section above. Most importantly, however, as all five solutions eventually reached temporal stability of α, the dissociative *vs* direct transfer pathways in these now stabilised systems could be interrogated.

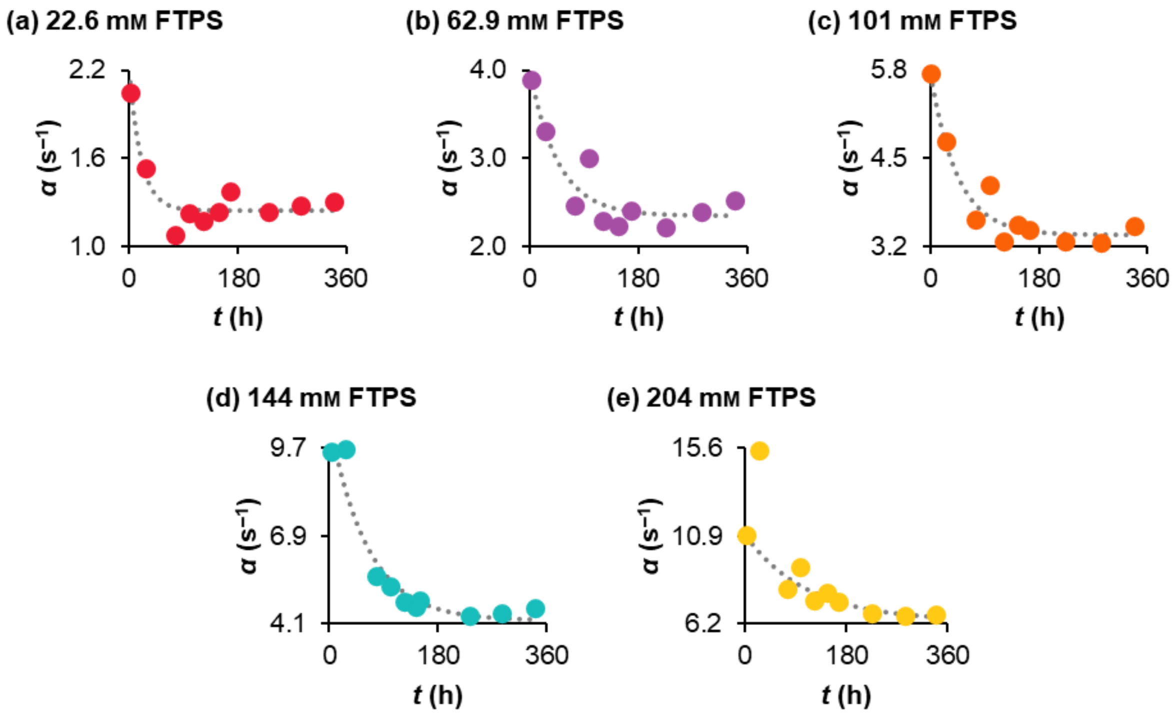

Figure 3.26: Heading towards temporal stability of the stabilised systems. See Table 3.2 for root mean square errors of the fits.

The exponential decay model from Equation 3.6 was fitted to the experimental data (dotted lines in plots in Figure 3.26a–e). The fitting parameters and root mean square errors (R) are presented in Table 3.2.

Table 3.2: Determined fitting parameters and root mean square errors (R) in the exponential decay of the observed exchange rate constant in the stabilised system.

[FTPS] (mM)	α_0 (s^{-1})	α_S (s^{-1})	k_S (h^{-1})	R (s^{-1})
18.1	2.16	1.24	0.0498	0.08
60.8	3.96	2.34	0.0211	0.19
100	5.79	3.37	0.0224	0.19
143	10.6	4.22	0.0158	0.53
202	11.0	6.39	0.00907	0.42

Two issues are noted regarding these models. Firstly, the second datapoint in α *vs* t for the 204 mM FTPS solution was treated as an outlier and discarded from the fitting, as discarding it gave a better fit for the last five datapoints. Secondly, although it was established that [FTPS] decreased by 23% overall in the 22.6 mM FTPS solution, the last three datapoints in the α *vs* t plot correspond to 18.9 mM, 18.0 mM and 17.5 mM FTPS. The experimental values of α for these three concentrations are in good agreement with one another and the model α_S determined for the solution (average of 1.27 s^{-1} compared to model α_S = 1.24 s^{-1}). It was therefore assumed that for this solution, once “stabilised”, α_s = 1.24 s^{-1} and [FTPS] = 18.0 mM (the average of the last three concentrations).

Finally, α_s was found to be a linear function of [FTPS] with slope = 27.3 M^{-1} s^{-1}, intercept = 0.656 s^{-1} and R^2 = 0.989. This plot is presented in Figure 3.27a. According to Equation 3.8 (similar to Equation 2.53, except the subscript “s” was given to α), the slope of the plot corresponds to the rate constant of the direct transfer pathway, k_2^{obs}, and the intercept – to the rate constant of the dissociative pathway, k_1^{obs}, both rate constants per fluorine atom of TBAT (*i.e.* the actual rate constants are double these values). Notably, this result shows that at least in the temporally-stabilised system (*via* addition of MS and D^{t}BP), the dissociative and direct transfer pathways proceed in parallel in the transfer of fluorine between TBAT and FTPS, and the contribution of each pathway depends on [FTPS], Equation 3.9 (where $c°$ = 1 M is the standard concentration). For example, for 1 M FTPS, direct transfer contributes to 98% of the overall rate of fluoride between the spins. This contribution decreases to 80% for 100 mM FTPS and to 29% for 10 mM FTPS.

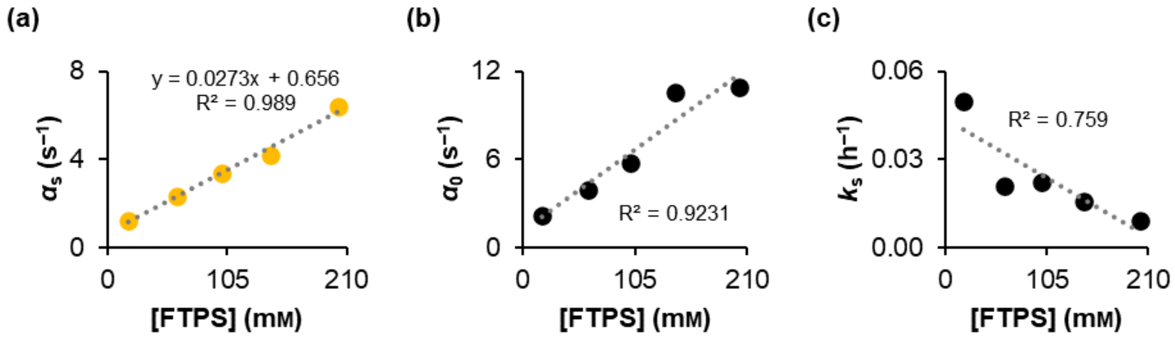

Figure 3.27: (a) The interrogation of the dissociative and direct fluoride transfer pathways in the stabilised TBAT/FTPS systems. (b and c) In comparison, irreproducibility is observed prior to the systems reaching stability.

3.8

$$\alpha_s = k_1^{\mathrm{obs}} + k_2^{\mathrm{obs}}[\mathrm{FTPS}]$$

3.9

$$\frac{k_2^{\mathrm{obs}} c^{\circ}}{k_1^{\mathrm{obs}}} = 41.6$$

The effect of the added D^{t}BP and MS on the stability and reproducibility of the systems is especially pronounced in comparison with corresponding plots of α_0 against [FTPS] and k_s against [FTPS] (Figure 3.27b–c), which do not show linear correlations.

3.3.4. Dissociative pathway in the non-stabilised system

Based on the discussion above, TBAT and FTPS exchange fluoride *via* both dissociative and direct pathways proceeding in parallel in the presence of di-*tert*-butylpyridine (D^{t}BP) and molecular sieves (MS) in THF. This observation may not be true for non-stabilised systems. Whilst an accurate kinetic analysis of these systems is challenging due to their temporal instability and high sensitivity to conditions, we sought to establish whether in these systems, evidence for the dissociative pathway could be shown. According to Equation 2.78, the rate of inversion transfer between TBAT and FTPS depends on the term $\alpha(r + 1)$, where r is the ratio of equilibrium magnetisations of TBAT and FTPS and the expression for α depends on the transfer pathway, Equation 2.53 (as opposed to the exchange rate, which depends on α[TBAT]).

2.78, recalled

$$M_z^{\mathrm{TBAT}} = x\left[e^{-\alpha(r+1)\tau} - e^{-\frac{\tau}{T_1^{\mathrm{obs}}}}\right] + M_{z,\mathrm{eq}}^{\mathrm{TBAT}}$$

2.53, recalled

$$\alpha = k_1^{\mathrm{obs}} + k_2^{\mathrm{obs}}[\mathrm{FTPS}]$$

The expression for $\alpha(r + 1)$ is therefore:

3.10

$$\alpha(r+1) = 2k_1^{\mathrm{obs}}\frac{[\mathrm{TBAT}]}{[\mathrm{FTPS}]} + k_1^{\mathrm{obs}} + 2k_2^{\mathrm{obs}}[\mathrm{TBAT}] + k_2^{\mathrm{obs}}[\mathrm{FTPS}]$$

The function described by Equation 3.10 was simulated for [TBAT] = 100 mM and 0 < [FTPS] ≤ 100 mM in three scenarios: (i) dissociative transfer only (Figure 3.28a), (ii) direct transfer only (Figure 3.28b), (iii) both direct and dissociative transfer with $k_2^{\mathrm{obs}}c°$ = 200k_1^{obs} (Figure 3.28c). In the simulations, the exchange rate constants k_1^{obs} and k_2^{obs} were assumed to be independent of time for simplicity. For the dissociative pathway, a titration of TBAT with FTPS should show a decrease in the rate constant of inversion transfer initially, followed by a plateau which equals k_1^{obs}. For direct transfer, a linear increase with [FTPS] should be observed with a slope and intercept of k_2^{obs} and 2k_2^{obs}[TBAT], respectively. For both pathways proceeding in parallel, an initial decrease, followed by a minimum and subsequent increase of the inversion transfer rate constant should be observed.

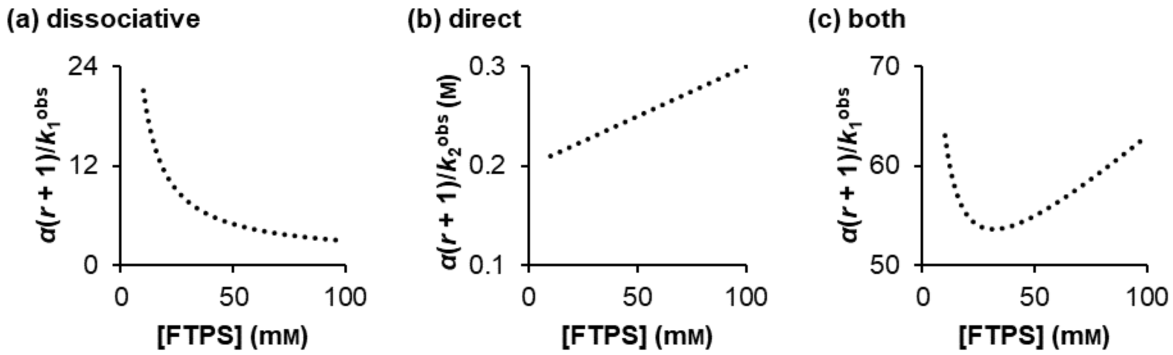

Figure 3.28: Simulations of the inversion transfer rate constant *vs* [FTPS] for: (a) dissociative TBAT/FTPS fluoride transfer, (b) direct TBAT/FTPS fluoride transfer and (c) competitive dissociative and direct TBAT/FTPS fluoride transfer ($k_2^{obs}c° = 200k_1^{obs}$). In all three scenarios, [TBAT] = 100 mM and the system does not exhibit temporal instability.

However, as the exchange rate in the non-stabilised systems inherently increases over time, the dissociative pathway, if present, may be overlooked. For example, a simulation of the dissociative transfer for concentrations similar to those in one of the titrations from Section 3.3.2 (100 mM TBAT and 70–150 mM FTPS in 20 mM increments) is presented in Figure 3.29a. In this simulation, the rate constant k_1^{obs} is independent of time, unlike in an analogous simulation presented in Figure 3.29b, where k_1^{obs} is a linear function of time. Here, an initial rate constant k_1^{obs} (at $t = 0$) increases by $0.5k_1^{obs}$ between $t = 0$ and the first measurement, and then between any two measurements. The dissociative transfer pathway of Figure 3.29b could be mistaken for direct, as $\alpha(r + 1)$ provides a good fit to a linear function of [FTPS]. Only upon a closer examination could one realise that “something is off”, as the intercept/slope, which should give 2[TBAT] = 200 mM for the direct transfer pathway, gave 126 mM instead. A simulation in Figure 3.29c, now shows both transfer pathways with $k_2^{obs}c° = 40k_1^{obs}$ (at $t = 0$); as a similar ratio was found for the stabilised systems in Section 3.3.3. The behaviour of k_1^{obs} *vs* t is identical to that in Figure 3.29b, whereas k_2^{obs} is independent of t. An even better linear fit characterises this simulation, and the intercept/slope is now 169 mM, much closer to 2[TBAT] = 200 mM expected for a “simple” direct pathway for this system. Changing the slope of k_1^{obs} increase from $0.5k_1^{obs}/\Delta t$ (where Δt is the period between $t = 0$ and the first measurement and between any two measurements) to $0.4k_1^{obs}/\Delta t$ gave excellent linear fits as well for both the dissociative pathway (Figure 3.29d) and competitive pathways (Figure 3.29e), this time with the intercept/slope of exactly 2[TBAT] = 200 mM.

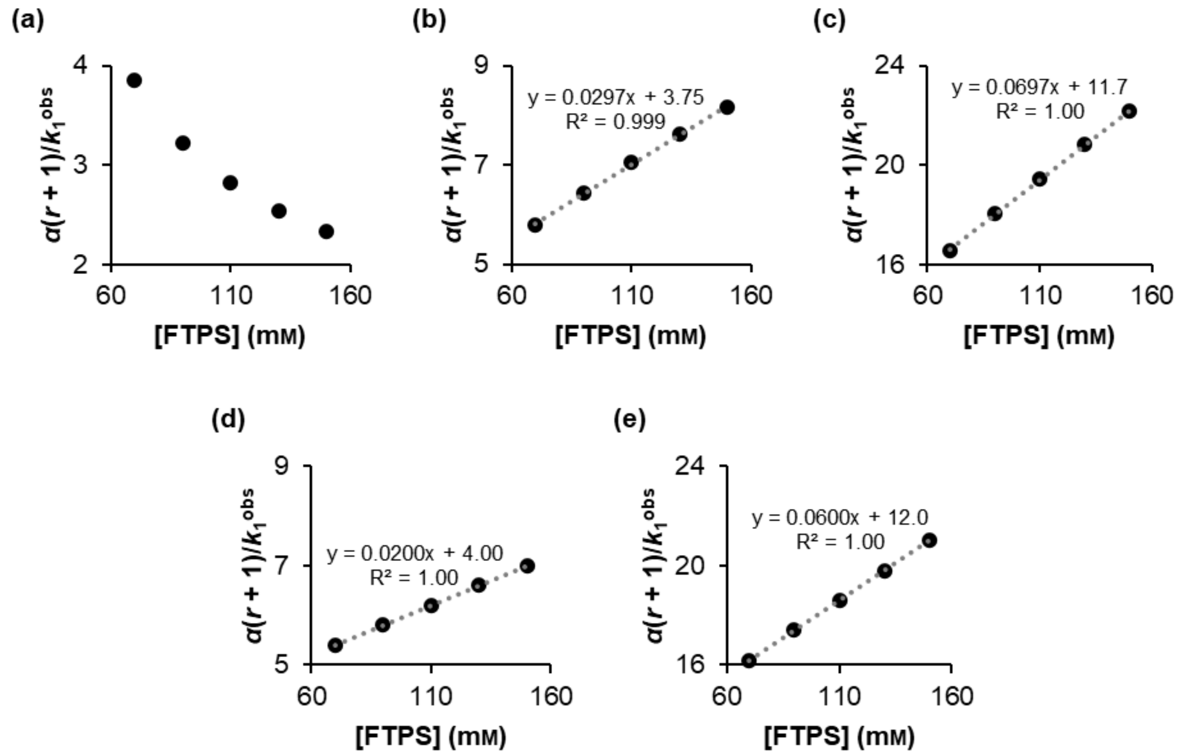

Figure 3.29: Simulations of the inversion transfer rate constant *vs* [FTPS] for: (a) "simple" dissociative TBAT/FTPS fluoride transfer, (b) dissociative TBAT/FTPS fluoride transfer with the initial exchange rate constant k_1^{obs} increasing by $0.5k_1^{obs}$ every Δt (Δt is the time period between $t = 0$ and the first measurement, and between any two measurements), (c) both dissociative and direct TBAT/FTPS fluoride transfer with the initial exchange rate constant k_1^{obs} increasing by $0.5k_1^{obs}$ every Δt (and $k_2^{obs}c° = 40k_1^{obs}$, independently of time), (e) dissociative TBAT/FTPS fluoride transfer with the initial exchange rate constant k_1^{obs} increasing by $0.4k_1^{obs}$ every Δt, (d) both dissociative and direct TBAT/FTPS fluoride transfer with the initial exchange rate constant k_1^{obs} increasing by $0.4k_1^{obs}$ every Δt (and $k_2^{obs}c° = 40k_1^{obs}$, independently of time). In all five scenarios, [TBAT] = 100 mM.

However, we envisaged that the dissociative transfer pathway could still be observed in a non-stabilised system – if present. A titration of TBAT with FTPS would provide conclusive proof of at least partial dissociative character to exchange if, despite the inherent rate increase overt time in the system, a decrease of the observed rate constant of inversion transfer, $\alpha(r + 1)$, was observed at least in the initial stage of the titration (*i.e.* if the decrease in the rate of inversion transfer as a result of addition of FTPS was greater than the temporal increase). In order to maximise the chance of observing this proposed decrease in rate of inversion transfer, a concentrated solution of TBAT (202 mM) was titrated in the glovebox with very small aliquots of solid FTPS, as rapidly as possible without compromising safety (see mathematical considerations in Section 7.1.3). After each aliquot, [FTPS] was quantitated against NAPH and inversion transfer between spins measured.

A plot of $\alpha(r + 1)$ *vs* [FTPS] is presented in Figure 3.30. It shows that $\alpha(r + 1)$ initially decreased with increased [FTPS] (first-to-second and second-to-third measurements). Then, after reaching a minimum around the third measurement, $\alpha(r + 1)$ started increasing. Evidently, fluoride transfer from TBAT to FTPS is at least partially dissociative in character in the non-stabilised system.

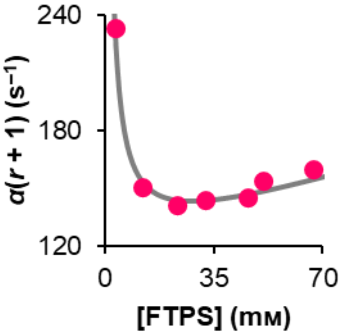

Figure 3.30: Proof of at least partially dissociative character of TBAT/FTPS fluoride transfer in the non-stabilised system in THF. (The grey line is not a fitted model but merely an aid to the eye).

3.3.5. Exchange in MeCN

The ^{19}F longitudinal relaxation time constant of FTPS in MeCN (at 300 K), T_1^{FTPS} is 16.6 s, and found to be independent of its concentration and significantly larger than the one of TBAT ($7.14 \geq T_1^{\text{TBAT}} \geq 4.46$ in the 14.1-229 mM concentration range studied herein). Similarly to solutions of TBAT and FTPS in THF, very rapid exchange was observed between ^{19}F spins at 300 K in MeCN, Figure 3.31a, with an inversion transfer rate constant $\alpha(r + 1) = 604$ s^{-1} ($I_{\text{eq}} = 1102$, $x = 396$, $x' = 588$, $R = 23$, see Section 5.2.6 for details of model fitting); and an averaged $T_1^{\text{obs}} = 7.88$ s (*cf*. the expected 8.07 s) for a solution of 48.8 mM TBAT and 45.8 mM FTPS (anhydrous system under N_2, ~1 hour from preparation of the solution). The exchange was found to be significantly more rapid than in THF ($\alpha^{\text{MeCN}}/\alpha^{\text{THF}} \approx 16$ for the solutions described herein and in Section 3.3.1), and extremely rapid on the longitudinal relaxation timescale, as illustrated by Figure 3.31b (expansion of the plot from Figure 3.31a showing the first eight datapoints, $\tau < 40$ ms). The initial decay of longitudinal magnetisation of TBAT reached an apparent plateau corresponding to a statistical distribution of the inverted ^{19}F spins between TBAT and FTPS, prior to pseudo-exponential relaxation of TBAT (and FTPS) with $T_1^{\text{obs}} = 7.88$ s. This statistical distribution was practically achieved before the third datapoint, $\tau = 5$ ms ($m^{\text{TBAT}} = 0.742$ *cf*. the minimum $m^{\text{TBAT}} = 0.734$ for

τ = 13.4 ms). The model fractional magnetisation of TBAT at τ = 0 was less than 1, m^{TBAT} = 0.913, due to non-negligible exchange between TBAT and FTPS during the selective inversion (the soft inversion pulse was ~1.3 ms long). At τ = 1 ms, m^{TBAT} decreased further to 0.831. Such rapid exchange between the spins rendered magnetisation transfer impractical for TBAT/FTPS systems in MeCN, at least at 300 K. Although shorter variable delays could be used in the experiments, very significant broadening of both TBAT and FTPS signals was observed (as presented in Figure 3.31c), which resulted in noisier data (Figure 3.31a–b, compared to inversion transfer in THF, Figure 3.11). Additionally, repeating the inversion transfer measurement of the sample two hours after the first one (*i.e.* three hours after preparation of the solution) gave an inversion transfer profile presented in Figure 3.31d, whereby the statistical distribution of magnetisation was reached prior to the measurement when τ = 1 ms.

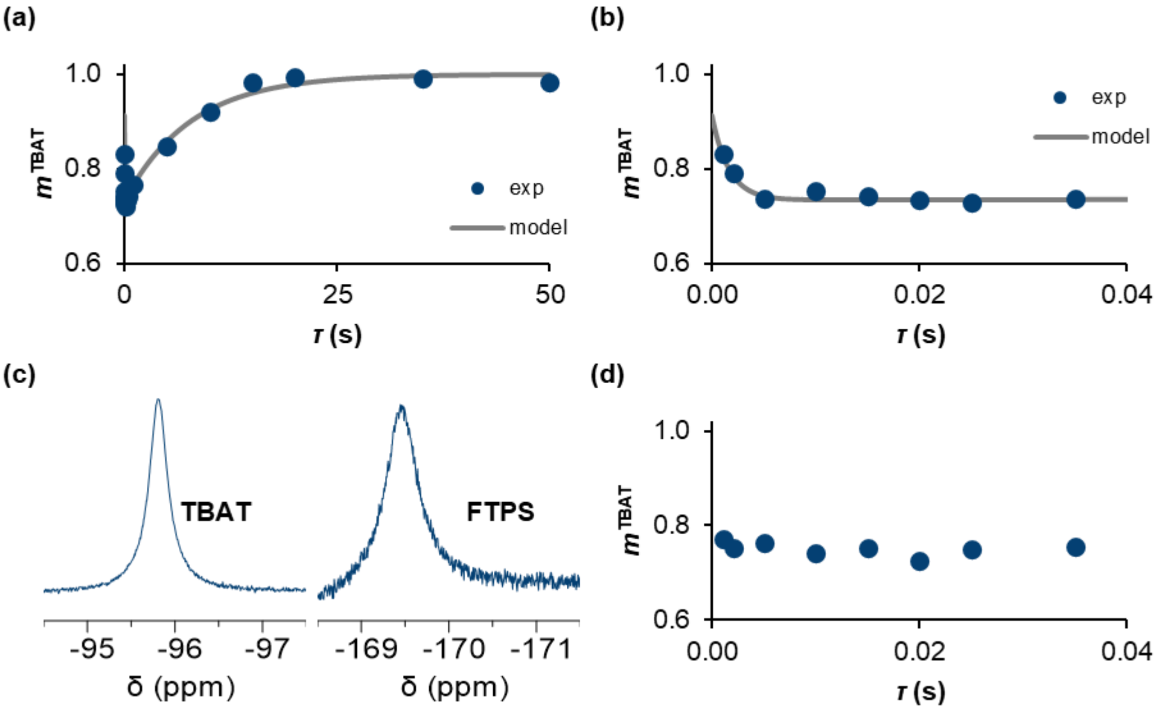

Figure 3.31: ^{19}F inversion transfer data from a solution of TBAT (48.8 mM) and FTPS (45.8 mM) in MeCN at 300 K. (a) A plot of experimental and model fractional magnetisation of TBAT, m^{TBAT}, against variable delay, τ, resulting from the selective inversion of FTPS. The chemical exchange between the spins is extremely rapid compared to their longitudinal relaxation, $\alpha T_1^{\mathrm{obs}} \approx 1500$. (b) An expansion of the plot from (a) showing the first eight experimental datapoints (τ < 40 ms). (c) Both TBAT and FTPS exhibited a very significant line broadening in the ^{19}F NMR spectrum of the solution (the spectrum was phase- but not baseline-corrected). (d) After two hours, the transfer rate in the sample increased to an extent that a statistical distribution of the magnetisation was reached before the τ = 1 ms time point (the last datapoint, τ = 50 s was used as the equilibrium integral for conversion into m^{TBAT}, and the τ < 40 ms part of the plot is presented).

Based on the observations discussed in Section 3.3.3, we envisaged that in the presence of D*t*BP and MS, the inversion transfer rate in the system would decrease over time, eventually reaching a plateau, analogous to systems in THF. Therefore, half of the solution prepared for the experiment above was transferred to a J Young® valve capped NMR tube preloaded with MS (~40 mg), and D*t*BP (~20 mM) added *via* a microsyringe. Indeed, the first measurement showed a significant, four-fold decrease in the inversion transfer rate, $\alpha(r + 1) = 149\ s^{-1}$ ($I_{eq} = 1155$, $x = 702$, $x' = 753$, $R = 10$), Figure 3.32a–b. This impressive decrease was confirmed by the appearance of the signals, Figure 3.32b, which exhibited less broadening (^{29}Si satellites were observed for both signals, *cf*. Figure 3.31c). An initial decrease of $\alpha(r + 1)$ was observed as expected. However, as opposed to plateauing, the exchange rate reached a minimum for $t \approx 7$ h prior to increasing with time again.

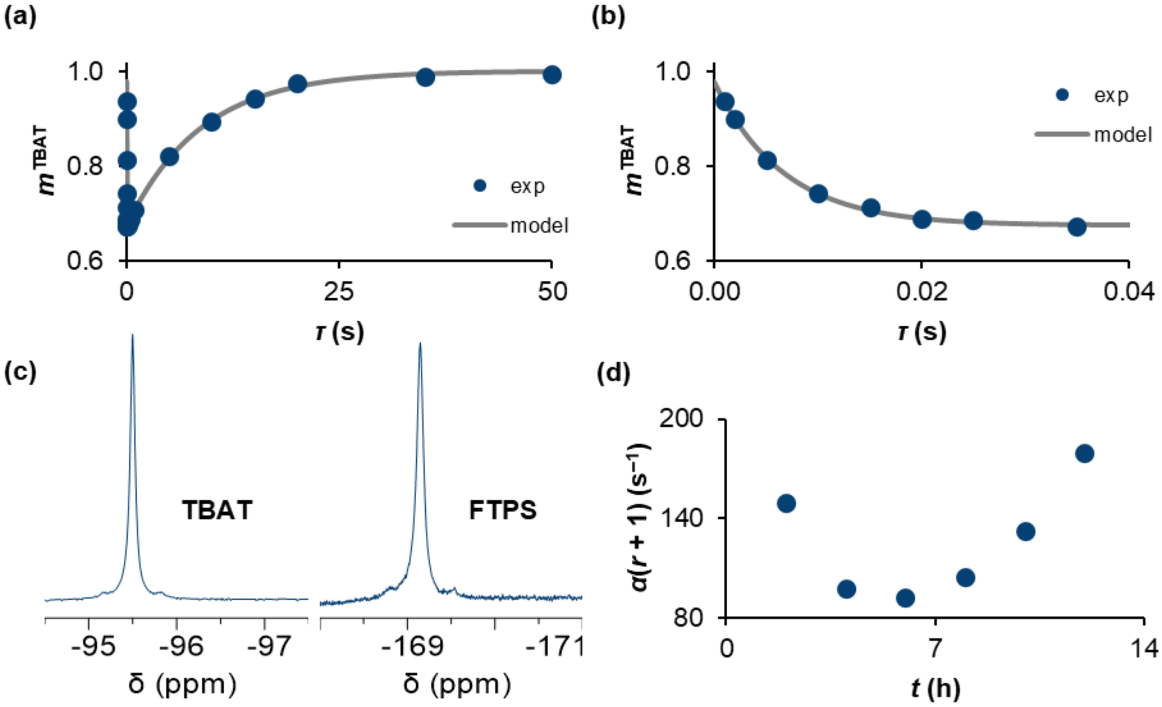

Figure 3.32: ^{19}**F inversion transfer data from a solution of TBAT (48.8 mM) and FTPS (45.8 mM) in MeCN at 300 K, in the presence of D*t*BP and MS. (a) A plot of experimental and model fractional magnetisation of TBAT, m^{TBAT}, against variable delay, *τ*, resulting from the selective inversion of FTPS (first measurement for the sample). The chemical exchange between the spins was slower compared to the system in the absence of these additives. (b) An expansion of the plot from (a) showing the first eight experimental datapoints (τ < 40 ms). (c) Both TBAT and FTPS exhibited far less line broadening in the** ^{19}**F NMR spectrum of the solution (the spectrum was phase- but not baseline-corrected). (d) Temporal evolution of the inversion transfer between the spins. An initial decrease in the exchange rate was followed by a minimum and subsequent increase, as opposed to the expected plateau.**

All these observations indicated that the TBAT/FTPS spin system in MeCN was unsuitable for interrogating the proposed exchange pathways. Therefore, we sought a different fluoride acceptor to study the fluoride transfer from TBAT in MeCN, as detailed in Section 3.4.

3.4. TBAT/ARSF exchange

3.4.1. Magnitude of exchange rate and inhibition by FTPS

Sharpless *et al*. reported that aryl fluorosulfates undergo rapid fluorine exchange in the presence of several fluoride sources, including TBAT (Scheme 1.8 in Section 1.2.3).[192] They proposed that the rapid equilibrium exchange is associative with respect to the sulfur centre and that the equilibrium position of the fluoride addition is shifted towards the neutral ester. Therefore, the exchange can be approximated to concerted substitution. The observed rate constant of exchange between 180 mᴍ TBAT and 18 mᴍ phenyl fluorosulfate ($PhOSO_2F$, **1.52**) in MeCN-d_3 was reported as 0.067 s^{-1} at 298 K. Hence, a commercially available aryl fluorosulfate, 2-naphthalenyl fluorosulfate (ARSF), was used as a second exchanging partner to TBAT in this study (Figure 3.33a).

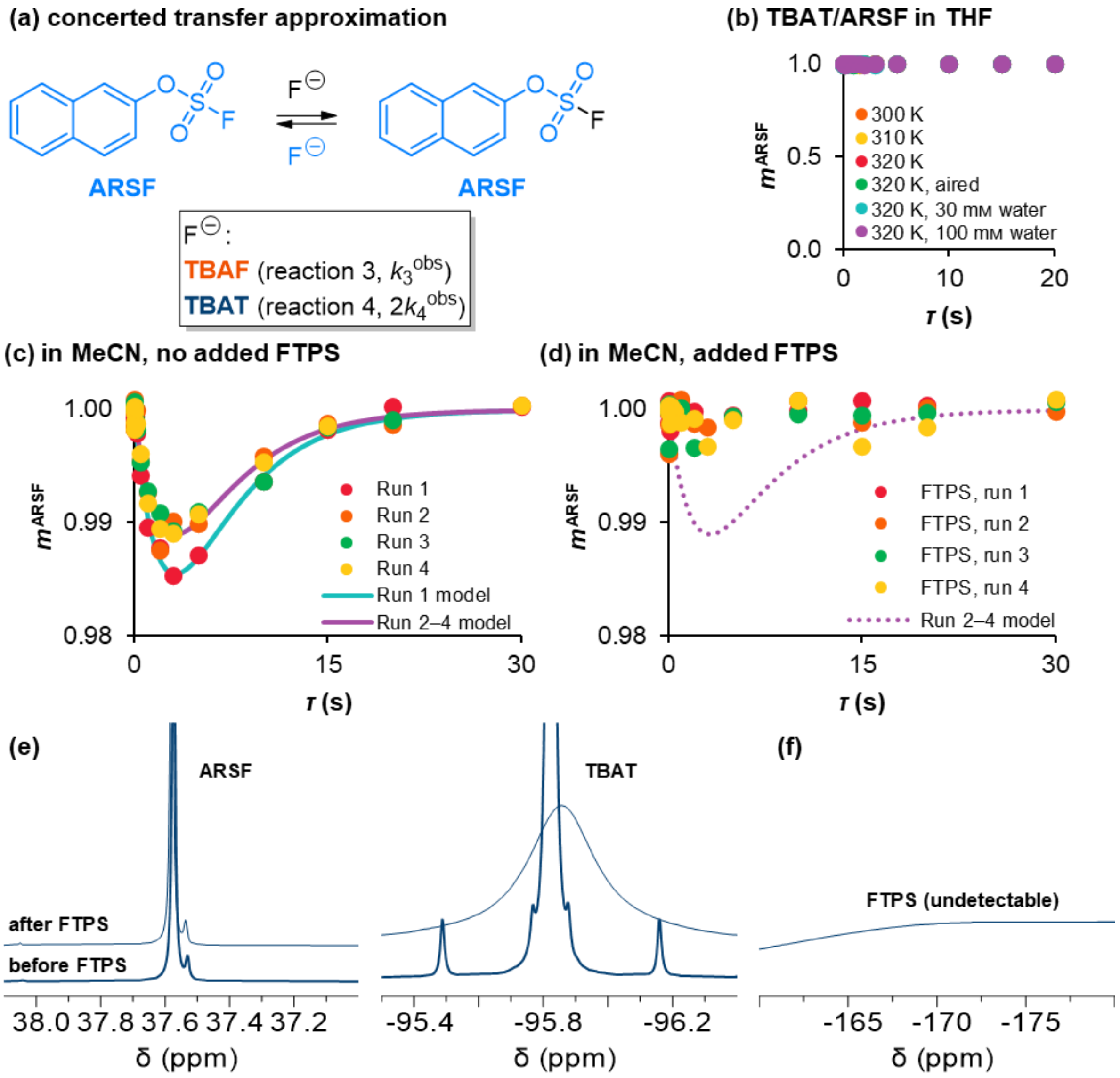

Figure 3.33: (a) Reaction scheme for a concerted approximation of the fluoride transfer between TBAT and ARSF, where the active fluoride donor may be TBAT and/or TBAF. (b) Magnetisation transfer between the spins was not detected in THF. (c) Magnetisation transfer between the spins was observed in MeCN and (d) proved to be inhibited by addition of a small amount of FTPS to the solution. (e) The ^{19}F NMR signal of ARSF did not exhibit line broadening upon addition of FTPS unlike that of TBAT. (f) The FTPS spin was too broad to detect.

When TBAT (196 mM) and ARSF (54.0 mM) were mixed in THF, no exchange was detected between the spins at 300 K, 310 K and 320 K. Neither opening the system to air, nor the addition of water (twice, ~30 mM and ~100 mM total [H_2O], respectively), resulted in detection of any magnetisation transfer in the TBAT/ARSF system in THF (both these operations were found to catalyse TBAT/FTPS exchange in THF, Section 3.3.2). As presented in Figure 3.33b, the (fractional) magnetisation of ARSF was unaffected by the inversion of TBAT in all six experiments. Individual m^{ARSF} profiles for $\tau \leq 0.5$ s are presented in the experimental section (Figure 5.15 in Section 5.6.1).

Magnetisation transfer was detected in MeCN at 300 K (inversion of 188 mM TBAT and detection of 52.3 mM ARSF), albeit on a significantly slower timescale than the exchange between TBAT and FTPS in THF or in MeCN. Figure 3.33c illustrates the extent of the inversion transfer in the system. Four inversion transfer measurements were performed on the sample, over ~3 hours from its preparation (runs 1–4). Across the four experiments, the fractional magnetisation of ARSF only decreased to 97–98% of its equilibrium magnetisation, prior to subsequent recovery. The longitudinal relaxation time constants determined for TBAT and ARSF in the solution *via* ^{19}F non-selective inversion-recovery measurements (4.73 s and 2.33 s, respectively) were unequal and in excellent agreement with the corresponding constants for isolated spins under these conditions (4.77 s and 2.49 s, respectively). Both these observations confirmed that the exchange between TBAT and ARSF is very slow on the timescale of longitudinal relaxation of these spins at 300 K in MeCN. Nevertheless, the inversion transfer model derived in Section 2.4 (Equations 2.119, 2.110 and 2.111 – recalled below, where *r* is the ratio of equilibrium magnetisations of TBAT to ARSF) gave excellent fits to the four experimental datasets. Interestingly, the rate of exchange decreased slightly between the first and second measurement (a 24% decrease of α from $1.91 \cdot 10^{-3}$ s^{-1} to $1.44 \cdot 10^{-3}$ s^{-1}), and then remained constant across runs 2–4 (average $\alpha = 1.45 \cdot 10^{-3}$ s^{-1}).

2.119, recalled

$$M_z^{\mathrm{ARSF}} \approx \frac{r\alpha M_{\mathrm{eq}}^{\mathrm{ARSF}}\left(1 - m_0^{\mathrm{TBAT}}\right)}{\gamma}\left[e^{(\beta-\gamma)\tau} - e^{(\beta+\gamma)\tau}\right] + M_{z,\mathrm{eq}}^{\mathrm{ARSF}}$$

2.110, recalled

$$\beta = -\frac{\alpha(r+1) + \frac{1}{T_1^{\mathrm{TBAT}}} + \frac{1}{T_1^{\mathrm{ARSF}}}}{2}$$

2.111, recalled

$$\gamma = \frac{\sqrt{\left(\alpha + \frac{1}{T_1^{\mathrm{TBAT}}} - r\alpha - \frac{1}{T_1^{\mathrm{ARSF}}}\right)^2 + 4r\alpha^2}}{2}$$

As discussed in Section 2.4, α in the TBAT/ARSF system should be a decreasing function of [FTPS] for the dissociative pathway, and independent of [FTPS] for the direct transfer pathway. A small aliquot of FTPS was therefore added to the solution in the NMR tube (~4 mM added FTPS), and the inversion transfer measurements were repeated for the newly obtained system. As presented in Figure 3.33d, the inversion transfer between TBAT and ARSF was inhibited by the addition of FTPS to below the detection limit (the model fitted to runs 2–4 before FTPS addition is included in this plot for comparison). Individual m^{ARSF} profiles for the solution before and after FTPS addition are presented in the experimental section (Figure 5.16 in Section 5.6.2).

The extent of the inhibition, and thus the contributions of the dissociative and direct transfer pathways to the overall fluoride exchange between TBAT and ARSF in the solution, were estimated. Firstly, the average (stabilised) $\alpha = 1.45 \cdot 10^{-3}$ s^{-1} from runs 2–4 prior to the inhibition was used as the observed exchange rate constant in the system without added FTPS. Secondly, although qualitatively no exchange was observed in the FTPS-inhibited solution, the model (Equations 2.119, 2.110 and 2.111) was fitted to the four datasets. For the first two runs, the fittings gave $\alpha = 0$ (exactly). The third and fourth run gave $\alpha = 1.01 \cdot 10^{-4}$ s^{-1} and $\alpha = 2.23 \cdot 10^{-4}$ s^{-1}, respectively. Assuming that the "true" α for the inhibited system lies between these two values, the direct transfer pathway corresponded to 7–15% of the overall exchange in the system prior to inhibition. If the dissociative pathway was not fully "switched off" by the added FTPS, the contribution of the direct pathway was even smaller. Hence, the fluoride exchange between TBAT and ARSF in the system (prior to the inhibition) was estimated as ≥85% dissociative in character.

Furthermore, a visual examination of the appearance of ARSF and TBAT ^{19}F signals before and after the inhibition by FTPS (presented in Figure 3.33e) showed that whilst the ARSF signal remained (apparently) unaffected by addition of FTPS, that for TBAT exhibited very significant line broadening, analogously to that of TBAT/FTPS mixtures in MeCN, see Section 3.3.5. The FTPS spin itself was broadened to an extent which rendered it undetectable by ^{19}F NMR spectroscopy; see Figure 3.33f (no baseline correction was applied to the spectra in Figure 3.33e–f).

3.4.2. Temporal profile

The magnitude of the exchange rate described above is just above zero. Although sufficient to qualitatively observe inhibition by added FTPS, a subsequent experiment was performed at 335 K in order to increase the rate of inversion transfer for more accurate quantitative analysis. A solution of 204 mM TBAT and 73.3 mM ARSF in MeCN was prepared, and the exchange rate measured at 335 K over ~10 hours. Both species exhibited some decomposition, as presented in Figure 3.34. The data for

TBAT appears to be relatively noisy towards the later reaction times, possibly due to gradual broadening of the signal. Nevertheless, the concentrations of both species decreased by ~10 mM over the course of the experiment (it appears from the models that slightly more TBAT decomposes than ARSF, although it may be due to experimental error, see 5.6.3 for details).

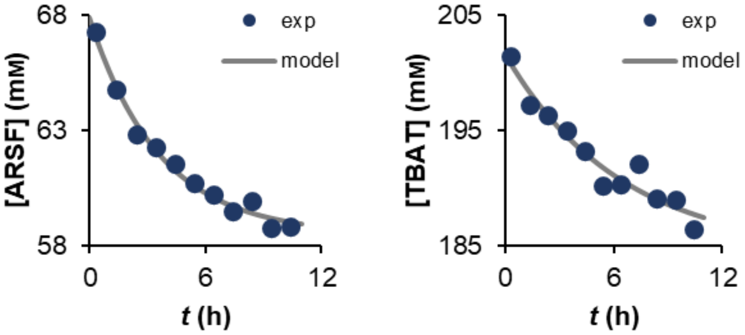

Figure 3.34: Apparent first-order decomposition of ARSF and TBAT in MeCN in a solution of the two species in MeCN, 335 K.

A rapid decomposition of phenyl fluorosilicate (an analogue of ARSF, **1.52**) in the presence of "anhydrous" TBAF was previously reported by Sharpless *et al*.[192] They proposed a defluorosulfation pathway, presented in Scheme 3.3. Similarly, we observed a gradual formation of two small signals resonating around the frequency of ARSF (Figure 3.35a; although their integrals did not make up for the decomposed ARSF and TBAT as presented in Figure 3.35b). We identified them as $^{-}OSO_2F$ (**3.3**), by spiking the sample with $KOSO_2F$ (Figure 3.35c); and SO_2F_2 (**3.2**), by analogy to the reported chemical shift. The by-product of TBAT decomposition, FTPS, was not observed in the spectra at any point, plausibly due to the line broadening of the signal. According to Sanford, fluorosulfates with electron-poor aryl moieties may be susceptible to nucleophilic aromatic substitution by fluoride.[224] Although we used 2-naphthalenyl fluorosulfate (ARSF) as the exchanging partner to TBAT, and 1-fluoronaphthalene (NAPH) as the internal standard, we tested the possibility of formation of NAPH in TBAT/ARSF systems in MeCN by preparing a sample according to the usual procedure, except in the absence of exogeneous NAPH. A ^{19}F NMR spectrum of the solution was acquired immediately and after approximately ten hours of keeping the sample at 335 K (Figure 3.35d). The previously observed decomposition products were observed, and no NAPH was detected in either spectrum.

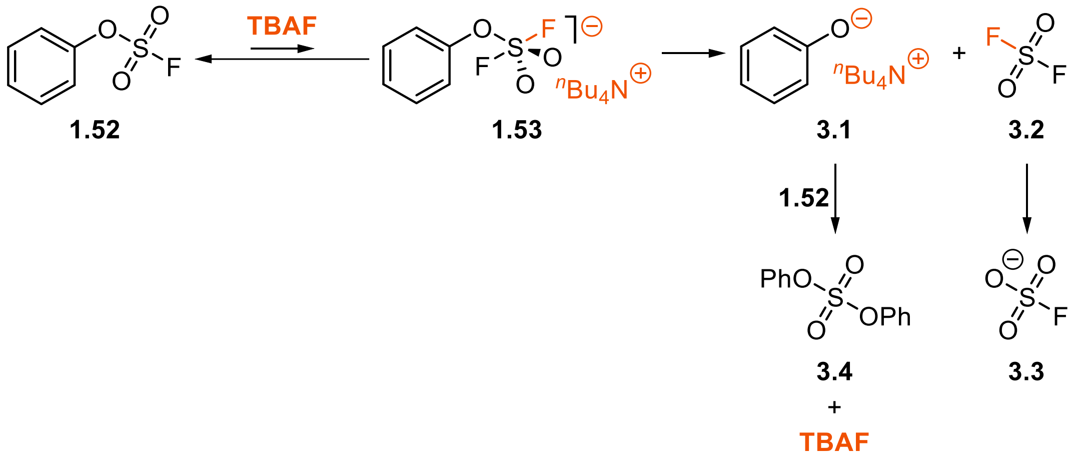

Scheme 3.3: Defluorosulfation of PhOSO$_2$F (1.52) in the presence of "anhydrous" TBAF, reported by Sharpless *et al.* [192]

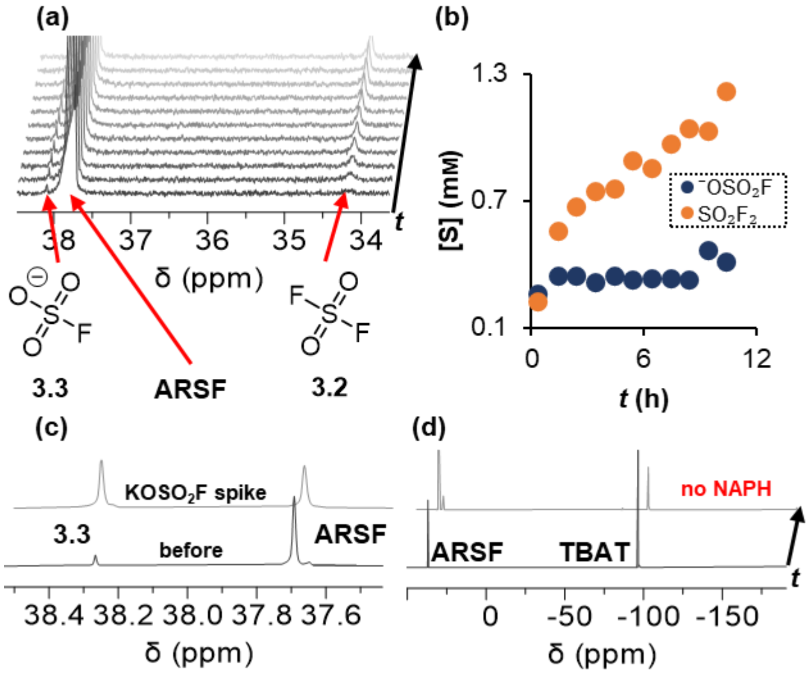

Figure 3.35: (a) ^{19}F NMR spectra of the TBAT/ARSF system in MeCN at 335 K, showing gradual decomposition of the species. Two new ^{19}F spins were observed, identified as $^-$OSO$_2$F (3.3) and SO$_2$F$_2$ (3.2). (b) The temporal evolution of the decomposition products. (c) Spiking of the solution with KOSO$_2$F. (d) Probing the formation of NAPH as a decomposition product.

Magnetisation transfer measurements on the system showed a decrease in the extent of inversion transfer in the solution over time (T_1^{TBAT} and T_1^{ARSF} were constant throughout the experiment, see Section 5.6.3 for details). In order to interrogate the exchange between the spins, α was first determined for each inversion transfer measurement, and the plot of α_t *vs* t is presented in Figure 3.36a. According to Equation 2.105, α is a linear function of [ARSF] and hence it is unsurprising that α_t decreased over time. However, the plot of α_t/[ARSF]$_t$ *vs* t in Figure 3.36b shows that

α_t decreased more rapidly than $[\text{ARSF}]_t$. From Equation 2.105, $\alpha/[\text{ARSF}]$ is independent of [TBAT] and [ARSF] for the direct exchange pathway, provided that the rate constant, k_4^{obs}, is independent of the changing conditions. For the dissociative pathway (again assuming that constants K_1^{obs} and k_3^{obs} are constant), $\alpha/[\text{ARSF}]$ depends on [TBAT] indirectly, as changing [TBAT] shifts the position of the dissociation equilibrium. Moreover, FTPS is a by-product of decomposition of TBAT, which also affects the equilibrium. Both these effects are governed by the presence of [FTPS] in the denominator of the dissociative pathway term in Equation 2.105. Therefore, here the plot of $\alpha_t/[\text{ARSF}]_t$ *vs* t is suggestive of at least a partially dissociative pathway, inhibited over time due to formation of FTPS from decomposing TBAT. The contributions of the dissociative and direct pathways and their temporal evolution were estimated in the following way. A three-parameter model as in Equation 2.107, was fitted to the experimental data, where: $K_1^{\text{obs}}k_3^{\text{obs}}$ and k_4^{obs} were the fitting parameters; α_t, $[\text{ARSF}]_t$ and $[\text{TBAT}]_t$ were known; and c^{FTPS} was the "initial concentration" of FTPS, *i.e.* the concentration of FTPS formed from decomposition of TBAT, $c^{\text{FTPS}} = [\text{TBAT}]_0 - [\text{TBAT}]_t$. The value of $K_1^{\text{obs}} \approx 0.0420$ mM was estimated based on the discrepancy between the concentration of TBAT weighed into the volumetric flask, $c^{\text{TBAT}} = 204$ mM, and $[\text{TBAT}]_0 = 201$ mM determined from the decomposition model (Section 5.6.3).

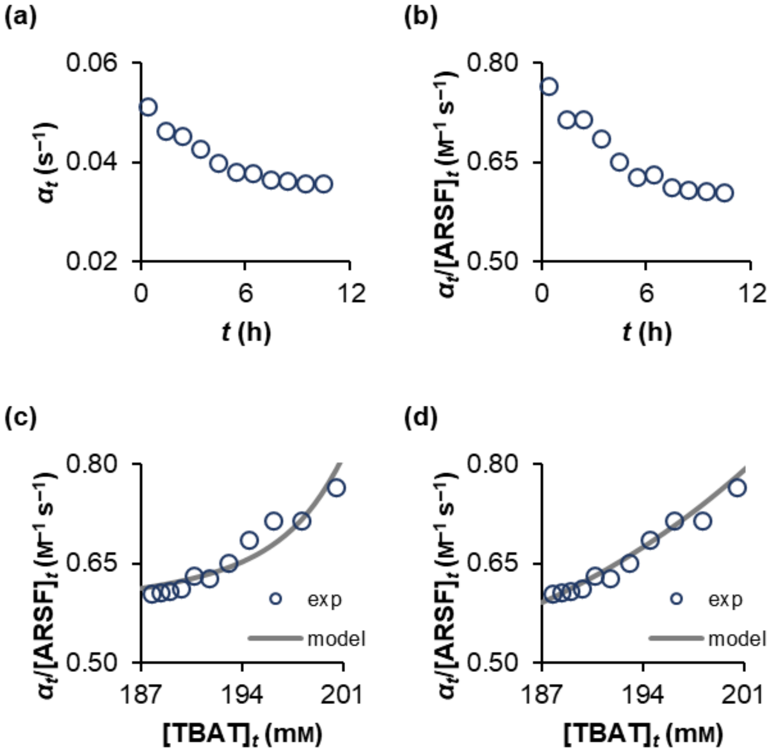

Figure 3.36: Plots of (a) *α vs t* and (b) *α*/[ARSF] *vs t* for the TBAT/ARSF system in MeCN, 335 K. (c) A simple dissociation model, where FTPS was formed both from the reversible dissociation of TBAT into FTPS and TBAF and irreversible decomposition of TBAT.

2.107, recalled

$$\alpha_t \approx [\mathrm{ARSF}]_t\left(\frac{K_1^{\mathrm{obs}}k_3^{\mathrm{obs}}}{c^{\mathrm{FTPS}}+\sqrt{(c^{\mathrm{FTPS}})^2+4K_1^{\mathrm{obs}}[\mathrm{TBAT}]_t}}+k_4^{\mathrm{obs}}\right)$$

This model gave a satisfactory fit to the experimental α_t/[ARSF]$_t$ data (Figure 3.36c), with $K_1^{\mathrm{obs}}k_3^{\mathrm{obs}} = 1.53 \cdot 10^{-3}$ s^{-1}, $k_4^{\mathrm{obs}} = 0.562$ M^{-1} s^{-1}, and the root mean square error, $R = 0.0168$ M^{-1} s^{-1}. Assuming this simple dissociation model, and based on the estimated value of K_1^{obs}, the total concentration of FTPS in the system increased from ~3.4 mM to ~14 mM between the first and the last inversion transfer measurement, where the contribution of the dissociation of TBAT to [FTPS] decreased from an initial 71% to 4% in the final run. The equilibrium concentration of TBAF, from TBAT dissociation, decreased from ~2.4 mM to ~0.55 mM. Considering that ~4 mM FTPS was undetectable in the system at 300 K (Section 3.4.1), these estimated concentrations of TBAF and FTPS could indeed be expected to remain below the detection limit at 335 K. Moreover, the ratio $k_3^{\mathrm{obs}}/k_4^{\mathrm{obs}} = 65.0$ confirms that TBAF is a significantly more potent fluoride donor (nucleophile) than TBAT. Most importantly, according to the model, the contributions of dissociative (*via* TBAF) and direct (*via* TBAT) transfer pathways were initially 28% and 72%, respectively (at t = 0.39 h). Over 10 hours (t = 10.4 h), the contribution of the dissociative pathway decreased to 9% (*cf*. 91% direct) due to the inhibition by formed FTPS.

Using K_1^{obs} as a third fitting parameter (Figure 3.36d) gave a better fit visually and with respect to the root mean square error, $R = 8.79 \cdot 10^{-3}$ M^{-1} s^{-1}. The fitting parameters were $K_1^{\mathrm{obs}}k_3^{\mathrm{obs}} = 0.0128$ s^{-1}, $k_4^{\mathrm{obs}} = 0.298$ M^{-1} s^{-1} and $K_1^{\mathrm{obs}} = 0.876$ mM. However, according to this model, the dissociation degree of TBAT was 6.2%, *i.e.* [TBAF] = 12 mM, in the initial run. This concentration may have indeed been undetectable in the ^{19}F NMR spectra at 335 K due to line broadening, but the decrease of [TBAT] would have been substantial. A decrease of the contribution of the dissociative pathway from the initial 61% to 50% in the final run would characterise the system in the case of this model.

Chapter 4

Conclusions and future work

4.1.1. Conclusions

This study was the first direct interrogation of the mechanism of fluoride transfer from TBAT in two solvents (THF and MeCN). We used a comprehensive set of methods in ^{1}H and ^{19}F NMR spectroscopy to describe the behaviour of TBAT in solution and the fluoride exchange between the reagent with two fluoride acceptors, FTPS and ARSF.

Firstly, we studied speciation of TBAT in solution with the emphasis on ion pairing and reversible cleavage of the Si–F bond. ^{1}H diffusion analysis of $Ph_3SiF_2^-$ and $^{n}Bu_4N^+$ showed strong ion pairing between the ions in THF-d_8 (300–320 K) and MeCN-d_3 (300–335 K), further confirmed by ^{1}H 1D NOESY. We then showed, *via* ^{19}F CEST experiments, that in both (non-deuteriated) solvents, TBAT dissociates reversibly into FTPS and TBAF, which are below the detection limit in ^{19}F pulse-acquire NMR spectroscopy, and where the latter may undergo further equilibria and/or decomposition (both these pathways leading to formation of TBABF). Therefore, we established that both direct (*via* TBAT) and dissociative (*via* TBAF) pathways of fluorine transfer from the reagent are plausible and moved onto kinetic studies of fluorine transfer between TBAT and FTPS *via* ^{19}F inversion transfer. We found that exchange between TBAT and FTPS in THF was rapid on the longitudinal relaxation timescale of the spins, leading to averaging of their longitudinal relaxation times. Although the system exhibited temporal instability with respect to exchange rate (*i.e.* gradually increasing) and a dramatic sensitivity to water (and perhaps slight changes in other conditions), we could stabilise it *via* addition of di-*tert*-butylpyridine and molecular sieve beads to the gas-tight system under N_2. In the stabilised system, the exchange was found to occur *via* both pathways in parallel, with the relative contributions of each pathway dependent upon the concentration of FTPS (or more generally, the electrophilic exchange partner). We also confirmed the presence of the dissociative pathway in the non-stabilised system by rapidly titrating a concentrated solution of TBAT with small amounts of FTPS, where the decrease in magnetisation transfer rate was greater than the inherent rate increases over time. The analogous system in MeCN underwent significantly more rapid fluoride exchange, approaching the limit of practicality of the measurement method. Moreover, both spins exhibited very significant line broadening and an increase in inversion transfer rate over time. Unlike the system in THF, the one in MeCN was not stabilised by the addition of base and molecular sieves, but rather the inversion transfer rate decreased initially, followed by an increase shortly afterwards. Thus, we confirmed by analysing solutions of TBAT that the cation and anion of the reagent are strongly paired in THF and MeCN, and that in both solvents TBAT dissociates into FTPS and TBAF (and exchanges with both these spins). Inversion transfer measurements in TBAT/FTPS systems confirmed that both the dissociative and direct transfer pathway contribute to the overall fluoride transfer from TBAT to FTPS, in THF. These findings are summarised in Scheme 4.1.

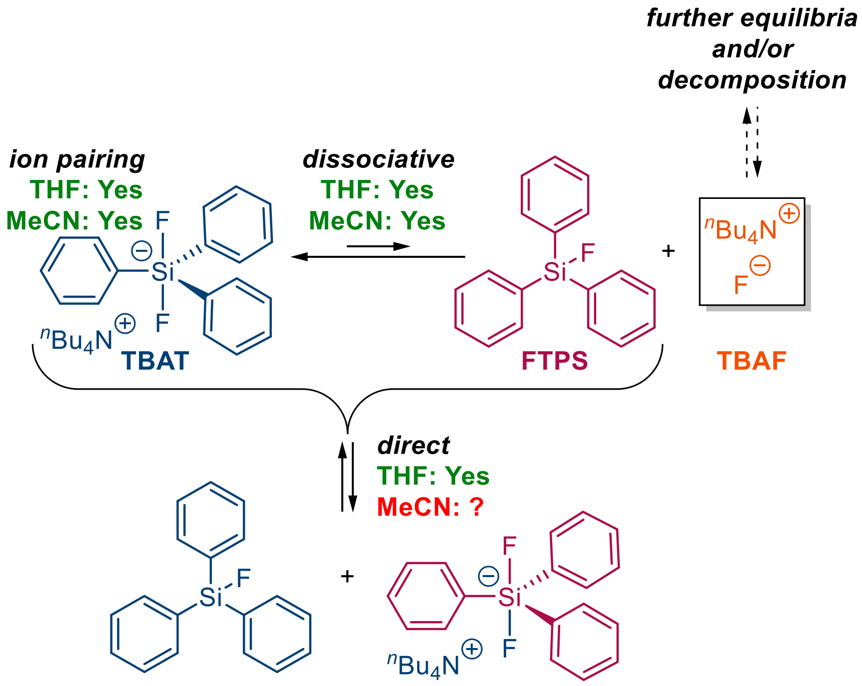

Scheme 4.1: Mechanistic conclusions drawn from the analysis of TBAT and TBAT/FTPS mixtures in THF and MeCN.

Although dissociation of TBAT was indeed confirmed in MeCN, we could not establish whether direct exchange pathway was present and if so, what the relative contributions of both pathways were. Therefore, exchange between TBAT and and a different fluoride acceptor, ARSF, was studied in this solvent. Inhibition of the inversion transfer between the spins (at 300 K) *via* addition a small amount of exogeneous FTPS confirmed that the dissociative exchange pathway was responsible for the fluoride transfer between the species in the system, at least partially – estimated at ≥85%. Due to very slow exchange in this system compared to the longitudinal relaxation of the spins, the subsequent experiment was performed at elevated temperature (335 K). Following the temporal evolution of the system over approximately ten hours showed gradual decomposition of both TBAT and ARSF. Two decomposition products of ARSF were observed, the fluorosulfate anion ($^{-}OSO_2F$) – confirmed by spiking the solution with $KOSO_2F$, and SO_2F_2 – by analogy, as phenyl fluorosulfate (**1.52**) was found in previous reports to partially decompose to SO_2F_2 (as well as $^{-}OSO_2F$) in the presence of TBAF.[192] In itself, the partial decomposition of ARSF to these products in the presence of TBAT was confirmative of the presence of TBAF in the system. Moreover, gradual inhibition of the exchange between TBAT and ARSF was observed, which we attributed to the formation of FTPS as a by-product of TBAT decomposition. The formation of “exogeneous” FTPS resulted in a temporal decrease of the degree of dissociation of TBAT and in turn, the concentration the unobservable TBAF. Although FTPS was not observed in the ^{19}F NMR spectra of the exchanging/decomposing system at any point (due to very significant signal broadening and overlap with baseline distortion), a simple equilibrium model, as presented in Scheme 4.2, gave a good fit to the observed exchange rate constants in the system. Based on the determined exchange parameters, the contributions of both fluoride transfer pathways were initially 28% dissociative and 72% direct transfer. Over the ten hour period, the contribution of the dissociative pathway decreased to 9% (*cf*. 91% direct) due to the progressive inhibition by FTPS. The magnetisation transfer measurements at two different temperatures (300 K and 335 K) also indicate the dependence of the relative contributions of both exchange pathways on temperature, an effect which may arise from different degrees of TBAT dissociation and/or ratios of the rate constants of reactions of TBAT and TBAF with ARSF, at these two temperatures.

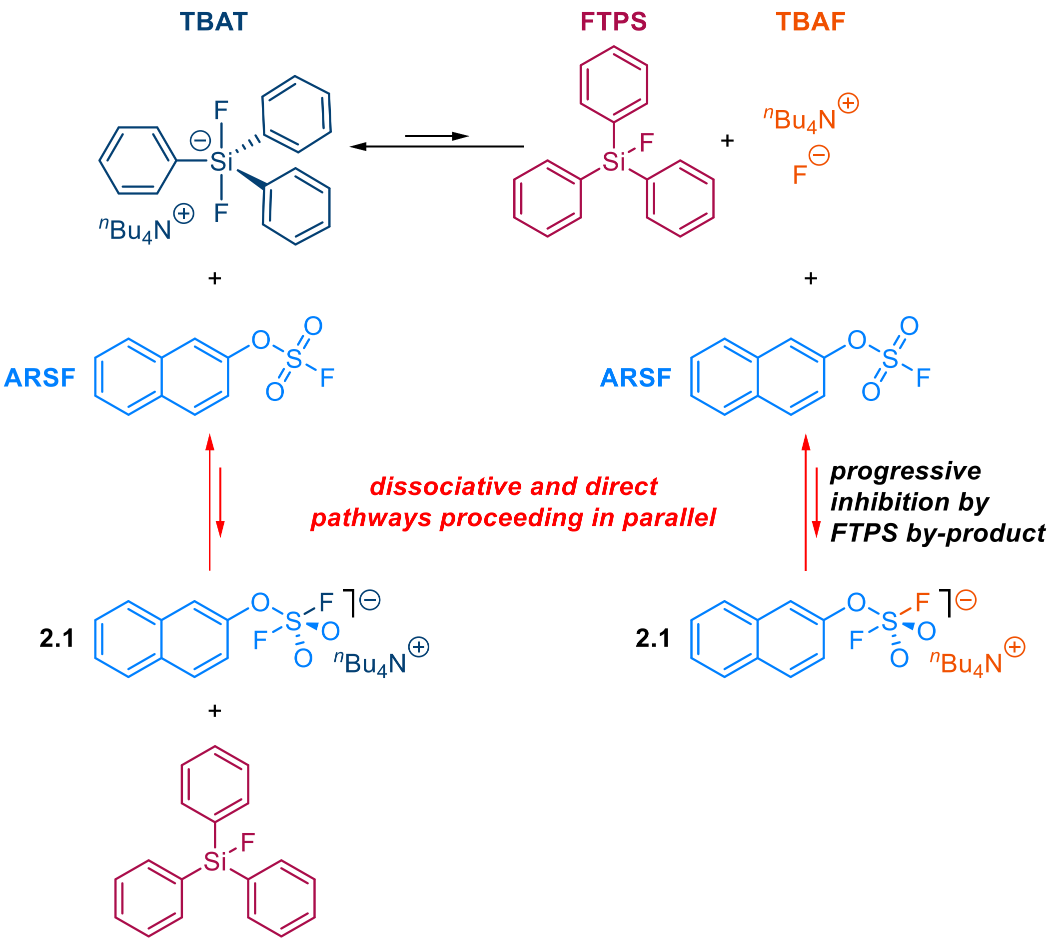

Scheme 4.2: Fluoride exchange between TBAT and ARSF was estimated as predominantly (at least 85%) dissociative in character (*i.e. via* TBAF) at 300 K in MeCN. At 335 K, gradual inhibition of the exchange was observed between the spins due to decomposition of TBAT into FTPS and as a result – a gradual decrease of the degree of its reversible dissociation, *i.e.* a decrease in [TBAF]. Due to the progressive inhibition of dissociative transfer, the contribution of the dissociative pathway decreased by nearly 70%, from approximately 30%, initially.

Overall, both dissociative and direct pathways were found as plausible fluoride transfer mechanisms in both THF and MeCN, although the dynamic behaviours of both TBAT/FTPS and TBAT/ARSF systems are vastly different in these two solvents, plausibly due to their different polarities, which affect the stabilisation of the ions and transition states. The relative contributions of each pathway depends on the fluoride acceptor and conditions.

4.1.2. Future work

Any (reliable) kinetic and mechanistic data may offer practical synthetic solutions for the reaction or reagent for which it is reported. Therefore, it is hoped that the characteristics and dynamic behaviour of TBAT reported herein will spark attempts at optimising reactions where the reagent is used. For example, whilst in many ways superior to TBAF, TBAT must often be used in super stoichiometric amounts. Perhaps the formation of FTPS as a by-product, and decomposition of TBAT reported in TBAT/ARSF system, are at least partially responsible for this issue, and hence stabilising the reagent against the decomposition, as well as removing FTPS from the reaction by additives irreversibly reacting with it, could be ways of overcoming it.

Moreover, this study could become a precedent for similar analyses for a range of difluorotriorganosilicates. The fluoride donor properties of these salts could be altered by changing the cation, or by a structural variation in the anion. A Hammett analysis could be conducted for derivatives of TBAT, however it may be complicated by the irreproducibility and instability of the exchanging systems. Finally, an analogue (or a series of analogues) of the reagent could perhaps be designed, where these complications are absent.

Lastly, the rapid exchange of fluorine between TBAT and FTPS represents a selection of a network of all possible pathways of fluorine transfer in solutions of the former, where, depending on conditions, several fluorine donors and/or acceptors may be present in equilibrium. In principle, fluorine can exchange in any donor-acceptor pair, *via* associative and/or interchange pathways. TBAT itself may be a fluorine acceptor in substitution or addition, where a hexacoordinate trifluorotriphenylsilicate is formed. This possibility may be of importance in catalytic systems, where low-concentration TBAT (in various possible equilibrium forms) often coexists with other Si–F species. Therefore, the plausibility of these other exchange pathways could be interrogated in systems of TBAT with ^{19}F spins other than FTPS. For example, $Ph_3SiF_2^-$/“F^-” systems (perhaps with 18-crown-6–K^+, likely to render the system air- and moisture-insensitive, as discussed in Section 1.2.3) could be used to interrogate the dissociative pathway analogously to TBAT/FTPS (as both “F^-” an FTPS are dissociation products of $Ph_3SiF_2^-$). However, these systems could also reveal direct $Ph_3SiF_2^-$/“F^-” exchange, where the silicate is a fluoride acceptor. This exchange pathway is invisible in TBAT/FTPS system studied herein, according to the steady-state approximation of the magnetisation of low-concentration TBAF (Section 2.3.4).

There are also some unknown issues with the NMR experiments presented throughout this study, which should be understood in order to prevent similar issues in other studies. Firstly, as discussed in Section 5.3.1, two ^{1}H diffusion analysis experiments failed to run with sufficiently long relaxation delays to ensure ≥99.3% recovery of the longitudinal magnetisations of the spins. Secondly, in one of the ^{19}F CEST experiments, the baseline changed (apparently) linearly with time during the acquisition. Lastly, although not critical for accurate integration, the NMR spectra acquired on samples in the presence of molecular sieves exhibited poor shimming, and it could be beneficial to design experimental procedures which would enable good shimming on such samples.

Chapter 5

Experimental

5.1. General information

5.1.1. Reagents and solvents

Reagents were obtained from commercial sources (TBAT and ARSF from Sigma-Aldrich; FTPS from Fluorochem; NaBARF from Thermo Scientific; ${}^{n}Bu_4NCl$ from VWR International). TBAT, ARSF and FTPS were stored in a nitrogen-filled glovebox (MBraun) and used as received. NaBARF and ${}^{n}Bu_4NCl$ were stored under ambient conditions and used as received. TBABARF was prepared by ion metathesis of NaBARF and ${}^{n}Bu_4NCl$ in water,[225] dried *in vacuo* and stored in the glovebox.

${}^{19}F$ NMR internal standards were obtained from commercial sources (NAPH from Fluorochem; PhF from Sigma-Aldrich), distilled, degassed (freeze-pump-thaw, five cycles) and stored in the glovebox under activated 3 Å molecular sieves for at least 72 hours prior to use. ${}^{1}H$ internal standard, TMB, was obtained from a commercial source (Sigma-Aldrich), stored in the glovebox and used as received.

THF (anhydrous and inhibitor-free) was dispensed from a solvent purification system (MBraun SPS-800, equipped with alumina columns under positive pressure of argon) fitted inside the glovebox and stored in the glovebox under activated 3 Å molecular sieves for at least 72 hours prior to use.[226] MeCN (anhydrous) was obtained from a commercial source (Sigma-Aldrich) and stored in the glovebox under activated 3 Å molecular sieves for at least 72 hours prior to use.[226]

Deuteriated solvents were obtained from commercial sources (THF-d_8, 99.5% D, and MeCN-d_3, 99.8% D, from Cambridge Isotope Laboratories; DMSO-d_6, 99.8% D, from VWR International) and stored in the glovebox under activated 3 Å molecular sieves for at least 72 hours prior to use.[226] Deionised water (RO grade) was sparged by nitrogen for 12 hours and used immediately.

Molecular sieves (3 Å beads, 1–2 mm) were obtained from a commercial source (Alfa Aesar), activated by heating in a microwave oven for 30 seconds, followed by cooling to room temperature *in vacuo* (five heating-cooling cycles) and stored in the glovebox.

Additives to solutions used in temporal stability experiments (other than 3 Å MS) were either obtained from commercial sources (D^{t}BP from Acros Organics; TMS_2O from Sigma-Aldrich), stored in the glovebox and used as received; or prepared in-house (powdered glass, prepared by manually grinding a Fisher Scientific borosilicate glass

Pasteur pipette, which was used for grinding as received; Figure 5.1) and stored in the glovebox.

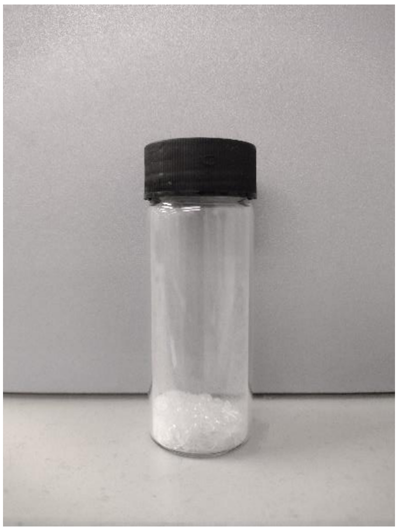

Figure 5.1: Powdered glass prepared from a Fisher Scientific borosilicate glass Pasteur pipette.

Room temperature corresponds to ~21 °C. Ambient conditions refer to a system (*e.g.* reaction mixture) open to air and kept at room temperature.

5.1.2. Sample preparation

Unless otherwise stated, solutions for measurements were prepared in the glovebox, in glassware dried according to the following procedure: all glassware (including the NMR tubes), as well as syringes, needles and spatulas were dried overnight in a vacuum oven (60–65 °C, 200 mbar) and transferred to the glovebox antechamber for two hours, prior to introducing them into the glovebox.

Unless otherwise stated, the solutions were prepared freshly by weighing the solutes directly into a 1 mL volumetric flask and dissolving them in the solvent up to the 1 mL mark. Where appropriate, the time of preparation of the solution was noted and times of the NMR measurements are reported relative to it. The solutions (~0.3–0.5 mL) were then transferred to (gas-tight) J Young® valve capped NMR tubes (GPE Scientific) and used for the NMR measurements. Any additives were added directly to the NMR tubes before or after the addition of the solution; or to the volumetric flask containing the solution before transferring it to the NMR tube.

Where a solution was titrated, aliquots were added directly to the NMR tube inside the glovebox, and the NMR tube shaken thoroughly (manually) for at least one minute before reinserting it in the probe. In titrations with solid aliquots, small vials (prepared by flame-sealing and detaching the upper part of a standard Norell borosilicate NMR tube) were used to aid the addition. In titrations with liquids, a 10 μL glass microsyringe was used.

5.1.3. NMR spectroscopy

All spectra were acquired on a Bruker Avance III 400 MHz NMR spectrometer equipped with a Prodigy cryoprobe (^{1}H 400 MHz, ^{19}F 377 MHz) in either manual or automation mode (without spinning). In ^{1}H NMR experiments, locking (tuned to ^{2}D frequency), tuning (^{1}H) and shimming (^{1}H) were performed prior to acquisition for each insertion of the sample into the probe and for each temperature change (in variable temperature experiments). In ^{19}F NMR experiments, the lock was off, shimming (^{1}H) and tuning (^{19}F) were performed prior to acquisition for each insertion of the sample into the probe and for each temperature change. The receiver gain was optimised for each NMR acquisition, regardless of acquisition mode. The probe temperature for each experiment is indicated in subsequent sections. MestReNova (versions 14.2.1 and 14.3.0) was used to process all data, except diffusion measurements, which were processed using Bruker's Dynamics Center (version 2.5.6). Chemical shifts are reported in parts per million (ppm), relative to residual solvent signals for ^{1}H (THF-*d*$_{7}$ δ_{H} 1.72 ppm, 3.58 ppm; MeCN-*d*$_{2}$ δ_{H} 1.94 ppm; DMSO-*d*$_{5}$ δ_{H} 2.50 ppm) and to NAPH for ^{19}F (δ_{F} = –123.95 ppm). Where $^{1}\Delta^{19}$F(^{32}S,^{34}S) isotope shifts are observed, the chemical shift of the major signal (^{32}S^{19}F) is reported, followed by $^{1}\Delta^{19}$F(^{32}S,^{34}S).

Processing and analysis of the NMR spectra were performed individually (pulse-acquire, 1D NOESY) or in stack (inversion-recovery, CEST, selective inversion-recovery). First, chemical shifts of the signals were referenced as described above. The spectra were then phase- and baseline-corrected, as follows, and the appropriate signals integrated. To each ^{1}H NMR spectrum, a manual zero-order phase correction was applied, with the centre of the spectrum used as pivot. A Whittaker smoother baseline correction was then applied on the entire spectral window with an auto-detected filter and smooth factor. To each ^{19}F NMR spectrum, manual zero- and first-order phase corrections were applied, with the highest intensity signal (of the signals of interest) used as pivot; in selective inversion-recovery NMR spectra, the initially non-inverted signal was used as pivot; and only zero-order phase correction was applied in the NMR spectra where one signal was of interest. A Whittaker smoother baseline correction was then applied on a frequency range covering the signals, with auto-detected filter and smooth factor. Processing of the diffusion analysis NMR spectra is described in Section 5.2.3.

5.1.4. Data analysis and model fitting

Microsoft Excel was used in the analysis and plotting of all numerical data presented in this work. Where models were fitted to numerical data, non-linear regression was used with a number of parameters specified in the corresponding sections. The Solver add-in was used for this purpose (minimising sum of squares, by changing variable parameter cells). No constraints were placed on the fits and the solving method used was generalised reduced gradient (GRG) nonlinear. Root mean square error (herein referred to as R) was used to assess goodness of the non-linear fits, whereas R-squared (R^2) was used for linear fits. Where an average of several values was taken, it is given with a 95%-confidence interval.

5.2. NMR experiments

5.2.1. ^{1}H and ^{19}F pulse-acquire

Quantitative ^{1}H and ^{19}F NMR spectra were acquired using a standard pulse-acquire sequence (zg), where a relaxation delay, D_1, was followed by a hard π/2 pulse and acquisition (with t_{acq} acquisition time). $D_1 \geq 5T_1 - t_{acq}$ was used to achieve at least 99.3% longitudinal magnetisation recovery, where T_1 was the longest longitudinal relaxation time constant among spins of interest in the system. Due to a broad frequency range of ^{19}F nuclei, quantification of each signal (TBAT, FTPS, ARSF, PhF) against the internal standard (NAPH) in a given system was performed in a separate experiment with the transmitter resonance placed at approximately the average frequency of that signal and NAPH. In each case, the spectral window was wide enough to cover both signals. The NMR parameters used in these experiments are given in subsequent sections.

In ^{19}F NMR spectra, the concentrations of the species of interest, [S], were calculated based on the concentrations of NAPH, [NAPH], and the integral ratios of the signals (I_{eq}^{S}/I_{eq}^{NAPH}), as presented in Equation 5.1 (n_F = 2 for TBAT; n_F = 1 for FTPS, ARSF and PhF).

5.1

$$[\mathrm{S}] = \frac{[\mathrm{NAPH}]I_{\mathrm{eq}}^{\mathrm{S}}}{n_{\mathrm{F}}I_{\mathrm{eq}}^{\mathrm{NAPH}}}$$

5.2.2. ^{1}H and ^{19}F inversion-recovery

^{1}H and ^{19}F longitudinal relaxation time constants, T_1, were determined using a standard non-selective inversion-recovery sequence (t1ir), where after a relaxation delay, D_1, a hard π pulse was used to invert the spins, followed by variable delay, τ. The resulting longitudinal magnetisations were detected using a hard π/2 pulse and acquisition (with t_{acq} acquisition time). This pulse sequence was repeated for a series of incremented variable delays, τ, which were optimised based on the longitudinal relaxation time constants of the spins. The first spectrum in each inversion-recovery experiment ($\tau = 0$) was discarded from data analysis due to phase distortion. $D_1 \geq 5T_1 - t_{\mathrm{acq}}$ was used to achieve at least 99.3% longitudinal magnetisation recovery, where T_1 was the longest longitudinal relaxation time constant among spins of interest in the system. Due to a broad frequency range of ^{19}F nuclei, the transmitter resonance in ^{19}F inversion-recovery experiments was placed according to the signals of interest in a given system. If two signals were measured in a single experiment, this was on approximately the average frequency of the two signals and if one signal was measured, this was on the frequency of the signal. In each case, the spectral window was wide enough to cover the signals. The NMR parameters used in these experiments are given in subsequent sections.

To the experimental integrals at each variable delay was fitted a three-parameter ($I_{\mathrm{eq}}^{\mathrm{S}}$, x, T_1^{S}) first-order longitudinal relaxation model, as presented in Equation 5.2, where I_{τ}^{S} is the integral of spin S at variable delay τ, $I_{\mathrm{eq}}^{\mathrm{S}}$ is the integral of spin S at magnetic equilibrium (*i.e.* fully recovered longitudinal magnetisation) and x is the correction parameter for imperfect inversion ($0 \leq x \leq 2$). The experimental and model integrals were then converted into fractional magnetisations (Equation 2.19).

5.2

$$I_{\tau}^{\mathrm{S}} = I_{\infty}^{\mathrm{S}}\left(1 - xe^{-\frac{\tau}{T_1^{\mathrm{S}}}}\right)$$

5.2.3. ^{1}H diffusion analysis

^{1}H diffusion analyses of the appropriate spins were performed using a longitudinal-eddy-current delay double stimulated-echo pulse sequence with a bipolar gradient pulse pair and two spoil gradients (ledbpgp2s; SINE.100 gradient pulses and spoil gradients, duration of gradient pulse: $\delta/2$ variable between experiments, duration of spoil gradient: 600 µs).[227] The delay for gradient recovery and eddy current suppression were of 200 µs and 5.00 ms, respectively. The diffusion time, Δ, and duration of gradient pulse, $\delta/2$, were optimised for each experiment and are given where appropriate. The pulse sequence was repeated for a series of gradient strengths, g. A relaxation delay $D_1 \geq 5T_1 - t_{\mathrm{acq}}$ was used to achieve at least 99.3% recovery of the longitudinal magnetisations of the spins, where T_1 was the longest of the longitudinal relaxation time constants of the spins of interest in a given system. The NMR parameters used in these experiments are given in subsequent sections.

The spectral sets were processed using the diffusion method in Bruker's Dynamics Center (version 2.5.6). Integration of the appropriate signals was performed manually as specified in subsequent chapters. To the experimental integrals at each gradient strength was fitted a two-parameter (I_0^{S}, D^{S}) model as presented in Equation 3.4. The experimental and model integrals were then normalised by dividing them by the determined I_0^{S}.

5.2.4. ^{1}H 1D NOESY

^{1}H 1D NOESY experiments were performed for two samples (TBAT in THF-d_8 and MeCN-d_3, 210 mM in each), using a standard 1D selective gradient NOESY pulse sequence (selnogp) with two gradient pulses in the selective refocusing period and two gradient pulses in the mixing period (SMSQ10.100, duration: 1.000 ms), a single frequency-selective refocusing π pulse in the selective refocusing period (Gaus1, duration: 8.820 ms, bandwidth: 100.0 Hz) and a single non-selective π pulse in the mixing period.[228–230] A delay for gradient recovery of 200 µs was used. A relaxation delay $D_1 \geq 5T_1 - t_{\mathrm{acq}}$ was used to achieve at least 99.3% recovery of the longitudinal magnetisations of the spins, where T_1 was the longest of the longitudinal relaxation time constants of the spins of interest in a given system (7 s for the sample in THF-d_8 and 30 s for one in MeCN-d_3). A mixing time of 0.5 s was used for THF-d_8 and 1.0 s for MeCN-d_3. The spectra were acquired with t_{acq} = 4.0 s, 4 dummy scans and 128 scans. The transmitter resonance was placed at 6.0 ppm, the centre frequencies for selective refocusing were 7.10 ppm and 8.03 ppm (in two separate experiments for each sample), and the spectral window was 20 ppm.

5.2.5. ^{19}F CEST

A standard CEST pulse sequence was used in ^{19}F chemical exchange saturation transfer (CEST) experiments.[231,232] After a relaxation delay, D_1, a series of n identical soft (frequency-selective) π/2 pulses (Gaus1, duration: 5.600 ms/pulse, bandwidth: 378.9 Hz) continuously saturated a selected frequency range over saturation time, t_{sat} = (5.600n) ms. The resulting longitudinal magnetisations were detected using a hard π/2 pulse and acquisition (with t_{acq} acquisition time). This pulse sequence was repeated for a series of frequency ranges. For each ^{19}F CEST experiment, t_{sat} was equal to the longitudinal relaxation time constant of TBAT in the given system, $t_{sat} = T_1^{TBAT}$ (1.10 s for the solutions in THF and 3.60 s – in MeCN); with n adjusted automatically to achieve this. $D_1 = 5T_1^{TBAT} - t_{acq} - t_{sat} = 4T_1^{TBAT} - t_{acq}$ was used to achieve 99.3% recovery of the longitudinal magnetisation of TBAT. The spectra were acquired with t_{acq} = 1.5 s acquisition time, 0 dummy scans, and 128 scans for the solutions in THF and 64 scans – in MeCN. The transmitter resonance was placed at –96 ppm, the spectral window was 200 ppm, and the frequency ranges were saturated from downfield to upfield.

The integrals, relative to an arbitrary baseline, were plotted against the centre frequencies of saturation pulses.

5.2.6. ^{19}F selective inversion-recovery

The pulse sequence used in ^{19}F selective inversion-recovery experiments is presented in Figure 1.4a (t1ir, modified by replacing the non-selective π pulse by a selective shaped π pulse). After a relaxation delay, D_1, a soft π pulse (iSnob, duration: 1.295 ms, bandwidth: 1.200 kHz) was used to selectively invert a range of frequencies, followed by variable delay, τ. The resulting longitudinal magnetisations were detected using a hard π/2 pulse and acquisition (with t_{acq} acquisition time). This pulse sequence was repeated for a series of incremented variable delays, τ, which were optimised based on the longitudinal relaxation time constants of the spins and the rates of exchange. The first spectrum in each selective inversion-recovery experiment ($\tau = 0$) was discarded from data analysis due to phase distortion. $D_1 \geq 5T_1 - t_{\text{acq}}$ was used to achieve at least 99.3% longitudinal magnetisation recovery, where T_1 was the longest longitudinal relaxation time constant among spins of interest in the system. The transmitter resonance was placed on one of the two exchanging signals (TBAT for TBAT/FTPS system and ARSF for TBAT/ARSF system). The centre of the soft π pulse was placed on the other signal in each system. The NMR parameters used in these experiments are given in subsequent sections.

In TBAT/FTPS solutions in THF, to the experimental integrals of TBAT at each variable delay was fitted a three-parameter ($M_{z,\text{eq}}^{\text{TBAT}}$, x, α) model as derived herein (Equations 2.78 and 2.54), where x is a pre-exponential term. The parameters r and T_1^{obs} were determined from ^{19}F pulse-acquire and ^{19}F inversion-recovery experiments. The experimental and model integrals were then converted into fractional magnetisations (Equation 2.19).

2.78, recalled

$$M_z^{\text{TBAT}} \approx \frac{M_{z,0}^{\text{TBAT}} - rM_{z,0}^{\text{FTPS}}}{r+1}\left[e^{-\alpha(r+1)\tau} - e^{-\frac{\tau}{T_1^{\text{obs}}}}\right] + M_{z,\text{eq}}^{\text{TBAT}} = x\left[e^{-\alpha(r+1)\tau} - e^{-\frac{\tau}{T_1^{\text{obs}}}}\right] + M_{z,\text{eq}}^{\text{TBAT}}$$

2.54, recalled

$$r = \frac{M_{z,\text{eq}}^{\text{TBAT}}}{M_{z,\text{eq}}^{\text{FTPS}}} = \frac{2[\text{TBAT}]}{[\text{FTPS}]} \approx \frac{2c^{\text{TBAT}}}{c^{\text{FTPS}}}$$

In TBAT/FTPS solutions in MeCN, to the experimental integrals of TBAT at each variable delay was fitted a four-parameter ($M_{z,\text{eq}}^{\text{TBAT}}$, x, x', α) model as derived herein (Equations 2.80 and 2.54), where x and x' are pre-exponential terms. The parameters r and T_1^{obs} were determined from ^{19}F pulse acquire and ^{19}F inversion-recovery experiments. The experimental and model integrals were then converted into fractional magnetisations (Equation 2.19).

2.80, recalled

$$\begin{aligned} M_z^{\text{TBAT}} &\approx \frac{M_{z,0}^{\text{TBAT}} - rM_{z,0}^{\text{FTPS}}}{r+1} e^{-\alpha(r+1)\tau} + \frac{r\left(M_0^{\text{TBAT}} + M_0^{\text{FTPS}} - M_{\text{eq}}^{\text{TBAT}}\right) - M_{\text{eq}}^{\text{TBAT}}}{r+1} e^{-\frac{\tau}{T_1^{\text{obs}}}} + M_{z,\text{eq}}^{\text{TBAT}} \\ &= xe^{-\alpha(r+1)\tau} - x'e^{-\frac{\tau}{T_1^{\text{obs}}}} + M_{z,\text{eq}}^{\text{TBAT}} \end{aligned}$$

In TBAT/ARSF system, to the experimental integrals of ARSF at each variable delay was fitted a three-parameter ($M_{z,\text{eq}}^{\text{ARSF}}$, m_0^{TBAT}, α) model as derived herein (Equations 2.119, 2.106, 2.110 and 2.111). The parameters r, T_1^{TBAT} and T_1^{ARSF} were determined from ^{19}F pulse acquire and ^{19}F inversion-recovery experiments. The experimental and model integrals were then converted into fractional magnetisations (Equation 2.19).

2.119, recalled

$$M_z^{\mathrm{ARSF}} \approx \frac{r\alpha M_{\mathrm{eq}}^{\mathrm{ARSF}}(1 - m_0^{\mathrm{TBAT}})}{\gamma}\left[e^{(\beta-\gamma)\tau} - e^{(\beta+\gamma)\tau}\right] + M_{z,\mathrm{eq}}^{\mathrm{ARSF}}$$

2.106, recalled

$$r = \frac{M_{z,\mathrm{eq}}^{\mathrm{TBAT}}}{M_{z,\mathrm{eq}}^{\mathrm{ARSF}}} = \frac{2[\mathrm{TBAT}]}{[\mathrm{ARSF}]} \approx \frac{2c^{\mathrm{TBAT}}}{c^{\mathrm{ARSF}}}$$

2.110, recalled

$$\beta = -\frac{\alpha(r+1) + \frac{1}{T_1^{\mathrm{TBAT}}} + \frac{1}{T_1^{\mathrm{ARSF}}}}{2}$$

2.111, recalled

$$\gamma = \frac{\sqrt{\left(\alpha + \frac{1}{T_1^{\mathrm{TBAT}}} - r\alpha - \frac{1}{T_1^{\mathrm{ARSF}}}\right)^2 + 4r\alpha^2}}{2}$$

5.3. ^{1}H diffusion analysis

5.3.1. Relative diffusion coefficients of $Ph_3SiF_2^-$ and $^nBu_4N^+$ (D^-/D^+) in solutions of TBAT in THF-d_8 and MeCN-d_3 (in the absence of internal standard)

Six solutions were prepared in the glovebox by weighing TBAT into vials and dissolving each sample in either THF-d_8 or MeCN-d_3 (~0.5 mL). The masses and resulting (approximate) concentrations of TBAT are presented in Table 5.1.

Table 5.1: Masses and concentrations of TBAT in solutions used for ^{1}H diffusion analyses.

Entry	Solvent	Mass of TBAT (mg)	Concentration of TBAT (mM)[a]
1	THF-d_8	58.6	220
2	THF-d_8	30.1	110
3	THF-d_8	8.76	30
4	MeCN-d_3	58.7	220
5	MeCN-d_3	32.7	120
6	MeCN-d_3	11.2	40

The solutions were transferred to J Young® valve capped NMR tubes. For each solution, ^{1}H inversion-recovery (Section 5.2.2) and ^{1}H diffusion analysis (Section 5.2.3) experiments were run at three temperatures: 300 K, 310 K and 320 K for solutions in THF-d_8; 300 K, 320 K and 335 K for solutions in MeCN-d_3. The ^{1}H

---

[a] To the nearest 10 mM.

inversion-recovery spectra were acquired with a D_1 = 20 s relaxation delay, t_{acq} = 4.0 s acquisition time, 0 dummy scans and 1 scan. The transmitter resonance was placed at 6.0 ppm and the spectral window was 20 ppm. The variable delays used in the experiments were, τ (s) {1, 2, 5, 7.5, 10, 12, 15, 20}. The ^{1}H inversion-recovery experiment was then repeated for the solutions in MeCN-d_3 due to incomplete relaxation of $Ph_3SiF_2^-$ for D_1 = 20 s. Unless stated otherwise, these new spectra were acquired with a D_1 = 60 s relaxation delay and the variable delays were, τ (s) {2, 5, 10, 15, 20, 30, 45, 60} (all other parameters remained unchanged. The ^{1}H diffusion analysis spectra were acquired with t_{acq} = 4.0 s acquisition time, 4 dummy scans, 8 scans for solutions in THF-d_8 and 4 scans for solutions in MeCN-d_3 (due to significantly longer relaxation delays). The transmitter resonance was placed at 6.0 ppm and the spectral window was 20 ppm. The pulse sequence was repeated for a series of 16 gradient strengths, g (G/mm) {0.170, 0.851, 1.19, 1.45, 1.68, 1.87, 2.05, 2.21, 2.37, 2.51, 2.64, 2.77, 2.89, 3.01, 3.13, 3.24}. The relaxation delay, D_1, was varied between the experiments based on longitudinal relaxation time constants of the spins (unless stated otherwise, $D_1 \geq 5T_1^- - 4.0$ s was used, where T_1^- was the longitudinal relaxation time constant of $Ph_3SiF_2^-$ determined for a given solution/temperature; as the anion relaxed more slowly than the cation among all datasets). Diffusion time, Δ, and duration of the gradient pulse pair, δ, were optimised for each experiment, and are presented below.

The ^{1}H inversion-recovery spectral sets were processed as described in Section 5.2.2. All signals corresponding to $Ph_3SiF_2^-$ were integrated together as total anion ("–") and all signals corresponding to $^nBu_4N^+$, as total cation ("+"). The determined ^{1}H longitudinal relaxation fitting parameters (I_{eq}, x and T_1) and root mean square errors (R) of $Ph_3SiF_2^-$ and $^nBu_4N^+$, as well as the plots of their experimental and model fractional magnetisations, m^- and m^+, against variable delay, τ, are presented in Section 7.4 (Table 7.2 and Figure 7.7–Figure 7.10). The ^{1}H diffusion analysis spectra were processed as described in Section 5.2.3. All signals corresponding to $Ph_3SiF_2^-$ were integrated together as total anion ("–") and all signals corresponding to $^nBu_4N^+$, as total cation ("+"). The determined ^{1}H diffusion fitting parameters (I_0 and D) and root mean square errors (R) of $Ph_3SiF_2^-$ and $^nBu_4N^+$ are presented in Table 5.2. The experimental and model I_g^-/I_0^- and I_g^+/I_0^+ against g are presented in Figure 5.2 (THF-d_8) and Figure 5.3 (MeCN-d_3).

Table 5.2: Variable NMR parameters (*Δ* and *δ*), ^{1}H diffusion fitting parameters and root mean square errors in ^{1}H diffusion analyses of $Ph_3SiF_2^-$ (“–”) and $^nBu_4N^+$ (“+”).

Entry	[TBAT] (mM)[a]	*T* (K)	*Δ* (ms), *δ* (ms)	$10^{-8}I_0$		*D* (mm^2/h)		$10^{-8}R$	
				–	+	–	+	–	+
1	220	300	100, 2.20	214	430	2.19	2.20	3	6
1	220	310	75.0, 2.20	199	421	4.07	4.13	2	5
1	220	320	75.0, 2.20	201	430	3.53	3.60	12	25
2	110	300	60.0, 2.20	205	440	4.96	5.05	1	1
2	110	310	75.0, 2.20	189	404	6.85	7.04	3	4
2	110	320	60.0, 2.00	189	418	19.4	19.2	2	5
3	30	300	75.0, 2.20	190	409	3.15	3.21	1	1
3	30	310	75.0, 2.20	180	393	3.76	3.84	1	3
3	30	320	60.0, 2.00	193	434	12.1	12.1	1	2
4	220	300	75.0, 2.20	112	248	4.85	4.65	1	3
4	220	320	75.0, 1.60[b]	101	238	11.7	11.8	3	6
4	220	335	75.0, 1.60[a]	98.5	237	21.2	21.9	5.7	14
5	120	300	75.0, 2.20	103	233	5.27	5.08	1	3
5	120	320	75.0, 1.60[a]	98.9	230	12.3	12.1	0.8	2
5	120	335	75.0, 1.60[a]	117	277	61.4	61.8	3	7
6	40	300	60.0, 2.00	94.5	216	5.62	5.44	0.6	1
6[c]	40	320	60.0, 2.00[a]	93.7	222	8.34	7.97	0.6	2
6[d]	40	335	60.0, 2.00	109	261	37.3	36.8	2	5

---

[a] To the nearest 10 mM.

[b] 2 scans in ^{1}H diffusion analysis experiment.

[c] For unknown reason, ^{1}H diffusion analysis experiment failed to run for $D_1 \geq 5T_1^- - 4.0$ s (53.9 s); D_1 was therefore decreased to 44.0 s, which resolved the issue and allowed for 98.4% longitudinal relaxation of $Ph_3SiF_2^-$.

[d] For unknown reason, ^{1}H diffusion analysis experiment failed to run for $D_1 \geq 5T_1^- - 4.0$ s (61.0 s); D_1 was therefore decreased to 44.0 s, which resolved the issue and allowed for 97.5% longitudinal relaxation of $Ph_3SiF_2^-$.

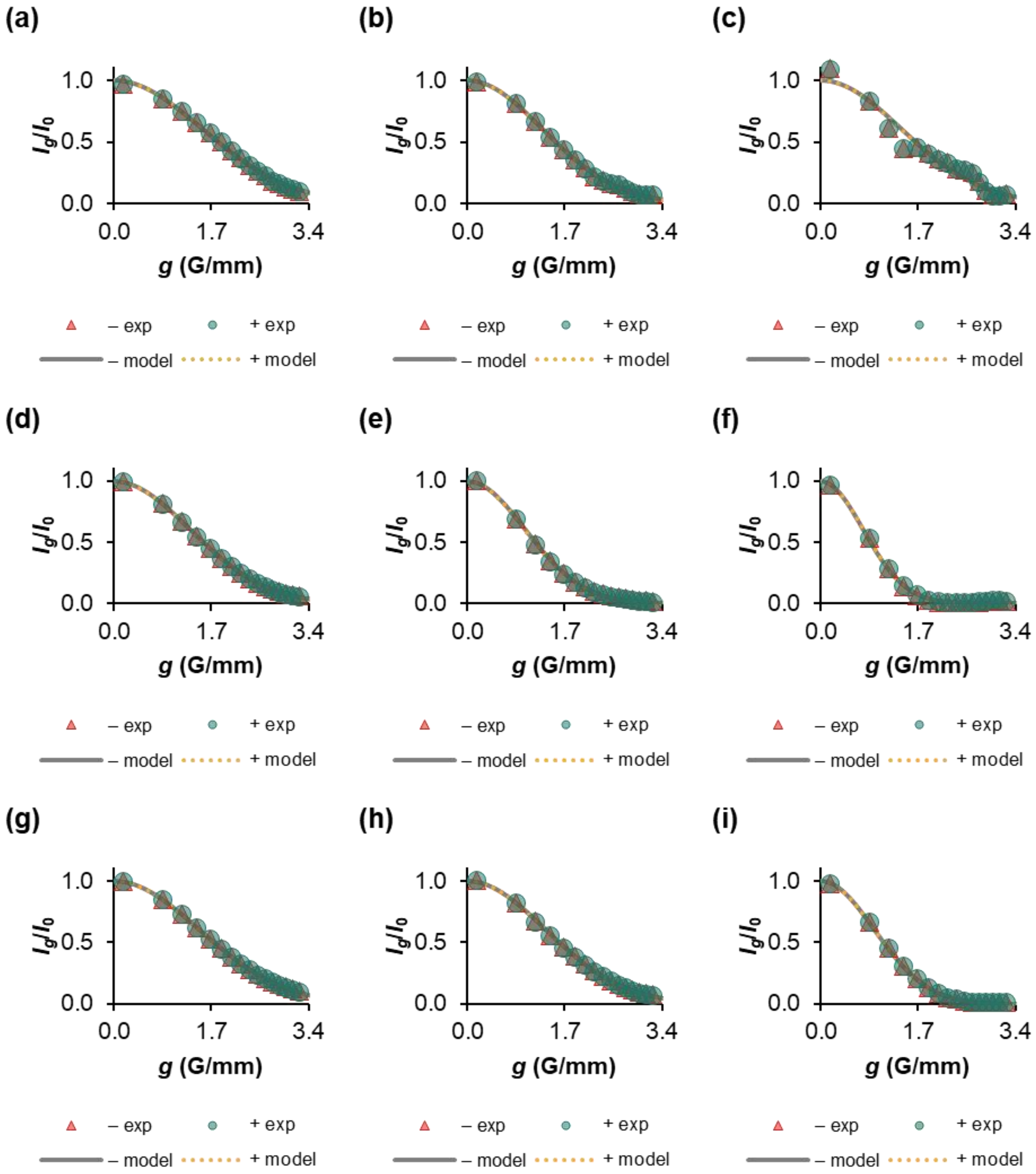

Figure 5.2: Plots of experimental (“exp”) and model I_g/I_0 of $Ph_3SiF_2^-$ (“–”) and $^nBu_4N^+$ (“+”) in ^1H diffusion analysis of TBAT in THF-d_8. (a) 220 mM at 300 K; (b) 220 mM at 310 K; (c) 220 mM at 320 K; (d) 110 mM at 300 K; (e) 110 mM at 310 K; (f) 110 mM at 320 K; (g) 30 mM at 300 K; (h) 30 mM at 310 K; (i) 30 mM at 320 K.

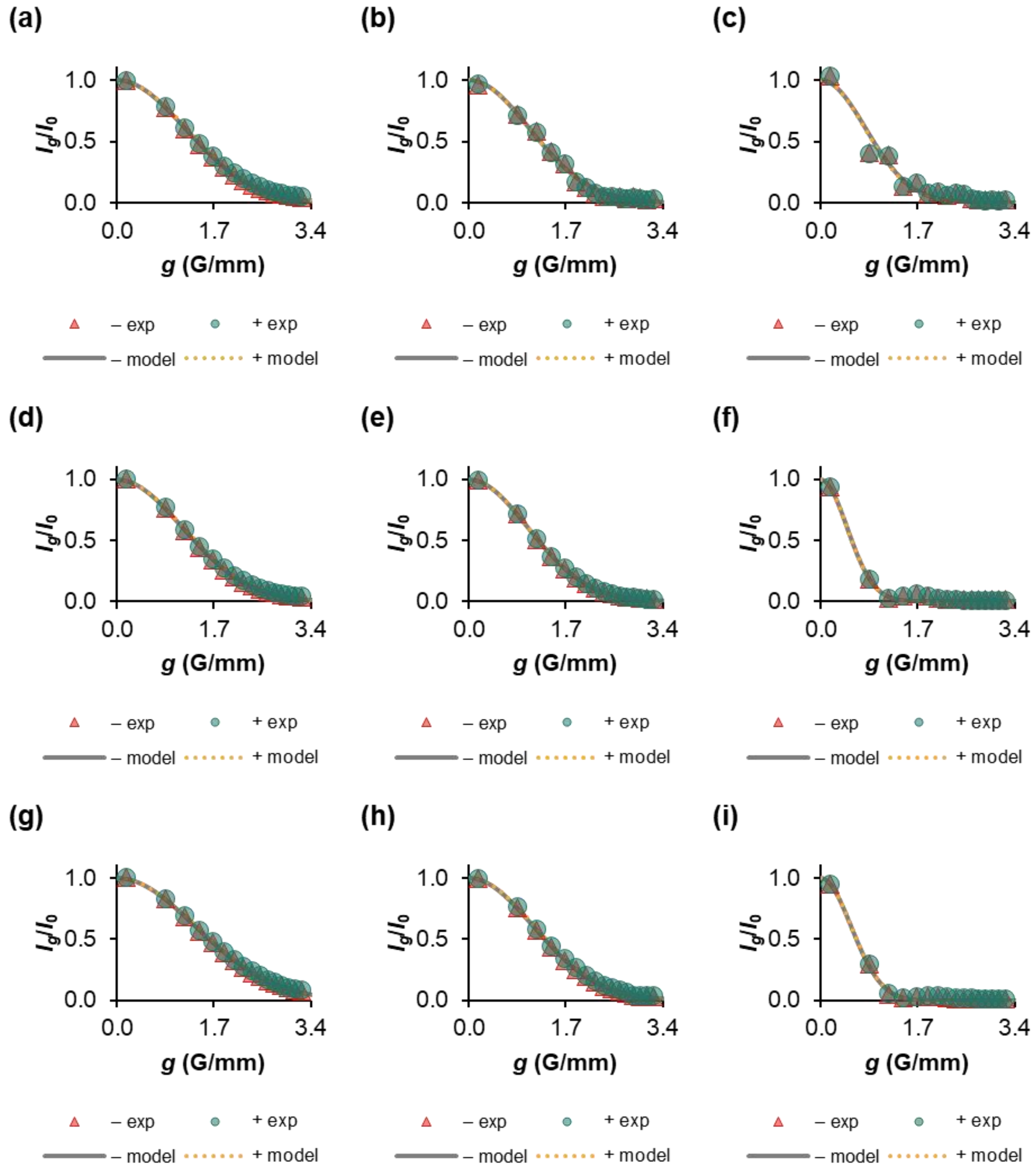

Figure 5.3: Plots of experimental (“exp”) and model I_g/I_0 of $Ph_3SiF_2^-$ (“–”) and $^nBu_4N^+$ (“+”) in ^{1}H diffusion analysis of TBAT in MeCN-d_3. (a) 220 mM at 300 K; (b) 220 mM at 320 K; (c) 220 mM at 335 K; (d) 120 mM at 300 K; (e) 120 mM at 320 K; (f) 120 mM at 335 K; (g) 40 mM at 300 K; (h) 40 mM at 320 K; (i) 40 mM at 335 K.

5.3.2. Diffusion coefficients of $Ph_3SiF_2^-$ and $^nBu_4N^+$ in solutions of TBAT in THF-d_8 and DMSO-d_6, relative to internal diffusion standard (TMB)

Two solutions were prepared in the glovebox by weighing TBAT and TMB into 1 mL volumetric flasks and dissolving them in THF-d_8 and DMSO-d_6, respectively, up to the 1 mL mark. The masses and amounts of TBAT and TMB, and the resulting concentrations in the solutions are presented in Table 5.3.

Table 5.3: Masses and concentrations of TBAT and TMB in solutions used for ^{1}H diffusion analyses.

Entry	Solvent	Mass (mg)		Concentration (mM)	
		TBAT	TMB	TBAT	TMB
1	THF-d_8	112	42.4	207	252
2[a]	DMSO-d_6	0.82	44.3	1.5	263

The solutions were transferred to J Young® valve capped NMR tubes. For each solution ^{1}H inversion-recovery (Section 5.2.2) and ^{1}H diffusion analysis (Section 5.2.3) experiments were run at 300 K. The ^{1}H inversion-recovery spectra were acquired with a D_1 = 20 s relaxation delay, t_{acq} = 4.0 s acquisition time, 0 dummy scans and 1 scan. The transmitter resonance was placed at 6.0 ppm and the spectral window was 20 ppm. The variable delays used in the experiments were, τ (s) {1, 2, 5, 7.5, 10, 12, 15, 20}. The ^{1}H diffusion analysis spectra were acquired with a D_1 = 12 s relaxation delay, t_{acq} = 4.0 s acquisition time, 4 dummy scans, 4 scans for the solution in THF-d_8 and 8 scans for the solution in DMSO-d_6. The transmitter resonance was placed at 6.0 ppm and the spectral window was 20 ppm. The pulse sequence was repeated for a series of 16 gradient strengths, g (G/mm) {0.170, 0.851, 1.19, 1.45, 1.68, 1.87, 2.05, 2.21, 2.37, 2.51, 2.64, 2.77, 2.89, 3.01, 3.13, 3.24}. Diffusion time, Δ, and duration of the gradient pulse pair, δ, were optimised for each experiment, and are presented below.

The ^{1}H inversion-recovery spectral sets were processed as described in Section 5.2.2. All signals corresponding to $Ph_3SiF_2^-$ were integrated together as total anion ("–") and three most upfield signals corresponding to ^{n}Bu$_4$N$^+$, as total cation ("+"). The determined ^{1}H longitudinal relaxation fitting parameters (I_{eq}, x and T_1) and root mean square errors (R) of $Ph_3SiF_2^-$ and ^{n}Bu$_4$N$^+$, as well as the plots of their experimental and model fractional magnetisations, m^- and m^+, against variable delay, τ, are presented in Section 7.4 (Table 7.3, Figure 7.11 and Figure 7.12). The ^{1}H diffusion analysis spectra were processed as described in Section 5.2.3. All signals corresponding to $Ph_3SiF_2^-$ were integrated together as total anion ("–") and all signals corresponding to ^{n}Bu$_4$N$^+$, as total cation ("+"). The methyl (CH_3) signal of TMB was used as internal diffusion standard (due to comparable longitudinal relaxation time to TBAT; Table 7.3, Figure 7.11 and Figure 7.12 in Section 7.4). The determined ^{1}H diffusion fitting parameters (I_0 and D) and root mean square errors (R) of $Ph_3SiF_2^-$,

---

[a] The mass and concentration of TBAT are given with two significant figures due to limit of balance accuracy.

^{n}Bu$_4$N$^+$ and TMB (CH$_3$) are presented in Table 5.4. The experimental and model I_g^-/I_0^-, I_g^+/I_0^+ and $I_g^{\mathrm{TMB}}/I_0^{\mathrm{TMB}}$ against g are presented in Figure 3.4.

Table 5.4: Variable NMR parameters (Δ and δ), ^{1}H diffusion fitting parameters and root mean square errors in ^{1}H diffusion analysis of Ph$_3$SiF$_2^-$ ("–"), ^{n}Bu$_4$N$^+$ ("+") and TMB (CH$_3$).

Entry	[TBAT] (mM)	T (K)	Δ (ms), δ (ms)	$10^{-8}I_0$		D (mm^2/h)		$10^{-8}R$	
				–	+	–	+	–	+
1[a]	207	300	100, 2.20	59.0	117	2.52	2.51	0.5	1
2[b]	1.5	300	100, 4.00	0.403	0.797	1.20	0.994	0.005	0.008

5.3.3. Diffusion coefficients of BARF$^-$ and ^{n}Bu$_4$N$^+$ in a solution of TBABARF in THF-d_8, relative to internal diffusion standard (TMB)

A solution was prepared in the glovebox by weighing TBABARF (222 mg, 201 mM) and TMB (43.0 mg, 256 mM) into a 1 mL volumetric flask and dissolving them in THF-d_8 up to the 1 mL mark. The solution was transferred to a J Young® valve capped NMR tube. ^{1}H inversion-recovery (Section 5.2.2) and ^{1}H diffusion analysis (Section 5.2.3) experiments were run at 300 K. The ^{1}H inversion-recovery spectra were acquired with a D_1 = 20 s relaxation delay, t_{acq} = 4.0 s acquisition time, 0 dummy scans and 1 scan. The transmitter resonance was placed at 6.0 ppm and the spectral window was 20 ppm. The variable delays used in the experiments were, τ (s) {1, 2, 5, 7.5, 10, 12, 15, 20}. The ^{1}H diffusion analysis spectra were acquired with a D_1 = 12 s relaxation delay, t_{acq} = 4.0 s acquisition time, 4 dummy scans and 4 scans. The transmitter resonance was placed at 6.0 ppm and the spectral window was 20 ppm. The pulse sequence was repeated for a series of 16 gradient strengths, g (G/mm) {0.170, 0.851, 1.19, 1.45, 1.68, 1.87, 2.05, 2.21, 2.37, 2.51, 2.64, 2.77, 2.89, 3.01, 3.13, 3.24}. Diffusion time, Δ, and duration of the gradient pulse pair, δ, were optimised, and are presented below.

The ^{1}H inversion-recovery spectral set was processed as described in Section 5.2.2. All signals corresponding to BARF$^-$ were integrated together as total anion ("–") and all signals corresponding to ^{n}Bu$_4$N$^+$, as total cation ("+"). The determined ^{1}H longitudinal relaxation fitting parameters (I_{eq}, x and T_1) and root mean square errors (R) of BARF$^-$ and ^{n}Bu$_4$N$^+$, as well as the plots of their experimental and model fractional magnetisations, m^- and m^+, against variable delay, τ, are presented in Section 7.4 (Table 7.4 and Figure 7.13). The ^{1}H diffusion analysis spectra were processed as described in Section 5.2.3. All signals corresponding to BARF$^-$ were

---

[a] $10^{-8}I_0^{\mathrm{TMB}} = 43.4$, $D_{\mathrm{T}}^{\mathrm{TMB}} = 5.39$ mm^2/h, $10^{-8}R^{\mathrm{TMB}} = 0.4$.

[b] $10^{-8}I_0^{\mathrm{TMB}} = 48.8$, $D_{\mathrm{T}}^{\mathrm{TMB}} = 1.70$ mm^2/h, $10^{-8}R^{\mathrm{TMB}} = 0.3$.

integrated together as total anion (“–”) and all signals corresponding to $^{n}Bu_4N^+$, as total cation (“+”). The methyl (CH_3) signal of TMB was used as internal diffusion standard. The determined ^1H diffusion fitting parameters (I_0 and D) and root mean square errors (R) of $BARF^–$, $^{n}Bu_4N^+$ and TMB (CH_3) are presented in Table 5.5. The experimental and model $I_g^–/I_0^–$, I_g^+/I_0^+ and I_g^{TMB}/I_0^{TMB} against g are presented in Figure 5.4.

Table 5.5: Variable NMR parameters (Δ and δ), ^1H diffusion fitting parameters and root mean square errors in ^1H diffusion analysis of $BARF^–$ (“–”), $^{n}Bu_4N^+$ (“+”) and TMB (CH_3).

Entry	[TBABARF] (mM)	T (K)	Δ (ms), δ (ms)	$10^{-8}I_0$		D_T (mm²/h)		$10^{-8}R$	
				–	+	–	+	–	+
9[a]	201	300	100, 2.20	36.7	86.7	2.78	2.99	0.7	1.6

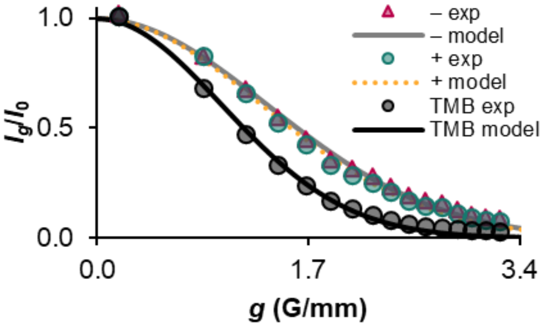

Figure 5.4: Plots of experimental (“exp”) and model I_g/I_0 of $BARF^–$ (“–”), $^{n}Bu_4N^+$ (“+”) and TMB (CH_3) in ^1H diffusion analysis of TBABARF and TMB in THF-d_8 (201 mM TBABARF, 256 mM TMB; 300 K).

5.4. ^{19}F longitudinal relaxation of TBAT, FTPS and ARSF

^{19}F longitudinal relaxation time constants of TBAT, FTPS and ARSF were measured in solutions of these species in THF and in MeCN (at 300 K in both solvents).

5.4.1. Variable-concentration ^{19}F longitudinal relaxation of TBAT

Solutions of TBAT in THF

Three solutions were prepared in the glovebox by weighing TBAT and NAPH into 1 mL volumetric flasks and dissolving them in THF up to the 1 mL mark. The masses of TBAT and NAPH, and the resulting concentrations in the solutions are presented in Table 5.6.

---

[a] $10^{-8}I_0^{TMB} = 36.6$, $D_T^{TMB} = 5.19$ mm²/h, $10^{-8}R^{TMB} = 0.8$.

Table 5.6: Masses, amounts and concentrations of TBAT and NAPH in the solutions of TBAT in THF.

Entry	Mass (mg)		Concentration (mᴍ)	
	TBAT	NAPH	TBAT	NAPH
1	5.13	27.0	9.50	185
2	32.1	30.8	59.5	211
3	76.0	77.3	141	529

The solutions were transferred to J Young® valve capped NMR tubes. For each solution, ^{19}F pulse-acquire (Section 5.2.1) and ^{19}F inversion-recovery (Section 5.2.2) experiments were run at 300 K. Each solution was then titrated with three solid aliquots of TBAT (all titrations were performed in the glovebox, as described in Section 5.1.2). ^{19}F pulse-acquire and ^{19}F inversion-recovery experiments were run (at 300 K) after each aliquot addition. The ^{19}F pulse-acquire NMR spectra were acquired with a D_1 = 40 s relaxation delay, t_{acq} = 1.5 s acquisition time, 0 dummy scans and 8 scans. The transmitter resonance was placed at –110 ppm and the spectral window was 120 ppm. The ^{19}F inversion-recovery NMR spectra for T_1^{TBAT} were acquired with a D_1 = 25 s relaxation delay, t_{acq} = 1.5 s acquisition time, 0 dummy scans and 1 scan. The transmitter resonance was placed at –96 ppm and the spectral window was 240 ppm. The variable delays used in the experiments were, τ (s) {0.2, 0.5, 1, 1.5, 2, 3, 5, 7.5, 10, 12.5, 15, 20}. The ^{19}F inversion-recovery experiments were repeated for the original three solutions to determine T_1^{NAPH}. These spectra were acquired with a D_1 = 50 s relaxation delay, t_{acq} = 1.5 s acquisition time, 0 dummy scans and 1 scan. The transmitter resonance was placed at –124 ppm and the spectral window was 240 ppm. The variable delays used in the experiments were, τ (s) {1, 2, 5, 7.5, 10, 12.5, 15, 20, 25, 30, 35, 40}.

The ^{19}F pulse-acquire NMR spectra were processed as described in Section 5.2.1 and the concentrations of TBAT (based on integral ratios of TBAT and NAPH), [TBAT], as well as chemical shifts of TBAT (referenced to NAPH), δ_F^{TBAT}, are presented in Table 5.7. An empirical model was fitted that describes δ_F^{TBAT} as a function of [TBAT] at 300 K (Equation 3.1 and Figure 5.5a; R = 0.03). The ^{19}F inversion-recovery spectral sets were processed as described in Section 5.2.2. The determined ^{19}F longitudinal relaxation fitting parameters (I_{eq}, x and T_1) and root mean square errors (R) are presented in Table 5.7. The plots of experimental and model fractional magnetisations, m^{TBAT}, against variable delay, τ, are presented in Figure 5.6 (the plots for NAPH are presented in Figure 7.14 in Section 7.5). An empirical model was fitted that describes T_1^{TBAT} as a function of [TBAT] at 300 K (Equation 3.2 and Figure 5.5b; R = 0.02).

Table 5.7: Chemical shifts, longitudinal relaxation fitting parameters and root mean square errors of TBAT in THF.

Entry	[TBAT] (mM)	δ_F^{TBAT} (ppm)	$10^{-3}I_{eq}^{TBAT}$	x^{TBAT}	T_1^{TBAT} (s)	$10^{-3}R^{TBAT}$
1[ab]	10.3	–96.76	1.30	1.85	2.00	0.00
1, aliq. 1[c]	17.4	–96.52	1.07	1.86	1.84	0.00
1, aliq. 2[d]	25.6	–96.31	0.797	1.86	1.74	0.004
1, aliq. 3	44.9	–96.01	0.685	1.87	1.58	0.002
2[e]	59.2	–95.85	0.950	1.85	1.52	0.003
2, aliq. 1	76.6	–95.73	1.22	1.84	1.47	0.00
2, aliq. 2	102	–95.60	1.60	1.84	1.41	0.00
2, aliq. 3	122	–95.53	1.89	1.84	1.37	0.00
3[f]	141	–95.43	2.20	1.84	1.28	0.01
3, aliq. 1	161	–95.39	2.50	1.83	1.27	0.01
3, aliq. 2	186	–95.35	2.82	1.83	1.23	0.01
3, aliq. 3	208	–95.32	3.15	1.83	1.22	0.02

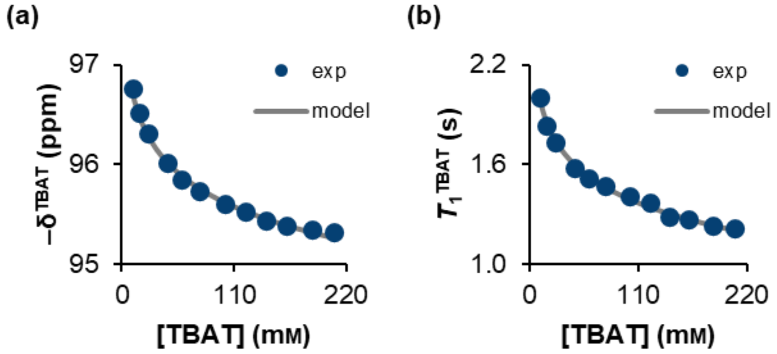

Figure 5.5: Plots of experimental (“exp”) and (empirical) model data for (a) chemical shift and (b) longitudinal relaxation time of TBAT in THF at 300 K.

---

[a] 8 scans in ^{19}F inversion-recovery experiment for T_1^{TBAT}.
[b] $10^{-3}I_{eq}^{NAPH} = 1.41$, $x^{NAPH} = 1.86$, $T_1^{NAPH} = 7.38$ s, $10^{-3}R^{NAPH} = 0.00$.
[c] 4 scans in ^{19}F inversion-recovery experiment for T_1^{TBAT}.
[d] 2 scans in ^{19}F inversion-recovery experiment for T_1^{TBAT}.
[e] $10^{-3}I_{eq}^{NAPH} = 1.53$, $x^{NAPH} = 1.85$, $T_1^{NAPH} = 7.07$ s, $10^{-3}R^{NAPH} = 0.00$.
[f] $10^{-3}I_{eq}^{NAPH} = 4.23$, $x^{NAPH} = 1.84$, $T_1^{NAPH} = 6.50$ s, $10^{-3}R^{NAPH} = 0.01$.

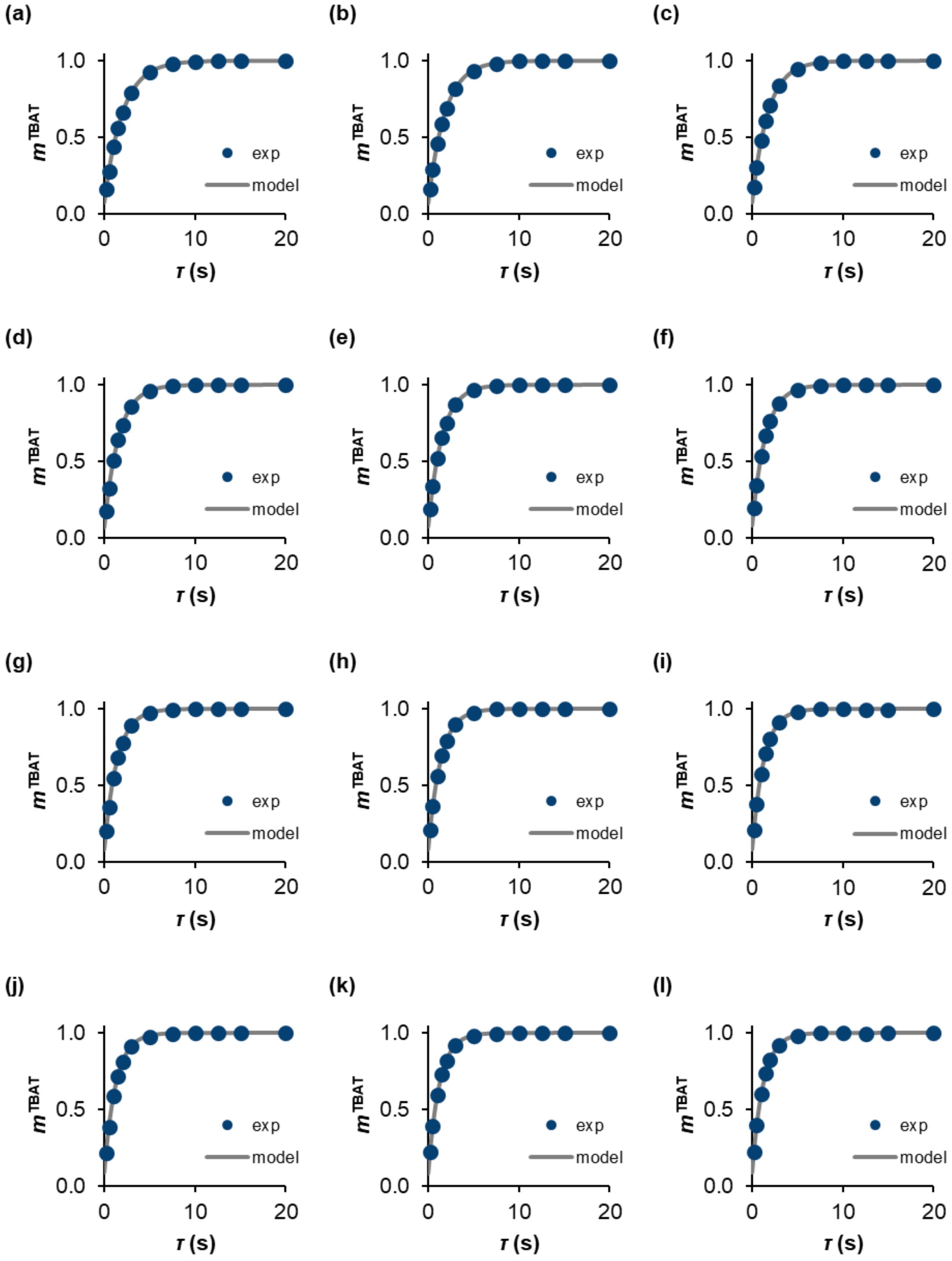

Figure 5.6: Plots of experimental (“exp”) and model fractional magnetisations of TBAT, m^{TBAT}, in ^{19}F longitudinal relaxation constant measurements of TBAT in THF at 300 K. (a) 10.3 mM; (b) 17.4 mM; (c) 25.6 mM; (d) 44.9 mM; (e) 59.2 mM; (f) 76.6 mM; (g) 102 mM; (h) 122 mM; (i) 141 mM; (j) 161 mM; (k) 186 mM; (l) 208 mM.

Solutions of TBAT in MeCN

Three solutions were prepared in the glovebox by weighing TBAT and NAPH into 1 mL volumetric flasks and dissolving them in NAPH up to the 1 mL mark. The masses and amounts of TBAT and NAPH, and the resulting concentrations in the solutions are presented in Table 5.8.

Table 5.8: Masses, amounts and concentrations of TBAT and NAPH in solutions.

Entry	Solvent	Mass (mg)		Concentration (mM)	
		TBAT	NAPH	TBAT	NAPH
1	MeCN	45.2	21.2	83.7	145
2	MeCN	89.8	23.2	166	159
3	MeCN	7.63	13.9	14.1	94.9

The solutions were transferred to J Young® valve capped NMR tubes. For each solution, ^{19}F pulse-acquire (Section 5.2.1) and ^{19}F inversion-recovery (Section 5.2.2) experiments were run at 300 K. Each solution was then titrated with three solid aliquots of TBAT (all titrations were performed in the glovebox, as described in Section 5.1.2). ^{19}F pulse-acquire and ^{19}F inversion-recovery experiments were run (at 300 K) after each aliquot addition. The ^{19}F pulse-acquire NMR spectra were acquired with a D_1 = 50 s relaxation delay, t_{acq} = 1.5 s acquisition time, 0 dummy scans and 1 scan. The transmitter resonance was placed at –110 ppm and the spectral window was 120 ppm. The ^{19}F inversion-recovery NMR spectra for T_1^{TBAT} were acquired with a D_1 = 50 s relaxation delay, t_{acq} = 1.5 s acquisition time, 0 dummy scans and 1 scan. The transmitter resonance was placed at –96 ppm and the spectral window was 120 ppm. The variable delays used in the experiments were, τ (s) {0.5, 1, 2, 3, 4, 5, 7, 10, 15, 20, 30, 40}.

The ^{19}F pulse-acquire NMR spectra were processed as described in Section 5.2.1 and the concentrations of TBAT (based on integral ratios of TBAT and NAPH), [TBAT], as well as chemical shifts of TBAT (referenced to NAPH), δ_F^{TBAT}, are presented in Table 5.9. Here, δ_F^{TBAT} = (–95.34 ± 0.01) ppm was independent of [TBAT] at 300 K (Figure 5.7a; there is a slight trend in the data whereby TBAT signal first moves downfield as its concentration increases, then upfield again; the changes are however very small and may be due to experimental/analysis error). The ^{19}F inversion-recovery spectral sets were processed as described in Section 5.2.2. The determined ^{19}F longitudinal relaxation fitting parameters (I_{eq}, x and T_1) and root mean square errors (R) are presented in Table 5.9. The plots of experimental and model fractional magnetisations,

m^{TBAT}, against variable delay, τ, are presented in Figure 5.8. An empirical model was fitted that describes T_1^{TBAT} as a function of [TBAT] at 300 K (Equation 3.3 and Figure 5.7b; R = 0.05).

Table 5.9: Chemical shifts, longitudinal relaxation fitting parameters and root mean square errors of TBAT in MeCN.

Entry	[TBAT] (mM)	δ_F^{TBAT} (ppm)	$10^{-3}I_{\mathrm{eq}}^{\mathrm{TBAT}}$	x^{TBAT}	T_1^{TBAT} (s)	$10^{-3}R^{\mathrm{TBAT}}$
1	79.4	–95.33	1.30	1.86	6.06	0.00
1, aliq. 1	98.8	–95.33	1.60	1.85	5.71	0.00
1, aliq. 2	121	–95.33	1.94	1.85	5.33	0.00
1, aliq. 3	142	–95.34	2.24	1.84	5.21	0.00
2	169	–95.35	2.63	1.84	4.94	0.00
2, aliq. 1	187	–95.35	2.89	1.83	4.83	0.01
2, aliq. 2	207	–95.36	3.15	1.84	4.65	0.01
2, aliq. 3	229	–95.36	3.43	1.83	4.46	0.01
3	14.1	–95.35	0.213	1.87	7.14	0.001
3, aliq. 1	34.0	–95.34	0.505	1.86	6.73	0.002
3, aliq. 2	53.4	–95.33	0.840	1.86	6.42	0.001
3, aliq. 3	72.7	–95.33	1.12	1.86	6.22	0.00

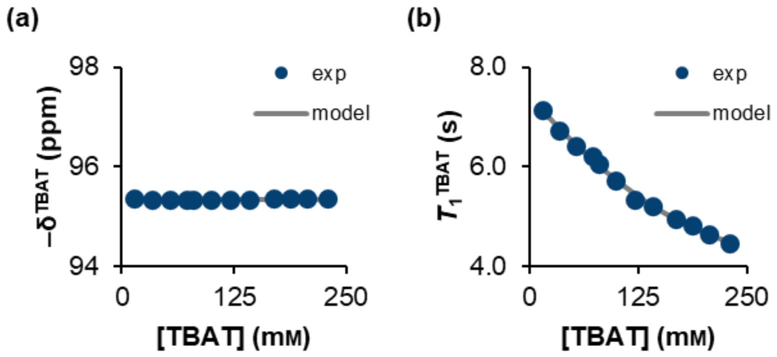

Figure 5.7: Plots of experimental (“exp”) and (empirical) model data for (a) chemical shift and (b) longitudinal relaxation time of TBAT in MeCN at 300 K.

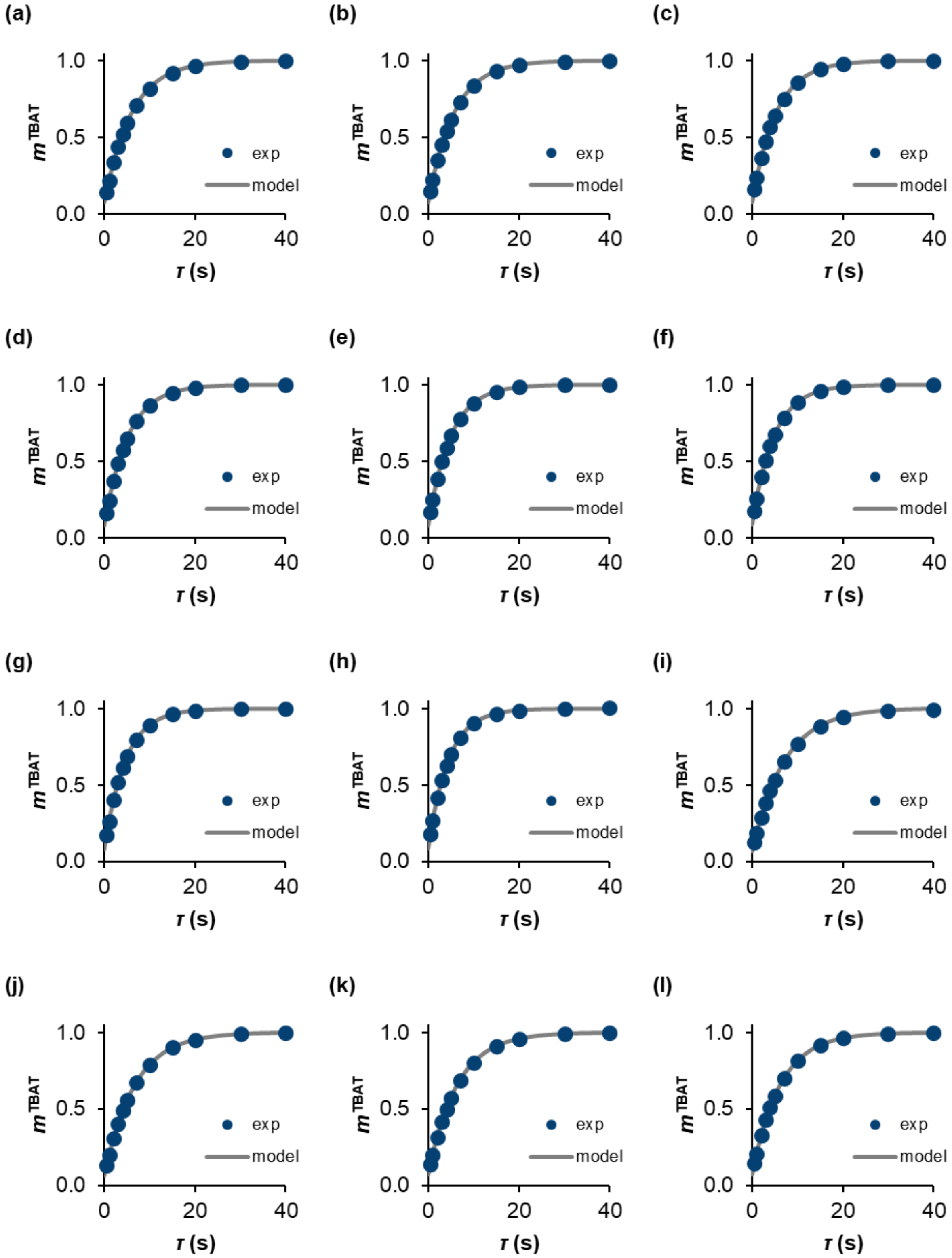

Figure 5.8: Plots of experimental (“exp”) and model fractional magnetisations of TBAT, m^{TBAT}, in ^{19}F longitudinal relaxation constant measurements of TBAT in MeCN at 300 K. (a) 79.4 mM; (b) 98.8 mM; (c) 121 mM; (d) 142 mM; (e) 169 mM; (f) 187 mM; (g) 207 mM; (h) 229 mM; (i) 14.1 mM; (j) 34.0 mM; (k) 53.4 mM); (l) 72.7 mM.

5.4.2. Variable-concentration ^{19}F longitudinal relaxation of FTPS

Solutions of FTPS in THF

Two solutions were prepared in the glovebox by weighing FTPS and NAPH into 1 mL volumetric flasks and dissolving them in THF up to the 1 mL mark. The masses and amounts of FTPS and NAPH, and the resulting concentrations in the solutions are presented in Table 5.10.

Table 5.10: Masses and concentrations of FTPS and NAPH in solutions.

Entry	Solvent	Mass (mg)		Concentration (mM)	
		FTPS	NAPH	FTPS	NAPH
1	THF	2.64	8.94	9.48[a]	61.2
2	THF	58.1	69.1	209[b]	472

The solutions were transferred to J Young® valve capped NMR tubes. The more concentrated solution was then diluted twice, by a factor of ~2 each time (*i.e.* by a factor ~2 and ~4 with respect to the original solution; ~100 mM and ~50 mM FTPS, respectively), by adding THF up to the 1 mL mark of the volumetric flask containing ~0.5 mL of the solution, mixing the solution thoroughly, transferring ~0.5 mL of the new solution to a fresh J Young® valve capped NMR tube, and repeating the process (both dilutions were performed in the glovebox). For each solution, ^{19}F pulse-acquire (Section 5.2.1) and ^{19}F inversion-recovery (Section 5.2.2) experiments were run at 300 K. The ^{19}F pulse-acquire NMR spectra were acquired with a D_1 = 70 s relaxation delay, t_{acq} = 1.5 s acquisition time, 0 dummy scans and 8 scans. The transmitter resonance was placed at –147 ppm and the spectral window was 120 ppm. The ^{19}F inversion-recovery NMR spectra for T_1^{FTPS} were acquired with a D_1 = 80 s relaxation delay, t_{acq} = 1.5 s acquisition time, 0 dummy scans and 1 scan. The transmitter resonance was placed at –170 ppm and the spectral window was 240 ppm. The variable delays used in the experiments were, τ (s) {1, 3, 5, 7, 10, 15, 20, 30, 40, 50, 60, 70}.

The ^{19}F pulse-acquire NMR spectra were processed as described in Section 5.2.1. The chemical shift of FTPS (referenced to NAPH), δ_F^{FTPS} = (–169.76 ± 0.00) ppm, was independent of its concentration. The ^{19}F inversion-recovery NMR spectral sets were processed as described in Section 5.2.2. The determined ^{19}F longitudinal relaxation fitting parameters (I_{eq}, x and T_1) and root mean square errors (R) are presented in

---

[a] [FTPS] = 10.4 mM based on integral ratio of FTPS and NAPH in ^{19}F pulse-acquire experiment.

[b] [FTPS] = (209 ± 1) mM based on integral ratios of FTPS and NAPH in ^{19}F pulse-acquire experiments.

Table 5.11. The plots of experimental and model fractional magnetisations, m^{FTPS}, against variable delay, τ, are presented in Figure 5.9. Although there is a decreasing trend of T_1^{FTPS} with increased concentration, a concentration change from 10 mM to 210 mM results in a 10% decrease in T_1^{FTPS}. For comparison, a 40% decrease in T_1^{TBAT} is observed for the same concentration change (Section 5.4.1). Hence, T_1^{FTPS} can be approximated to the average of the four values, (12.0 ± 0.3) s. Nonetheless, a linear (empirical) model as presented in Equation 5.3 can be fitted with $R = 0.07$.

Table 5.11: Concentrations (to the nearest 10 mM) and chemical shifts (determined from ^{19}F pulse-acquire experiments) and the longitudinal relaxation fitting parameters and root mean square errors (determined from ^{19}F inversion-recovery experiments) of FTPS.

Entry	[FTPS] (mM)[a]	δ_F^{FTPS} (ppm)	$10^{-3}I_{eq}^{\mathrm{FTPS}}$	x^{FTPS}	T_1^{FTPS} (s)	$10^{-3}R^{\mathrm{FTPS}}$
1	10	–169.75	1.91	1.87	12.4	0.01
2	210	–169.75	4.92	1.87	11.2	0.02
2, *d.f.* ~2	100	–169.76	1.87	1.86	12.0	0.01
2, *d.f.* ~4[b]	50	–169.76	1.29	1.86	12.3	0.01

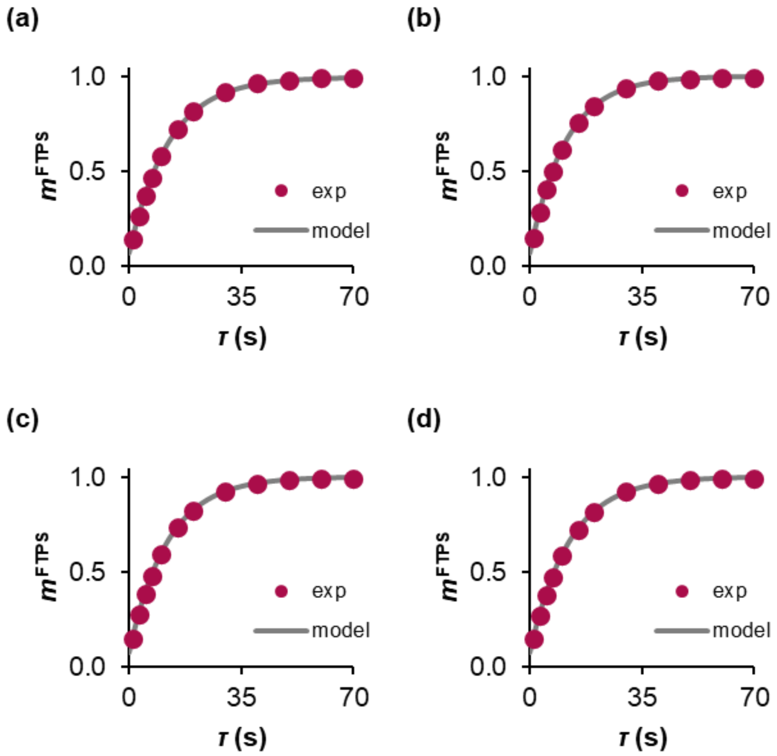

Figure 5.9: Plots of experimental ("exp") and model fractional magnetisations of FTPS, m^{FTPS}, in ^{19}F longitudinal relaxation constant measurements of FTPS in THF at 300 K. (a) ~10 mM; (b) ~210 mM; (c) ~100 mM; (d) ~50 mM.

---

[a] To the nearest 10 mM.

[b] 2 scans in ^{19}F inversion-recovery experiment for T_1^{FTPS}.

5.3

$$\frac{T_1^{\mathrm{FTPS}}}{\mathrm{s}} = -0.006073\frac{[\mathrm{FTPS}]}{\mathrm{m\textsc{m}}} + 12.57$$

Solutions of FTPS in MeCN

A solution was prepared in the glovebox by weighing FTPS (11.5 mg, 41.3 mᴍ) and NAPH (26.6 mg, 182 mᴍ) into a 1 mL volumetric flask and dissolving them in MeCN up to the 1 mL mark. The solution was transferred to a J Young® valve capped NMR tube. ^{19}F pulse-acquire (Section 5.2.1) and ^{19}F inversion-recovery (Section 5.2.2) experiments were run at 300 K. The solution was then titrated with three solid aliquots of FTPS (all titrations were performed in the glovebox, as described in Section 5.1.2). ^{19}F pulse-acquire and ^{19}F inversion-recovery experiments were run (at 300 K) after each aliquot addition. The ^{19}F pulse-acquire NMR spectra were acquired with a D_1 = 100 s relaxation delay, t_{acq} = 1.0 s acquisition time, 0 dummy scans and 1 scans. The transmitter resonance was placed at –147 ppm and the spectral window was 120 ppm. The ^{19}F inversion-recovery NMR spectra for T_1^{FTPS} were acquired with a D_1 = 100 s relaxation delay, t_{acq} = 1.0 s acquisition time, 0 dummy scans and 1 scan. The transmitter resonance was placed at –170 ppm and the spectral window was 120 ppm. The variable delays used in the experiments were, τ (s) {1, 2, 3, 5, 7, 10, 15, 20, 30, 45, 60, 80}.

The ^{19}F pulse-acquire NMR spectra were processed as described in Section 5.2.1 and the concentrations of FTPS (based on integral ratios of FTPS and NAPH), [FTPS], are presented in Table 5.12. The chemical shift of FTPS (referenced to NAPH), $\delta_{\mathrm{F}}^{\mathrm{FTPS}}$ = (–169.07 ± 0.01) ppm, was independent of its concentration (there is a slight trend in the data whereby FTPS signal moves upfield as its concentration increases; the changes are however very small and may be due to experimental/analysis error). The ^{19}F inversion-recovery NMR spectral sets were processed as described in Section 5.2.2. The determined ^{19}F longitudinal relaxation fitting parameters (I_{eq}, x and T_1) and root mean square errors (R) are presented in Table 5.12. The plots of experimental and model fractional magnetisations, m^{FTPS}, against variable delay, τ, are presented in Figure 5.10. T_1^{FTPS} = (16.6 ± 0.5) s was therefore found independent of [FTPS] in the given concentration range.

Table 5.12: Concentrations and chemical shifts (determined from ^{19}F pulse-acquire experiments) and the longitudinal relaxation fitting parameters and root mean square errors (determined from ^{19}F inversion-recovery experiments).

Entry	[FTPS] (mM)	δ_F^{FTPS} (ppm)	$10^{-3}I_{eq}^{FTPS}$	x^{FTPS}	T_1^{FTPS} (s)	$10^{-3}R^{FTPS}$
1	40.2	–169.06	0.846	1.90	16.1	0.011
1, aliq. 1	63.1	–169.07	1.29	1.90	15.4	0.02
1, aliq. 2	105	–169.07	2.16	1.87	17.8	0.01
1, aliq. 3	164	–169.09	3.34	1.87	17.0	0.03

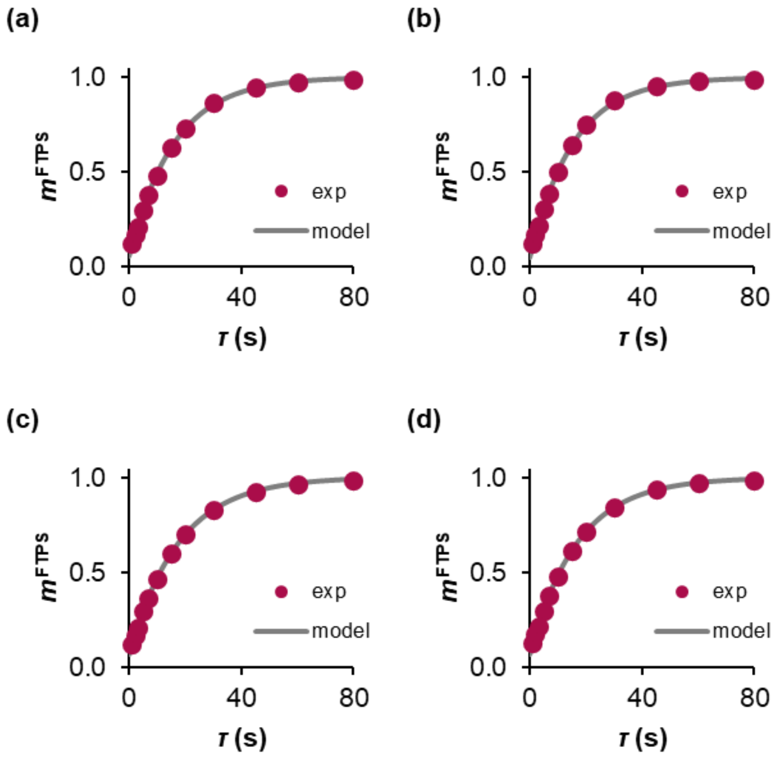

Figure 5.10: Plots of experimental ("exp") and model fractional magnetisations of FTPS, m^{FTPS}, in ^{19}F longitudinal relaxation constant measurements of FTPS in MeCN at 300 K. (a) 40.2 mM; (b) 63.1 mM; (c) 105 mM; (d) 164 mM.

5.4.3. Variable-concentration ^{19}F longitudinal relaxation of ARSF

Solutions of ARSF in THF

A solution was prepared in the glovebox by weighing ARSF (11.7 mg, 51.5 mM) and NAPH (17.2 mg, 118 mM) into a 1 mL volumetric flask and dissolving them in THF up to the 1 mL mark.[a] The solution was transferred to a J Young® valve capped NMR tube. The solution was then diluted twice, by a factor of ~2 each time (*i.e.* by a factor ~2 and ~4 with respect to the original solution; ~25 mM and ~15 mM ARSF, respectively), by adding THF up to the 1 mL mark of the volumetric flask containing ~0.5 mL of the original solution, mixing the solution thoroughly, transferring ~0.5 mL

---

[a] [ARSF] = (50.4 ± 0.4) mM based on integration against NAPH in the three solutions.

of the new solution to a fresh J Young® valve capped NMR tube, and repeating the process (both dilutions were performed in the glovebox).

For each solution, ^{19}F pulse-acquire (Section 5.2.1) and ^{19}F inversion-recovery (Section 5.2.2) experiments were run at 300 K. The ^{19}F pulse-acquire NMR spectra were acquired with a D_1 = 40 s relaxation delay, t_{acq} = 1.5 s acquisition time, 0 dummy scans and 1 scan. The transmitter resonance was placed at –44 ppm and the spectral window was 240 ppm. The ^{19}F inversion-recovery NMR spectra for T_1^{ARSF} were acquired with a D_1 = 20 s relaxation delay, t_{acq} = 1.5 s acquisition time, 0 dummy scans and 1 scan. The transmitter resonance was placed at 36 ppm and the spectral window was 240 ppm. The variable delays used in the experiments were, τ (s) {0.1, 0.2, 0.5, 0.75, 1, 2, 3, 4, 6, 8, 10, 12}.

The ^{19}F pulse-acquire NMR spectra were processed as described in Section 5.2.1. The chemical shift of ARSF (referenced to NAPH), δ_F^{ARSF} = (37.46 ± 0.01) ppm, and the isotope shift, $^1\Delta^{19}$F(^{32}S,^{34}S) = (43.6 ± 0.0) ppb, were independent of its concentration. The ^{19}F inversion-recovery NMR spectral sets were processed as described in Section 5.2.2. The determined ^{19}F longitudinal relaxation fitting parameters (I_{eq}, x and T_1) and root mean square errors (R) are presented in Table 5.13. The plots of experimental and model fractional magnetisations, m^{ARSF}, against variable delay, τ, are presented in Figure 5.11. T_1^{ARSF} = (2.14 ± 0.01) s was therefore found independent of [ARSF] in the given concentration range.

Table 5.13: Concentrations (to the nearest 5 mM) and chemical shifts (determined from ^{19}F pulse-acquire experiments) and the longitudinal relaxation fitting parameters and root mean square errors (determined from ^{19}F inversion-recovery experiments) of ARSF.

[ARSF] (mM)[a]	δ_F^{ARSF} (ppm)[b]	I_{eq}	x	T_1 (s)	R
50	37.46	1219	1.83	2.14	9
25	37.46	688	1.84	2.15	5
15	37.47	288	1.85	2.14	2

---

[a] To the nearest 5 mM.

[b] $^1\Delta^{19}$F(^{32}S,^{34}S) = 43.6 ppb for all three solutions.

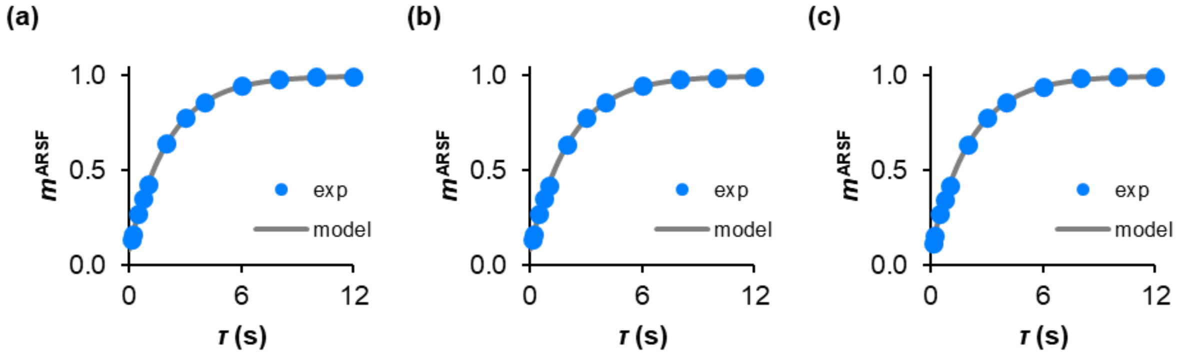

Figure 5.11: Plots of experimental and model fractional magnetisations of ARSF, m^{ARSF}, in ^{19}F longitudinal relaxation constant measurements of ARSF in THF at 300 K. (a) ~50 mM; (b) ~25 mM; (c) ~15 mM.

Solutions of ARSF in MeCN

Two solutions were prepared in the glovebox by weighing ARSF and NAPH into 1 mL volumetric flasks and dissolving them in MeCN up to the 1 mL mark. The masses and amounts of ARSF and NAPH, and the resulting concentrations in the solution are presented in Table 5.14.

Table 5.14: Masses, amounts and concentrations of ARSF and NAPH in solutions.

Entry	Solvent	Mass (mg)		Amount (μmol)		Concentration (mM)	
		ARSF	NAPH	ARSF	NAPH	ARSF	NAPH
1	MeCN	9.72	9.40	43.0	64.3	43.0[a]	64.3
2	MeCN	89.1	41.1	394	281	394[b]	281

The solutions were transferred to J Young® valve capped NMR tube. The more concentrated solution was then diluted by a factor of ~2 (~200 mM ARSF), by adding MeCN up to the 1 mL mark of the volumetric flask containing ~0.5 mL of the solution, mixing the solution thoroughly and transferring ~0.5 mL of the new solution to a fresh J Young® valve capped NMR tube (in the glovebox). For each solution, ^{19}F pulse-acquire (Section 5.2.1) and ^{19}F inversion-recovery (Section 5.2.2) experiments were run at 300 K. The ^{19}F pulse-acquire NMR spectra were acquired with a D_1 = 80 s relaxation delay, t_{acq} = 1.5 s acquisition time, 0 dummy scans and 1 scan. The transmitter resonance was placed at –44 ppm and the spectral window was 200 ppm. The ^{19}F inversion-recovery NMR spectra for T_1^{ARSF} were acquired with a D_1 = 25 s relaxation delay, t_{acq} = 1.5 s acquisition time, 0 dummy scans and 1 scan. The transmitter resonance was placed at 36 ppm and the spectral window was 80 ppm.

---

[a] [ARSF] = 41.8 mM based on integral ratio of ARSF and NAPH in ^{19}F pulse-acquire experiment.
[b] [ARSF] = (393 ± 0) mM based on integral ratios of ARSF and NAPH in ^{19}F pulse-acquire experiments.

The variable delays used in the experiments were, τ (s) {0.2, 0.5, 1, 1.5, 2, 3, 5, 7.5, 10, 12.5, 15, 20}.

The ^{19}F pulse-acquire NMR spectra were processed as described in Section 5.2.1. The chemical shift of ARSF (referenced to NAPH), δ_F^{ARSF} = (38.06 ± 0.04) ppm, and the isotope shift, $^{1}\Delta^{19}F(^{32}S,^{34}S)$ = (43.6 ± 0.0) ppb, were independent of its concentration (a very small linear change of the chemical shift was observed; this is however negligible considered its magnitude and the concentration range and may be due to experimental/analysis error). The ^{19}F inversion-recovery NMR spectral sets were processed as described in Section 5.2.2. The determined ^{19}F longitudinal relaxation fitting parameters (I_{eq}, x and T_1) and root mean square errors (R) are presented in Table 5.15. The plots of experimental and model fractional magnetisations, m^{ARSF}, against variable delay, τ, are presented in Figure 5.12.

Table 5.15: Concentrations (to the nearest 10 mM) and chemical shifts (determined from ^{19}F pulse-acquire experiments) and the longitudinal relaxation fitting parameters and root mean square errors (determined from ^{19}F inversion-recovery experiments) of ARSF.

Entry	[ARSF] (mM)[a]	δ_F^{ARSF} (ppm)[b]	I_{eq}	x	T_1 (s)	R
1	40	38.09	1598	1.87	2.55	5
2	390	38.02	13038	1.86	2.42	11
2, *d.f.* ~2	200	38.06	7577	1.86	2.50	19

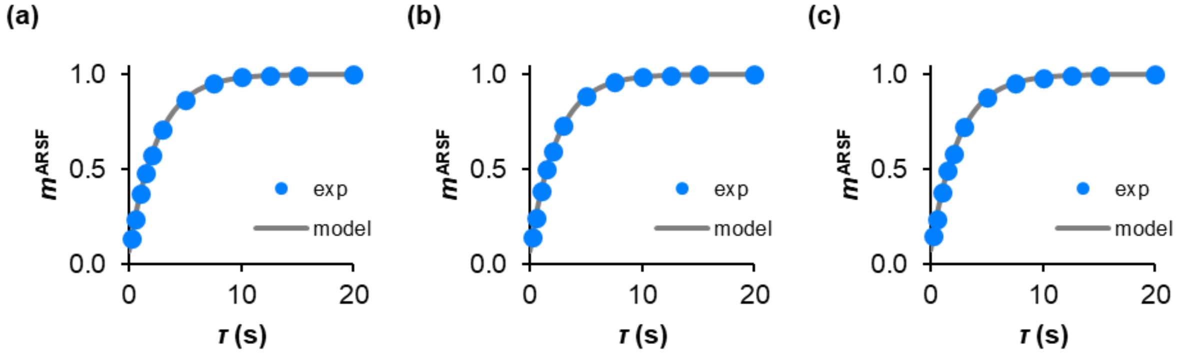

Figure 5.12: Plots of experimental ("exp") and model fractional magnetisations of ARSF, m^{ARSF}, in ^{19}F longitudinal relaxation constant measurements of ARSF in MeCN at 300 K. (a) ~40 mM; (b) ~390 mM; (c) ~200 mM.

Although there seems to be a decreasing trend of T_1^{ARSF} with increased concentration, a concentration change from 40 mM to 390 mM results in a 5% decrease in T_1^{ARSF},

---

[a] To the nearest 10 mM.

[b] $^{1}\Delta^{19}F(^{32}S,^{34}S)$ = 43.6 ppb for all three solutions.

which is negligible considering the concentration range. Hence, T_1^{ARSF} can be approximated to the average of the three values, (2.49 ± 0.07) s.

5.5. TBAT/FTPS system

5.5.1. Magnitude of exchange rate between TBAT and FTPS in THF

A solution was prepared in the glovebox by weighing TBAT (28.5 mg, 52.8 mM), FTPS (23.6 mg, 84.8 mM) and NAPH (31.7 mg, 217 mM) into a 1 mL volumetric flask and dissolving them in THF up to the 1 mL mark. The solution was transferred to a J Young® valve capped NMR tube.

^{19}F pulse-acquire (Section 5.2.1), ^{19}F inversion-recovery (Section 5.2.2) and ^{19}F selective inversion-recovery (Section 5.2.6) experiments were run at 300 K. Two ^{19}F pulse-acquire NMR spectra were acquired (for quantitation of TBAT and FTPS, both against NAPH) with a D_1 = 20 s relaxation delay, t_{acq} = 1.5 s acquisition time, 0 dummy scans and 1 scan. The transmitter resonance was placed at –110 ppm for TBAT/NAPH and –147 ppm for FTPS/NAPH, and the spectral window was 120 ppm. The ^{19}F inversion-recovery NMR spectral set for T_1^{TBAT} and T_1^{FTPS} was acquired with a D_1 = 20 s relaxation delay, t_{acq} = 1.5 s acquisition time, 0 dummy scans and 1 scan. The transmitter resonance was placed at –133 ppm and the spectral window was 240 ppm. The variable delays used in the experiment were, τ (s) {0, 0.25, 1.25, 2.5, 3.75, 5, 7.5, 10, 15}. The ^{19}F selective inversion-recovery NMR spectral set was acquired with a D_1 = 20 s relaxation delay, t_{acq} = 1.5 s acquisition time, 0 dummy scans and 1 scan. The transmitter resonance was placed at –96 ppm, the centre frequency for the inversion pulse was placed at –170 ppm and the spectral window was 240 ppm. The variable delays used in the experiment were, τ (s) {0.001, 0.002, 0.005, 0.01, 0.02, 0.05, 0.1, 0.2, 0.5, 1, 2, 5, 7.5, 10, 12.5, 15}.

The ^{19}F pulse-acquire NMR spectra were processed as described in Section 5.2.1. The concentrations of TBAT and FTPS, based on the NAPH internal standard, were [TBAT] = 52.5 mM and [FTPS] = 83.9 mM (99.5% and 98.9% of the values based on masses, respectively). The ^{19}F inversion-recovery NMR spectral set was processed as described in Section 5.2.2. The ^{19}F longitudinal relaxation fitting parameters (I_{eq}, x and T_1) and root mean square errors (R) obtained for TBAT and FTPS are presented in Table 5.16a. The ^{19}F selective inversion-recovery NMR spectral set was processed as described in Section 5.2.6. The ^{19}F exchange fitting parameters (I_{eq}, x and α) and root mean square error (*R*) obtained for (the initially non-inverted) TBAT are presented in Table 5.16b, and the plot of experimental and model fractional magnetisations of TBAT, m^{TBAT}, against variable delay, τ – in Figure 3.11. The pre-exponential term *x*, determined in the fitting, corresponds to $m_0^{\mathrm{FTPS}} = 0.0669$ (*i.e.* 93.3% inversion of FTPS by the selective pulse).

Table 5.16: The fitting parameters and root mean square errors (*R*) obtained from (a) ^{19}F inversion-recovery of TBAT and FTPS and (b) ^{19}F inversion transfer between inverted FTPS and non-inverted TBAT in solution.

(a) ^{19}F inversion-recovery				
Species	I_{eq}	x	T_1 **(s)**	R
TBAT	821	1.35	2.43	1
FTPS	622	1.43	2.47	4
(b) ^{19}F selective inversion-recovery				
Species	I_{eq}	x	α **(s^{-1})**	R
TBAT	1782	1476	12.1	8

5.5.2. Initial titrations of TBAT with FTPS in THF

Four solutions were prepared in the glovebox by weighing TBAT, FTPS and NAPH into 1 mL volumetric flasks and dissolving them in THF up to the 1 mL mark. The solutions were transferred to J Young® valve capped NMR tubes. Masses of the solutes and the resulting concentrations in the solutions are presented in Table 5.17.

Table 5.17: Masses and concentrations of TBAT, FTPS and NAPH.

Entry	Solvent	Mass (mg)			Concentration (mM)		
		TBAT	FTPS	NAPH	TBAT	FTPS	NAPH
1	THF	108	28.0	31.5	200	101	215
2	THF	80.9	29.6	30.6	150	106	209
3	THF	54.1	17.4	28.8	100	62.5	197
4	THF	28.0	4.42	43.3	51.8	15.9	296

^{19}F pulse-acquire (Section 5.2.1) and ^{19}F selective inversion-recovery (Section 5.2.6) experiments were run at 300 K. For each solution, two ^{19}F pulse-acquire NMR spectra were acquired (for quantitation of TBAT and FTPS, both against NAPH) with a D_1 = 40 s relaxation delay, t_{acq} = 1.5 s acquisition time, 0 dummy scans and 8 scans. The transmitter resonance was placed at –110 ppm for TBAT/NAPH and –147 ppm for FTPS/NAPH, and the spectral window was 80 ppm. The ^{19}F selective inversion-recovery NMR spectral sets were acquired for each solution with the $D_1 \geq 5T_1^{\mathrm{obs}} - 1.5$ s relaxation delay varied between the runs (where T_1^{obs} is the averaged relaxation time of TBAT and FTPS in a given solution, predicted from Equations 2.69 and 3.2, and T_1^{FTPS} = 12.0 s), t_{acq} = 1.5 s acquisition time, 0 dummy scans and 1 scan. The transmitter resonance was placed at –96 ppm, the centre frequency for the inversion pulse was placed at –170 ppm and the spectral window was 120 ppm. A series of 24 variable delays were used in the experiments: the first 16 values, τ (s) {0.001, 0.002, 0.003, 0.005, 0.007, 0.01, 0.015, 0.02, 0.025, 0.05, 0.1, 0.15, 0.2, 0.25, 0.5, 1}, were identical for all runs, and the remaining eight – optimised for each solution based on T_1^{obs}.

Each solution was then titrated with five solid aliquots of FTPS, inside the glovebox. After each solid addition, the NMR tube was shaken thoroughly, and the ^{19}F pulse-acquire (for quantitation of FTPS only), as well as ^{19}F selective inversion-recovery experiments were repeated as described above.

The ^{19}F pulse-acquire NMR spectra were processed as described in Section 5.2.1. The concentrations of TBAT (determined for the original solutions and assumed constant throughout the titrations) and FTPS (determined for each solution), based on the NAPH internal standard, are presented in Table 5.18, along with the T_1^{obs} values predicted from T_1^{TBAT} and T_1^{FTPS} as isolated spins for these concentrations. The ^{19}F selective inversion-recovery NMR spectral sets were processed as described in Section 5.2.6 (r and T_1^{obs} from Table 5.18 were used). The ^{19}F exchange fitting parameters (I_{eq}, x and α) and root mean square error (R) obtained for (the initially non-inverted) TBAT are presented in Table 5.18.

Table 5.18: Quantitation of TBAT and FTPS in the initial titration experiments and the results of ^{19}F inversion-recovery measurements.

[TBAT] (mM)	[FTPS] (mM)	T_1^{obs} (s)	I_{eq}	x	α (s^{-1})	R
202	97.0	1.47	5925	2221	14.6	32
202	113	1.51	5820	2453	18.3	34
202	134	1.56	5776	2765	22.9	32
202	155	1.61	5740	3051	27.7	41
202	180	1.68	5715	3374	34.7	38
202	194	1.71	5714	3549	44.2	51
150	104	1.67	4374	2122	7.33	30
150	120	1.73	4348	2324	15.6	51
150	136	1.79	4365	2512	23.3	76
150	155	1.85	4354	2726	32.3	88
150	174	1.92	4391	2951	42.9	104
150	191	1.98	4432	3199	77.4	128
99.0	60.2	1.76	2974	1336	11.3	15
99.0	74.4	1.84	2928	1518	14.6	23
99.0	94.6	1.96	2910	1796	18.6	25
99.0	109	2.04	2896	1958	22.6	23
99.0	133	2.17	2882	2202	26.5	27
99.0	148	2.25	2852	2294	30.9	28
52.9	17.2	1.77	12467	3382	3.11	48
52.9	36.4	2.01	3016	1466	7.21	17
52.9	54.1	2.21	1485	942	11.7	16
52.9	71.3	2.40	1502	1150	14.8	16
52.9	85.5	2.55	1484	1259	17.8	13
52.9	111	2.81	1488	1426	22.7	12

5.5.3. Condition-sensitivity and temporal instability of the system

A representative example of an experiment for the measurement of inversion transfer rate increase between TBAT and FTPS in THF over time.

A solution was prepared in the glovebox by weighing TBAT (28.5 mg, 52.8 mM), FTPS (13.9 mg, 49.8 mM) and NAPH (36.6 mg, 250 mM) into a 1 mL volumetric flask and dissolving them in THF up to the 1 mL mark. The solution was then split into two parts, which were transferred to J Young® valve capped NMR tubes. The date and time of preparation of the solution was noted. One sample was immediately removed from the glovebox and kept in the spectrometer autosampler between NMR measurements (sample “AS”). The other one remained in the glovebox, except when NMR measurements were performed (“sample GB”).

Eleven sets of ^{19}F pulse-acquire (Section 5.2.1), ^{19}F inversion-recovery (Section 5.2.2) and ^{19}F selective inversion-recovery (Section 5.2.6) experiments were performed at 300 K on the AS sample, and three sets on the GB one. The date and time of acquisition of each set (more specifically, of the ^{19}F selective inversion-recovery experiment in a given set) were converted to the time interval between preparation of the sample and the acquisition, *t*. Two ^{19}F pulse-acquire NMR spectra were acquired per set (for quantitation of TBAT and FTPS, both against NAPH) with a D_1 = 40 s relaxation delay, t_{acq} = 1.5 s acquisition time, 0 dummy scans and 1 scan. The transmitter resonance was placed at –110 ppm for TBAT/NAPH and –147 ppm for FTPS/NAPH, and the spectral window was 80 ppm. The ^{19}F inversion-recovery NMR spectra for T_1^{obs} (of TBAT) were acquired with a D_1 = 10 s relaxation delay, t_{acq} = 1.5 s acquisition time, 0 dummy scans and 1 scan. The transmitter resonance was placed at –96 ppm and the spectral window was 120 ppm. The variable delays used in the experiments were, τ (s) {0.1, 0.2, 0.5, 0.75, 1, 2, 3, 4, 6, 8, 10, 12}. The ^{19}F selective inversion-recovery NMR spectra were acquired with a D_1 = 10 s relaxation delay, t_{acq} = 1.5 s acquisition time, 0 dummy scans and 1 scan. The transmitter resonance was placed at –96 ppm, the centre frequency for the inversion pulse was placed at –170 ppm and the spectral window was 120 ppm. The variable delays used in the experiments were, τ (s) {0.001, 0.002, 0.003, 0.005, 0.007, 0.01, 0.015, 0.02, 0.025, 0.05, 0.1, 0.15, 0.2, 0.25, 0.5, 1, 2, 3, 4, 5, 6, 8, 10, 12}.

The ^{19}F pulse-acquire NMR spectra were processed as described in Section 5.2.1, and the ^{19}F inversion-recovery NMR spectral sets, as described in Section 5.2.2. The concentrations of TBAT and FTPS based on the NAPH internal standard, as well as the ^{19}F longitudinal relaxation fitting parameters (I_{eq}, x and T_1^{obs}) and root mean square errors (*R*) are presented in Table 5.19 for both samples at each time, *t*.

Table 5.19: Concentrations of TBAT and FTPS, and longitudinal relaxation fitting parameters (and *R*) for AS and GB samples.

Sample	*t* (h)	[TBAT] (mM)	[FTPS] (mM)	I_{eq}	x	T_1^{obs} (s)	*R*
AS	0.414	52.3	48.2	780	1.40	2.04	8
AS	1.40	52.1	47.4	792	1.39	2.10	8
AS	2.40	51.5	46.7	791	1.38	2.11	4
AS	3.34	51.2	46.6	867	1.38	2.10	5
AS	4.40	52.4	45.0	770	1.39	2.04	7
AS	5.40	51.4	45.6	811	1.38	2.10	6
AS	7.40	50.8	45.1	814	1.37	2.15	4
AS	14.1	52.4	46.9	804	1.38	2.09	7
AS	25.9	49.9	43.0	887	1.38	2.11	10
AS	36.8	50.0	44.8	897	1.38	2.14	10
AS	50.5	51.0	44.2	894	1.38	2.11	12
GB	13.6	52.0	46.8	808	1.37	2.15	5
GB	25.4	51.8	45.7	884	1.39	2.08	8
GB	37.3	51.4	45.9	887	1.38	2.11	8
GB	50.1	51.8	45.0	N/A	N/A	N/A	N/A

The ^{19}F selective inversion-recovery NMR spectral sets were processed as described in Section 5.2.6. The ^{19}F exchange fitting parameters, I_{eq}, x and $\alpha(r + 1)$, and root mean square error (R) obtained for (the initially non-inverted) TBAT are presented in Table 5.20.

Table 5.20: ^{19}F inversion transfer between TBAT and FTPS in the representative rate increase experiment.

Sample	*t* (h)	I_{eq}	*x*	$\alpha(r + 1)$ (s^{-1})	*R*
AS	0.414	1527	838	26.7	8
AS	1.40	1518	835	33.7	7
AS	2.40	1498	827	42.0	7
AS	3.34	1494	818	49.3	10
AS	4.40	1478	816	56.1	8
AS	5.40	1382	777	62.8	7
AS	7.40	1377	776	72.1	8
AS	14.1	1351	764	89.4	11
AS	25.9	1614	972	104	13
AS	36.8	1616	970	118	14
AS	50.5	1607	966	130	17
GB	13.6	1406	807	77	18
GB	25.4	1524	915	97	12
GB	37.3	1647	984	107	17
GB	50.1	1720	1059	117	29

5.5.4. Effect of [FTPS] on exchange rate in the temporally stabilised system

Five solutions were prepared in the glovebox by weighing TBAT, FTPS and NAPH into 1 mL volumetric flasks and dissolving them in THF up to the 1 mL mark. D^{t}BP (5.00 µL, 23.1 mᴍ) was added to each solution *via* a microsyringe, and each solution was shaken thoroughly. The solutions were then transferred to J Young® valve capped NMR tubes (~0.5 mL, each) preloaded with six 3 Å molecular sieve beads (~40 mg), and again shaken thoroughly. Masses of the solutes and the resulting concentrations in the solutions are presented in Table 5.21. The date and time of preparation of each solution was also noted.

Table 5.21: Masses and concentrations of TBAT, FTPS and NAPH in the solution for measurements of exchange rate in the stabilised system.

Entry	Solvent	Mass (mg)			Concentration (mᴍ)		
		TBAT	FTPS	NAPH	TBAT	FTPS	NAPH
1	THF	54.4	6.30	53.1	101	22.6	363
2	THF	54.3	17.5	63.1	101	62.9	431
3	THF	54.5	28.1	40.7	101	101	279
4	THF	54.6	40.1	46.6	101	144	319
5	THF	54.4	56.8	51.1	101	204	349

Ten sets of ^{19}F pulse-acquire (Section 5.2.1), ^{19}F inversion-recovery (Section 5.2.2) and ^{19}F selective inversion-recovery (Section 5.2.6) experiments were performed at

300 K for each solution. The date and time of acquisition of each set (more specifically, of the ^{19}F selective inversion-recovery experiment in a given set) were converted to the time interval between preparation of the sample and the acquisition, t.

Two ^{19}F pulse-acquire NMR spectra were acquired per set (for quantitation of TBAT and FTPS, both against NAPH) with a D_1 = 40 s relaxation delay, t_{acq} = 1.5 s acquisition time, 0 dummy scans and 1 scan. The transmitter resonance was placed at –110 ppm for TBAT/NAPH and –147 ppm for FTPS/NAPH, and the spectral window was 80 ppm. The ^{19}F inversion-recovery NMR spectra for T_1^{obs} (of TBAT) were acquired with a D_1 = 20 s relaxation delay, t_{acq} = 1.5 s acquisition time, 0 dummy scans and 1 scan. The transmitter resonance was placed at –96 ppm and the spectral window was 120 ppm. The variable delays used in the experiments were, τ (s) {0.1, 0.2, 0.5, 0.75, 1, 2, 3, 4, 6, 10, 15, 20}. The ^{19}F selective inversion-recovery NMR spectra were acquired with a D_1 = 20 s relaxation delay, t_{acq} = 1.5 s acquisition time, 0 dummy scans and 1 scan. The transmitter resonance was placed at –96 ppm, the centre frequency for the inversion pulse was placed at –170 ppm and the spectral window was 120 ppm. The variable delays used in the experiments were, τ (s) {0.001, 0.002, 0.005, 0.01, 0.015, 0.02, 0.025, 0.035, 0.05, 0.075, 0.1, 0.15, 0.2, 0.25, 0.3, 0.4, 0.5, 1, 3, 5, 8, 12, 15, 20}.

The ^{19}F pulse-acquire NMR spectra were processed as described in Section 5.2.1, and the ^{19}F inversion-recovery NMR spectral sets, as described in Section 5.2.2. The concentrations of TBAT, [TBAT], and FTPS, [FTPS], based on the NAPH internal standard, as well as the ^{19}F longitudinal relaxation fitting parameters (I_{eq}, x and T_1^{obs}) and root mean square errors (R) are presented in Table 5.22 for each solution at each time, t and the corresponding plots – in Figure 5.13.

Table 5.22: Quantitation of the spins and longitudinal relaxation fitting parameters under the stabilising conditions.

t (h)	[TBAT] (mM)	[FTPS] (mM)	I_{eq}	x	T_1^{obs} (s)	R
2.36	99.3	22.6	1634	1.60	1.50	8
26.7	100	20.5	1475	1.75	1.48	20
75.8	98.8	21.7	1799	1.54	1.47	18
100	98.3	21.9	1805	1.56	1.46	31
123	99.1	20.5	1763	1.62	1.43	38
148	99.4	19.7	1791	1.56	1.48	18
168	99.4	19.8	1843	1.57	1.45	14
232	98.4	18.9	1493	1.76	1.45	15
284	98.1	18.0	1609	1.74	1.47	9
340	98.3	17.5	1676	1.75	1.45	10
1.69	99.8	62.3	1644	1.45	1.63	35
25.8	99.6	60.8	1483	1.56	1.66	27
75.1	99.8	59.7	1821	1.39	1.62	25
97.8	98.9	61.6	1842	1.41	1.63	47
122	99.7	62.9	1815	1.45	1.56	32
147	99.7	61.2	1783	1.49	1.52	66
167	101	61.5	1840	1.44	1.54	35
224	99.2	60.9	1601	1.58	1.57	40
284	99.5	58.8	1490	1.59	1.57	36
339	100	58.3	1687	1.60	1.56	35
0.741	99.6	100	1589	1.32	1.82	24
24.7	99.1	101	1449	1.42	1.82	28
73.7	98.8	100	1738	1.28	1.76	42
96.7	98.5	101	1615	1.34	1.73	55
121	98.1	102	1676	1.39	1.58	72
145	97.7	99.0	1758	1.37	1.66	77
165	98.7	102	1798	1.36	1.70	58
223	98.8	96.9	1520	1.48	1.66	54
283	98.1	98.9	1531	1.49	1.63	55
339	97.1	98.6	1617	1.48	1.66	49
3.16	98.7	146	1610	1.19	2.00	15
27.6	99.5	142	1462	1.32	1.93	38
76.6	100	146	1802	1.18	1.93	38
101	98.8	145	1809	1.19	1.93	39
124	99.3	144	1769	1.24	1.86	63
149	98.0	144	1793	1.23	1.87	52
144	98.6	142	1807	1.24	1.82	60
233	99.7	141	1472	1.36	1.78	56
285	98.4	141	1428	1.37	1.80	55
341	99.5	141	1635	1.36	1.80	58
1.56	99.1	203	1611	1.10	2.17	22
25.6	99.5	199	1470	1.16	2.28	12
75.0	99.7	204	1537	1.11	2.03	51
97.6	98.5	204	1594	1.09	2.15	28
122	98.6	206	1753	1.13	2.08	57
146	100	201	1787	1.10	2.07	49
167	98.3	202	1836	1.12	2.07	39
224	99.6	200	1556	1.22	2.06	55
284	99.4	203	1597	1.22	2.04	53
339	99.0	199	1643	1.22	2.03	59

(a) 22.6 mM FTPS

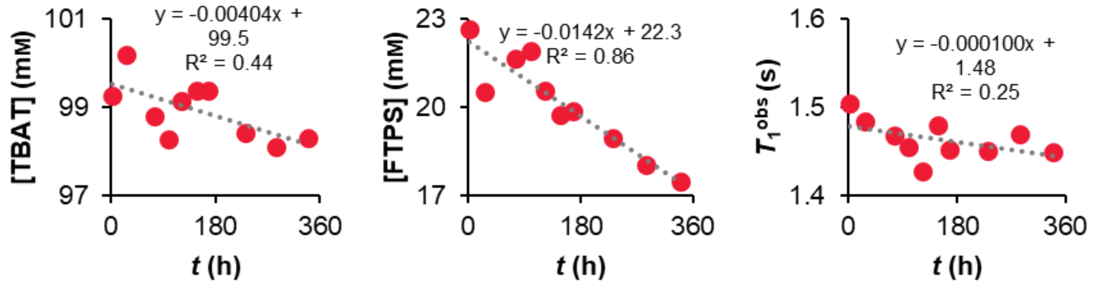

(b) 62.9 mM FTPS

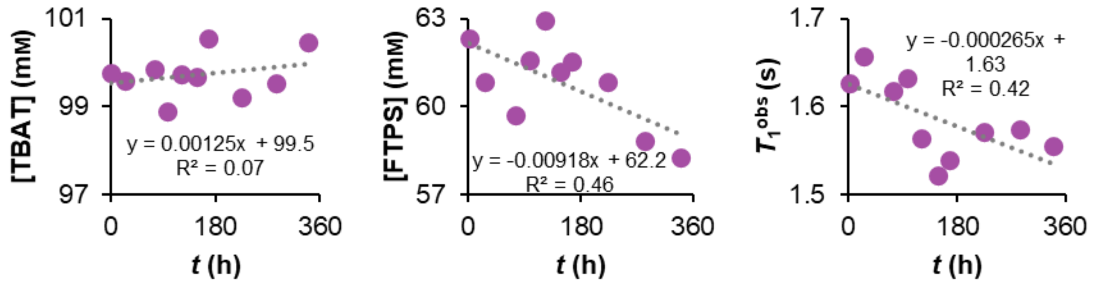

(c) 101 mM FTPS

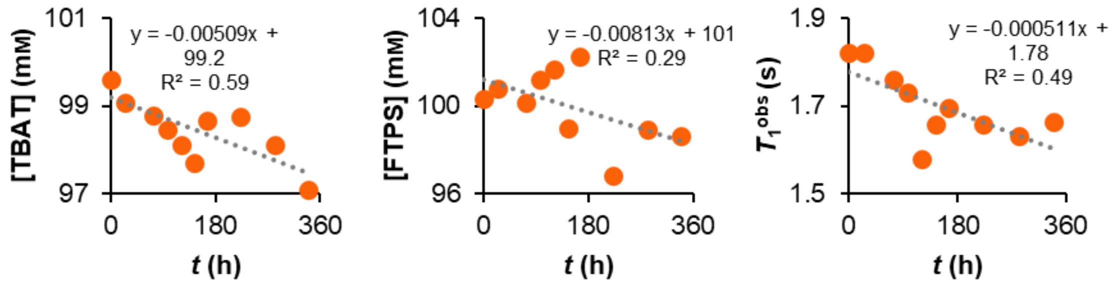

(d) 144 mM FTPS

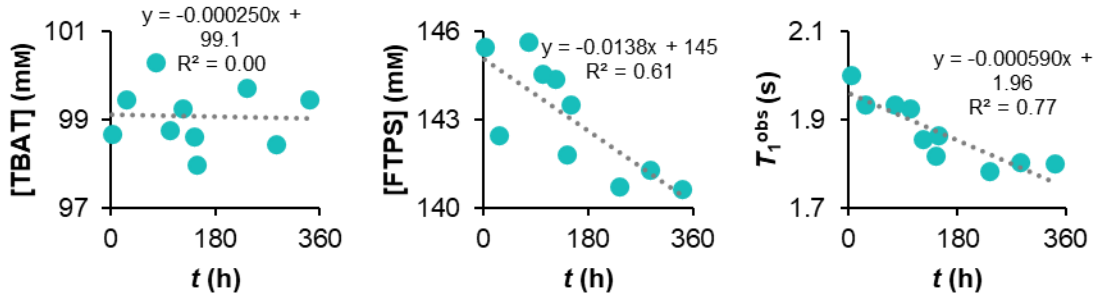

(e) 204 mM FTPS

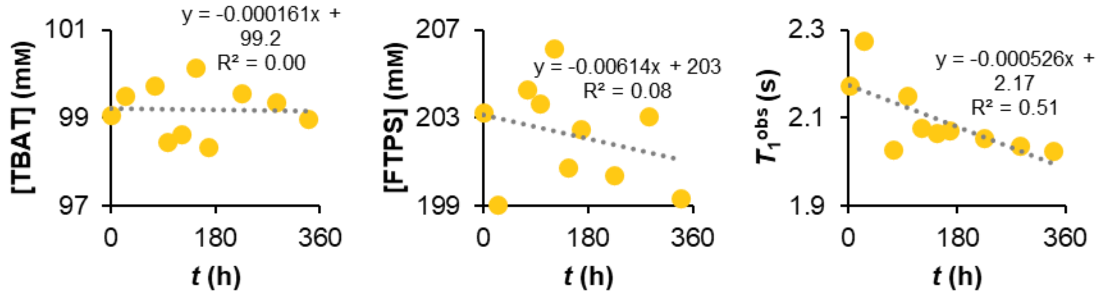

Figure 5.13: Temporal evolution of concentrations of the spins and longitudinal relaxation time under the stabilising conditions.

The ^{19}F selective inversion-recovery NMR spectral sets were processed as described in Section 5.2.6. The ^{19}F exchange fitting parameters (I_{eq}, x and α) and root mean square error (R) obtained for (the initially non-inverted) TBAT are presented in Table 5.23.

Table 5.23: Evolution of inversion transfer rate under stabilising conditions.

t (h)	[TBAT] (mM)	[FTPS] (mM)	I_{eq}	*x*	*α* (s^{-1})	*R*
2.36	99.3	22.6	2400	480	2.05	31
26.7	100	20.5	2942	598	1.54	32
75.8	98.8	21.7	2293	451	1.08	13
100	98.3	21.9	2272	409	1.23	18
123	99.1	20.5	2783	506	1.17	18
148	99.4	19.7	2840	474	1.24	26
168	99.4	19.8	2936	509	1.37	17
232	98.4	18.9	2983	528	1.23	6
284	98.1	18.0	2927	510	1.28	4
340	98.3	17.5	3350	556	1.31	4
1.69	99.8	62.3	2388	1097	3.89	36
25.8	99.6	60.8	2948	1413	3.32	31
75.1	99.8	59.7	2297	1058	2.46	19
97.8	98.9	61.6	2322	1007	3.01	26
122	99.7	62.9	2875	1283	2.29	32
147	99.7	61.2	2831	1267	2.23	23
167	101	61.5	2927	1282	2.40	19
224	99.2	60.9	2900	1359	2.22	19
284	99.5	58.8	2967	1397	2.39	15
339	100	58.3	3360	1579	2.52	16
0.741	99.6	100	2369	1496	5.76	12
24.7	99.1	101	2693	1823	4.75	41
73.7	98.8	100	2195	1414	3.60	24
96.7	98.5	101	2372	1475	4.10	49
121	98.1	102	2724	1763	3.29	24
145	97.7	99.0	2799	1777	3.53	17
165	98.7	102	2841	1831	3.44	30
223	98.8	96.9	2771	1876	3.28	18
283	98.1	98.9	2808	1903	3.26	21
339	97.1	98.6	3228	2159	3.51	22
3.16	98.7	146	2380	1818	9.58	27
27.6	99.5	142	2864	2338	9.65	25
76.6	100	146	2277	1806	5.64	21
101	98.8	145	2307	1713	5.29	23
124	99.3	144	2809	2185	4.83	42
149	98.0	144	2837	2170	4.84	26
144	98.6	142	2875	2232	4.64	27
233	99.7	141	2917	2434	4.35	38
285	98.4	141	2835	2384	4.45	28
341	99.5	141	3275	2748	4.60	48
1.56	99.1	203	2390	2223	10.9	20
25.6	99.5	199	2899	2796	15.5	34
75.0	99.7	204	3429	3283	8.08	50
97.6	98.5	204	2307	2087	9.21	28
122	98.6	206	2735	2529	7.46	49
146	100	201	2841	2587	7.87	40
167	98.3	202	2864	2646	7.38	35
224	99.6	200	2806	2784	6.78	34
284	99.4	203	2850	2836	6.66	39
339	99.0	199	3238	3220	6.74	58

5.5.5. Proof of dissociative pathway in the non-stabilised system

A solution was prepared in the glovebox by weighing TBAT (120 mg, 222 mM) and NAPH (39.3 mg, 269 mM) into a 1 mL volumetric flask and dissolving them in THF up to the 1 mL mark. The solution was transferred to a J Young® valve capped NMR tube. Seven solid aliquots of FTPS were added to the solution. After each aliquot addition, the NMR tube was shaken thoroughly, and ^{19}F pulse-acquire (Section 5.2.1) and ^{19}F selective inversion-recovery (Section 5.2.6) experiments were run at 300 K. Last acquisition ended ~1.5 h after the solution was prepared.

Two ^{19}F pulse-acquire NMR spectra were acquired for the first FTPS aliquot (for quantitation of TBAT and FTPS, both against NAPH). For each subsequent aliquot, one spectrum was acquired for quantitation of FTPS. The spectra were acquired with a D_1 = 40 s relaxation delay, t_{acq} = 1.5 s acquisition time, 0 dummy scans and 1 scan. The transmitter resonance was placed at –110 ppm for TBAT/NAPH and –147 ppm for FTPS/NAPH, and the spectral window was 120 ppm. The ^{19}F selective inversion-recovery NMR spectral sets were acquired with a D_1 = 5.5 s relaxation delay, t_{acq} = 1.5 s acquisition time, 0 dummy scans and 1 scan. The transmitter resonance was placed at –96 ppm, the centre frequency for the inversion pulse was placed at –170 ppm and the spectral window was 120 ppm. The variable delays used in the experiments were, τ (s) {0.001, 0.002, 0.005, 0.01, 0.015, 0.02, 0.025, 0.035, 0.05, 0.075, 0.1, 0.15, 0.2, 0.25, 0.3, 0.4, 0.5, 0.75, 1, 2, 3, 4, 5.5, 7}.

The ^{19}F pulse-acquire NMR spectra were processed as described in Section 5.2.1. The concentration of TBAT, based on NAPH, was [TBAT] = 218 mM. The concentrations of FTPS are presented in Table 5.24. The ^{19}F selective inversion-recovery NMR spectral sets were processed as described in Section 5.2.6; except with T_1^{obs} as a fourth fitting parameter, and $\alpha(r + 1)$ as a fitting parameter instead of α. The fitting parameters and root mean square error (R) obtained for (the initially non-inverted) TBAT are presented in Table 5.24. The experimental and model inversion transfer profiles for each [FTPS] are presented in Figure 5.14 (expansion of the plot for $\tau \leq 0.05$ is presented on the right). The plot of $\alpha(r + 1)$ *vs* [FTPS] is presented in Figure 3.30.

Table 5.24: The fitting parameters and root mean square errors (*R*) for the inversion transfer between TBAT and FTPS.

[FTPS] (mм)	I_{eq}	x	$\alpha(r+1)$ (s^{-1})	T_1^{obs} (s)	R
3.31	7681	191	234	1.31	15
11.9	7754	464	151	1.24	14
23.1	7782	756	142	1.27	16
32.1	7640	952	144	1.16	20
45.7	7487	1254	145	1.25	19
50.9	7496	1406	154	1.26	24
67.0	7451	1715	160	1.31	17

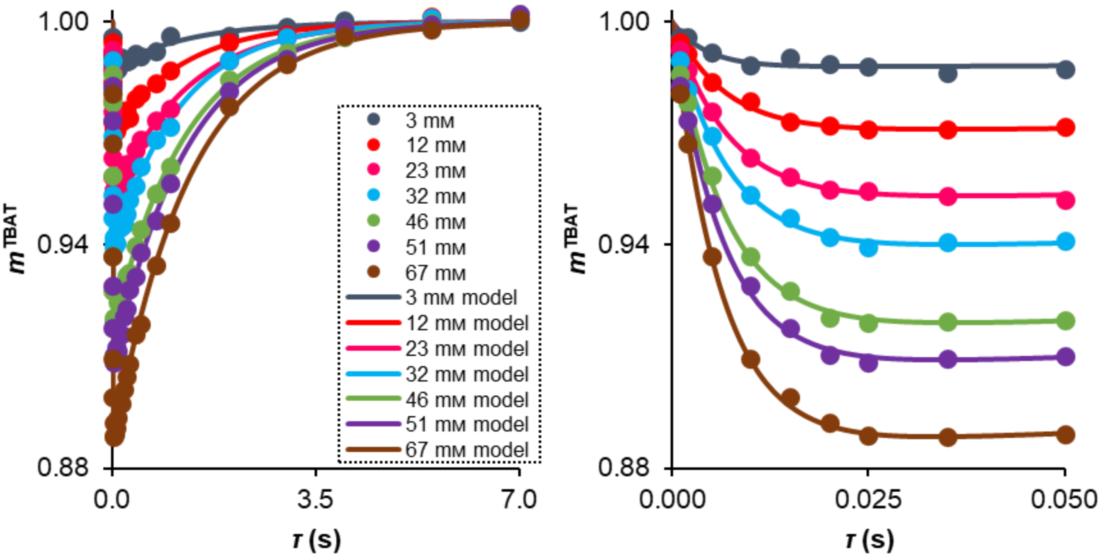

Figure 5.14: Inversion transfer profiles in titration of TBAT with FTPS.

5.6. TBAT/ARSF system

5.6.1. ^{19}F selective inversion-recovery in THF

A solution was prepared in the glovebox by weighing TBAT (107 mg, 198 mм), ARSF (13.3 mg, 58.6 mм) and NAPH (33.2 mg, 227 mм) into a 1 mL volumetric flask and dissolving them in THF up to the 1 mL mark. The solution (~0.4 mL) was transferred to a J Young® valve capped NMR tube. ^{19}F pulse-acquire (Section 5.2.1), ^{19}F inversion-recovery (Section 5.2.2) and ^{19}F selective inversion-recovery (Section 5.2.6) experiments were run at 300 K, 310 and 320 K. The NMR tube was open to air for ~30 s, closed, shaken thoroughly and the same set of experiments was run at 320 K. Then, two aliquots of a solution of water in THF were added to the sample under air (~0.2 mL of water was dissolved in THF up to 2 mL total volume under air; 2 µL and 5 µL of the resulting solution were added to the NMR tube *via* a microsyringe, corresponding to ~30 and 100 mM total added water, respectively). After each aliquot addition, the tube was shaken thoroughly, and the same set of experiments was run at 320 K.

The ^{19}F pulse-acquire NMR spectra were acquired twice per each set of experiments (for quantitation of TBAT and ARSF, both against NAPH) with a D_1 = 40 s relaxation delay, t_{acq} = 1.5 s acquisition time, 0 dummy scans and 1 scan. The transmitter resonance was placed at –110 ppm for TBAT/NAPH and –44 ppm for ARSF/NAPH, and the spectral window was 200 ppm. The ^{19}F inversion-recovery NMR spectra for T_1^{TBAT} and T_1^{ARSF} were acquired with a D_1 = 20 s relaxation delay, t_{acq} = 1.5 s acquisition time, 0 dummy scans and 1 scan. The transmitter resonance was placed at –30 ppm and the spectral window was 240 ppm. The variable delays used in the experiments were, τ (s) {0.5, 1, 1.5, 2, 3, 4, 5, 7.5, 10, 12.5, 15, 20}. The ^{19}F selective inversion-recovery NMR spectra were acquired with a D_1 = 20 s relaxation delay, t_{acq} = 1.5 s acquisition time, 0 dummy scans and 1 scan. The transmitter resonance was placed at 37 ppm, the centre frequency for the inversion pulse was placed at –96 ppm and the spectral window was 120 ppm. The variable delays used in the experiments were, τ (s) {0.01, 0.02, 0.05, 0.1, 0.2, 0.3, 0.5, 0.75, 1, 1.5, 2, 3, 5, 10, 15, 20}.

The ^{19}F pulse-acquire NMR spectra were processed as described in Section 5.2.1. The ^{19}F inversion-recovery NMR spectral sets were processed as described in Section 5.2.2. The concentrations of TBAT and ARSF based on the internal standard, as well as the determined ^{19}F longitudinal relaxation fitting parameters (I_{eq}, x and T_1) and root mean square errors (R) for TBAT and ARSF are presented in Table 5.25a and Table 5.25b (for TBAT and ARSF, respectively).

Table 5.25: Concentrations (based on the internal standard, NAPH), longitudinal relaxation fitting parameters and root mean square errors (from ^{19}F inversion-recovery experiments) for (a) TBAT and (b) ARSF in the solution of TBAT and ARSF in THF.

(a)

Conditions	**[TBAT] (mM)**	I_{eq}^{TBAT}	x^{TBAT}	T_1^{TBAT} **(s)**	R^{TBAT}
300 K	197	11493	0.557	1.22	19
310 K	196	10157	0.549	1.42	11
320 K	195	9523	0.559	1.60	7
320 K, aired	192	6483	0.548	1.56	19
320 K, 30 mM water	174	5939	0.605	1.42	67
320 K, 100 mM water	152	4712	0.564	1.50	115

(b)

Conditions	**[ARSF] (mM)**	I_{eq}^{ARSF}	x^{ARSF}	T_1^{ARSF} **(s)**	R^{ARSF}
300 K	55.1	1616	0.574	1.74	5
310 K	53.8	1393	0.554	1.85	4
320 K	53.3	1307	0.531	2.01	5
320 K, aired	52.4	897	0.513	2.05	2
320 K, 30 mM water	54.2	1038	0.569	1.94	2
320 K, 100 mM water	52.8	971	0.562	1.93	2

The ^{19}F selective inversion-recovery NMR spectral sets were processed as described in Section 5.2.6. The plots of experimental fractional magnetisations of ARSF, m^{ARSF}, against variable delay, τ, are presented in Figure 3.33b in Section 3.4.1, as well as in Figure 5.15 below (individual plots for each experiment for $\tau \leq 0.5$ s; all experimental data for $\tau \leq 0.5$ s are within the m^{ARSF} range shown in the plots). The equilibrium integrals, I_{eq}^{ARSF}, were determined by taking an average of the experimental integrals for all 16 variable delays in a given inversion transfer experiment in each plot in Figure 5.15.

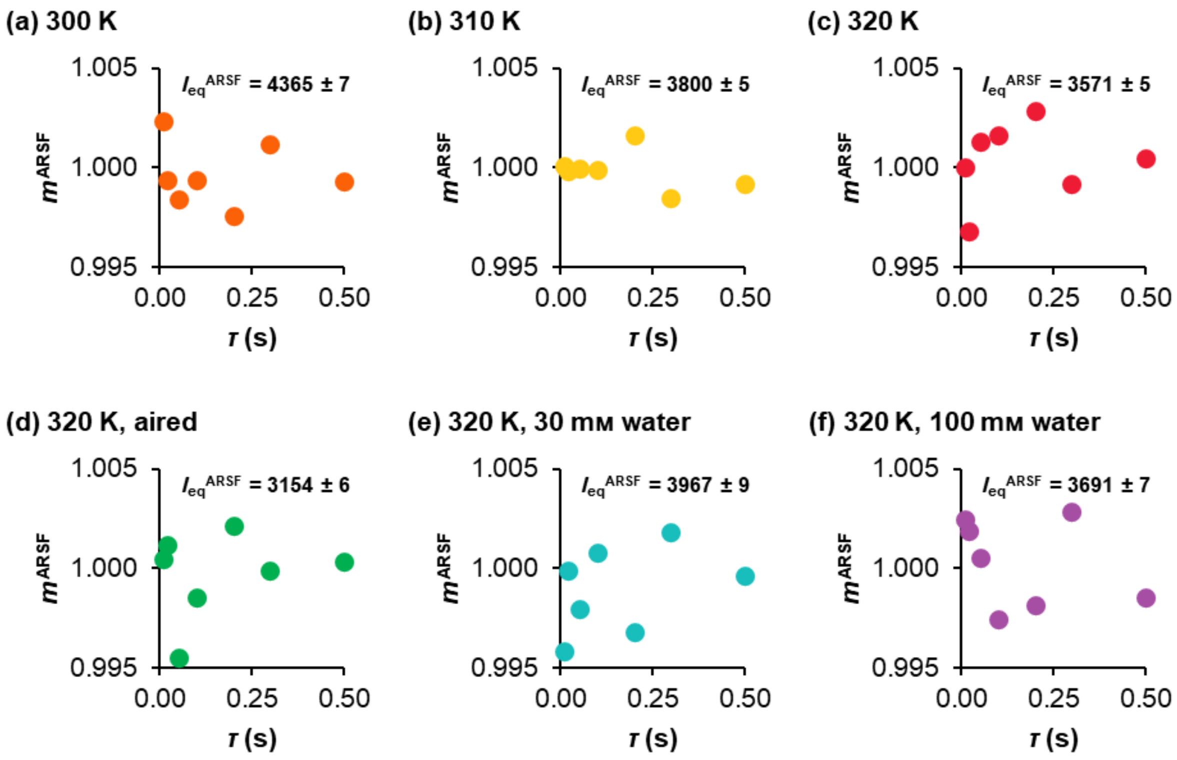

Figure 5.15: Plots of experimental fractional magnetisations of ARSF, m^{ARSF} *vs* τ (for $\tau \leq 0.5$ s) in ^{19}F selective inversion-recovery experiments between TBAT and ARSF in THF. I_{eq}^{ARSF}, used to convert experimental integrals in each experiment to the corresponding fractional magnetisations, are their averages (and given in the plots).

5.6.2. Selective inversion-recovery in MeCN and inhibition by FTPS

A solution was prepared in the glovebox by weighing TBAT (103 mg, 191 mM), ARSF (12.9 mg, 56.9 mM) and NAPH (26.8 mg, 184 mM) into a 1 mL volumetric flask and dissolving them in MeCN up to the 1 mL mark. The solution (~0.4 mL) was transferred to a J Young® valve capped NMR tube. Four sets of ^{19}F pulse-acquire (Section 5.2.1), ^{19}F inversion-recovery (Section 5.2.2) and ^{19}F selective inversion-recovery (Section 5.2.6) experiments were run at 300 K and within ~3 hours from sample preparation (except ^{19}F inversion-recovery, which was run only in the first set of experiments). A small solid aliquot of FTPS was then added to the solution (~0.5 mg, corresponding to ~4 mM FTPS), and the NMR tube shaken thoroughly. The same four sets of NMR experiments were repeated (except for ^{19}F inversion-recovery), again over ~3 hours.

The ^{19}F pulse-acquire NMR spectra were acquired twice per each set of experiments (for quantitation of TBAT and ARSF, both against NAPH) with a D_1 = 80 s relaxation delay, t_{acq} = 1.5 s acquisition time, 0 dummy scans and 1 scan. The transmitter resonance was placed at –110 ppm for TBAT/NAPH and –44 ppm for ARSF/NAPH, and the spectral window was 200 ppm. The ^{19}F inversion-recovery NMR spectra for T_1^{TBAT} and T_1^{ARSF} were acquired with a D_1 = 35 s relaxation delay, t_{acq} = 1.5 s acquisition time, 0 dummy scans and 1 scan. The transmitter resonance was placed at –30 ppm and the spectral window was 240 ppm. The variable delays used in the experiments were, τ (s) {1, 1.5, 2, 3, 4, 5, 7.5, 10, 12.5, 15, 20, 30}. The ^{19}F selective inversion-recovery NMR spectra were acquired with a D_1 = 35 s relaxation delay, t_{acq} = 1.5 s acquisition time, 0 dummy scans and 1 scan. The transmitter resonance was placed at 37 ppm, the centre frequency for the inversion pulse was placed at –96 ppm and the spectral window was 120 ppm. The variable delays used in the experiments were, τ (s) {0.001, 0.005, 0.01, 0.02, 0.05, 0.1, 0.2, 0.5, 1, 2, 3, 5, 10, 15, 20, 30}.

The ^{19}F pulse-acquire NMR spectra were processed as described in Section 5.2.1, and the concentrations of TBAT and ARSF based on NAPH are presented in Table 5.26. Based on this data, [ARSF] = (52.3 ± 0.1) mM for each experimental dataset (92% of the theoretical value based on the mass of the solute). The concentration of TBAT, however, seems vastly different before and after the addition of FTPS, [TBAT] = (188 ± 1) mM and (173 ± 2) mM, respectively (99% and 91% of the theoretical value). However, as presented in Figure 3.33e in Section 3.4.1, the presence of even such small amount of FTPS (~4 mM, *cf*. ~190 mM TBAT) caused significant line broadening in TBAT. The FTPS signal was broadened to below the detection limit (Figure 3.33f). The line broadening in TBAT/FTPS systems in MeCN was previously found to have an apparently decreasing effect on the integrals of the spins, whilst their concentrations likely remain constant. Therefore, the average of four concentrations of TBAT from before the spiking, [TBAT] = (188 ± 1) mM was used for all experimental datasets.

The ^{19}F inversion-recovery NMR spectral set was processed as described in Section 5.2.2. The determined ^{19}F longitudinal relaxation fitting parameters and root mean square errors (I_{eq}, x, T_1, R) for TBAT and ARSF were: (13633, 0.625, 4.73 s, 5) and (1896, 0.567, 2.33 s, 5). These T_1 values are nearly identical to those determined for isolated TBAT and ARSF in Section 5.4.

The ^{19}F selective inversion-recovery NMR spectral sets were processed as described in Section 5.2.6. The model as described in Section 2.4 was fitted to the four dataset from prior to the addition of FTPS, except that two fitting parameters, I_{eq} and α, were independent for each dataset, whereas the third parameter, m_0^{TBAT}, was assumed to be equal in all of them (*i.e.* the sum of 64 squares was minimised by changing 9 variable parameters, all in one fitting). The fitting parameters I_{eq} and α obtained for (the initially non-inverted) ARSF, are presented in Table 5.26. The "mutual" fitting parameter, $m_0^{TBAT} = 0.0768$, and the overall root mean square error, $R = 5$ (individual ones are given in the table). Then, fitting was performed analogously for the four datasets obtained after spiking the sample with FTPS, except m_0^{TBAT} was fixed as 0.0768 (the value obtained in the fitting of the four datasets above). This modification to the fitting procedure (as opposed to fitting each dataset individually) was applied due to the inversion transfer being much slower than relaxation. Because of this discrepancy in the rates of both processes, the absolute values of α and m_0^{TBAT} fitting parameters were prone to significant errors, but the relative changes in α between datasets were relatively independent of m_0^{TBAT} used/returned in the fitting. For example, the starting values in the fitting used herein were: the last measured integral of ARSF ($\tau = 30$ s) as I_{eq} in the given dataset, $m_0^{TBAT} = 0.07$ (approximately the value of m_0^{FTPS} in Section 5.5.1), α (s^{-1}) {0.002, 0.0015, 0.0015, 0.0015} (as these values gave good visual fits). In this case, the returned m_0^{TBAT} was very close to the starting value, and so were α for each dataset. The determined α decreased by 24.4% between the first and second run, and remained constant throughout runs 2–4. When an arbitrary $m_0^{TBAT} = 0.5$ was used as a starting value (*i.e.* saturation of TBAT as opposed to inversion), with all the remaining starting parameters unchanged, the returned $m_0^{TBAT} = 0.253$ and the newly determined $\alpha = 2.37 \cdot 10^{-3}$ s^{-1} for the first run was 24.1% larger than previously, with nearly unchanged visual fit and $R = 5$. However, the relative decrease between the first and second run was nearly identical as previously, at 24.7%.

Table 5.26: Concentrations of TBAT and ARSF (based on the internal standard, NAPH), inversion transfer fitting parameters and root mean square errors (from ^{19}F selective inversion-recovery experiments) for the solution of TBAT and ARSF in MeCN.

Conditions	[TBAT] (mM)	[ARSF] (mM)	I_{eq}	α (s^{-1})	R
Run 1	190	52.2	3183	$1.91 \cdot 10^{-3}$	4
Run 2	188	52.3	3214	$1.44 \cdot 10^{-3}$	7
Run 3	188	52.4	3217	$1.44 \cdot 10^{-3}$	5
Run 4	187	52.4	3216	$1.46 \cdot 10^{-3}$	5
FTPS, run 1	176	52.3	3170	0 (exactly)	5
FTPS, run 2	172	52.2	3172	0 (exactly)	10
FTPS, run 3	173	52.4	3183	$1.01 \cdot 10^{-4}$	9
FTPS, run 4	170	52.4	3185	$2.23 \cdot 10^{-4}$	8

The plots of experimental and model fractional magnetisations of ARSF, m^{ARSF}, against variable delay, τ, are presented in Figure 3.33c in Section 3.4.1, and individually in Figure 5.16a–d below, for the runs in the absence of added FTPS. As both fitting parameters are nearly identical for runs 2–4, a single model plot is given for these runs (with averages of the parameters determined for these runs used to construct the model and convert the experimental integrals of ARSF to fractional magnetisations). The plots for the runs in the presence of added FTPS are presented in Figure 3.33d and individually in Figure 5.16e–h below (experimental profiles only).

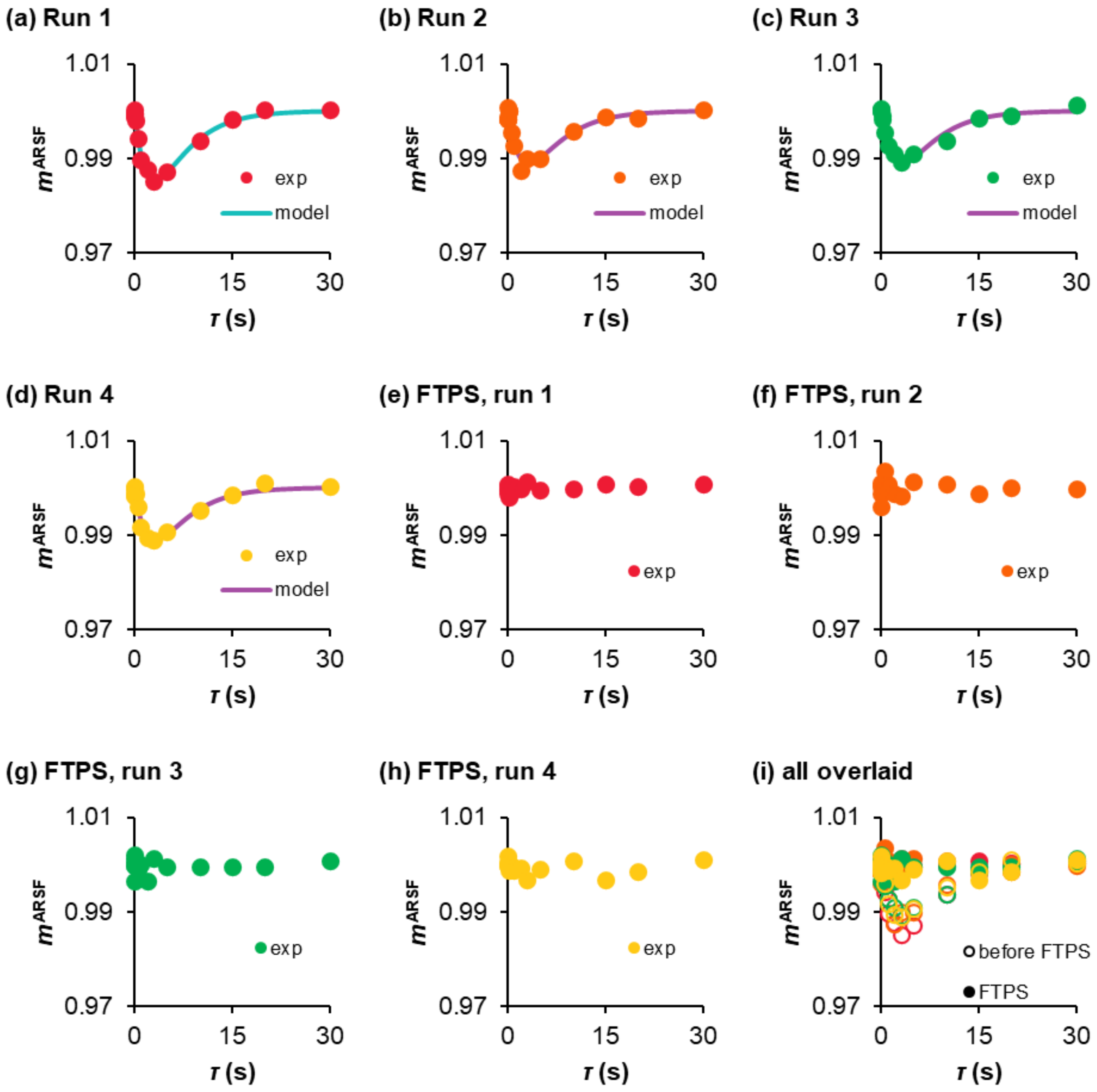

Figure 5.16: Plots of experimental (and model, where applicable) fractional magnetisations of ARSF, m^{ARSF} *vs* τ in ^{19}F selective inversion-recovery experiments between TBAT and ARSF in MeCN in the absence (a–d) and presence (e–h) of added FTPS.

5.6.3. Temporal profile

A solution was prepared in the glovebox by weighing TBAT (110 mg, 204 mM), ARSF (16.6 mg, 73.3 mM) and NAPH (54.0 mg, 370 mM) into a 1 mL volumetric flask and dissolving them in MeCN up to the 1 mL mark. The solution was transferred to a J Young® valve capped NMR tube. The date and time of preparation of the solution was also noted.

The solution was immediately inserted into the NMR probe preheated to 335 K and remained there for the duration of the experiment. Eleven sets of ^{19}F pulse-acquire (Section 5.2.1), ^{19}F inversion-recovery (Section 5.2.2) and ^{19}F selective inversion-recovery (Section 5.2.6) experiments were performed at 335 K. The date and time of each acquisition was converted to the time interval between preparation of the sample and the acquisition, t. Two ^{19}F pulse-acquire NMR spectra were acquired per set (for quantitation of TBAT and ARSF, both against NAPH) with a D_1 = 80 s relaxation delay, t_{acq} = 1.5 s acquisition time, 0 dummy scans and 1 scan. The transmitter resonance was placed at –110 ppm for TBAT/NAPH and –44 ppm for ARSF/NAPH, and the spectral window was 200 ppm. The ^{19}F inversion-recovery NMR spectra for T_1^{TBAT} and T_1^{ARSF} were acquired with a D_1 = 50 s relaxation delay, t_{acq} = 1.5 s acquisition time, 0 dummy scans and 1 scan. The transmitter resonance was placed at –30 ppm and the spectral window was 240 ppm. The variable delays used in the experiments were, τ (s) {1, 1.5, 2, 3, 4, 5, 7.5, 10, 12.5, 15, 20, 30}. The ^{19}F selective inversion-recovery NMR spectra were acquired with a D_1 = 50 s relaxation delay, t_{acq} = 1.5 s acquisition time, 0 dummy scans and 1 scan. The transmitter resonance was placed at 37 ppm, the centre frequency for the inversion pulse was placed at –96 ppm and the spectral window was 120 ppm. The variable delays used in the experiments were, τ (s) {0.01, 0.02, 0.05, 0.1, 0.2, 0.3, 0.5, 0.75, 1, 1.5, 2, 3, 5, 10, 20, 30}.

The ^{19}F pulse-acquire NMR spectra were processed as described in Section 5.2.1, and the concentrations of TBAT and ARSF based on NAPH are presented in Table 5.27. Both [ARSF] and [TBAT] decreased over time. The plot of [ARSF] against t is given in Figure 3.34. A first-order decomposition model, $[\mathrm{ARSF}] = [\mathrm{ARSF}]_\infty + ([\mathrm{ARSF}]_0 - [\mathrm{ARSF}]_\infty)e^{-kt}$ gave an excellent fit with the following fitting parameters and root mean square error (R): $[\mathrm{ARSF}]_\infty$ = 58.5 mM, $[\mathrm{ARSF}]_0$ = 67.9 mM, k = 0.275 h^{-1}, R = 0.3 mM. This models was used to calculate the concentration of ARSF during each magnetisation transfer experiment. The plot of [TBAT] against t is given in Figure 3.34. The decomposition exhibited apparent first-order kinetics for all solutions as well, $[\mathrm{TBAT}] = [\mathrm{TBAT}]_\infty + ([\mathrm{TBAT}]_0 - [\mathrm{TBAT}]_\infty)e^{-kt}$, albeit with slightly more noise as gradual broadening of the signal was observed. The fitting parameters and root mean square error (R) were: $[\mathrm{TBAT}]_\infty$ = 184 mM, $[\mathrm{TBAT}]_0$ = 201 mM, k = 0.154 h^{-1}, R = 1 mM.

Table 5.27: Evolution of concentrations of TBAT and ARSF (based on NAPH).

***t* (h), TBAT**	**[TBAT] (mM)**	***t* (h), ARSF**	**[ARSF] (mM)**
0.268	201	0.316	67.3
1.38	197	1.40	64.8
2.37	196	2.40	62.8
3.38	195	3.40	62.3
4.38	193	4.41	61.5
5.39	190	5.41	60.7
6.39	190	6.41	60.2
7.38	192	7.40	59.5
8.38	189	8.40	60.0
9.39	189	9.41	58.8
10.4	186	10.4	58.9

The ^{19}F inversion-recovery NMR spectral sets were processed as described in Section 5.2.2. The determined ^{19}F longitudinal relaxation fitting parameters and root mean square errors (I_eq, x, T_1, R) for TBAT and ARSF are presented in Table 5.28. An average of both constants were taken, T_1^TBAT = (5.70 ± 0.10) s and T_1^ARSF = (3.42 ± 0.07) s, and used for fitting the inversion transfer model to data.

Table 5.28: Fitting parameters and root mean square errors for non-selective inversion-recovery measurements.

***t* (h)**	**TBAT**				**ARSF**			
	I_eq	x	T_1 (s)	R	I_eq	x	T_1 (s)	R
0.594	12312	0.672	5.74	68	2020	0.522	3.65	12
1.61	12196	0.676	5.71	42	1968	0.524	3.54	13
2.61	12215	0.684	5.68	79	1930	0.527	3.43	13
3.61	12048	0.686	5.40	69	1919	0.523	3.55	11
4.61	12094	0.672	5.84	63	1892	0.531	3.38	12
5.62	11929	0.676	5.54	66	1882	0.527	3.39	12
6.62	11908	0.678	5.53	72	1862	0.523	3.41	10
7.61	11926	0.678	5.76	80	1851	0.529	3.36	11
8.61	11993	0.669	5.91	83	2020	0.522	3.33	12
9.62	11925	0.673	5.93	99	1968	0.524	3.29	11
10.6	11776	0.682	5.62	79	1930	0.527	3.33	13

The ^{19}F selective inversion-recovery NMR spectral sets were processed as described in Section 5.2.6. The ^{19}F exchange fitting parameters (I_eq, m_0^TBAT and α), and root mean square errors (R) obtained for (the initially non-inverted) ARSF, are presented in Table 5.29.

Table 5.29: Evolution of concentrations of TBAT and ARSF (based on NAPH).

t (h)	I_{eq}	m_0^{TBAT}	α (s^{-1})	R
0.387	3392	0.263	0.0512	11
1.41	3286	0.286	0.0464	11
2.41	3282	0.324	0.0452	11
3.42	3240	0.329	0.0427	14
4.42	3202	0.319	0.0399	15
5.42	3171	0.320	0.0380	12
6.43	3143	0.332	0.0380	14
7.42	3129	0.332	0.0366	15
8.42	3100	0.347	0.0362	15
9.42	3092	0.348	0.0359	17
10.4	3071	0.363	0.0357	12

Chapter 6

References

1 K. K. J. Chan and D. O'Hagan, in *Methods in Enzymology*, Elsevier Inc., 1st edn., 2012, vol. 516, pp. 219–235.

2 L. E. X. Leong, S. Khan, C. K. Davis, S. E. Denman and C. S. McSweeney, *J. Anim. Sci. Biotechnol.*, 2017, **8**, 55.

3 D. O'Hagan, *Chem. Soc. Rev.*, 2008, **37**, 308–319.

4 L. Pauling, *J. Am. Chem. Soc.*, 1932, **54**, 3570–3582.

5 J. C. Slater, *J. Chem. Phys.*, 1964, **41**, 3199–3204.

6 C. M. Timperley and W. E. White, *J. Fluor. Chem.*, 2003, **123**, 65–70.

7 Y. Ogawa, E. Tokunaga, O. Kobayashi, K. Hirai and N. Shibata, *iScience*, 2020, **23**, 101467.

8 M. Inoue, Y. Sumii and N. Shibata, *ACS Omega*, 2020, **5**, 10633–10640.

9 C. Zhang, *ACS Omega*, 2022, **7**, 18206–18212.

10 C. J. Wenthur, M. R. Bennett and C. W. Lindsley, *ACS Chem. Neurosci.*, 2014, **5**, 14–23.

11 L. M. Bang and L. J. Scott, *Drugs*, 2003, **63**, 2413–2424.

12 J. D. Croxtall and K. McKeage, *Drugs*, 2011, **71**, 363–380.

13 B. Ameduri, *Chem. – A Eur. J.*, 2018, **24**, 18830–18841.

14 B. Améduri, *Macromol. Chem. Phys.*, 2020, **221**, 1900573.

15 S. Casa and M. Henary, *Molecules*, 2021, **26**, 1160–1196.

16 R. Ragni, A. Punzi, F. Babudri and G. M. Farinola, *European J. Org. Chem.*, 2018, **2018**, 3500–3519.

17 M. Hird, *Chem. Soc. Rev.*, 2007, **36**, 2070–2095.

18 F. X. Tian and J. Qu, *J. Org. Chem.*, 2022, **87**, 1814–1829.

19 M. G. Hill, W. M. Lamanna and K. R. Mann, *Inorg. Chem.*, 1991, **30**, 4687–4690.

20 R. J. LeSuer, C. Buttolph and W. I. Geiger, *Anal. Chem.*, 2004, **76**, 6395–6401.

21 W. E. Geiger and F. Barrière, *Acc. Chem. Res.*, 2010, **43**, 1030–1039.

22 S. D. Lepore and D. Mondal, *Tetrahedron*, 2007, **63**, 5103–5122.

23 S. Kobayashi, M. Sugiura, H. Kitagawa and W. W. L. Lam, *Chem. Rev.*, 2002, **102**, 2227–2302.

24 M. Aufiero and R. Gilmour, *Acc. Chem. Res.*, 2018, **51**, 1701–1710.

25 L. E. Zimmer, C. Sparr and R. Gilmour, *Angew. Chem. Int. Ed.*, 2011, **50**, 11860–11871.

26 C. Thiehoff, Y. P. Rey and R. Gilmour, *Isr. J. Chem.*, 2017, **57**, 92–100.

27 E. M. Tanzer, L. E. Zimmer, W. B. Schweizer and R. Gilmour, *Chem. Eur. J.*, 2012, **18**, 11334–11342.

28 N. S. Keddie, A. M. Z. Slawin, T. Lebl, D. Philp and D. O'Hagan, *Nat. Chem.*, 2015, **7**, 483–488.

29 K. E. Arntson and W. C. K. Pomerantz, *J. Med. Chem.*, 2016, **59**, 5158–5171.

30 P. W. A. Howe, *Prog. Nucl. Magn. Reson. Spectrosc.*, 2020, **118**–**119**, 1–9.

31 A. J. R. Smith, R. York, D. Uhrín and N. G. A. Bell, *RSC Adv.*, 2022, **12**, 10062–10070.

32 Y. Ben-Tal, P. J. Boaler, H. J. A. Dale, R. E. Dooley, N. A. Fohn, Y. Gao, A. García-Domínguez, K. M. Grant, A. M. R. Hall, H. L. D. Hayes, M. M. Kucharski, R. Wei and G. C. Lloyd-Jones, *Prog. Nucl. Magn. Reson. Spectrosc.*, 2022, **129**, 28–106.

33 J. W. Emsley, L. Phillips and V. Wray, *Prog. Nucl. Magn. Reson. Spectrosc.*, 1976, **10**, 83–752.

34 D. Le Bars, *J. Fluor. Chem.*, 2006, **127**, 1488–1493.

35 S. Preshlock, M. Tredwell and V. Gouverneur, *Chem. Rev.*, 2016, **116**, 719–766.

36 M. P. Sibi and Y. Landais, *Angew. Chem. Int. Ed.*, 2013, **52**, 3570–3572.

37 M. K. Nielsen, C. R. Ugaz, W. Li and A. G. Doyle, *J. Am. Chem. Soc.*, 2015, **137**, 9571–9574.

38 I. Sharma, in *Encyclopedia of Reagents for Organic Synthesis*, John Wiley & Sons, Ltd, Chichester, UK, 2014, pp. 1–2.

39 D. Mandal, S. Maji, T. Pal, S. K. Sinha and D. Maiti, *Chem. Commun.*, 2022, 10442–10468.

40 W. J. Middleton, *J. Org. Chem.*, 1975, **40**, 574–578.

41 N. Shibata, *Bull. Chem. Soc. Jpn.*, 2016, **89**, 1307–1320.

42 G. Pupo, F. Ibba, D. M. H. Ascough, A. C. Vicini, P. Ricci, K. E. Christensen, L. Pfeifer, J. R. Morphy, J. M. Brown, R. S. Paton and V. Gouverneur, *Science*, 2018, **360**, 638–642.

43 T. Umemoto, R. P. Singh, Y. Xu and N. Saito, *J. Am. Chem. Soc.*, 2010, **132**, 18199–18205.

44 H. Jia, A. P. Häring, F. Berger, L. Zhang and T. Ritter, *J. Am. Chem. Soc.*, 2021, **143**, 7623–7628.

45 N. Yoneda, *Tetrahedron*, 1991, **47**, 5329–5365.

46 G. R. B. T. V. (Babu) RajanBabu, William J. Middleton, Victor J. Tortorelli, Myriam Roy, Richard E. Taylor, Kellie L. Weeks, in *Encyclopedia of Reagents for Organic Synthesis*, 2019.

47 N. S. Simpkins, F. E. Nytko, P. DeShong, M. Vayer and N. Maulide, in *Encyclopedia of Reagents for Organic Synthesis*, Wiley, 2020, pp. 1–14.

48 K. Hirano, *Synth.*, 2022, **54**, 3708–3718.

49 G. Pupo and V. Gouverneur, *J. Am. Chem. Soc.*, 2022, **144**, 5200–5213.

50 O. E. Okoromoba, J. Han, G. B. Hammond and B. Xu, *J. Am. Chem. Soc.*, 2014, **136**, 14381–14384.

51 H.-Y. Li, H. Sun and S. G. DiMagno, in *Encyclopedia of Reagents for Organic Synthesis*, John Wiley & Sons, Ltd, Chichester, UK, 2007.

52 X. Liu, C. Xu, M. Wang and Q. Liu, *Chem. Rev.*, 2015, **115**, 683–730.

53 C. Zhang, *Org. Biomol. Chem.*, 2014, **12**, 6580–6589.

54 J. Charpentier, N. Früh and A. Togni, *Chem. Rev.*, 2015, **115**, 650–682.

55 E. Differding and H. Ofner, *Synlett*, 1991, **1991**, 187–189.

56 M. Rueda-Becerril, C. Chatalova Sazepin, J. C. T. Leung, T. Okbinoglu, P. Kennepohl, J. F. Paquin and G. M. Sammis, *J. Am. Chem. Soc.*, 2012, **134**, 4026–4029.

57 J. H. Clark, *Chem. Rev.*, 1980, **80**, 429–452.

58 R. Schwesinger, R. Link, P. Wenzl and S. Kossek, *Chem. Eur. J.*, 2006, **12**, 438–445.

59 R. K. Sharma and J. L. Fry, *J. Org. Chem.*, 1983, **48**, 2112–2114.

60 D. P. Cox, J. Terpinski and W. Lawrynowicz, *J. Org. Chem.*, 1984, **49**, 3216–3219.

61 H. Sun and S. G. DiMagno, *J. Am. Chem. Soc.*, 2005, **127**, 2050–2051.

62 A. S. Pilcher, H. L. Ammon and P. DeShong, *J. Am. Chem. Soc.*, 1995, **117**, 5166–5167.

63 C. J. Handy, Y. F. Lam and P. DeShong, *J. Org. Chem.*, 2000, 65, 3542–3543.

64 R. Bujok and M. Mąkosza, *Synlett*, 2004, 371–373.

65 D. Albanese, D. Landini and M. Penso, *Tetrahedron Lett.*, 1995, **36**, 8865–8866.

66 M.-R. Brescia and P. DeShong, *J. Org. Chem.*, 1998, **63**, 3156–3157.

67 M. E. Mowery and P. DeShong, *J. Org. Chem.*, 1999, **64**, 3266–3270.

68 M. E. Hoke, M. Brescia, S. Bogaczyk, P. DeShong, B. W. King and M. T. Crimmins, *J. Org. Chem.*, 2002, **67**, 327–335.

69 B. B. Liau, B. C. Milgram and M. D. Shair, *J. Am. Chem. Soc.*, 2012, **134**, 16765–16772.

70 J. Naidoo, H. De Jesus-Cortes, P. Huntington, S. Estill, L. K. Morlock, R. Starwalt, T. J. Mangano, N. S. Williams, A. A. Pieper and J. M. Ready, *J. Med. Chem.*, 2014, **57**, 3746–3754.

71 Y. Kasai, N. Matsumori, H. Ueno, K. Nonomura, S. Yano, M. Michio and T. Oishi,

Org. Biomol. Chem., 2011, **9**, 1437–1442.

72 V. Gracias, G. L. Milligan and J. Aubé, *J. Org. Chem.*, 1996, **61**, 10–11.

73 P. Adler, C. J. Teskey, D. Kaiser, M. Holy, H. H. Sitte and N. Maulide, *Nat. Chem.*, 2019, **11**, 329–334.

74 V. Gurvich, H. Y. Kim, R. P. Hodge, C. M. Harris and T. M. Harris, *Nucleosides and Nucleotides*, 1999, **18**, 2327–2333.

75 E. Lee, J. M. Hooker and T. Ritter, *J. Am. Chem. Soc.*, 2012, **134**, 17456–17458.

76 J. Y. Yang, X. H. Xu and F. L. Qing, *J. Fluor. Chem.*, 2016, **186**, 45–51.

77 R. F. Gamache, C. Waldmann and J. M. Murphy, *Org. Lett.*, 2016, **18**, 4522–4525.

78 O. Tamura, A. Toyao and H. Ishibashi, *Synlett*, 2002, 1344–1346.

79 A. E. Mattson, A. M. Zuhl, T. E. Reynolds and K. A. Scheldt, *J. Am. Chem. Soc.*, 2006, **128**, 4932–4933.

80 M. J. Campbell, P. D. Pohlhaus, G. Min, K. Ohmatsu and J. S. Johnson, *J. Am. Chem. Soc.*, 2008, **130**, 9180–9181.

81 J. C. Killen, L. C. Axford, S. E. Newberry, T. J. Simpson and C. L. Willis, *Org. Lett.*, 2012, **14**, 4194–4197.

82 X. Frogneux, N. von Wolff, P. Thuéry, G. Lefèvre and T. Cantat, *Chem. Eur. J.*, 2016, **22**, 2930–2934.

83 M. E. McCallum, G. M. Smith, T. Matsumaru, K. Kong, J. A. Enquist and J. L. Wood, *J. Antibiot. (Tokyo).*, 2016, **69**, 331–336.

84 N. von Wolff, J. Char, X. Frogneux and T. Cantat, *Angew. Chem. Int. Ed.*, 2017, **56**, 5616–5619.

85 M. E. Hayes, H. Shinokubo and R. L. Danheiser, *Org. Lett.*, 2005, **7**, 3917–3920.

86 C. D. Gilmore, K. M. Allan and B. M. Stoltz, *J. Am. Chem. Soc.*, 2008, **130**, 1558–1559.

87 T. Ikawa, S. Masuda, H. Nakajima and S. Akai, *J. Org. Chem.*, 2017, **82**, 4242–

4253.

88 Y. Okugawa, Y. Hayashi, S. Kawauchi, K. Hirano and M. Miura, *Org. Lett.*, 2018, **20**, 3670–3673.

89 H. Ryu, J. Seo and H. M. Ko, *J. Org. Chem.*, 2018, **83**, 14102–14109.

90 A. Shamsabadi and V. Chudasama, *Chem. Commun.*, 2018, **54**, 11180–11183.

91 B. Cheng, Y. Li, B. Zu, T. Wang, R. Wang, Y. Li and H. Zhai, *Tetrahedron*, 2019, **75**, 1–6.

92 T. Lim and B. M. Kim, *J. Org. Chem.*, 2020, **85**, 13246–13255.

93 J. Seo, D. Kim and H. M. Ko, *Adv. Synth. Catal.*, 2020, **362**, 2739–2743.

94 Q. Wang, Y. An, G. Du, Z. H. Cai, B. Dai and L. He, *J. Org. Chem.*, 2020, **85**, 14210–14218.

95 P. Xie, S. Yang, Y. Guo, Z. Cai, B. Dai and L. He, *J. Org. Chem.*, 2020, **85**, 8872–8880.

96 J. Lei, W. Xie, J. Li, Y. Wu and X. Xie, *European J. Org. Chem.*, 2021, **2021**, 4364–4387.

97 F. Shi, R. Mancuso and R. C. Larock, *Tetrahedron Lett.*, 2009, **50**, 4067–4070.

98 M. Scherübl, C. G. Daniliuc and A. Studer, *Angew. Chem. Int. Ed.*, 2021, **60**, 711–715.

99 M. K. Zilla, S. Mahajan, R. Khajuria, V. K. Gupta, K. K. Kapoor and A. Ali, *RSC Adv.*, 2021, **11**, 3477–3483.

100 K. Donnelly and M. Baumann, *J. Org. Chem.*, 2022, **87**, 8279–8288.

101 L. Li, C. Shan, J. Shi, W. Li, Y. Lan and Y. Li, *Angew. Chem. Int. Ed.*, 2022, **61**, 1–8.

102 J. C. Haber, M. A. Lynch, S. L. Spring, A. D. Pechulis, J. Raker and Y. Wang, *Tetrahedron Lett.*, 2011, **52**, 5847–5850.

103 D. C. Rogness, N. A. Markina, J. P. Waldo and R. C. Larock, *J. Org. Chem.*, 2012, **77**, 2743–2755.

104 S. Yoshida and T. Hosoya, *Chem. Lett.*, 2013, **42**, 583–585.

105 A. Bunescu, Q. Wang and J. Zhu, *Org. Lett.*, 2014, **16**, 1756–1759.

106 A. C. Wright, C. K. Haley, G. Lapointe and B. M. Stoltz, *Org. Lett.*, 2016, **18**, 2793–2795.

107 S. M. Bronner, D. Lee, V. Bacauanu and P. Cyr, *Synlett*, 2017, **28**, 799–804.

108 B. Cheng, B. Bao, B. Zu, X. Duan, S. Duan, Y. Li and H. Zhai, *RSC Adv.*, 2017, **7**, 54087–54090.

109 C. D. Vogt, A. G. Bart, R. Yadav, E. E. Scott and J. Aubé, *Org. Biomol. Chem.*, 2021, **19**, 7664–7669.

110 C. M. Reeves, D. C. Behenna and B. M. Stoltz, *Org. Lett.*, 2014, **16**, 2314–2317.

111 B. Furman and M. Dziedzic, *Tetrahedron Lett.*, 2003, **44**, 6629–6632.

112 A. J. Blake, G. M. P. Giblin, D. T. Kirk, N. S. Simpkins and C. Wilson, *Chem. Commun.*, 2001, **24**, 2668–2669.

113 N. Hara, N. Uemura and Y. Nakao, *Chem. Commun.*, 2021, **57**, 5957–5960.

114 T. Bootwicha, D. Panichakul, C. Kuhakarn, S. Prabpai, P. Kongsaeree, P. Tuchinda, V. Reutrakul and M. Pohmakotr, *J. Org. Chem.*, 2009, **74**, 3798–3805.

115 C. J. Hayes, N. S. Simpkins, D. T. Kirk, L. Mitchell, J. Baudoux, A. J. Blake and C. Wilson, *J. Am. Chem. Soc.*, 2009, **131**, 8196–8210.

116 E. DiMauro and A. J. Fry, *Tetrahedron Lett.*, 1999, **40**, 7945–7949.

117 R. F. Cunico, *Tetrahedron Lett.*, 2002, **43**, 355–358.

118 M. Dziedzic, G. Lipner, J. M. Illangua and B. Furman, *Tetrahedron*, 2005, **61**, 8641–8647.

119 Y. Li and J. Hu, *Angew. Chem. Int. Ed.*, 2007, **46**, 2489–2492.

120 N. Wu, B. Wahl, S. Woodward and W. Lewis, *Chem. Eur. J.*, 2014, **20**, 7718–7724.

121 B. Wahl, A. Cabré, S. Woodward and W. Lewis, *Tetrahedron Lett.*, 2014, **55**, 5829–5831.

122 Y. Cai, W. Zhu, S. Zhao, C. Dong, Z. Xu and Y. Zhao, *Org. Lett.*, 2021, **23**, 3546–3551.

123 K. Kikushima, H. Koyama, K. Kodama and T. Dohi, *Molecules*, , DOI:10.3390/molecules26051365.

124 G. K. Surya Prakash, R. Mogi and G. A. Olah, *Org. Lett.*, 2006, **8**, 3589–3592.

125 M. Fuertes, C. Masdeu, E. Martin-Encinas, A. Selas, G. Rubiales, F. Palacios and C. Alonso, *Molecules*, 2020, **25**, 3252.

126 A. Ben Jamaa, M. Latrache, E. Riguet and F. Grellepois, *J. Org. Chem.*, 2020, **85**, 9585–9598.

127 G. K. S. Prakash, M. Mandal and G. A. Olah, *Angew. Chemie Int. Ed.*, 2001, **40**, 589–590.

128 G. K. S. Prakash, M. Mandal and G. A. Olah, *Org. Lett.*, 2001, **3**, 2847–2850.

129 G. K. S. Prakash, M. Mandal and G. A. Olah, *Synlett*, 2001, 77–78.

130 C. P. Johnston, T. H. West, R. E. Dooley, M. Reid, A. B. Jones, E. J. King, A. G. Leach and G. C. Lloyd-Jones, *J. Am. Chem. Soc.*, 2018, **140**, 11112–11124.

131 C. Masusai, D. Soorukram, C. Kuhakarn, P. Tuchinda, V. Reutrakul and M. Pohmakotr, *J. Fluor. Chem.*, 2013, **154**, 37–42.

132 A. García-Domínguez, T. H. West, J. J. Primozic, K. M. Grant, C. P. Johnston, G. G. Cumming, A. G. Leach and G. C. Lloyd-Jones, *J. Am. Chem. Soc.*, 2020, **142**, 14649–14663.

133 F. Wang, T. Luo, J. Hu, Y. Wang, H. S. Krishnan, P. V. Jog, S. K. Ganesh, G. K. S. Prakash and G. A. Olah, *Angew. Chem. Int. Ed.*, 2011, **50**, 7153–7157.

134 G. K. Friestad, C. S. Korapala and H. Ding, *J. Org. Chem.*, 2006, **71**, 281–289.

135 A. S. Pilcher and P. DeShong, *J. Org. Chem.*, 1996, **61**, 6901–6905.

136 S. Yamasaki, K. Fujii, R. Wada, M. Kanai and M. Shibasaki, *J. Am. Chem. Soc.*, 2002, **124**, 6536–6537.

137 A. García-Domínguez, P. H. H. De Oliveira, G. T. Thomas, A. R. Sugranyes and G. C. Lloyd-Jones, *ACS Catal.*, 2021, **11**, 3017–3025.

138 G. K. Friestad and H. Ding, *Angew. Chem. Int. Ed.*, 2001, **40**, 4491–4493.

139 N. A. Romero, W. O. Parker and T. M. Swager, *Macromolecules*, 2019, **52**, 8256–8265.

140 A. Motoshige, J. Kakinuma, T. Iyoda and T. Sanji, *Polym. Chem.*, 2016, **7**, 2323–2328.

141 T. Sanji and T. Iyoda, *J. Am. Chem. Soc.*, 2014, **136**, 10238–10241.

142 R. Shimazumi, K. Morita, T. Yoshida, K. Yasui and M. Tobisu, *Synthesis (Stuttg).*, 2021, **53**, 3037–3044.

143 S. Large, N. Roques and B. R. Langlois, *J. Org. Chem.*, 2000, **65**, 8848–8856.

144 L. Finck and M. Oestreich, *Chem. Eur. J.*, 2021, **27**, 11061–11064.

145 H. Fujioka, T. Okitsu, T. Ohnaka, R. Li, O. Kubo, K. Okamoto, Y. Sawama and Y. Kita, *J. Org. Chem.*, 2007, **72**, 7898–7902.

146 E. D. Soli and P. DeShong, *J. Org. Chem.*, 1999, **64**, 9724–9726.

147 D. C. Behenna, J. T. Mohr, N. H. Sherden, S. C. Marinescu, A. M. Harned, K. Tani, M. Seto, S. Ma, Z. Novák, M. R. Krout, R. M. McFadden, J. L. Roizen, J. A. Enquist, D. E. White, S. R. Levine, K. V. Petrova, A. Iwashita, S. C. Virgil and B. M. Stoltz, *Chem. Eur. J.*, 2011, **17**, 14199–14223.

148 J. Huang and I. Marek, *European J. Org. Chem.*, 2020, **2020**, 3133–3137.

149 Z. Nelson, N. A. Romero, J. Tiepelt, M. Baldo and T. M. Swager, *Macromolecules*, 2021, **54**, 6698–6704.

150 É. Bélanger, K. Cantin, O. Messe, M. Tremblay and J. F. Paquin, *J. Am. Chem. Soc.*, 2007, **129**, 1034–1035.

151 B. M. Trost and M. K. Brennan, *Org. Lett.*, 2006, **8**, 2027–2030.

152 T. Kawatsu, S. Kataoka, N. Fukaya, J. C. Choi, K. Sato and K. Matsumoto, *ACS Omega*, 2021, **6**, 12853–12857.

153 J. Yun and S. L. Buchwald, *Org. Lett.*, 2001, **3**, 1129–1131.

154 B. I. Estipona, B. P. Pritchett, R. A. Craig and B. M. Stoltz, *Tetrahedron*, 2016,

72, 3707–3712.

155 X. Zong, S. Liu, Z. Zhang, L. Ji, T. Zhang, Z. Jia and T. P. Loh, *J. Org. Chem.*, 2022, **87**, 6918–6926.

156 J. Krüger and E. M. Carreira, *J. Am. Chem. Soc.*, 1998, **120**, 837–838.

157 T. Risgaard, K. V. Gothelf and K. A. Jørgensen, *Org. Biomol. Chem.*, 2003, **1**, 153–156.

158 B. L. Pagenkopf, J. Krüger, A. Stojanovic and E. M. Carreira, *Angew. Chem. Int. Ed.*, 1998, **37**, 3124–3126.

159 B. Bazán-Tejeda, G. Bluet, G. Broustal and J. M. Campagne, *Chem. Eur. J.*, 2006, **12**, 8358–8366.

160 B. Lecachey, L. Palais, B. de Courcy, S. Bouauli, M. Durandetti, H. Oulyadi, A. Harisson-Marchand, J. Maddaluno, H. Gérard, E. Vrancken and J. M. Campagne, *Chem. Eur. J.*, 2021, **27**, 7942–7950.

161 J. Takino, A. Kotani, T. Ozaki, W. Peng, J. Yu, Y. Guo, S. Mochizuki, K. Akimitsu, M. Hashimoto, T. Ye, A. Minami and H. Oikawa, *Angew. Chem. Int. Ed.*, 2021, **60**, 23403–23411.

162 A. García-Domínguez, P. H. Helou de Oliveira, G. T. Thomas, A. R. Sugranyes and G. C. Lloyd-Jones, *ACS Catal.*, 2021, **11**, 3017–3025.

163 A. García-Domínguez, A. G. Leach and G. C. Lloyd-Jones, *Acc. Chem. Res.*, 2022, **55**, 1324–1336.

164 N. H. Angello, R. E. Wiley, C. J. Abelt and J. R. Scheerer, *Molecules*, 2020, **25**, 3358.

165 M. Gonay, C. Batisse and J. F. Paquin, *J. Org. Chem.*, 2020, **85**, 10253–10260.

166 B. M. Trost and M. K. Brennan, *Org. Lett.*, 2007, **9**, 3961–3964.

167 D. Chusov and A. A. Tsygankov, *ACS Catal.*, 2021, **11**, 13077–13084.

168 B. M. Trost and C. Jiang, *J. Am. Chem. Soc.*, 2001, **123**, 12907–12908.

169 B. M. Trost, W. H. Chan and S. Malhotra, *Chem. Eur. J.*, 2017, **23**, 4405–4414.

170 K. Kikushima, M. Grellier, M. Ohashi and S. Ogoshi, *Angew. Chem. Int. Ed.*, 2017, **56**, 16191–16196.

171 N. E. Kanitz, M. Fresia, P. G. Jones and T. Lindel, *European J. Org. Chem.*, 2021, **2021**, 3573–3578.

172 G. Takikawa, K. Toma and K. Uneyama, *Tetrahedron Lett.*, 2006, **47**, 6509–6511.

173 Y. Nakamura and K. Uneyama, *J. Org. Chem.*, 2007, **72**, 5894–5897.

174 K. Fuchibe, R. Takayama, T. Yokoyama and J. Ichikawa, *Chem. Eur. J.*, 2017, **23**, 2831–2838.

175 R. García-Vázquez, U. M. Battisti, V. Shalgunov, G. Schäfer, M. Barz and M. M. Herth, *Macromol. Rapid Commun.*, 2022, **43**, 1–7.

176 K. M. Peese and D. Y. Gin, *J. Am. Chem. Soc.*, 2006, **128**, 8734–8735.

177 F. Klanberg and E. L. Muetterties, *Inorg. Chem.*, 1968, **7**, 155–160.

178 R. K. Marat and A. F. Janzen, *Can. J. Chem.*, 1977, **55**, 1167–1174.

179 S. Yamaguchi, S. Akiyama and K. Tamao, *Organometallics*, 1999, **18**, 2851–2854.

180 S. Spirk, F. Belaj, M. Nieger, H. Köfeler, G. N. Rechberger and R. Pietschnig, *Chem. Eur. J.*, 2009, **15**, 9521–9529.

181 R. K. Marat and A. F. Janzen, *Can. J. Chem.*, 1977, **55**, 3845–3849.

182 R. Damrauer and S. E. Danahey, *Organometallics*, 1986, **5**, 1490–1494.

183 S. E. Johnson, R. O. Day and R. R. Holmes, *Inorg. Chem.*, 1989, **28**, 3182–3189.

184 S. E. Johnson, J. S. Payne, R. O. Day, J. M. Holmes and R. R. Holmes, *Inorg. Chem.*, 1989, **28**, 3190–3198.

185 R. Damrauer, B. O'Connell, S. E. Danahey and R. Simon, *Organometallics*, 1989, **8**, 1167–1171.

186 K. Tamao, T. Hayashi, Y. Ito and M. Shiro, *Organometallics*, 1992, **11**, 182–191.

187 C. Chuit, R. J. P. Corriu, C. Reye and J. C. Young, *Chem. Rev.*, 1993, **93**, 1371–1448.

188 H. J. Frohn and V. V. Bardin, *J. Organomet. Chem.*, 1995, **501**, 155–159.

189 N. L. Dean and J. S. McIndoe, *Can. J. Chem.*, 2018, **96**, 587–590.

190 M. Mąkosza and R. Bujok, *J. Fluor. Chem.*, 2005, **126**, 209–216.

191 R. Schwesinger, R. Link, P. Wenzl and S. Kossek, *Chem. Eur. J.*, 2005, **12**, 438–445.

192 Q. Zheng, H. Xu, H. Wang, W. G. H. Du, N. Wang, H. Xiong, Y. Gu, L. Noodleman, K. B. Sharpless, G. Yang and P. Wu, *J. Am. Chem. Soc.*, 2021, **143**, 3753–3763.

193 O. Planas, V. Peciukenas, M. Leutzsch, N. Nöthling, D. A. Pantazis and J. Cornella, *J. Am. Chem. Soc.*, 2022, **144**, 14489–14504.

194 A. D. Blum, S. H. Smallcombe and R. L. Baldwin, *J. Mol. Biol.*, 1978, **118**, 305–316.

195 H. S. Gutowsky and A. Saika, *J. Chem. Phys.*, 1953, **21**, 1688–1694.

196 H. S. Gutowsky and C. H. Holm, *J. Chem. Phys.*, 1956, **25**, 1228–1234.

197 Z. Luz and S. Meiboom, *J. Chem. Phys.*, 1963, **39**, 366–370.

198 A. Allerhand and H. S. Gutowsky, *J. Chem. Phys.*, 1964, **41**, 2115–2126.

199 A. Allerhand and H. S. Gutowsky, *J. Chem. Phys.*, 1965, **42**, 1587–1599.

200 S. Forsén and R. A. Huffman, *J. Chem. Phys.*, 1963, **39**, 2892–2901.

201 S. Forsén and R. A. Hoffman, *J. Chem. Phys.*, 1964, **40**, 1189–1196.

202 C. L. Perrin and T. J. Dwyer, *Chem. Rev.*, 1990, **90**, 935–967.

203 R. E. D. Mcclung and G. H. M. Aarts, *J. Magn. Reson. Ser. A*, 1995, **115**, 145–154.

204 A. D. Bain and D. A. Fletcher, *Mol. Phys.*, 1998, **95**, 1091–1098.

205 F. W. Dahlquist, K. J. Longmuir and R. B. D. Vernet, *J. Magn. Reson.*, 1975, **17**, 406–410.

206 J. R. Alger and J. H. Prestegard, *J. Magn. Reson.*, 1977, **27**, 137–141.

207 T. R. Brown and S. Ogawa, *Proc. Nat. Acad. Sci.*, 1977, **74**, 3627–3631.

208 G. A. Morris and R. Freeman, *J. Magn. Reson.*, 1978, **29**, 433–462.

209 P. Vallurupalli, A. Sekhar, T. Yuwen and L. E. Kay, *J. Biomol. NMR*, 2017, **67**, 243–271.

210 D. Columbus, V. Arunachalam, F. Glang, L. Avram, S. Haber, A. Zohar, M. Zaiss and M. Leskes, *J. Am. Chem. Soc.*, 2022, **144**, 9836–9844.

211 R. Freeman, *Prog. Nucl. Magn. Reson. Spectrosc.*, 1998, **32**, 59–106.

212 G. Liu, X. Song, K. W. Y. Chan and M. T. Mcmahon, *NMR Biomed.*, 2013, **26**, 810–828.

213 F. Bloch, *Phys. Rev.*, 1946, **70**, 460–474.

214 H. M. McConnell, *J. Chem. Phys.*, 1958, **28**, 430–431.

215 C. R. Malloy, A. D. Sherry and R. L. Nunnally, *J. Magn. Reson.*, 1985, **64**, 243–254.

216 C. L. Perrin and E. R. Johnston, *J. Magn. Reson.*, 1979, **33**, 619–626.

217 M. Grassi, B. E. Mann, B. T. Pickup and C. M. Spencer, *J. Magn. Reson.*, 1986, **69**, 92–99.

218 A. D. Bain and J. A. Cramer, *J. Magn. Reson. - Ser. A*, 1996, **118**, 21–27.

219 K. Uğurbil, *J. Magn. Reson.*, 1985, **64**, 207–219.

220 J. B. Lambert and J. W. Keepers, *J. Magn. Reson.*, 1980, **38**, 233–244.

221 P. S. Pregosin, *Magn. Reson. Chem.*, 2017, **55**, 405–413.

222 R. Dewan and M. N. Roy, *Phys. Chem. Liq.*, 2011, **49**, 145–154.

223 P. S. Pregosin, *Pure Appl. Chem.*, 2009, **81**, 615–633.

224 S. D. Schimler, R. D. J. Froese, D. C. Bland and M. S. Sanford, *J. Org. Chem.*, 2018, **83**, 11178–11190.

225 L. Merakeb, S. Bennaamane, J. De Freitas, E. Clot, N. Mézailles and M. Robert,

Angew. Chemie Int. Ed., 2022, **61**, e20220989.

226 D. B. G. Williams and M. Lawton, *J. Org. Chem.*, 2010, **75**, 8351–8354.

227 D. H. Wu, A. Chen and C. S. Johnson, *J. Magn. Reson. Ser. A*, 1995, 115, 260–264.

228 H. Kessler, H. Oschkinat, C. Griesinger and W. Bermel, *J. Magn. Reson.*, 1986, **70**, 106–133.

229 J. Stonehouse, P. Adell, J. Keeler and A. J. Shaka, *J. Am. Chem. Soc.*, 1994, **116**, 6037–6038.

230 K. Stott, J. Keeler, T. L. Hwang, A. J. Shaka and J. Stonehouse, *J. Am. Chem. Soc.*, 1995, **117**, 4199–4200.

231 J. Zhou and P. C. M. va. Zijl, *Prog. Nucl. Magn. Reson. Spectrosc.*, 2006, **48**, 109–136.

232 P. C. M. Van Zijl and N. N. Yadav, *Magn. Reson. Med.*, 2011, **65**, 927–948.

Chapter 7

Appendices

7.1. Mathematics

7.1.1. Relaxation rate constants of $\mathrm{TBAT}^{\blacktriangledown\blacktriangledown}$ and $\mathrm{TBAT}^{\blacktriangledown\blacktriangle}$ relative to T_1^{TBAT}

The relaxation of TBAT (Scheme 2.3) is a sequence of two consecutive first order processes. Assuming that the relaxation of each of the equivalent ^{19}F nuclei in TBAT is independent of the magnetisation state of the other, the first step is twice as likely as the second one, 2*k* and *k*, respectively (Scheme 7.1). The integrated rate law for this reaction sequence is shown in Equations 7.1–7.3 (where x^{AA}, x^{AB} and x^{BB} are the molar fractions of AA, AB and BB, and assuming initially only AA is present, $x_0^{\mathrm{AA}} = 1$).

$$\mathbf{AA} \xrightarrow{2k} \mathbf{AB} \xrightarrow{k} \mathbf{BB}$$

Scheme 7.1: A sequence of two consecutive unimolecular reactions where equivalent and independent reactive sites A react to form B.

7.1

$$x^{\mathrm{AA}} = e^{-2kt}$$

7.2

$$x^{\mathrm{AB}} = -2(e^{-2kt} - e^{-kt})$$

7.3

$$x^{\mathrm{BB}} = 1 + e^{-2kt} - 2e^{-kt}$$

The fractional conversion (in Scheme 7.1 that of reactive sites A into B), which corresponds to the fractional magnetisation of TBAT (for AA ≡ $\mathrm{TBAT}^{\blacktriangledown\blacktriangledown}$, AB ≡ $\mathrm{TBAT}^{\blacktriangledown\blacktriangle}$ and BB ≡ $\mathrm{TBAT}^{\blacktriangle\blacktriangle}$), is therefore given by $x^{\mathrm{AB}}/2 + x^{\mathrm{BB}}$. From Equations 7.2 and 7.3, this gives:

7.4

$$\frac{x^{\mathrm{AB}}}{2} + x^{\mathrm{BB}} = 1 - e^{-kt}$$

According to the standard T_1 inversion-recovery equation:

7.5

$$\frac{M_z^{\mathrm{TBAT}}}{M_{z,\mathrm{eq}}^{\mathrm{TBAT}}} = 1 - 2e^{-\frac{\tau}{T_1^{\mathrm{TBAT}}}}$$

Equation 7.5 can be expressed as fractional magnetisation, m^{TBAT}, *vs* variable delay (see Equation 2.22):

7.6

$$m^{\mathrm{TBAT}} = 1 - e^{-\frac{\tau}{T_1^{\mathrm{TBAT}}}}$$

The fractional magnetisation in Equation 7.6 corresponds to the fractional conversion in Equation 7.4 and therefore:

7.7

$$e^{-\frac{\tau}{T_1^{\mathrm{TBAT}}}} = e^{-kt}$$

Where t and τ both correspond to reaction time (from *time* = 0) and hence represent the same value.

Therefore, $1/T_1^{\mathrm{TBAT}}$ is equal to the rate constant of the second relaxation step, k, (*i.e.* half the rate constant of the first step), as shown in Scheme 2.3.

7.1.2. Derivation of constants c_1–c_4

The constants c_1–c_4 can be determined as follows (where m_0^{TBAT} and m_0^{FTPS} are the fractional magnetisations of TBAT and FTPS at $\tau = 0$).

Firstly, Equations 2.61 and 2.62 at $\tau = 0$ give:

7.8

$$m_0^{\mathrm{TBAT}} = c_1 + c_2 + 1$$

7.9

$$m_0^{\mathrm{FTPS}} = c_3 + c_4 + 1$$

The first derivatives of Equations 2.61 and 2.62 at $\tau = 0$ are:

7.10

$$\left(\frac{dm^{\mathrm{TBAT}}}{d\tau}\right)_0 = \beta(c_1 + c_2) + \gamma(c_1 - c_2)$$

7.11

$$\left(\frac{dm^{\mathrm{FTPS}}}{d\tau}\right)_0 = \beta(c_3 + c_4) + \gamma(c_3 - c_4)$$

Also, Equations 2.55 and 2.56 at $\tau = 0$ are:

7.12

$$\left(\frac{dm^{\mathrm{TBAT}}}{d\tau}\right)_0 = \frac{1}{T_1^{\mathrm{TBAT}}}\left(1 - m_0^{\mathrm{TBAT}}\right) + \alpha\left(m_0^{\mathrm{FTPS}} - m_0^{\mathrm{TBAT}}\right)$$

7.13

$$\left(\frac{dm^{\mathrm{FTPS}}}{d\tau}\right)_0 = \frac{1}{T_1^{\mathrm{FTPS}}}\left(1 - m_0^{\mathrm{FTPS}}\right) + r\alpha\left(m_0^{\mathrm{TBAT}} - m_0^{\mathrm{FTPS}}\right)$$

Solving the system of Equations 7.8–7.13 gives the constants c_1–c_4.

2.65, recalled

$$c_1 = \frac{\alpha\left(m_0^{\mathrm{FTPS}} - m_0^{\mathrm{TBAT}}\right) + \left(\beta - \gamma + \frac{1}{T_1^{\mathrm{TBAT}}}\right)\left(1 - m_0^{\mathrm{TBAT}}\right)}{2\gamma}$$

2.66, recalled

$$c_2 = -\frac{\alpha\left(m_0^{\mathrm{FTPS}} - m_0^{\mathrm{TBAT}}\right) + \left(\beta + \gamma + \frac{1}{T_1^{\mathrm{TBAT}}}\right)\left(1 - m_0^{\mathrm{TBAT}}\right)}{2\gamma}$$

2.67, recalled

$$c_3 = \frac{r\alpha\left(m_0^{\mathrm{TBAT}} - m_0^{\mathrm{FTPS}}\right) + \left(\beta - \gamma + \frac{1}{T_1^{\mathrm{FTPS}}}\right)\left(1 - m_0^{\mathrm{FTPS}}\right)}{2\gamma}$$

2.68, recalled

$$c_4 = -\frac{r\alpha\left(m_0^{\mathrm{TBAT}} - m_0^{\mathrm{FTPS}}\right) + \left(\beta + \gamma + \frac{1}{T_1^{\mathrm{FTPS}}}\right)\left(1 - m_0^{\mathrm{FTPS}}\right)}{2\gamma}$$

7.1.3. Dissociative pathway in the non-stabilised TBAT/FTPS system

We start from Equation 2.77, which describes the fractional magnetisation of TBAT in TBAT/FTPS systems upon selective inversion of FTPS.

2.77, recalled

$$m^{\mathrm{TBAT}} = \frac{\Delta m_0}{r+1}\left[e^{-\alpha(r+1)\tau} - e^{-\frac{\tau}{T_1^{\mathrm{obs}}}}\right] + 1$$

The (concentration-dependent) observed rate constant of inversion transfer between the spins is $\alpha(r + 1)$, where:

2.53, recalled

$$\alpha = k_1^{\mathrm{obs}} + k_2^{\mathrm{obs}} c^{\mathrm{FTPS}}$$

2.54, recalled

$$r = \frac{M_{z,\mathrm{eq}}^{\mathrm{TBAT}}}{M_{z,\mathrm{eq}}^{\mathrm{FTPS}}} = \frac{2[\mathrm{TBAT}]}{[\mathrm{FTPS}]} \approx \frac{2c^{\mathrm{TBAT}}}{c^{\mathrm{FTPS}}}$$

We start with a solution of TBAT (c^{TBAT}) and FTPS (c^{FTPS}) and measure $\alpha(r + 1)$ using a selective inversion-recovery experiment. We then titrate the solution with solid FTPS and measure $\alpha(r + 1)$ after each aliquot addition. To simplify mathematical operations, we assume the following:

- Each aliquot increases the concentration of FTPS by c^{FTPS} (*i.e.* its concentration in the original solution).

- The selective inversion-recovery experiments are acquired in equal time intervals (*t*) and themselves are of negligible duration. The time between preparation of the original solution and the first acquisition is also *t*.
- k_1^{obs} is a linear function of time with slope = *a* and intercept = *b*, which are independent of the concentration of FTPS.
- $k_2^{\text{obs}} = 0$, independently of time.

Then:

7.14

$$\alpha(r+1) = (b + at + ait)\left(\frac{2c^{\text{TBAT}}}{c^{\text{FTPS}} + ic^{\text{FTPS}}} + 1\right) = (b + at + ait)\left(\frac{r}{i+1} + 1\right)$$

Where *i* is the aliquot number (*i* = 0 is the original solution, *i* = 1 is the solution after first aliquot *etc*.).

Taking a derivative of this equation with respect to *i*:

7.15

$$\frac{d[\alpha(r+1)]}{di} = \frac{atc^{\text{FTPS}}(i+1) - 2bc^{\text{TBAT}}}{c^{\text{FTPS}}(i+1)^2} = \frac{at(i+1) - br}{(i+1)^2}$$

This function is decreasing when:

7.16

$$(i+1) < \frac{2bc^{\text{TBAT}}}{atc^{\text{FTPS}}} = \frac{br}{at}$$

Of course, *i* is fixed as {0, 1, 2…}. Assuming that the coefficients *a* and *b* are also fixed (*i.e.* the inherent temporal instability of the system cannot be changed), there are two ways to maximise the chance of observing a decrease in exchange rate between TBAT and FTPS in a titration of the former with the latter: (i) maximising *r* and (ii) minimising *t*. In other words, preparing a very concentrated solution of TBAT and titrating it with very small amounts of FTPS (although large enough for sufficient signal-to-noise ratio) may show a decrease in the exchange rate, followed by an increase towards higher *i*. Decreasing time, *t*, between the runs will also have an effect.

Similarly, minimising c^{FTPS} will decrease the relative contribution of direct transfer pathway to the net exchange rate. Assuming all of the above, except this time $k_2^{\text{obs}} > 0$ (and independent of time).

7.17

$$\alpha(r+1) = \left(b + at + ait + k_2^{\mathrm{obs}}c^{\mathrm{FTPS}} + k_2^{\mathrm{obs}}ic^{\mathrm{FTPS}}\right)\left(\frac{2c^{\mathrm{TBAT}}}{c^{\mathrm{FTPS}} + ic^{\mathrm{FTPS}}} + 1\right)$$

$$= \left(b + at + ait + k_2^{\mathrm{obs}}c^{\mathrm{FTPS}} + k_2^{\mathrm{obs}}ic^{\mathrm{FTPS}}\right)\left(\frac{r}{i+1} + 1\right)$$

7.18

$$\frac{d[\alpha(r+1)]}{di} = \frac{\left(at + k_2^{\mathrm{obs}}c^{\mathrm{FTPS}}\right)c^{\mathrm{FTPS}}(i+1)^2 - 2bc^{\mathrm{TBAT}}}{c^{\mathrm{FTPS}}(i+1)^2} = \frac{\left(at + k_2^{\mathrm{obs}}c^{\mathrm{FTPS}}\right)(i+1)^2 - br}{(i+1)^2}$$

7.19

$$(i+1) < \sqrt{\frac{2bc^{\mathrm{TBAT}}}{\left(at + k_2^{\mathrm{obs}}c^{\mathrm{FTPS}}\right)c^{\mathrm{FTPS}}}} = \sqrt{\frac{br}{at + k_2^{\mathrm{obs}}c^{\mathrm{FTPS}}}}$$

7.2. Water content in FTPS

In the glovebox, MeCN-d_3 (0.300 mL, accurately) was transferred to a J Young® valve capped NMR tube *via* a microsyringe, and a ^{1}H NMR spectrum of the sample was acquired. The solution was then titrated with five aliquots of solid FTPS (also in the glovebox). After each aliquot addition, the NMR tube was shaken thoroughly, and a ^{1}H NMR spectrum of the sample was acquired.

The concentration of the residual solvent peak was determined as [CHD_2CN] = 115 mM, based on integration of the signal against FTPS (Table 7.1); which corresponds to the isotopic purity of 99.8% (the minimum purity assured by the supplier).

Table 7.1: Integration of residual CHD_2CN against FTPS.

Aliquot	Mass of FTPS in aliquot (mg)	Total concentration of FTPS (mM)	Integral ratio (FTPS/solvent)
1	12.2	146	18.7
2	14.2	315	41.0
3	11.8	457	59.8
4	14.0	624	81.7
5	17.8	837	109

Water was quantified against ^{13}C satellites of the solvent peak (each of the two satellites corresponded to 636 µM). The calculated concentrations of water were plotted against the total concentration of FTPS, [FTPS], and are presented in Figure 7.1a. The water content in the final sample (837 mM FTPS) was then re-measured over ~2 h, and the calculated concentrations of water were plotted against time (t, from addition of the final aliquot of FTPS); Figure 7.1b. The plots show that water content in the sample was unaffected by addition of FTPS (*i.e.* the water came solely from the solvent and/or the glassware) and constant over time (*i.e.* no hydrolytic decomposition of FTPS). The average concentration of water, from all ten measurement, was $[H_2O] = (206 \pm 11)$ µM.

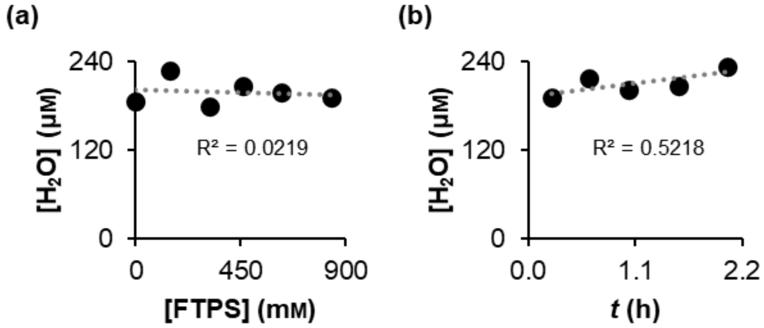

Figure 7.1: (a) Water content in the sample *vs* total concentration of FTPS in a titration of MeCN-d_3 with solid FTPS. (b) Water content in the sample obtained from the final addition of FTPS, measured over time.

7.3. Assignment of ^{1}H and ^{13}C NMR spectra of TBAT

The ^{1}H NMR spectra of TBAT in THF-d_8 and MeCN-d_3 are presented in Figure 3.1b (Section 3.1) and recalled in Figure 7.2 below.

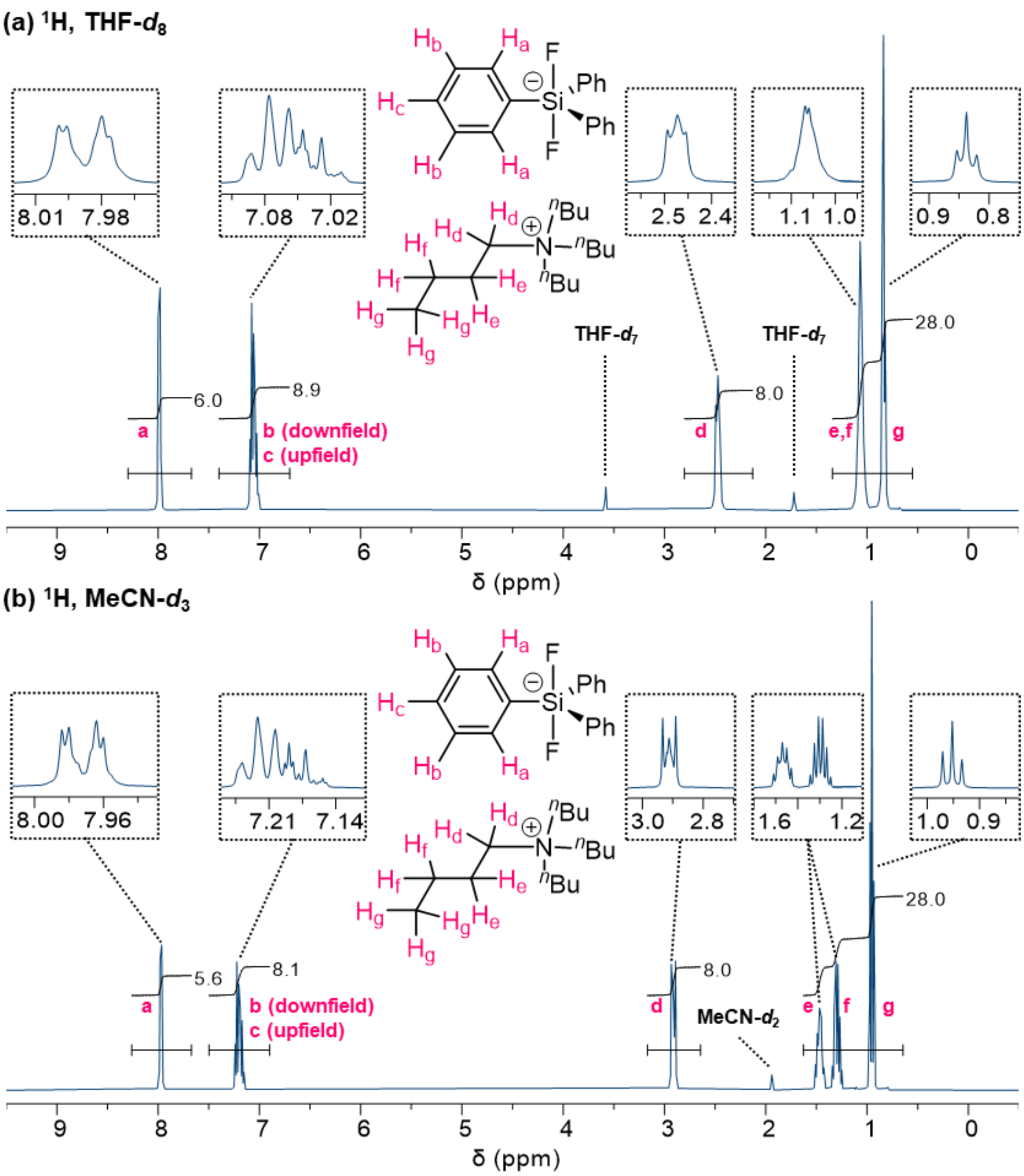

Figure 7.2: ^{1}H NMR spectra of TBAT in (a) THF-d_8 and (b) MeCN-d_3.

Aliphatic protons (^{n}Bu$_4$N$^+$)

In both solvents, the most upfield signal (triplet; THF-d_8: 0.84 ppm, $^3J_{HH}$ = 6.70 Hz; MeCN-d_3: 0.95 ppm, $^3J_{HH}$ = 7.35 Hz) was readily assigned to C(H$_g$)$_3$; and the most downfield aliphatic one (multiplet; THF-d_8: 2.45–2.49 ppm; MeCN-d_3: 2.89–2.93 ppm) – to C(H$_d$)$_2$N. The remaining C(H$_{e,f}$)$_2$ spins are not resolved in THF-d_8 (multiplet, 1.00–1.12 ppm). In MeCN-d_3, these signal are resolved: C(H$_f$)$_2$ (apparent sextet; 1.30 ppm, $^3J_{HH}$ = 7.35 Hz); C(H$_e$)$_2$ (multiplet; 1.43–1.51 ppm).

Aromatic protons ($Ph_3SiF_2^-$)

In both solvents, there are two signals in the aromatic region: a downfield doublet of doublets (THF-d_8: 7.99 ppm, $^3J_{HH}$ = 7.87 Hz, $^4J_{HH}$ = 1.60 Hz; MeCN-d_3: 8.09 ppm, $^3J_{HH}$ = 8.00 Hz, $^4J_{HH}$ = 1.58 Hz) and an upfield multiplet (THF-d_8: 7.00–7.10 ppm; MeCN-d_3: 7.15–7.25 ppm). The ratio of integrals (2:3 downfield to upfield) indicates that C(H_c) is part of the multiplet, and the splitting pattern of the doublet of doublets (one *ortho* and one *meta* coupling) – that it is C(H_a). The upfield multiplet was analysed further with the aid of ^{1}H–^{1}H COSY (pulse sequence: cosygpmfqf; 128 dummy scans, 4 scans, D_1 = 1.50 s, t_{acq} = 0.262 s); the aromatic regions of these spectra are presented in Figure 7.3. C(H_a) and the left-hand-side of the multiplet show strong coupling, indicating that the latter is C(H_b). Weaker coupling is shown between C(H_a) and the right-hand-side of the multiplet, C(H_c). Within the multiplet, C(H_b) and C(H_c) show strong coupling to each other (overlapping diagonal and cross-peaks).

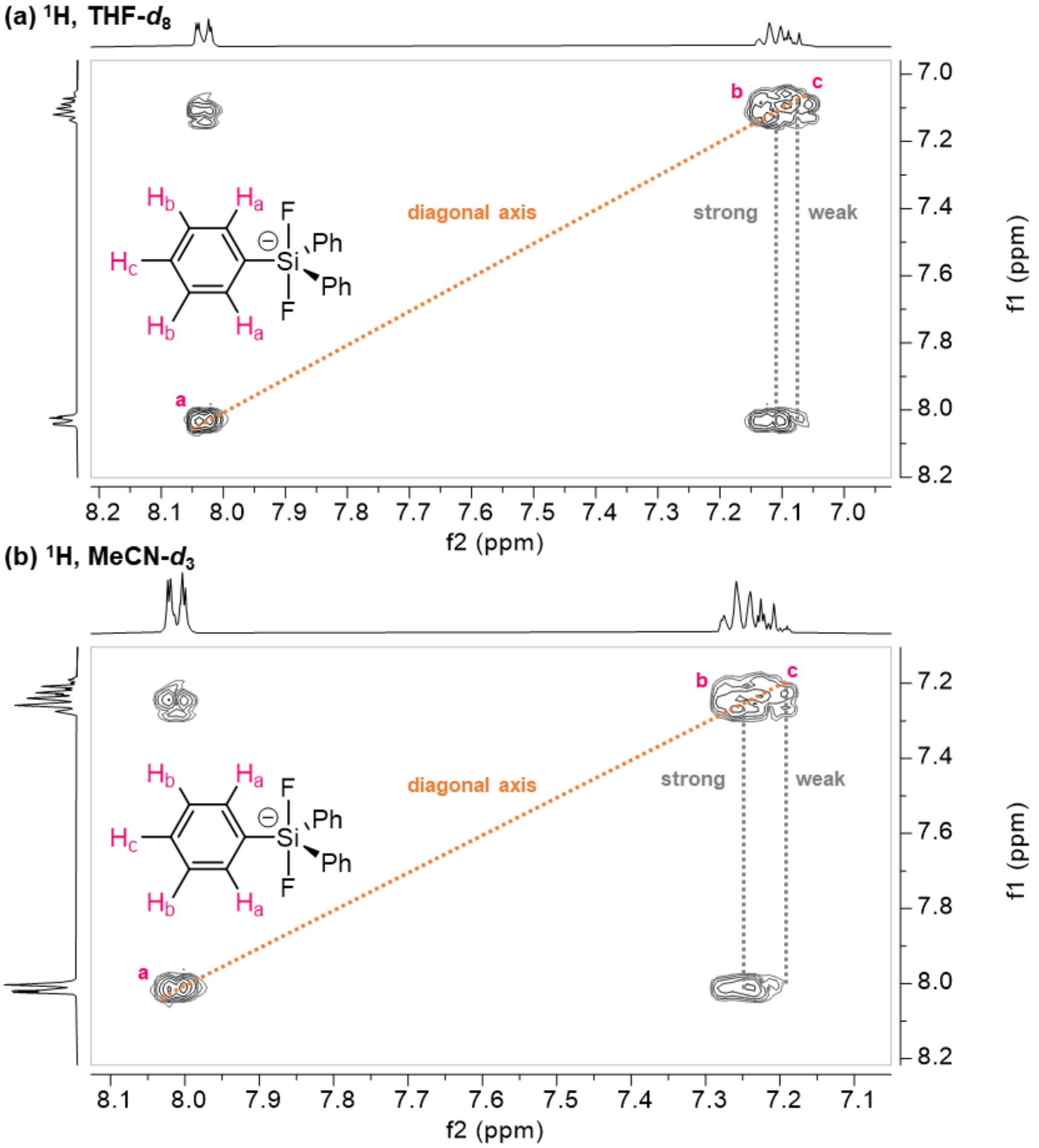

Figure 7.3: Aromatic regions of the ^{1}H–^{1}H COSY spectra of TBAT in (a) THF-d_8 and (b) MeCN-d_3.

^{13}C NMR and ^{1}H–^{13}C correlations

This assignment of the aromatic ^{1}H signals was confirmed by ^{1}H–^{13}C HSQC (pulse sequence: hsqcetgpsp; 128 dummy scans, 2 scans, D_1 = 1.50 s, t_{acq} = 0.262 s) and HMBC (pulse sequence: hmbcetgpl2nd; 128 dummy scans, 2 scans, D_1 = 1.50 s, t_{acq} = 0.262 s) experiments. The ^{13}C NMR spectra of TBAT are presented in Figure 7.4a–b (the aliphatic ^{13}C signals were assigned based on ^{1}H–^{13}C HSQC). The aromatic regions of the spectra show: a triplet (THF-d_8: 152.7 ppm, $^2J_{FC}$ = 41.9 Hz; MeCN-d_3: 151.8 ppm, $^2J_{FC}$ = 41.5 Hz), a second triplet (THF-d_8: 138.6 ppm, $^3J_{FC}$ = 7.15 Hz; MeCN-d_3: 138.0 ppm, $^3J_{FC}$ = 6.95 Hz), and further upfield – a singlet (THF-d_8: 126.9 ppm; MeCN-d_3: 127.4 ppm) and a broad signal (perhaps a triplet with very weak coupling; THF-d_8: 126.9 ppm, $^4J_{FC} < 2$ Hz; MeCN-d_3: 127.3 ppm, $^4J_{FC} < 2$ Hz), which are partially resolved. Based on the splitting patterns of the signals and measured couplings, the signals were assigned as (from downfield to upfield and with respect to the Si substituent): *ipso*, *ortho*, *para*, *meta*; Figure 7.4a–b. Indeed, the aromatic regions of the ^{1}H–^{13}C HSQC spectra (Figure 7.5 and Figure 7.6 for THF-d_8 and MeCN-d_3, respectively) show correlations between C_2 and H_a, C_3 and H_b, and C_4 and H_c (no correlation was observed for C_1). In the ^{1}H–^{13}C HMBC spectra (aromatic regions, Figure 7.5 and Figure 7.6 for THF-d_8 and MeCN-d_3, respectively), C_1 showed strong correlations with H_a and H_b, and a weak one with H_c. C_2 showed a single-bond correlation with H_a (which is not uncommon in HMBC), a strong correlation with H_c and a weaker one with H_b.

(a) ^{13}C, THF-d_8

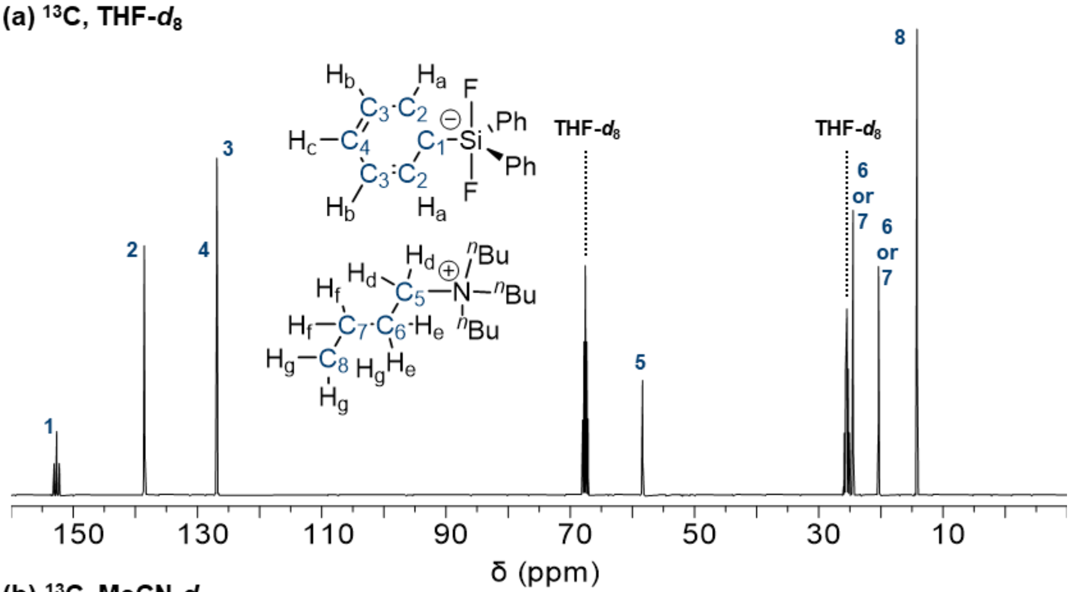

(b) ^{13}C, MeCN-d_3

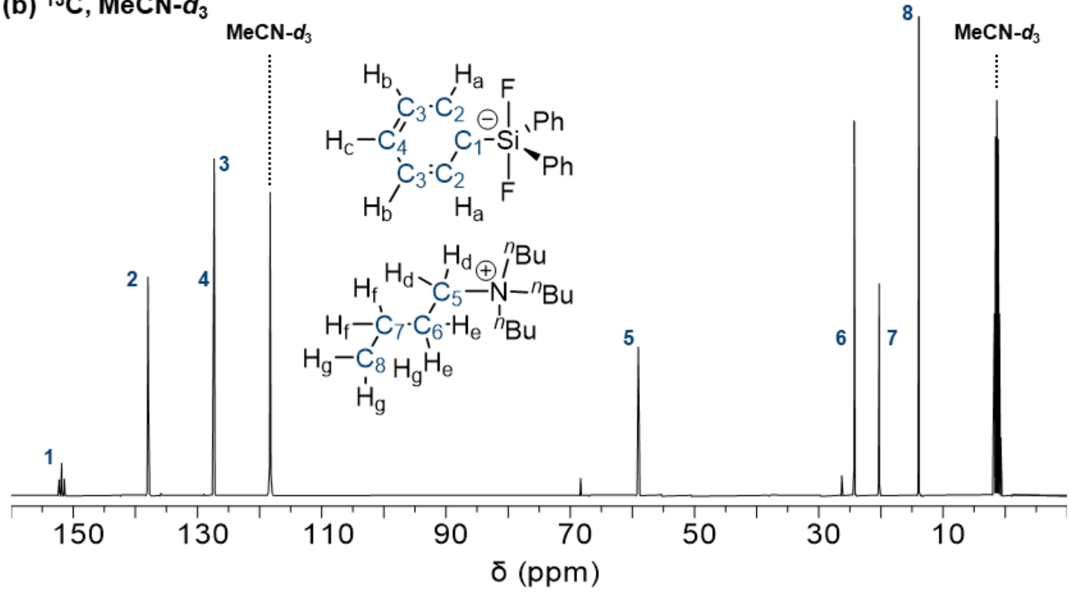

Figure 7.4: ^{13}C NMR spectra of TBAT in (a) THF-d_8 and (b) MeCN-d_3.

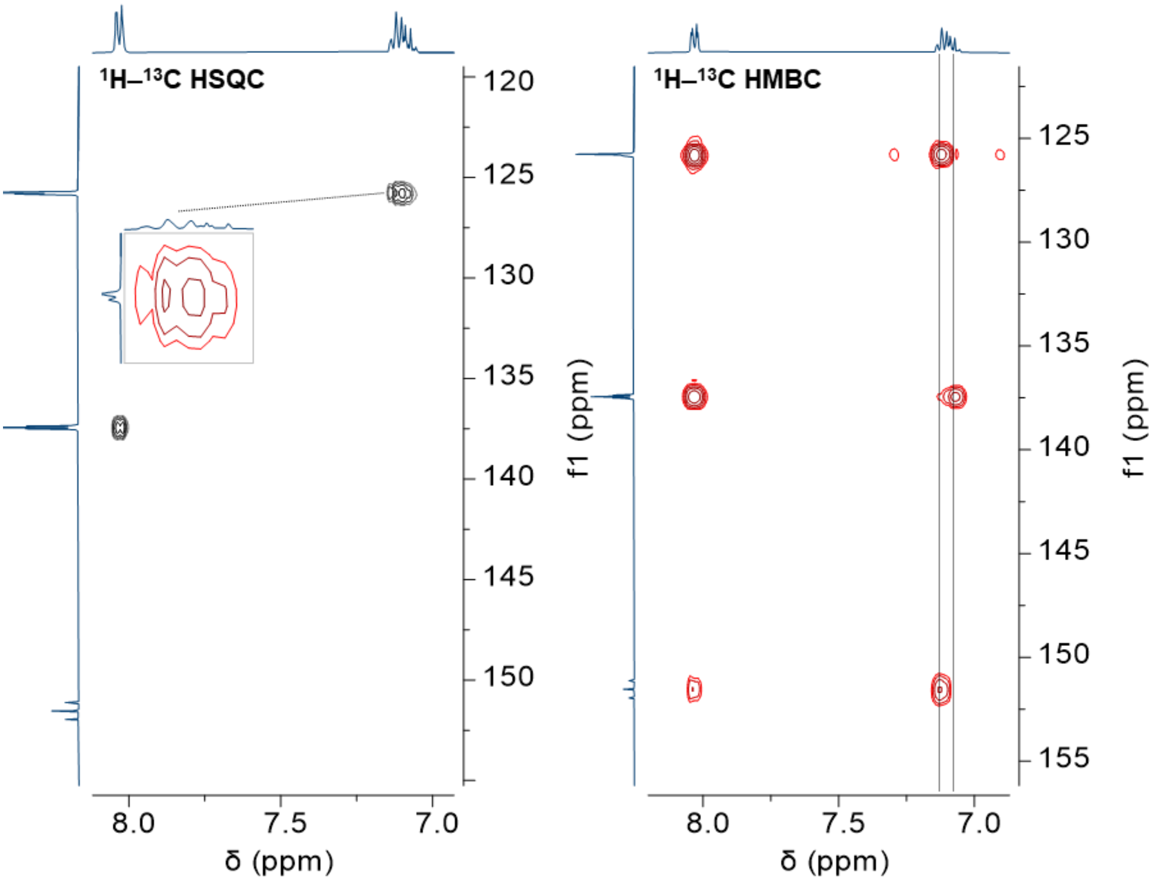

Figure 7.5: Aromatic regions of the ^{1}H–^{13}C HSQC and ^{1}H–^{13}C HMBC spectra of TBAT in THF-d_8.

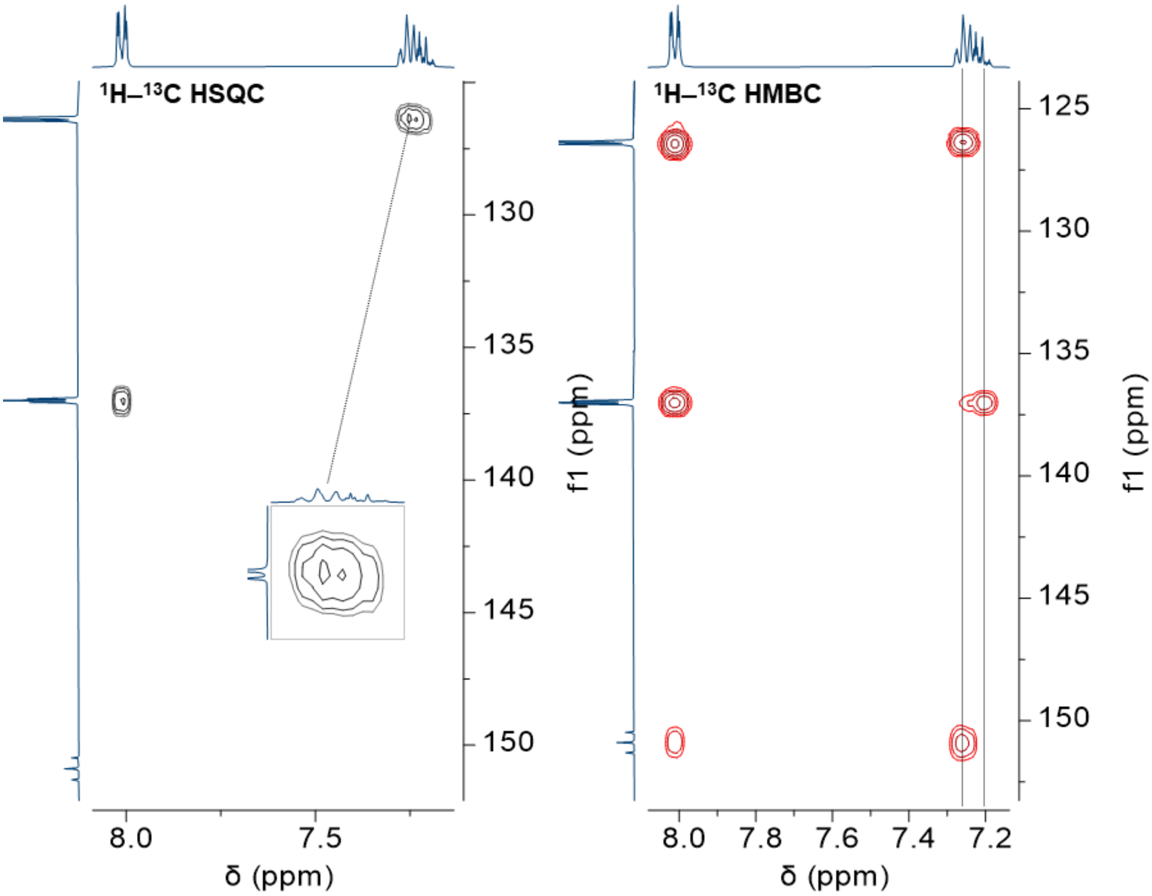

Figure 7.6: Aromatic regions of the ^1H–^{13}C HSQC and ^1H–^{13}C HMBC spectra of TBAT in MeCN-d_3.

7.4. ^{1}H longitudinal relaxation rate constant measurements

Table 7.2: Longitudinal relaxation fitting parameters and root mean square errors for $Ph_3SiF_2^-$ ("–") and ^{n}Bu$_4$N$^+$ ("+") in ^{1}H inversion-recovery experiments of solutions in Table 5.2.

Entry	[TBAT] (mM)[a]	T (K)	$10^{-3}I_{eq}$		x		T_1 (s)		$10^{-3}R$	
			–	+	–	+	–	+	–	+
1	220	300	63.1	152	1.78	1.06	2.06	0.954	0.2	0
1	220	310	62.8	151	1.78	1.07	2.34	1.08	0.2	1
1	220	320	68.6	165	1.78	1.14	2.68	1.16	0.3	1
2	110	300	55.3	133	1.79	1.07	2.34	1.02	0.2	1
2	110	310	58.7	141	1.80	1.14	2.66	1.11	0.2	1
2	110	320	55.7	134	1.81	1.20	2.99	1.24	0.2	1
3	30	300	64.6	156	1.81	1.13	2.81	1.14	0.2	1
3	30	310	63.5	154	1.82	1.18	3.20	1.29	0.2	2
3	30	320	67.3	164	1.84	1.28	3.56	1.39	0.1	2
4	220	300	66.7	154	1.79	1.51	6.64	1.49	0.3	1
4	220	320	63.2	155	1.82	1.57	8.46	1.95	0.2	2
4	220	335	59.9	158	1.88	1.57	8.49	2.34	0.9	2
5	120	300	56.3	140	1.81	1.55	8.02	1.65	0.3	1
5	120	320	52.7	144	1.88	1.61	8.52	2.11	0.3	2
5	120	335	55.8	138	1.90	1.66	9.25	2.38	0.6	2
6	40	300	44.9	156	1.83	1.61	9.42	1.83	0.2	2
6	40	320	66.0	160	1.85	1.64	11.6	2.39	0.2	3
6[b]	40	335	43.1	171	1.81	1.70	13.0	2.66	0.1	2

---

[a] To the nearest 10 mM.

[b] D_1 = 80 s; τ (s) {0, 5, 10, 15, 25, 35, 50, 65, 80}.

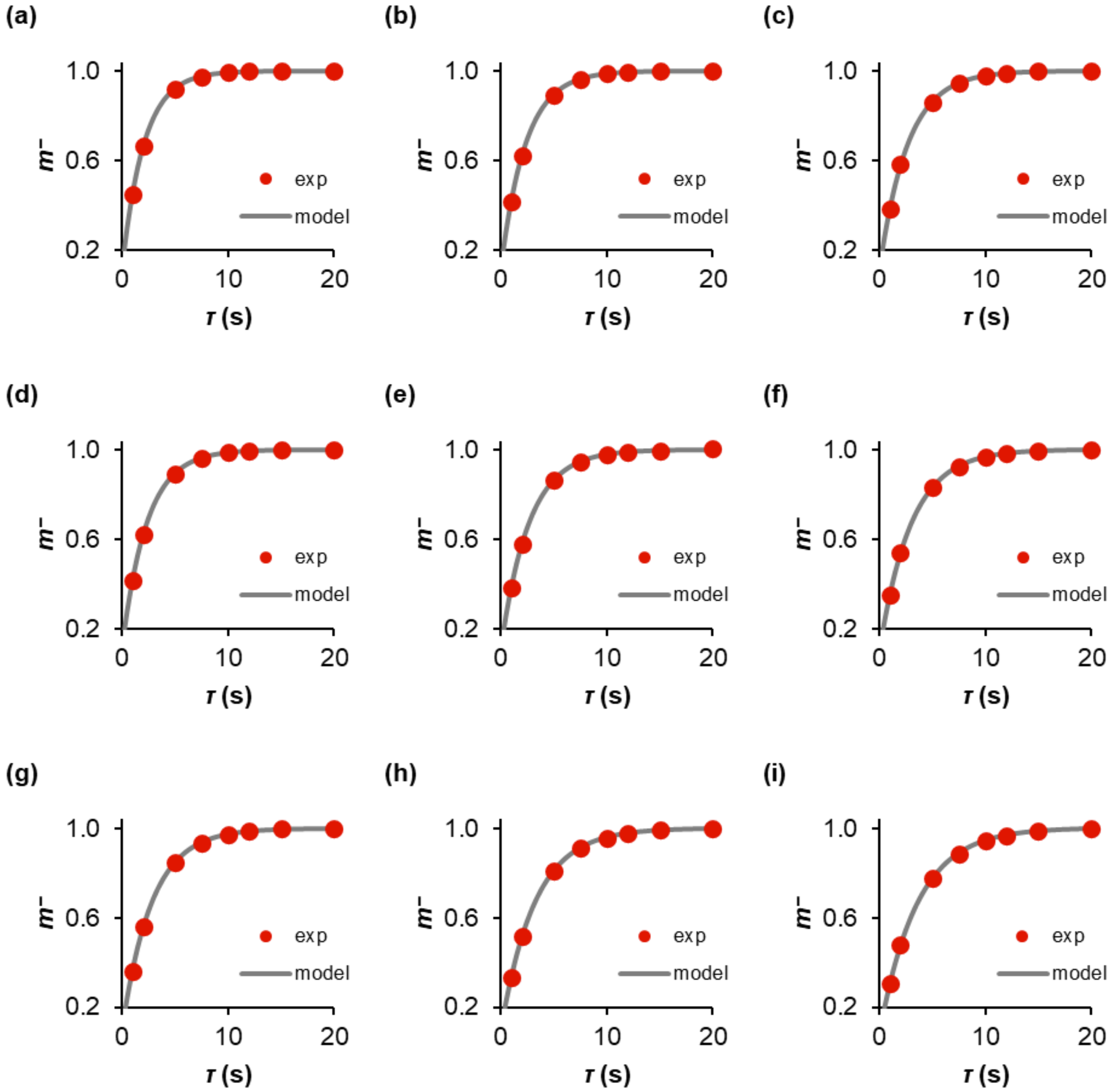

Figure 7.7: Plots of experimental ("exp") and model fractional magnetisations of Ph$_3$SiF$_2^-$, m^-, in ^{1}H longitudinal relaxation constant measurements of TBAT in THF-d_8. (a) 220 mM at 300 K; (b) 220 mM at 310 K; (c) 220 mM at 320 K; (d) 110 mM at 300 K; (e) 110 mM at 310 K; (f) 110 mM at 320 K; (g) 30 mM at 300 K; (h) 30 mM at 310 K; (i) 30 mM at 320 K.

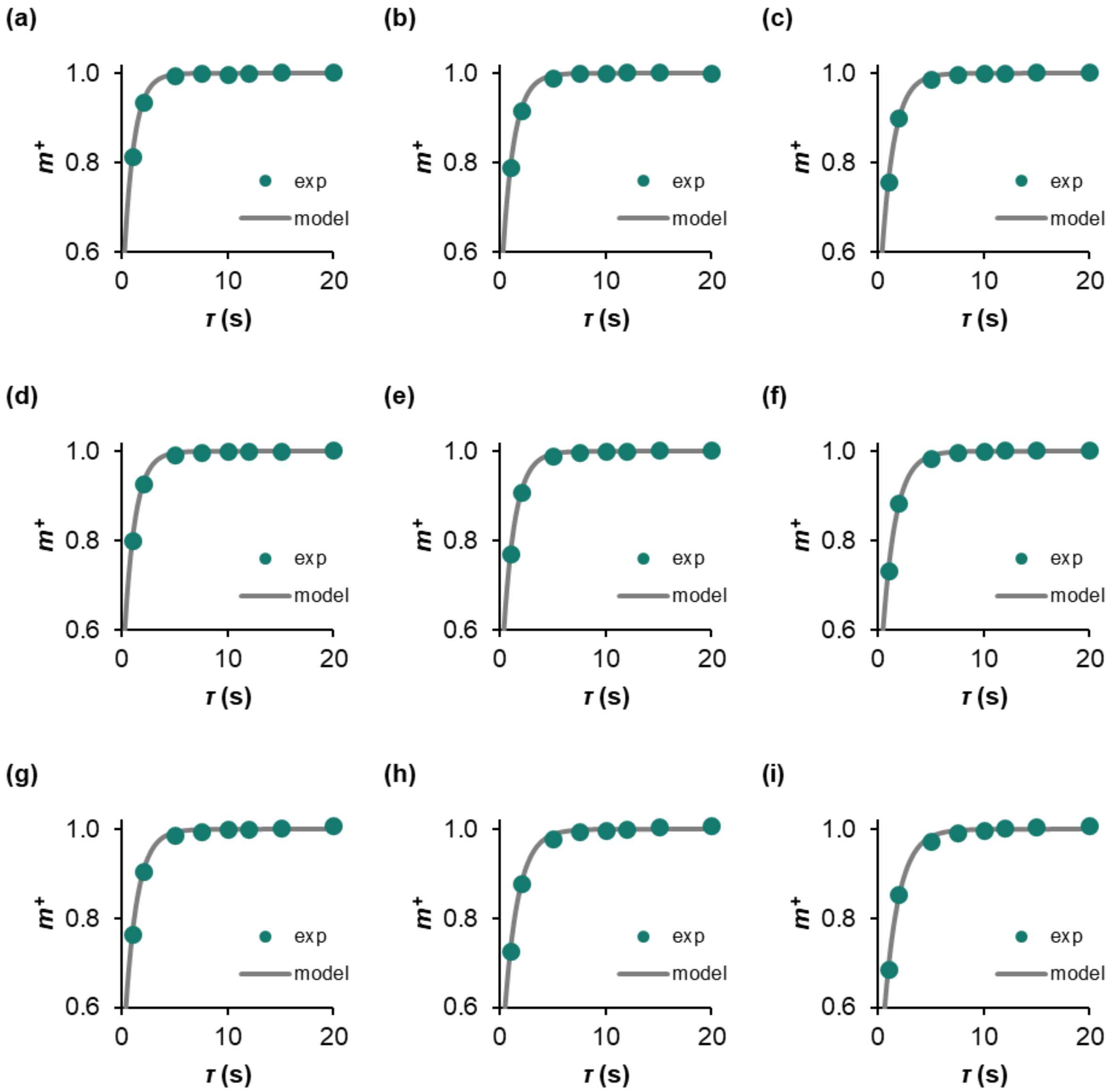

Figure 7.8: Plots of experimental ("exp") and model fractional magnetisations of ^{n}Bu$_4$N$^+$, m^+, in ^{1}H longitudinal relaxation constant measurements of TBAT in THF-d_8. (a) 220 mM at 300 K; (b) 220 mM at 310 K; (c) 220 mM at 320 K; (d) 110 mM at 300 K; (e) 110 mM at 310 K; (f) 110 mM at 320 K; (g) 30 mM at 300 K; (h) 30 mM at 310 K; (i) 30 mM at 320 K.

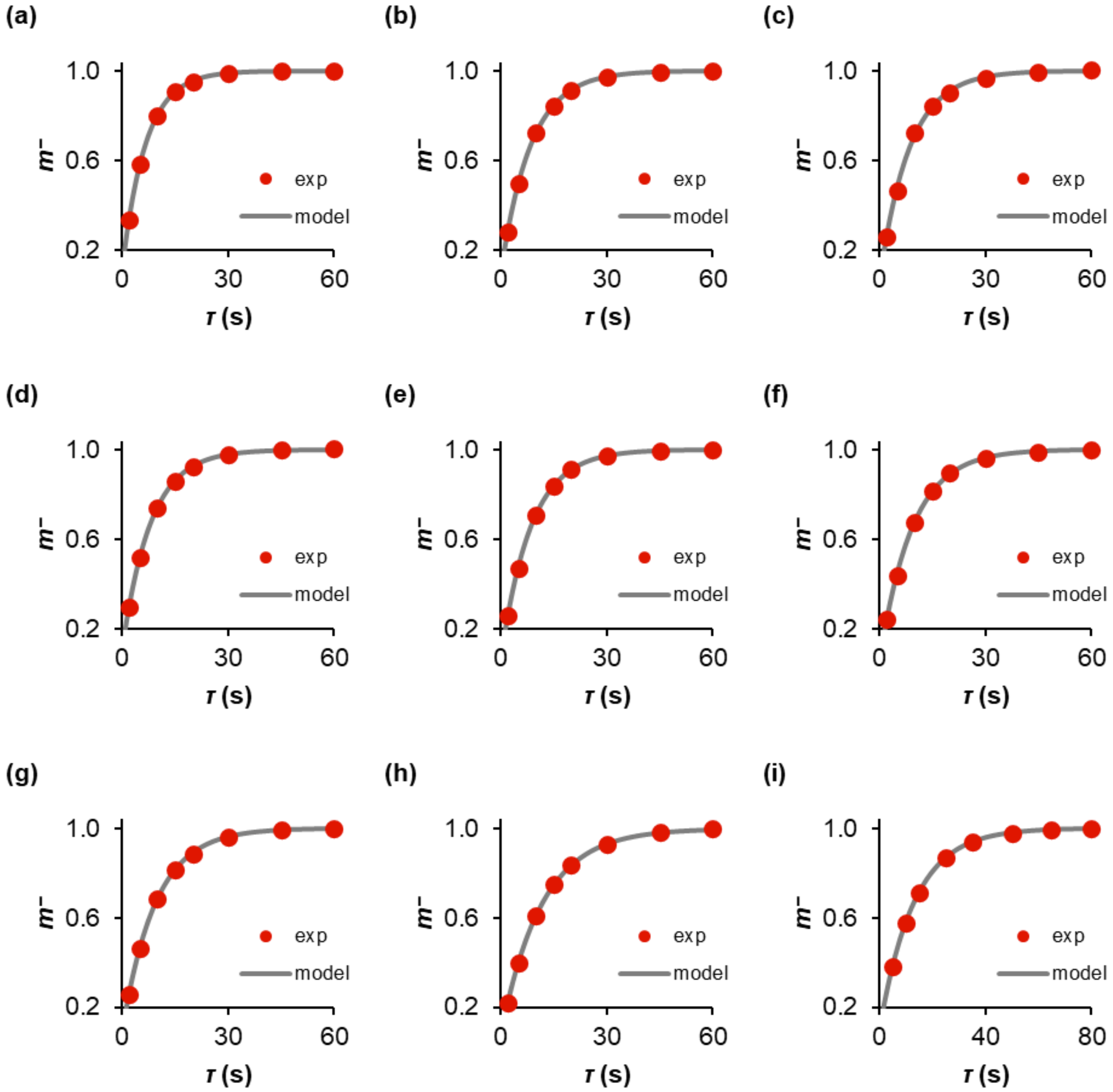

Figure 7.9: Plots of experimental (“exp”) and model fractional magnetisations of $Ph_3SiF_2^-$, m^-, in ^1H longitudinal relaxation constant measurements of TBAT in MeCN-d_3. (a) 220 mM at 300 K; (b) 220 mM at 320 K; (c) 220 mM at 335 K; (d) 120 mM at 300 K; (e) 120 mM at 320 K; (f) 120 mM at 335 K; (g) 40 mM at 300 K; (h) 40 mM at 320 K; (i) 40 mM at 335 K.

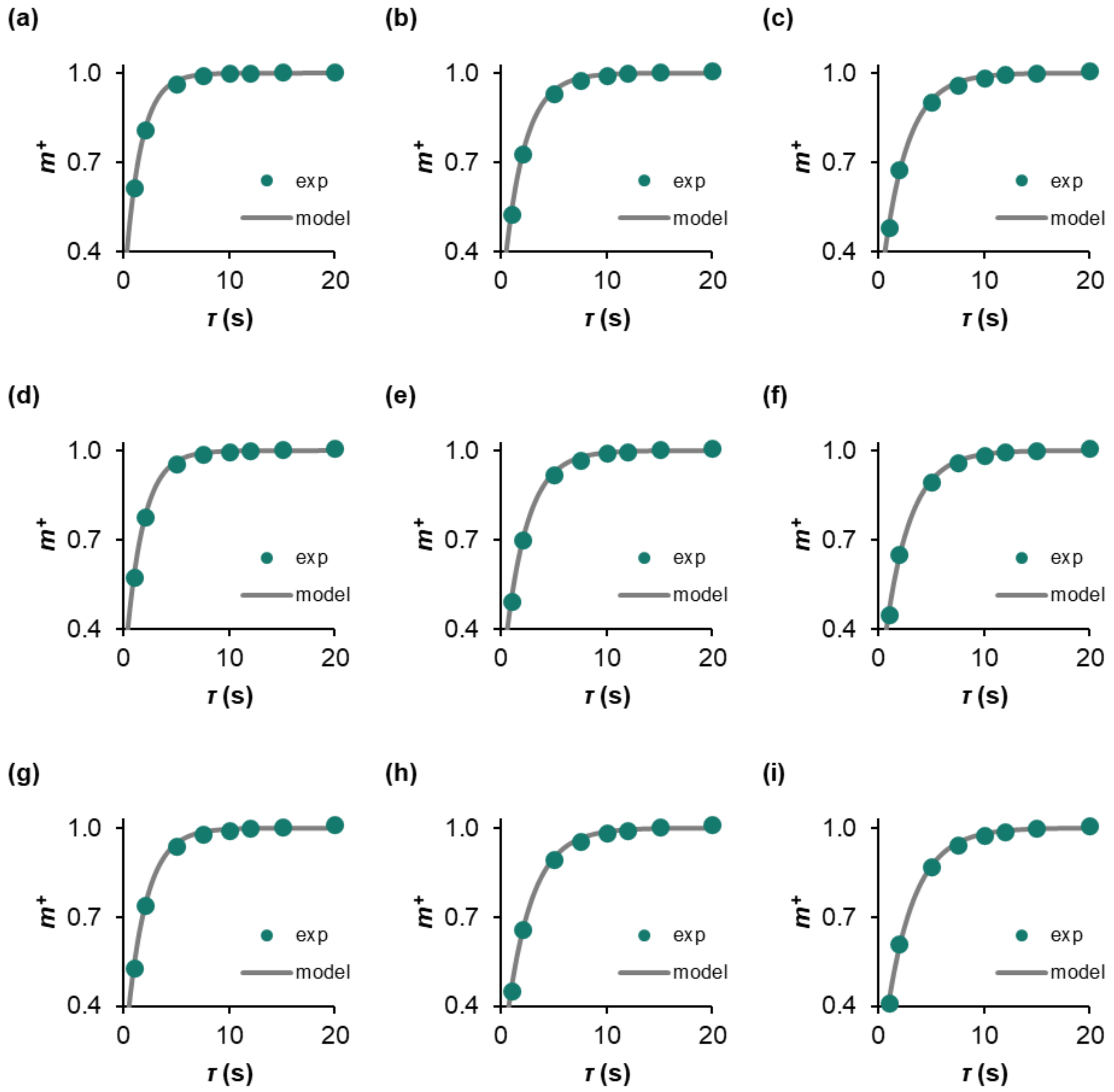

Figure 7.10: Plots of experimental ("exp") and model fractional magnetisations of ^{n}Bu$_4$N$^+$, m^+, in ^{1}H longitudinal relaxation constant measurements of TBAT in MeCN-d_3. (a) 220 mM at 300 K; (b) 220 mM at 320 K; (c) 220 mM at 335 K; (d) 120 mM at 300 K; (e) 120 mM at 320 K; (f) 120 mM at 335 K; (g) 40 mM at 300 K; (h) 40 mM at 320 K; (i) 40 mM at 335 K.

Table 7.3: Longitudinal relaxation fitting parameters and root mean square errors for $Ph_3SiF_2^-$ ("–"), ^{n}Bu$_4$N$^+$ ("+") and TMB (CH_3) in ^{1}H inversion-recovery experiments of solutions in Table 5.4.

Entry	[TBAT] (mM)	T (K)	$10^{-3}I_{eq}$		x		T_1 (s)		$10^{-3}R$	
			–	+	–	+	–	+	–	+
1[a]	207	300	47.5	114	1.78	1.05	1.99	0.935	0.3	0
2[b]	0.0015	300	1.09	2.37	1.81	1.27	2.90	1.02	0.01	0.01

---

[a] $10^{-3}I_{eq}^{TMB} = 35.5$, $x^{TMB} = 1.85$, $T_1^{TMB} = 2.99$ s, $10^{-3}R^{TMB} = 0.0$.
[b] $10^{-3}I_{eq}^{TMB} = 125$, $x^{TMB} = 1.83$, $T_1^{TMB} = 1.58$ s, $10^{-3}R^{TMB} = 0$.

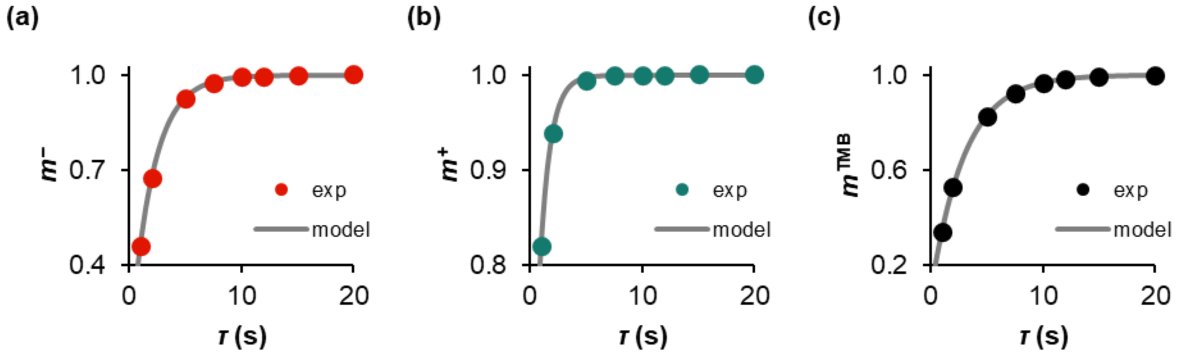

Figure 7.11: Plots of experimental ("exp") and model fractional magnetisations of (a) $Ph_3SiF_2^-$, m^-, (b) $^nBu_4N^+$, m^+, and (c) TMB (CH_3), m^{TMB}, in ^1H longitudinal relaxation constant measurements of TBAT in THF-d_8 at 300 K (207 mM TBAT, 252 mM TMB).

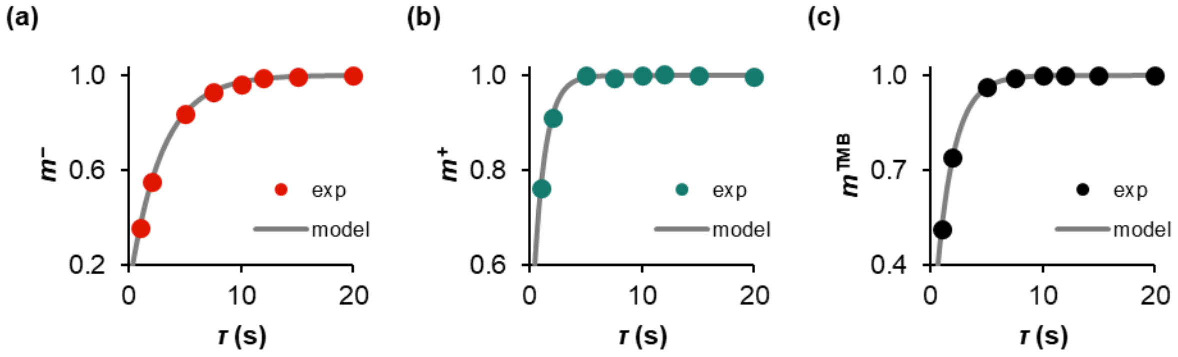

Figure 7.12: Plots of experimental ("exp") and model fractional magnetisations of (a) $Ph_3SiF_2^-$, m^-, (b) $^nBu_4N^+$, m^+, and (c) TMB (CH_3), m^{TMB}, in ^1H longitudinal relaxation constant measurements of TBAT in DMSO-d_6 at 300 K (0.0015 mM TBAT, 263 mM TMB).

Table 7.4: Longitudinal relaxation fitting parameters and root mean square errors for BARF⁻ ("–"), $^nBu_4N^+$ ("+") and TMB (CH_3) in ^1H inversion-recovery experiments of the solution in Table 5.5.

Entry	[TBAT] (mM)	T (K)	$10^{-3}I_{eq}$		x		T_1 (s)		$10^{-3}R$	
			–	+	–	+	–	+	–	+
1[a]	201	300	41.8	115	1.72	1.25	2.70	1.16	0.5	1

---

[a] $10^{-3}I_{eq}^{TMB} = 40.4$, $x^{TMB} = 1.83$, $T_1^{TMB} = 2.88$ s, $10^{-3}R^{TMB} = 0.0$.

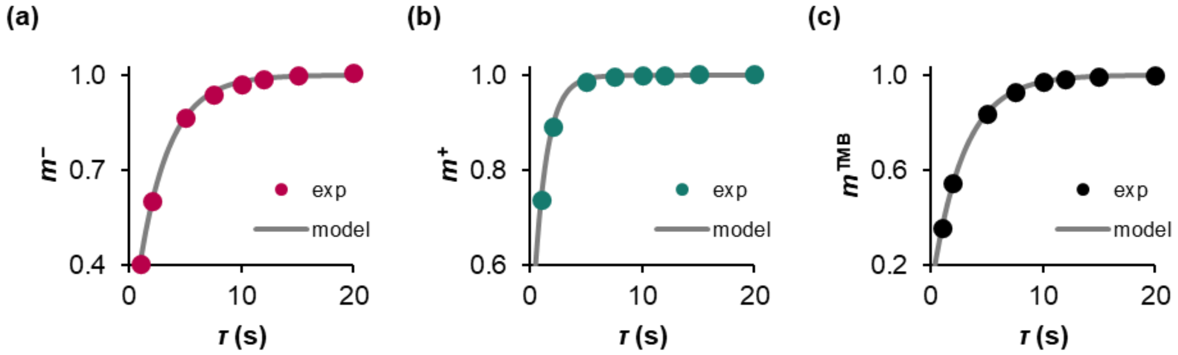

Figure 7.13: Plots of experimental (“exp”) and model fractional magnetisations of (a) BARF⁻, m^-, (b) ^{n}Bu$_4$N$^+$, m^+, and (c) TMB (CH$_3$), m^{TMB}, in ^{1}H longitudinal relaxation constant measurement of TBABARF in THF-d_8 at 300 K (201 mM TBABARF, 256 mM TMB).

7.5. ^{19}F longitudinal relaxation rate constant measurements

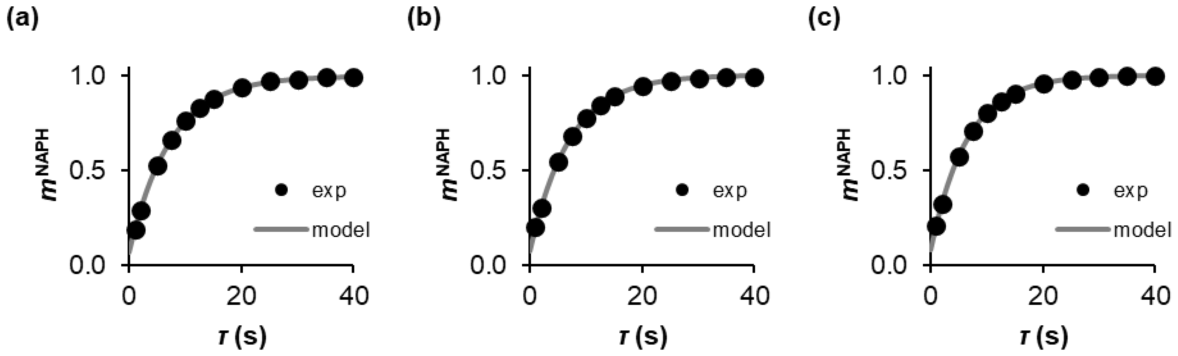

Figure 7.14: Plots of experimental (“exp”) and model fractional magnetisations of NAPH, m^{NAPH}, in ^{19}F longitudinal relaxation constant measurements of NAPH in THF at 300 K. (a) 185 mM; (b) 211 mM; (c) 529 mM.